Synthesis and characterization of carbon-based nanostructured material electrodes for designing novel hybrid supercapacitors

by

Oyedotun Kabir Oyeniran

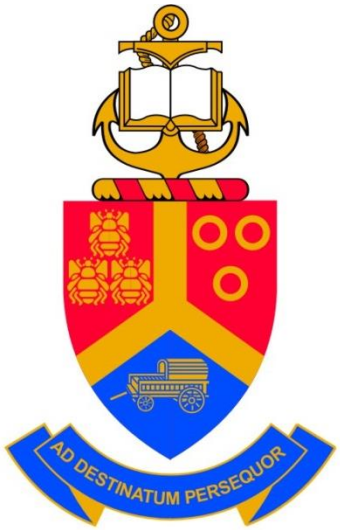

A thesis submitted in partial fulfillment of the requirements for the degree of

DOCTOR OF PHILOSOPHY (PhD.) IN PHYSICS

Faculty of Natural and Agricultural Sciences

University of Pretoria

Hatfield Pretoria

July 2018

Supervisor/promoter: **Prof. N. I. Manyala**

Declaration

I, **OYEDOTUN KABIR OYENIRAN**, student number 14451850, declare that this thesis, which I hereby submit for the degree of Doctor of Philosophy in Physics at the University of Pretoria, is my own work and has not been previously submitted by me for a degree at this or any other tertiary institution.

SIGNATURE: .....

DATE: .....

Dedication

To the Glory of Almighty God,

And my late mother,

Mrs Zikrat Adunni Oyedotun.

Acknowledgements

My foremost and sincere appreciation goes to Almighty God the most beneficent, the merciful who has been my guide and provider throughout the course of my program and in the course of carrying out this research work.

My heartfelt gratitude goes to my supervisor/promoter, Prof. Ncholu Manyala for his relentless effort and assistance rendered in ensuring the success of this work. I acknowledge his unending guidance, support, trust and the great input to my academic career.

I am very grateful to Prof. C. Theron, head of Physics Department for his immeasurable contribution towards the successful completion of the program. I sincerely appreciate the financial support from the University of Pretoria and National Research Foundation (NRF) for this PhD study.

I acknowledge Dr. Andre Botha, Dr. Eudri Venter, Dr. Chantelle Venter, Irene, Adna, Antoinette and others in the microscopy unit for their technical assistance during the SEM, TEM and EDX measurements; Mrs Wiebke Grote and J. E. Strydom for assistance with the XRD and XRF measurements; as well as Dr. Mbuso Mlambo for the Raman and FTIR measurements and training.

My sincere appreciation goes to Mrs Suzette Seymore, Isbe VanDerWesthuizen and Allette at the Institute for Advanced Materials laboratory, South Campus for their endless assistance in materials procurement and laboratory work.

Special appreciations go to Dr. Julien K. Dangbegnon, Dr. Abdulhakeem Bello, Dr. D. Y. Momodu, Dr. T. M. Masikhwa, Dr, Jack Madito, Dr. Farshad Barzegar, Dr. Abubakar

Khaleed, and Dr. Bridget Mutuma of the Carbon and Advanced Nanomaterials group for their selfless supports during the course of the study.

My sincere gratitude to the rest of my colleagues in the Carbon and Advanced Nanomaterials group; Mr. Abdulmajid Mirghni, Mr. O. Olaniyan, Mrs Faith Ochai Ejhei, Ms Maty, Ms Belinda Moyo, Mr. Tjatji Jebane, Mr. O. Fasakin, and Badr Mohammed for their reliable assistance when required and a pleasant working environment. I love you all.

I am very grateful to Dr. Ezekiel Omotoso and his family for the invaluable inputs into my life and my family as a whole. I really appreciate Dr. Omotoso for his assistance of all kinds towards the success of this program. Dr. Emmanuel Igumbor is also appreciated for his assistance.

A special and unending gratitude to my ever-loving and understanding wife, Mrs Florence Olufunmilayo Oyedotun, and my daughter, Miss Anam Oluwafeyikemi Oyedotun for their patience, prayers and supports of all kinds during the course of the study.

My sincere gratitude to the His Royal Highness, Oba Nureni Abioye, The Olubode of Bode-Osi, my fatherly mentor, Dr. A. Z. Solomon, my aged father, Mr. Muili Iyanda Oyedotun and all my family members for their endless prayer and support towards the completion of the study.

Abstract

Recent research efforts are focused on alternative energy production instead of fossil fuels. Meanwhile, the developments of more efficient energy storage devices are driven by many factors. One is related to our environment. There is a need to significantly control emission of greenhouse gases, and reduce the amount of global warming majorly caused by fossil fuels. The products of combustion processes from fossil fuel usually lead to environmental pollution and poisonous atmospheric smog in our environment. In spite of growing developments in addressing various issues inherent to energy storage devices, supercapacitors continue to exhibit low energy density when compared with lithium ion batteries. The study in this thesis has utilized low-cost and environmentally-friendly carbon-based nanostructured hybrid materials as electrodes for designing a novel hybrid supercapacitor, which allows for a bolstering alliance of characteristics of dissimilar components in synergistic combinations, therefore providing enhanced energy and power densities by combining battery and supercapacitor materials storage mechanisms. Morphologies, compositions, structures and surface area/pore size distribution of the as-prepared materials nanocomposites were characterized using field-emission scanning electron microscopy (FESEM), transmission electron microscopy (TEM), energy dispersive X-ray spectroscopy (EDX), X-ray powder diffraction (XRD), Raman spectroscopy, Fourier transform infrared (FTIR) spectroscopy, thermal gravimetric analysis (TGA), X-ray photoelectron spectroscopy (XPS), Brunauer-Emmett-Teller (BET) and X-ray fluorescence (XRF), while the performance characteristics were electrochemically evaluated through cyclic voltammetry and charge/discharge cycling in both three- and two-electrode configurations. Electrodes fabricated from both graphene oxide (GO) nanogel gel and carbon nanorods materials gave a maximum specific capacitance of

436.5 F g^{-1} and 719.5 F g^{-1} corresponding to specific capacities of 48.5 mAh g^{-1} and 80.8 mAh g^{-1} at a specific current of 0.5 A g^{-1} respectively. The assembled hybrid asymmetric supercapacitor with carbonized iron cations (C-FP) selected as the negative electrode, NiCo-MnO_2//C-FP proved a specific capacitance of 130.67 F g^{-1}, high energy and power densities of 48.83 Wh kg^{-1} and 896.88 W kg^{-1} at 1 A g^{-1} respectively, with an excellent cycling stability for up to 10,000 cycles. Also, an assembled Ti_3C_2-Mn_3O_4//C-FP delivered a specific capacity of 78.9 mAh g^{-1}, high energy and power densities of 28.3 Wh kg^{-1} and 463.4 W kg^{-1} at 1 A g^{-1} respectively. The device showed good cycling stability with an energy efficiency of 90.2% and capacitance retention of 92.6% for up to 10,000 cycles at a specific current of 3 A g^{-1} over a voltage window of 1.5 V. It is can be observed that electrolyte selection is critically important to achieving better performance for carbon-based material electrodes for enhanced supercapacitors electrochemical performance. Thus, this work is subjected to further studies by exploiting organic and ionic liquid electrolytes that may greatly enhanced the energy density and stability of the device.

TABLE OF CONTENTS

List of Figures

List of Equations

Chapter 1

1.1 Introduction

1.2 Background and motivation of the study

Most of the electrical energy used in the world is currently supplied from fossil fuels. Therefore, measures are being adopted in a variety of different fields to help prevent global warming by reducing CO_2 emissions. Hence, the automotive industry has become a focal point when considering the impact of fossil fuel use on our environment. The ever increasing human population concomitant with increasing energy consumption and demand has left the energy sector with a huge challenge of meeting the ever increasing energy demand owing to the consistent rise in human population. Therefore, this is making energy research technologies a crucial aspect in the scientific world. The over dependence on fossil fuels and other associated natural resources pose high risks to human life due to associated environmental degradation through climate changes and toxic gas emissions that may result in high cost of management. Thus, a model shift from fossil fuels to a greener, environmentally-friendly and cost effective energy source is necessary to meet up with the ever increasing energy demand for convenient management and sustainability of available energy, as well as to keep up with the appeal for environmental protection [1], [2]. Hence, the use of renewable energy sources that can further improve the energy efficiency has been identified as potential solution to achieve the goal. Solar and wind energy technologies are becoming promising sources with large fluctuations in the generation of electricity. Today, numerous exciting renewable energy technologies are being developed, such as mechanical, thermal, physical,

chemical and electrochemical energy storage systems. Batteries are mostly being used to store energy, nevertheless, their reliability does not seem to stand the ever-growing demands in technological applications. Electrochemical capacitors also known as supercapacitors are energy storage devices with high power capability, long cyclic life, fast charge propagation dynamics with cost-effectiveness and are thus, a perfect fit as an alternative to batteries for energy storage applications [2].

Supercapacitors have attracted attention due to their potential to be used in electric/hybrid electric vehicles, backup memories, airplane emergency doors, micro-devices and portable electronics. They store charges in a highly reversible pathway which enable them to be useful in long term applications paving the way for the development of fast energy storage technology [2]–[4]. They have also been identified to possess superior power density relative to batteries with a higher energy density than conventional capacitors. Supercapacitors performances depend on the materials' properties, thus, optimization of materials' properties plays a crucial role in energy conversion and storage technologies.

More importantly, advances in environmental technology, such as the emergence of hybrid electric vehicles in the 1990's, have brought innovation to an era when vehicles have been traditionally powered by gasoline [2], [4]. Consequently, the challenge facing the energy research world remains the development of efficient intermediate hybrid materials with a blend of both batteries and capacitors features. Carbon based materials have been playing a crucial role in the development of alternative clean and sustainable energy technologies such as batteries, supercapacitors, and fuel cells owing to their unique properties which include high specific surface area, electrical conductivity, thermal and chemical stability as well as cost-effectiveness [5], [6]. Carbon materials find an application in supercapacitors which are characterized by a low energy density, and are mainly used in hybrid systems, providing the

high power that a lithium battery is unable to deliver reversibly. In this case, the electrode materials are based on high specific surface area nanostructured carbons [5], [7]. However, there is need to search for new and optimized carbon materials with well-controlled nanostructure and surface functionality, in order to improve the storage capacity and the cycle ability of the power supply [4], [5].

Supercapacitors (SCs) can be divided into three categories viz: (1) Electric double-layer capacitors (EDLCs) which arise as a result of charge separation at an electrode/electrolyte interface (electric double-layer capacitive behaviour), (2) pseudocapacitors and redox SCs which use the charge-transfer arising from redox reactions occurring on the surface of the electrode (Faradaic behaviour) and (3) hybrid capacitors which combine both the EDLCs properties with a battery-type electrode material to form asymmetric SCs or hybrid systems [8].

EDLCs are mainly carbon materials that store energy through charge accumulation at the interface between electrode and electrolyte via induced polarization with a mechanism similar to that of a conventional capacitor. Nevertheless, they store a higher magnitude of charges compared to the conventional capacitor due to their superior specific surface area and the short charge separation distance [9]. Unlike batteries, the electrolyte ions that accounts for charge mobility in-between electrode material and the electrolyte interface requires very fast processes [4]. This is responsible for their short-term pulse (dynamic charge-propagation), making them highly useful in evolving technologies like electric trains, emergency doors, hybrid electric cars etc., that require initial high specific power.

Pseudocapacitive and redox electrochemical capacitors store energy using fast charge transfer through a redox process, which uses metal oxides, metal hydroxides, layered double hydroxides and conducting polymers as active electrode materials. They possess high

theoretical specific capacitances cum battery-like capacitive behavior compared to the EDLCs, but differ from batteries in terms of charge and discharge behavior, which occurs within seconds or minutes [8], [10]. A hybrid material is one that is composed of at least two components (usually an organic and an inorganic component), which are molecularly distributed throughout the material [11]. It is a special case of composites with a blend of the various components on the molecular length scale.

Hybrid capacitors/devices on the other hand, combine both the EDLCs and battery-like electrode materials' properties to form asymmetric SCs or hybrid systems. The hybrid (asymmetric) capacitor can overcome the energy density limitation of the conventional EDLCs since it employs a hybrid system of a battery-like (Faradaic) electrode and a capacitor-like (non-Faradaic) electrode, producing higher working voltage and capacitance/capacity [12], [13].

In spite of the current global research efforts towards generating alternative energy sources from renewable energy to combat global warming and toxic gas emissions, there is still a considerable amount of energy consumption from fossil fuels and other natural resources. Therefore, there is a need for a double edge approach that involves efforts on the generation of alternative energy sources with their corresponding energy storage systems and proper environmental management. This will help in combating the detrimental effects of the remaining fossil fuels usage, as its exploitation has not being completely terminated and is still a dominant source of energy production in a country like South Africa. Today, researchers are focusing more on the fabrication of SCs that can compete favorably with batteries as far as specific energy and long cycle life are concerned. In order to improve the energy density of SCs, scientists search for new electrode materials, new electrolytes and new electrochemical concepts to meet the increasing demand [14]–[16].

An assessment of various research studies related to energy storage device technology has shown extensive efforts by many experts in the field to produce materials with desirable properties [17]. This led to the emergence of various syntheses techniques of new materials, most of which require high temperature reaction environments and a continuous power supply to obtain the final products [8,16,17].

Transition metal hydroxides/oxides nanomaterials have attracted much attention as potential candidates for energy storage devices applications. Generally, transition metal oxides/hydroxides are plagued with a low electrical conductivity but high specific capacity due to their characteristic redox reaction. As such, they do not yield a high performance under high-rate specific currents [19], [20]. On the other hand, transition metal hydroxides/oxides have been intensely studied with a view to overcome the above limitation and refine their properties to fit the desired use [21]. Transition metal hydroxides/oxides are semi-conductive materials among which Ni based oxides have been taken into account as a promising candidate as electrode materials for electrochemical capacitors owing to their cost effectiveness, natural abundance as well as adequate electrochemical performance [22]. The latest progress of NiCo-based application for supercapacitor and battery have been reported in the literature [22]–[24]. Nevertheless, the demonstrated electrochemical performances of the so called supercapacitor electrodes are nonetheless not enough, particularly in terms of energy density.

Carbon materials are suitable for supercapacitor applications due to their good electrical conductivity, high corrosion resistance, large specific surface area, cost-effectiveness, good cycle life, good thermal and chemical stability as well as good substrate materials for other materials deposition for composites synthesis. Forms of carbon suitable for this application

include graphene, onion-like carbons, carbon nanorods/nanotubes and activated carbons, among others [4], [18], [25], [26].

In this thesis, hybrid materials comprising carbon-based materials and transition-metal hydroxide/oxide have been selected as electrode materials with a view to enhancing the energy density and electrochemical stability of supercapacitors, by forming a synergy of the individual electrochemical features of these materials.

1.3 Objectives of the study

The study is focused at investigating the mechanism and enhancing properties of the synthesized samples inclusively, which have not been studied concentratedly still. And to develop a robust 3D network architecture with an anti-aggregation attributes for improved specific energy and long-time cycling via the assembly of a continual 1D carbon-based nanostructures, which provides sharp ion/electron transport tracks cum adequate electrode-electrolyte contact as well as short ion diffusion farness compared with many other nanostructures.

The specific objectives of this research are to:

(i) synthesize sample materials for the preparation of carbon-based nanostructured electrodes with good potentials for energy storage applications;

(ii) synthesize graphene oxide (GO) gel and carbon nanorods obtained from the GO gel using a modified Hummers' method and force-driven reflux process respectively;

(iii) synthesize NiCo-MnO_2 nanocomposite from their mixed metal hydroxides, and carbonized iron cation via salt hydrolysis and annealing processes;

(iv) synthesize two-dimensional Ti_3C_2-Mn_3O_4 nanocomposite and carbonized iron cation (C-FP) using solvothermal technique and an annealing process respectively;

(v) study the electrical, structural, morphological and elemental composition of the samples using various techniques;

(vi) test the suitability of the prepared nanostructured electrode materials as a possible route for preparing supercapacitor materials. The galvanostatic charge-discharge performances cum cyclic voltammetry of the samples will be tested by using an electrochemical workstation.

1.4 Structure of the thesis

This thesis is split into five chapters:

Chapter 1 presents the detailed background introduction and motivation of the research work, aims and objectives and the structure of the thesis

Chapter 2 presents a literature review on supercapacitors (electrochemical capacitors).

Chapter 3 describes the details of the synthesis procedures and characterization techniques employed in this work.

Chapter 4 describes the results obtained from the synthesis, characterization and electrochemical measurements of the as-prepared carbon based nanostructured materials.

Chapter 5 depicts the general conclusion derived from this study as well as recommendations on the future study.

Chapter 2

2.1 Literature review

2.1.1 Energy storage systems

An energy storage device is an apparatus used to store electrical energy when needed and release the stored energy when required. The role of energy storage device technology in fields such as renewable energy generation and electric/hybrid electric automobile systems has become increasingly important in modern society as a measure of checking the ever increasing global warming. Among common electrical energy storage devices in use are lead–acid batteries, lithium ion batteries (LIBs) and supercapacitors. Batteries with high energy density and supercapacitors (SCs) with excellent power density are currently considered to meet the needs of increasing energy demand [27]. LIBs can store a large amount of energy, as high as 150-200 Wh kg^{-1}, but are confined to their low power density (below 1000 W kg^{-1}) and poor cycle life (usually less than 1000 cycles) [28].

The most widespread known energy storage devices are the batteries, particularly, secondary batteries also known as rechargeable batteries such as lithium ion batteries (LIBs), which are often used in energy storage applications. One of the most promising and effective methods to store energy is through a LIB due to its high specific energy density and light weight [27]. Rechargeable batteries like LIBs are in great demand in modern society due to the development of numerous portable consumer electronic devices such as mobile phones and laptops, and the emergence of plug-in electric/hybrid electric vehicles. Capacitors store rather small amounts of energy and are widely used in electronic devices [29]. A supercapacitor is a

special type of capacitor which has a larger energy density than conventional capacitors. Supercapacitors possess capacitances that are a much orders of magnitude higher compared to the conventional capacitors [30]. They can store 10 to 100 times more energy per unit volume/mass than conventional capacitors, accept and deliver charge much faster than batteries, and tolerate many more charge and discharge cycles than rechargeable batteries [31]. A Ragone chart in Fig. 2.1 shows relationship between the power and energy densities of various energy storage devices.

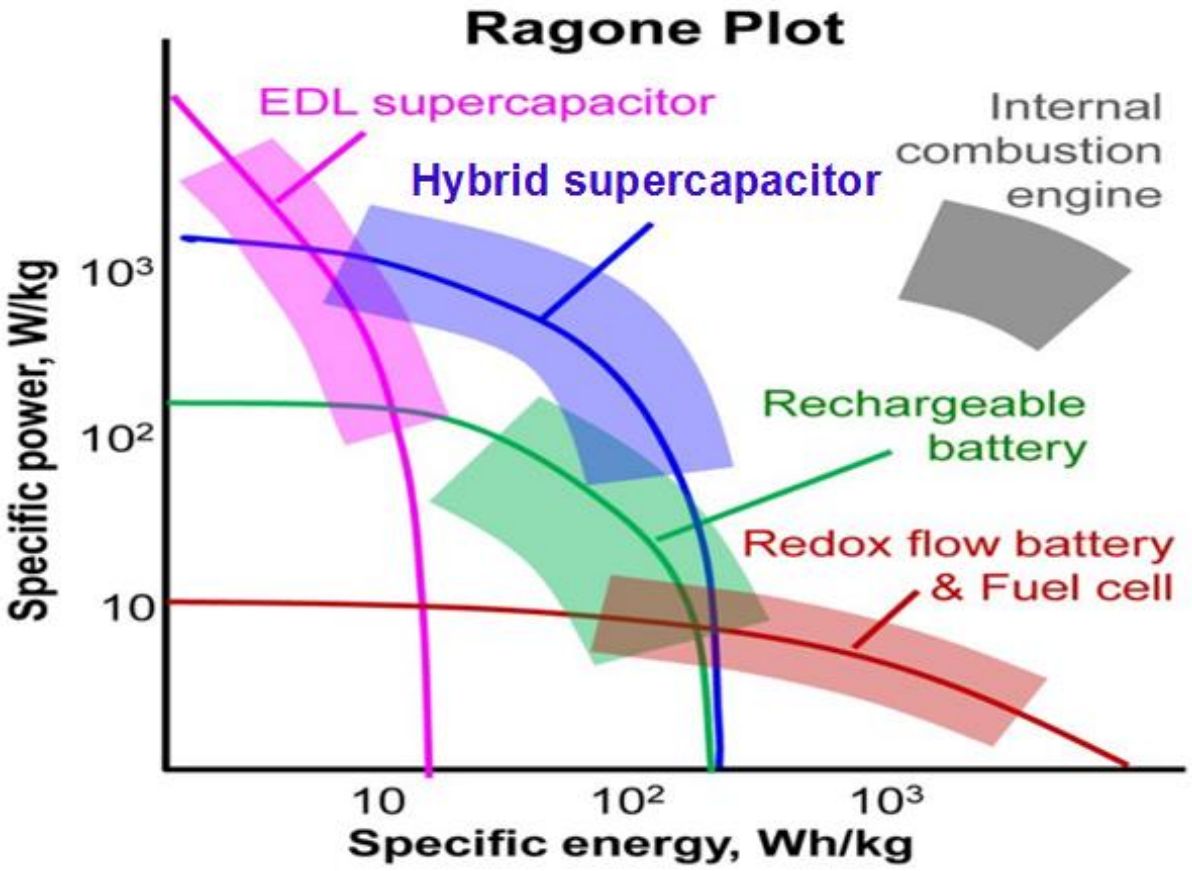

Figure 2.1: Ragone chart showing energy density as a function of power density of various capacitors and batteries (adapted from [32])

2.1.2 Capacitors (Cs)

Capacitors can be divided into three categories namely, electrolytic capacitors, non-electrolytic capacitors and supercapacitors [29], which can be specified further through materials combinations [33]. Generally, a capacitor comprises two conducting metal plates and a dielectric medium in between, and stores energy electrostatically [29]. Fig. 2.2 shows the composition and working principle of an ideal parallel plate capacitor. In a charged capacitor the metal plates are oppositely charged and an electric field is formed in the dielectric medium [29]. When charged, the energy is stored in a static electric that permeates the dielectric between the electrodes. The total energy increases with the amount of stored charge, which in turn correlates linearly with the potential between the plates. The maximum potential difference between the plates is limited by the dielectric's breakdown field strength. The capacitance, C can be defined as [29,32]:

$$C = \frac{Q}{V} \qquad \mathbf{1}$$

where Q refers to the charge (Coulomb) and V to the potential (volts). Furthermore, the capacitance C of a parallel plate capacitor can be described as:

$$C = \in_o \in_r \frac{A}{d} \qquad \mathbf{2}$$

where $\in_o$ is the vacuum permittivity and $\in_r$ is the relative permittivity of the medium. A is the electrode area (m^2) and d is the distance (m) between the electrodes.

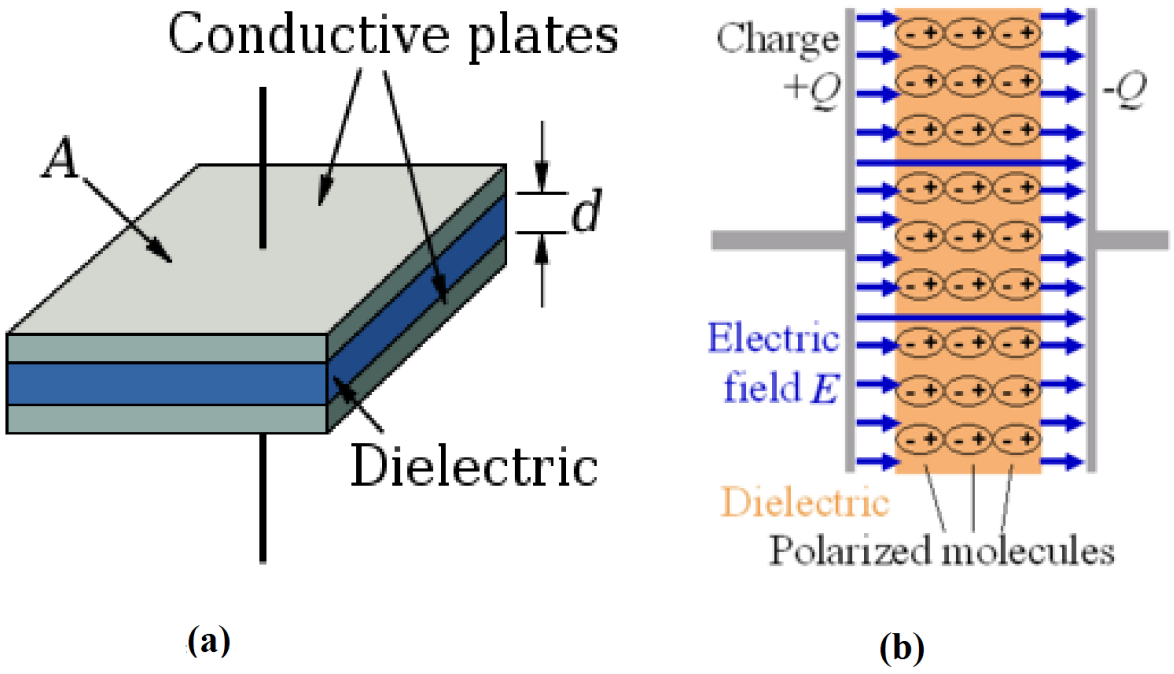

Figure 2.2: A schematic diagram of (a) the design of a parallel plate capacitor (adapted from [35]); and (b) a charged parallel plate capacitor (adapted from [34]).

2.1.2.1 Supercapacitors (SCs)

Supercapacitors are a general term for various types of electrochemical capacitors. They are a high-capacity device with capacitance values much higher than that of the conventional capacitors but with lower voltage limits, that bridge the gap between electrolytic capacitors and rechargeable batteries. They typically store 10 to 100 times more energy per unit volume or mass than conventional capacitors. Supercapacitors can accept and deliver charge much faster than batteries, and tolerate many more charge and discharge cycles than rechargeable batteries [9]. They can be used to complement batteries or to extend the life-time of batteries by balancing temporary power peaks [36], [37]**.** SCs can be divided into electric double layer capacitors (EDLCs), pseudo-/Faradaic capacitors (PCs), and hybrid capacitors (HCs)

according to the mode of energy storage. Fig.2.3 shows a family tree of supercacitors including the sub-groups with some examples of active electrode materials.

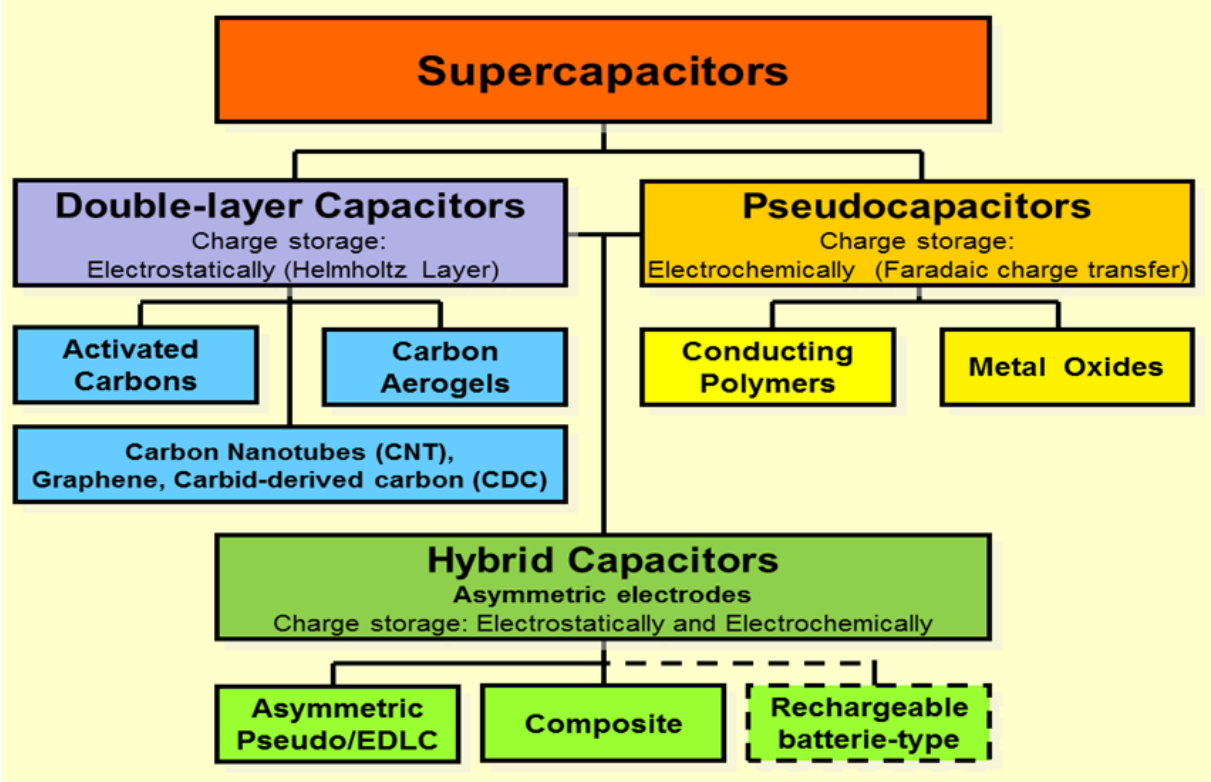

Figure 2.3:: Supercapacitor types; electrochemical double-layer capacitors and pseudocapacitors as well as hybrid capacitors are defined over their electrode designs (adapted from [38]).

2.1.2.2 Electrochemical double-layer capacitors (EDLCs)

Electric double-layer capacitors (EDLCs) are a type of supercapacitors that employ electrostatic charge separation at the interface between the electrode surface and the

electrolyte. The electrostatic charge transfer in this device is fully reversible, which gives rise to efficient devices with long cycle life. EDLCs comprise at least two electrodes separated by an ion permeable separator that prevents short circuits between the electrodes. When charging, two layers (electric double-layer described by different models) of opposite charges are formed at the electrode/electrolyte interface [9]. EDLCs are comparable to the parallel plate capacitors, which is due to electrodes polarization, resulting in adsorption of oppositely charged ions as shown in Fig. 2.4a. The energy storage mechanism of the EDLCs called the Helmholtz model, was first established by Helmholtz in 1987 [39]. The capacitance of the EDLCs can be estimated by:

$$C = \frac{\varepsilon_r \varepsilon_0 A}{d} \qquad \mathbf{3}$$

where ε_r is the electrolyte solution permittivity, ε_0 is the dielectric constant of a vacuum, A is the active material surface area, and d is the distance of the charge separation or effective thickness of the double-layer.

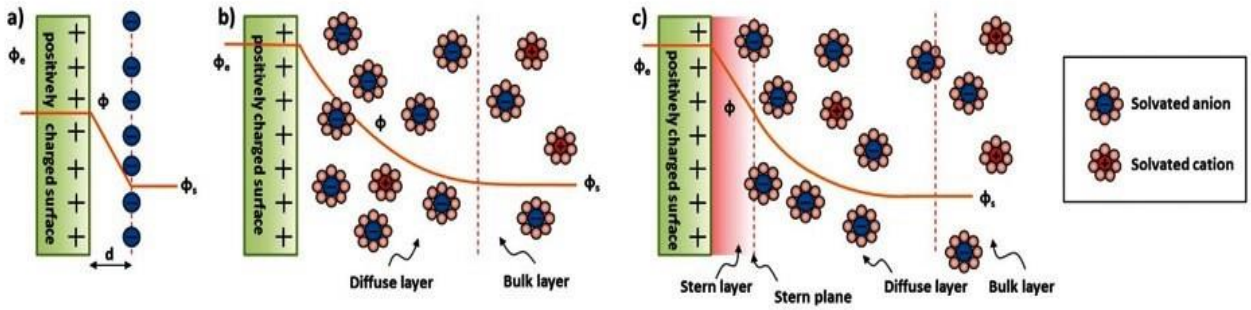

Figure 2.4: EDLCs models at the positive electrode (a) Helmholtz model (b) Gouy-Chapman model (c) Stern model (adapted from [4]).

Gouy and Chapman later improved on the Helmholtz model by suggesting the existence of a diffuse layer within the electrolyte due to ionic build-up close to the active material surface as shown in Fig. 2.4b [3], [4], [40]. Stern later combined both the Helmholtz and Gouy-Chapman models due to the failure of the Helmholtz and Gouy-Chapman models to properly account for various crucial factors. The Helmholtz model failed to account for the diffusion of ions within the electrolyte, and the relations of the dipole moment of the electrolyte and active material. Two ionic distribution regions are involved in the Stern model: the outer region (diffuse layer) and the inner region (Stern layer or compact layer) [41], as depicted in Fig. 2.4c. The two layers are equivalent to two series capacitors with capacitances C_H and C_D corresponding to capacitance from the Helmholtz layer and diffuse layer respectively, while the electrode equivalent capacitance, C_{Eq} can be estimated as [40]:

$$\frac{1}{C_{Eq}} = \frac{1}{C_H} + \frac{1}{C_D} \quad \textbf{4}$$

The electrochemical performance of the active material in an EDLC system is governed by the electric field across the active material, the electrolyte ions, solvent used to dissolve the electrolyte ions, as well as the chemical affinity between the active material surface and the adsorbed ions.

2.1.2.3 Pseudo-/Faradaic capacitors

Supercapacitors that store energy electrochemically are known as pseudo-/Faradaic capacitors. They use the charge-transfer arising from redox reactions occurring on the surface of the electrode (Faradaic behaviour). Electrodes are mostly doped with transition metal oxides, e. g. MnO_2, or coated with conducting polymers [42]. The Faradaic processes in pseudocapacitors are faster than those in rechargeable batteries but slower than the

electrostatic charge separation in EDLCs. The same trend applies to the reversibility and life-time of the devices. Pseudocapacitive reactions show a better reversibility than rechargeable batteries since they produce a smaller amount of reaction products, but EDLCs do not perform any phase changes and thus have the longest life-time. Nevertheless, pseudo-/Faradaic capacitive reactions increase the capacitance of a supercapacitor [8], [42].

2.1.2.4 Hybrid supercapacitors

Hybrid supercapacitors are energy storage devices that combine pseudo-/Faradaic capacitances with double-layer capacitances using two disimilar electrodes [15]. One electrode contains a material that conducts a pseudo-/Faradaic capacitive process, while in the other electrode; charge separation occurs due to double-layer formation only. The associated specific problems with either supercapacitor or battery devices could be compensated for by appropriate design of a hybrid device [15], [43]. Supercapacitors may have either a symmetric or asymmetric electrode configuration. In the case of the symmetric configuration, both electrodes have the same capacitance, while asymmetric configurations possess essentially different capacitance values for each electrode [15], [43], [44]. Asymmetric supercapacitor designs are mostly associated with the combination of electrode materials with different storage mechanisms, ideally, a capacitive EDLC material and a battery-type Faradaic or pseudocapacitive material, in a type of design called a hybrid supercapacitor. It has different anode and cathode materials which could include hybrid materials. In a hybrid device, the battery-type electrode provides high energy density while the capacitor electrode furnishes the system with high power capability [15], [45].

2.1.2.4.1 Supercapattery

A supercapattery is a term used to describe a hybrid supercapacitor which integrates the conventional supercapacitor behaviours with those of the battery. Such a device is neither a supercapacitor nor a battery owing to its energy storage mechanisms, and thus is capable of enhanced technical/electrochemical performances [32].

2.1.3 Batteries

In this section of the thesis, a brief explanation of the working principle of lithium ion batteries (LIBs) as an example of secondary batteries will be given, with some differences between secondary batteries (LIBs) and supercapacitors.

A battery is a transducer that converts chemical energy into electrical energy and vice versa. It contains an anode, a cathode, and an electrolyte. The anode, in the case of a lithium ion battery, is the source of lithium ions. The cathode is the sink for the lithium ions and is chosen to optimize a number of parameters, discussed below. The electrolyte which serves as a simple buffer, provides for internal ionic transport between the electrodes, and in a perfect battery the lithium ionic transport number will be unity in the electrolyte [46], [47]. The cell potential is determined by the difference between the chemical potential of the lithium in the anode and cathode. Li^+ ions move from the cathode to the anode via the electrolyte/separator during charging and back when discharging, and simultaneously, the electrons flow out of the external circuit to provide the electrical power [46] as shown in Fig. 2.5.

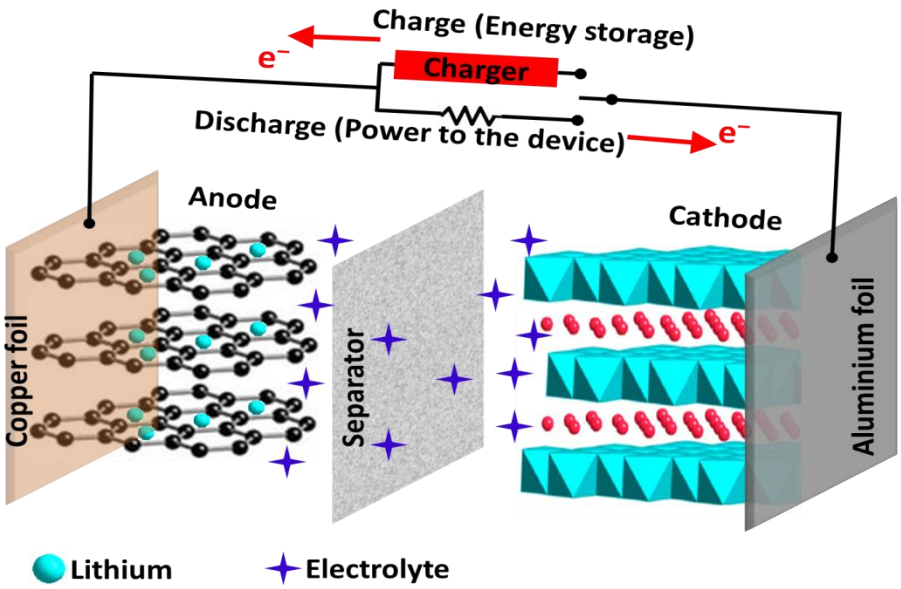

Figure 2.5: Schematic representation of a typical lithium ion battery containing an intercalation cathode on an aluminium collector, an electrolytic solution, and an anode on a copper current collector.

Generally, batteries are more of a chemical than an electrical energy storage device. They employ chemical reactions to store and deliver energy [29]. In secondary batteries such as LIBs batteries, reversible electrode reactions take place during charging and discharging. These redox processes are not fully reversible, hence batteries have a shorter life-time compared to supercapacitors. Besides, the chemical reactions in batteries are slow compared to the fast electrostatic charge separation in supercapacitors, giving rise to long charge and discharge times [29], [46]. Fig. 2.6 shows the difference between a supercapacitor and a battery in terms of energy and power. Batteries can hold the charge much longer and maintain the voltage while supercapacitors will self-discharge much quicker. Supercapacitors have about 5 to 10 times less energy density than Li-ion battery, however due to low internal resistance, the power that it can put out is 10 times that of battery.

Fig. 2.6: The difference between a supercapacitor and a battery (Courtesy: Elcap).

2.2 Electrolytes

An electrolyte is a substance which when dissolved in a solvent like water, produces an electrically conducting solution, with the dissolved electrolyte being separated into cations and anions which are evenly dispersed within the solvent. The solution is electrically neutral. The electrochemical performance of a supercapacitor is greatly influenced not only by the choice of material but also the electrolyte [48]. They both determine and limit the electrical properties. Mostly, the pore structure and pore size of the active material and the size of the electrolyte ions dictate the capacitance. The size of the ions/solvated ions determines the packaging density of the ions at the electrode surface. The maximum operating potential is another crucial property of the electrolyte. This limits the amount of energy that can be stored

in a supercapacitor. Electrolytes can be divided into three categories, namely, (1) aqueous, (2) organic and (3) ionic liquid electrolytes [40].

2.2.1 Aqueous electrolytes

In supercapacitors, aqueous electrolytes comprise mainly non-toxic and inexpensive acidic, basic and neutral electrolytes such as KOH, Na_2SO_4, H_2SO_4, and NH_4Cl among others [49]. They have a low operating potential due to the water electrolysis above 1.23V, but display higher ionic conductivities resulting from their excellent ionic concentration and smaller ionic radius compared to organic electrolytes, owing to their active proton transport process [49], [50]. The limited operating potential (1.23V) makes aqueous electrolytes less advantageous in terms of energy densities compared to organic and ionic liquids electrolytes. Aqueous electrolyte performance can be enhanced for use in supercapacitors by addition of surfactant such as sodium dodecyl sulphate (SDS), and tetrapropylammonium bromide (TPAB) among others, in low concentration. Such a surfactant decreases the surface tension in the electrode/electrolyte interface and allows better penetration of electrolyte into the pores. This, improves the accessibility of the electrolyte to the surface of the electrode [51], [52].

2.2.2 Organic electrolytes

Supercacitors with organic electrolytes can operate at higher potentials of up to ~3.5 V. They are most widely selected for industrial applications to avoid solvent decomposition and to achieve optimum operating potentials. Acetonitrile (ACN), propylene carbonate, (PC), tetraethylammonium tetrafluoroborate (TEA BF4), triethylmethylammonium tetrafluroborate (TEMABF4) and/or their mixtures are some of the commonly used organic electrolytes [53], [54]. ACN, a volatile, toxic and flammable liquid facilitates high conductivities due to its low

viscosity and achieves high energy and power densities. However, environmental instability, toxicity, and high flammability restrict its use to controlled environments [55]. Supercapacitors with organic solvents exhibit lower capacitances compared to those with aqueous electrolytes. Organic electrolytes show much lower conductivities (typically one order of magnitude) than aqueous electrolytes.

2.2.3 Ionic liquid electrolytes

Ionic liquids can operate at much wider electrochemical potentials of up to 6V due to their non-volatility, low vapor pressure and non-flammability [56]. Some ionic liquids melt (their salts) at room temperature, composing of positive and negative ions. However, ionic liquids are costly and often have high viscosities and low electrical conductivities [57]. The high viscosity does not only limit the charge transportation speed but also limits the accessibility of the electrolyte to smaller pores in the electrode surface. Poor chemical stability may also limit their employment as electrolyte in supercapacitors in some cases [57], [58]. Their conductivity can be enhanced by addition of solvents such as propylene carbonate or acetonitrile. Typical examples include quaternary ammonium salts (tetraalkylammonium $[R_4N]^+$), and cyclic amines (aromatic pyridinium, imidazolium and saturated piperidinium, and pyrrolidinium) among others [58], [59].

2.3 Electrode materials for supercapacitors

In supercapacitors, the role of active materials in energy generation and storage is very crucial, thus, electro active materials development that can meet the required energy demand is ultimately important. Supercapacitors capacitance depends on the specific surface area of

the electrode materials. The choice of electrode determines and limits the electrical properties of a supercapacitor [60]. Especially the pore structure and pore size of the active material and the size of the electrolyte ions affect the capacitance. However, it has been shown that there is no linear relationship between the area and the measured capacitance [61], since the entire surface area is not fully electrochemically accessible to the electrolyte. Moreover, charge screening and ion size affect the accessibility of small micropores to the electrolyte. Electrochemical doping of density of states and quantum capacitance all have an effect on the capacitance of the material. Hence, for the electrochemically accessible surface area, "electrochemical active surface area" may be appropriate to describe the behavior of electrode materials capacitance. The pore size as well as the pore size distribution (PSD) of the electrode material also play an important role and thus have a great impact on the capacitance [18], [62]. In general, supercapacitor electrode materials are categorized into three types namely: carbon materials, conducting polymers, transition metal oxides/hydroxide and their composites [9], [63].

2.3.1 Carbon electrode materials

The excellent properties such as good electrical conductivity, high specific surface area, natural abundance, cost-effectiveness, wide operating temperature, and high chemical inertness among others make carbon electrode materials a best choice for industrial application [3], [64]. They are classified into various categories namely, onion-like carbon, carbon nanotubes, graphene, activated carbons, carbon black and carbide-derived carbons. The zero-dimensional ("quasi 0D") quasi-spherical called onion-like carbon comprises concentric graphitic shells materials prepared by annealing nanodiamond powders in vacuum or argon or detonation nanodiamond, resulting in bulk nanoparticles of few nanometres. They

possess relatively high specific surface area (SSA) ranging from 500-600 m^2 g^{-1} compared to activated carbon which is mostly accessible to ion adsorption due to its lack of porous network within the carbon. They have been known to demonstrate modest gravimetric capacitance at about one-third that of activated carbon in previous studies [64].

The one-dimensional ("quasi 1D") carbon nanotubes have gained extensive studies for supercapacitors applications in recent years owing to their unique pore structure, superior electrical properties, good mechanical and thermal stability [26]. They can be classified as single-walled carbon nanotubes (SWNTs), double-walled carbon nanotubes (DWCNTs) and multi-walled carbon nanotubes (MWNTs), of which all have been extensively studied as supercapacitors electrode materials. They are known to have potential as high-power electrode materials owing to their great electrical conductivity and readily accessible surface area. Besides, the tubular network combined with high mechanical resilience make them a good support for active materials [26], [64], [65].

Activated carbons have gained popularity as supercapacitors electrode materials as a result of their high surface area. They are usually prepared via oxidation of bulk carbon in water vapor, KOH, or CO_2 in an activation process. The process creates a three-dimensional porous network with micropores (pore size <2 nm) and mesopores (2-50 nm) giving rise to the high specific surface area of about 2000 m^2 g^{-1} in the carbon materials. Low-cost activated carbons can be produced from carbonization and activation of natural carbon precursors such as wood, coconut shells, palm kernel shell, or anthracite, which are amorphous with a network structure majorly consisting of sp^2 and some sp^3 bonded atoms [16]. A structure that contains chemical moieties like oxygen, nitrogen among other atoms, with oxygen-containing functional groups results in a decrease in conductivity. This leads to the need for addition of acetylene black or carbon black as a conducting agent to such carbon electrodes [16]. They are widely used in

commercial devices due to their cost-effectiveness, high capacitance and scalable manufacturing.

Another large family of the carbon called carbide-derived carbon (CDC) are derived from carbide precursors that are transformed into pure carbon via a physical process such as high-temperature treatment/thermal decomposition, or a chemical process like chlorination or halogenation [66], [67]. Their unique properties, which include high specific surface area and tunable pore size with a narrow size distribution acquired by halogenation, makes them an ideal supercapacitor or absorbent electrode [67]. Their bulk porosity is widely determined by the carbide structure. When metal atoms are extracted from the carbide lattice, the remaining carbon forms microporous structures known as carbide-derived carbon (CDC). Various techniques and precursors have been employed to obtain CDC with controllable nanostructure and pore characteristics for use as supercapacitor electrodes. The choice of precursor, particle size and other parameters, and most importantly, synthesis temperature has a great influence on the capacitance of the materials. CDC derived from zirconium carbide (ZrC-CDC) and titanium carbide (TiC-CDC) are some of the most commonly used examples of carbide-derived carbon materials [67], [68].

Graphene is a two-dimensional lattice of hexagonally arranged sp^2-bonded carbon atoms, forming a one-atom-thick monolayer [69]. Fig. 2.7 shows the structure of graphene and graphite (an allotrope of carbon that has a planar structure and is composed of many layers of graphene) [69]. Graphene oxide (GO) describes a monolayer of chemically modified graphene. Electrically, GO acts as an insulator, owing to the disturbance of its sp^2 bonding networks. Reducing the GO helps it recover the honeycomb hexagonal lattice of graphene, and restores its electrical conductivity. Graphene is a zero-gap semiconductor with significant electronic properties. It exhibits linear dispersion at a high symmetry point in the reciprocal

space, resulting in effective dynamics of electrons similar to that of massless relativistic Dirac Fermions [70]. It provides not only significant electronic properties, but excellent optical, thermal, mechanical and electrochemical properties that are superior to other allotropes of carbon such as graphite and carbon nanotubes among others [70]–[72].

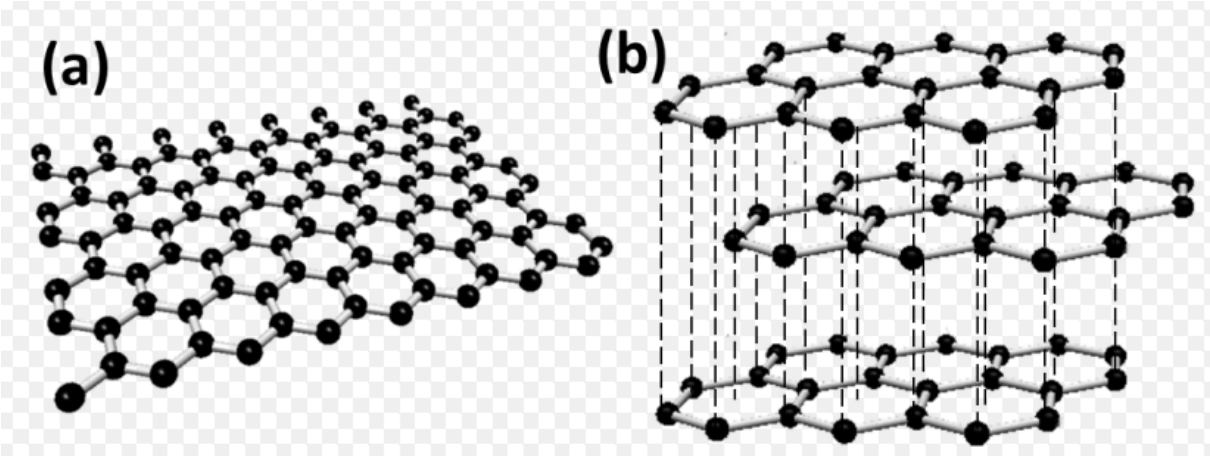

Fig: 2.7: Structure of (a) graphene and (b) graphite [73].

It can be obtained by dispersing graphite oxide in a solvent accompanied by intensive exfoliation. The GO used in this work was synthesized by a modified Hummers technique [17].

2.3.2 Conducting polymers

Good properties like high conductivity, high potential window, good storage capacity/reversibility, adjustable redox activity via chemical modification and cost-effectiveness among others, associated with conducting polymers make them suitable as supercapacitor electrode materials [74]–[76]. They make use of redox processes, during oxidation; ions are transferred to the polymer backbone, and are released into the electrolyte during reduction. Polyaniline (PANI), polypyrrole (PPy), polythiophene (PTh), and poly(3,4-

ethylene-dioxythiophene) (PEDOT) are some of the most commonly studied conducting polymers for supercapacitor applications [75], [77], [78]. Nevertheless, the swelling and shrinking associated with conducting polymers during intercalation/deintercalation process results in mechanical degradation of the electrode as well as poor electrochemical performance during cycling hindering their commercialization as electrode materials [78].

2.3.3 Transition metals oxides/hydroxides

Transition metal oxides/hydroxides materials exhibit electrochemical Faradaic reactions between electrode materials and ions within appropriate potential windows [79], [80]. TMOs such as RuO_2, MnO_2/$Mn(OH)_2$, NiO/$Ni(OH)_2$, Co_3O_4 /$Co(OH)_2$, SnO_2, TiO_2 and V_2O_5 [81]–[87] among others have been explored and investigated as electrode materials for supercapacitor applications..

Generally, transition metal hydroxides are plagued with low electrical conductivity but high specific capacitance due to their characteristic redox reactions. As such, they do not yield a high performance under high-rate current densities [19], [20]. On the other hand, transition metal hydroxides/oxides have been intensely studied with a view to overcome the above limitation and refine their properties to fit the desired use [16], [21]. Transition metal hydroxides/oxides are semi-conductive materials among which Ni based oxides have been shown to be a promising candidate as an electrode material for electrochemical capacitors owing to its cost effectiveness, natural abundance as well as adequate electrochemical performance [20], [88]. They can provide higher energy density for supercapacitors than carbon materials and better electrochemical stability than conducting polymer materials.

However, transition metal oxides/hydroxides are disadvantageous as electrode materials due to their small potential, poor electron and ion exchange, and low conductivity [89].

2.3.4 Composite materials

Composite materials provide an attractive alternative approach for combining materials with different electrochemical behavior. For instance, pseudo-capacitive metal oxides or conducting polymers can be combined with a capacitive carbon material to take advantages of properties offered by the individual material. This results in an enhanced electrochemical performance of supercapacitors. The individual material in the composites provides a synergistic effect resulting in minimized particle size, enhanced specific surface area and induced porosity. This prevents agglomeration of particles, facilitating electron and proton conduction, expanding active sites, extending the potential window, protecting active materials from mechanical degradation, improving cycling stability, and of course providing extra pseudocapacitance [16]. The resulting composite materials could achieve higher electrochemical performance. Nevertheless, a reverse effect might occur, hence a compromise in the individual substance compositions and an optimized molar ratio of the individual constituent is required [16].

2.4 Supercapacitor electrodes and device fabrication, testing and evaluation

2.4.1 Electrode fabrication for supercapacitors

In supercapacitors, electrodes are fabricated by mixing the active materials with a carbon or acetylene black as a conductive agent to improve the conductivity of the materials, and a

binder usually polyvinylidene fluoride (PVDF) or polytetrafluoroethylene (PTFE) in a small amount of N-methyl-2-pyrolidone (NMP) solvent with slow stirring at room temperature to form homogeneous slurry. The prepared slurry is then smeared on a current collector made of materials with good electronic conductivity and corrosion resistance. Materials include nickel foam [90], [91], carbon cloth or paper [90], and some metal foils. The electrode material's slurry application determines the thickness of the electrode.

2.4.2 Electrode testing for supercapacitors

Electrochemical measurements for supercapacitor electrodes are normally carried out in both a three-electrode (single or half-cell) configuration and/or a two-electrode (full-cell (device)) configuration. A three-electrode set-up shown in Fig. 2.8 is used primarily to examine the electrochemical behaviours of an electrode material. These properties include specific capacitance/capacity, working potential, and cycle life among others. The set-up comprises a working electrode usually the as-prepared active material, counter and reference electrodes, as well as a preferred electrolyte [91]. The counter electrode is made up of highly conductive materials that are chemically inert such as glassy or vitreous carbon, and platinum. The counter electrode is responsible for the generation of an amount of current required at the working electrode, by altering its potential in the electrolyte. The reference electrode on the other hand, serves as the reference point for voltage regulation and measurements in a three-electrode configuration, without allowing a flow of current across it. The choice of both the counter and reference electrodes relies on the nature of the electrolytes employed for a particular measurement [92]. A platinum or glassy carbon counter electrode is selected for use with acidic and neutral electrolytes, with a saturated calomel electrode (SCE) or silver/silver chloride electrode (Ag/AgCl) as reference electrode. Mercury/mercury oxide (Hg/HgO) is the

ideal choice of reference electrode for alkaline electrolytes, while the choice of reference electrode for the non-aqueous electrolytes is determined by the electrolyte in question [92]–[94].

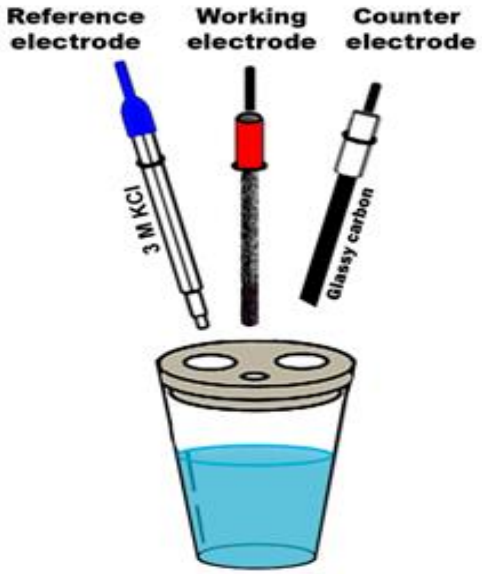

Fig. 2.8: A three-electrode configuration set-up [95].

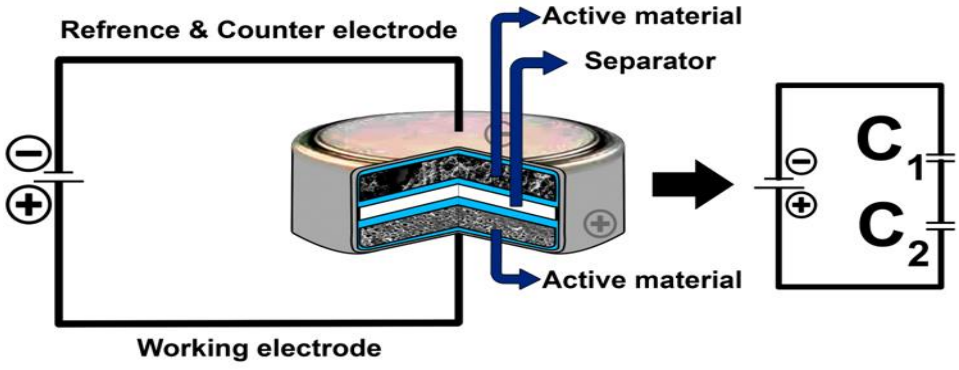

Fig. 2.9: A two-electrode configuration set-up [95].

Fig. 2.9 shows the pictorial set-up of a supercapacitor two-electrode configuration. It can be used to fully evaluate the electrochemical properties of a material, since the heightened sensitivity of a three-electrode configuration could over-project the storage capability of an electrode material for practical supercapacitor use [96]. A two-electrode system can comprise two symmetric (same material) or asymmetric (two dissimilar materials) materials, as both the negative and positive electrodes with a separator in-between them in an electrolyte. The anode, separator, and cathode are impacted by a metallic spacer to ensure tight contact as shown in Fig. 2.9. Electrochemical properties of a supercapacitor such as energy and power densities, and longer cycle life among others, can be estimated with a two-electrode measurement [97]–[99]. Theoretically, the equivalent specific capacitance (F g^{-1}) of a symmetric cell is equal to ¼ of the specific capacitance measured for a three-electrode (half-cell) [95], [97]. The theoretical factor of ¼ automatically converts the equivalent specific capacitance of the cell as well as effective mass of the two electrodes to that evaluated in a three-electrode system [99]. Nonetheless, the specific capacitance measured for one of the electrodes in a device is practically not the same as that of the electrode of a half-cell since the solvated cation and anion vary in sizes, and also due to potential variations in the oppositely charged electrodes during the charge-discharge test.

2.5 Supercapacitor device fabrication

2.5.1 Symmetric device

A symmetric device is one that has both the anode and cathode made from the same material, and therefore both electrodes have the same capacitance. If $C_1 = C_2$, then $C_T = C_1/2$. The total

capacitance, C_T equals half the capacitance of a single electrode [100]. From the fact that the galvanostatic charge/discharge plots been based on two-electrode cells, the specific capacitance, C_S (F g^{-1}) of a single electrode, the maximum energy density, E_D (Wh kg^{-1}) and the maximum power density, P_D (kW kg^{-1}) of the supercapacitor can be estimated using the equations below [99]:

$$C_S = 4C_T = \frac{4\, I\, \Delta t}{m\, \Delta V} \quad \textbf{5}$$

$$E_D = \frac{1}{2}\, C\, (\Delta V)^2 = \frac{1000 \times C_S \times \Delta V^2}{2 \times 4 \times 3600} = \frac{C_S \times \Delta V^2}{28.8} \quad \textbf{6}$$

$$P_D = \frac{3600 \times E_D}{1000 \times \Delta t} = \frac{3.6 \times E_D}{\Delta t} \quad \textbf{7}$$

where C_s is the equivalent specific capacitance of the cell, I is the constant discharge current (A), **Δt** is the discharge time (s), m is the total mass (g) of the active material in both electrodes, and ΔV is the working potential (V).

2.5.2 Asymmetric device

Asymmetric supercapacitors comprise two dissimilar materials as the anode and cathode. The electrodes are of different capacitances, and one of them is usually of a higher capacitance than the other. [100].

The potential window is a function of the active material's capacitance in each electrode. Thus, for optimal performance of the asymmetry device, the mass on each electrode must be balanced using the charge balance equation, $Q_+ = Q_-$, with the charge stored on each electrode expressed as [101]:

$$Q = C_s \times m\, \Delta V \quad \textbf{8}$$

where Q (C) is the stored charge on the electrode, C_S (F g^{-1}) is the specific capacitance of the electrode based on the mass of active material, m (g) is the mass of active material, and ΔV (V) is the potential window.

The mass balance between the positive and negative electrodes can accurately be determined by further considering [102]:

$$\frac{m_+}{m_-} = \frac{C_{s-}\ \Delta V_-}{C_{s+}\ \Delta V_+} \quad \textbf{9}$$

With proper mass balancing, capacitance of the respective electrode becomes equal, thus, the device behaves like a symmetric device. Hence, equations 3-5 can be applied to estimate the specific capacitance as well as energy and power densities [103].

The maximum constant-current discharge power density, P_{max} of the device can be predicted using the effective solution resistance, R_s (ohm) determined from the Z'-intercept of the Nyquist plots of frequency analysis according to the relation below [104], [105]:

$$P_{max} = \frac{V^2}{4mR_s} \quad \textbf{10}$$

Where V (V) and m (g) are the potential window as well as the mass loading of the active material respectively.

2.6 Evaluation of supercapacitor electrodes

Electrochemical performances of supercapacitor electrode materials can be evaluated using cyclic voltammetry (CV), galvanostatic charge-discharge (GCD), and electrochemical impedance spectroscopy (EIS) irrespective of whether a three or two electrode configuration is considered.

2.6.1 Cyclic Voltammetry (CV)

CV is a common technique used to investigate the thermodynamic effect, as well as electron transport dynamics at the boundary in-between the active material and the electrolyte in the supercapacitor. The technique is used to interpret the reactions occurring on the surface of the active material. The measurement is done within a specific working potential, with the applied potential measured at various scan rates. The current response at the cathodic and anodic sweeps plays a crucial role in determining the electrochemical performance of the electrode material. The gravimetric specific capacitance, C_s (F g^{-1}) of a half-cell can be derived from the CV curves according to the formula stated in equation 11 below [106].

$$C_s = \frac{\int I_D dV}{v\Delta V} \quad \textbf{11}$$

where I_D (current divided by the mass of the electrode) is the average specific current, ΔV is the potential window, and v is the scan rate (mV s^{-1}).

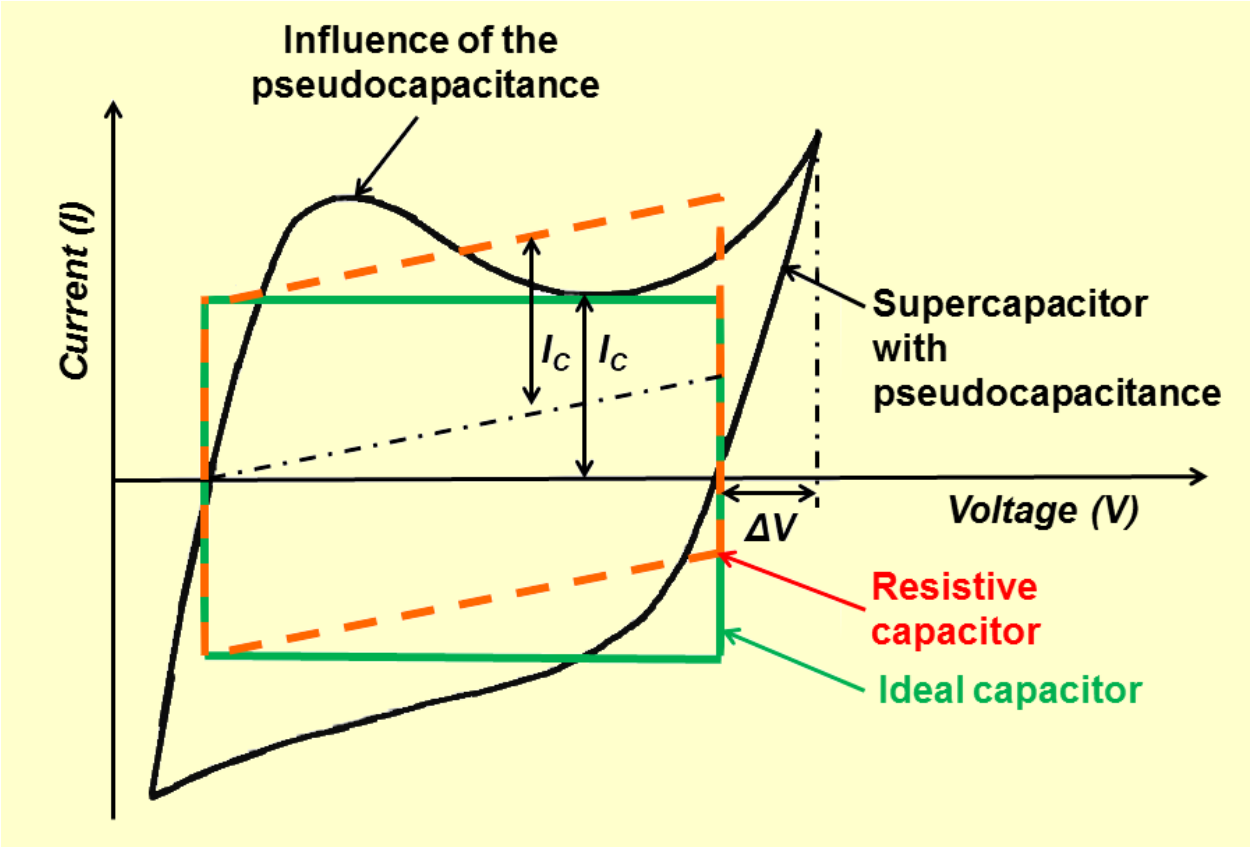

Fig. 2.10: CV curves showing fundamental differences between static capacitance (rectangular) and pseudo-/Faradaic capacitance (curved) (adapted from [95]).

In figure 2.10, the ideal rectangular shape confirms a typical reversible capacitive behavior of an ideal EDLC material, exhibiting no chemical reaction. The curved CV profile for the pseudocapacitve material is evident of the reversible oxidation and reduction peaks, indicating a Faradaic redox process. For a reversible electrochemical process, the following properties can be deduced:

(i) The potential peak position does not depend on scan rate.

(ii) The potential difference between the oxidation and reduction peaks must be small (usually ~ 59 mV n^{-1}, where n is the number of electrons).

(iii) The peak current ratio must be equal to unity.

(iv) The peak currents are directly proportional to the square root of the sweep rate following the power law; $I = v^{1/2}$ (diffusion controlled process normally existing in pseudocapacitive materials), while the peak current in the case of mass a transport process (EDLCs) is proportional to the sweep rate, i.e. I α v where I is the current and v the scan rate.

2.6.2 Galvanostatic charge-discharge (GCD)

GCD is a powerful and important tool for the study of electrochemical properties of supercapacitors. Specific capacitance/capacity, power and energy densities, specific current, rate capability and efficiency of a supercapacitor are evaluated from the GCD measurement. In a GCD measurement, the lower and upper voltage boundaries are fixed, as the charge-discharge process runs, the potential increases until the upper fixed potential is attained. Thus, a current reversal occurs and results in a potential decrease to its lower limit as shown in Fig. 2.11(a and c). The next cycle begins after a fixed lower potential is reached due to the reversed current at the lower fixed potential (Fig. 2.11b and d). The nature of the GCD profiles as in the case of the CV curves, dictates the nature and properties of an active material. A linear GCD profile is an indication of ideal EDLCs, due to their constant charge distributions during the charge-discharge process. The pseudo-/Faradaic supercapacitors exhibit a non-linear GCD profile resulting from the oxidation and reduction reactions during the charge-discharge process. The GCD measurement is necessary to further investigate the electrochemical performance of a supercapacitor electrode. It is adopted to further determine electrochemical properties such as energy and power densities, capacitance/capacity retention,

maximum constant-current discharge power and diffusion rate of a supercapacitor electrode, among others. The energy density of a supercacitor is a function of the its working potential. The larger the working potential, the higher the energy density, the power density increases with an increase in a material's specific current.

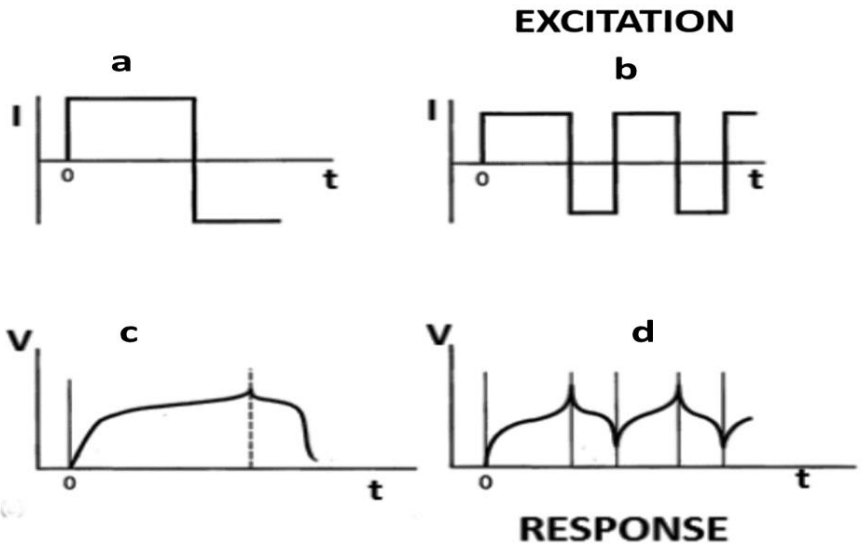

Fig. 2.11: The figure shows (a) current vs. time plot for current reversal, and (b) current vs. time profile for cyclic GCD, (c) voltage vs. time plot for an typical Faradaic behavior, (d) voltage vs. time plot for a cyclic Faradaic behavior (adapted from [95]).

The gravimetric discharge specific capacitance, $\boldsymbol{C_s}$ of a supercapacitor can be estimated via GCD profiles according to the following equations [17]:

$$C_s = \frac{2I_D}{V^2}\int V(t)dt \qquad \textbf{12}$$

where C_s is the discharge specific capacitance (F g^{-1}), t is the discharge time (s), I_D is a specific current (A g^{-1}), and V is the applied potential (V).

For an EDLC material in which the potential is proportional to the charge-discharge time, equation 8 reduces to [107]:

$$C_s = {}^{I_D t}/_{\Delta V} \quad \textbf{13}$$

where I_D is a specific current (A), t is the discharge time (s), m is the mass of active material (g), and ΔV is the voltage range (V).

For a supercapacitor exhibiting Faradaic behavior, specific capacity rather than specific capacitance is evaluated, according to the equation stated below [108]:

$$Q = {}^{It}/_{3.6m} \quad \textbf{14}$$

where Q is the discharge specific capacity (mAh g^{-1}), t is the discharge time (s), I is the applied current (mA), and m is the mass of active material (g) [109]. The corresponding energy density E_D of such a material's full cell can be evaluated by integrating the area under the discharge curve according to the following equation:

$$E_D = I/3.6m \int V dt \quad [\text{Wh kg}^{-1}] \quad \textbf{15}$$

where I is the discharge current in Amperes (A), m is the mass loading of the active material in grams (g), V is the operating potential window in volts (V), and t in seconds is the electrode discharge time respectively.

2.6.3 Stability test for supercapacitors

2.6.3.1 Cycle life

Supercapacitors can be subjected to charge-discharge over a number of cycles. The cycle life depends on the actual conditions under which the cycling is set up [110]. The applied current,

potential limits, device history, as well as temperature are important parameters during cycling. Cyclic galvanostatic charge–discharge (CGCD) is the standard method used to test the performance and cycle life of supercapacitors.

Efficiency (coulombic or energy) is amongst some crucial parameters used to determine the electrochemical behavior of a *SC.* The coulombic efficiency $\boldsymbol{\varepsilon_t}$ can be estimated in the case of an EDLC SC while energy efficiency $\boldsymbol{\eta_E}$ is estimated for a faradaic SC. They are both deduced from the GCD curves according the relations [108]:

$$\varepsilon_t = \frac{t_D}{t_C} \times 100 \qquad \textbf{16}$$

where t_D and t_C are the discharge and charge time respectively.

$$\eta_E = \frac{E_d}{E_c} \times 100 \qquad \textbf{17}$$

where E_d and E_c are the discharge and charge energy respectively.

2.6.3.2 Self-discharge

Figure 2.12 shows the self-discharge curve of a supercapacitor. Self-discharge is a measure of the voltage drop on a charged device with no load, over a specific period of time. For a realistic measure of the leakage (self-discharge) currents, a device is required to be subjected to several hours of charging, and then allowed to discharge with no load on it. The test is aimed at evaluating the energy loss over the test interval and estimating the decrease in capacitance of the device's voltage during the test [111], [112].

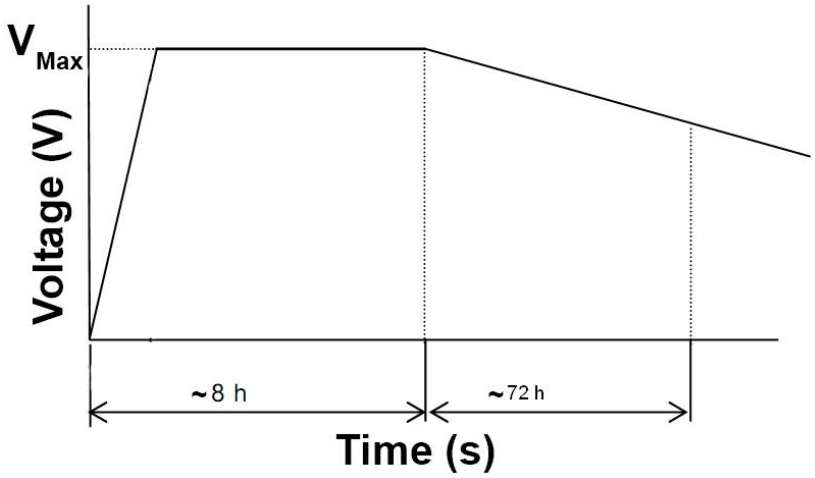

Fig. 2.12: Self-discharge curve of a supercapacitor [112].

From the curve (Fig. 2.12), the voltage maintenance rate, VMR (%), as a measured parameter can be estimated according to the relation:

$$VMR = \frac{V_{End}}{V_{Max}} \times 100\% \qquad \textbf{18}$$

where V_{End} is the voltage between open device terminals after ~72 h, and V_{Max} is the rated voltage [112].

2.6.3.3 Floating or voltage-holding test

Floating or voltage-holding has been established as an alternative and reliable method to analyze the stability of supercapacitor electrodes. It is carried out at a constant load by holding the device at the highest voltage and calculating the capacitance over the entire period as shown in figure 2.13, and in a sequence usually repeated several times [90]. The floating test provides direct insights into the possible effect and degradation phenomena that might occur during the electrochemical process in EDLC devices at elevated cell voltages when compared with the traditional cycling test which often shows no degradation. It also gives a

true resistance effect after being subjected to maximum voltage that may be close to practical relevance [90], [113].

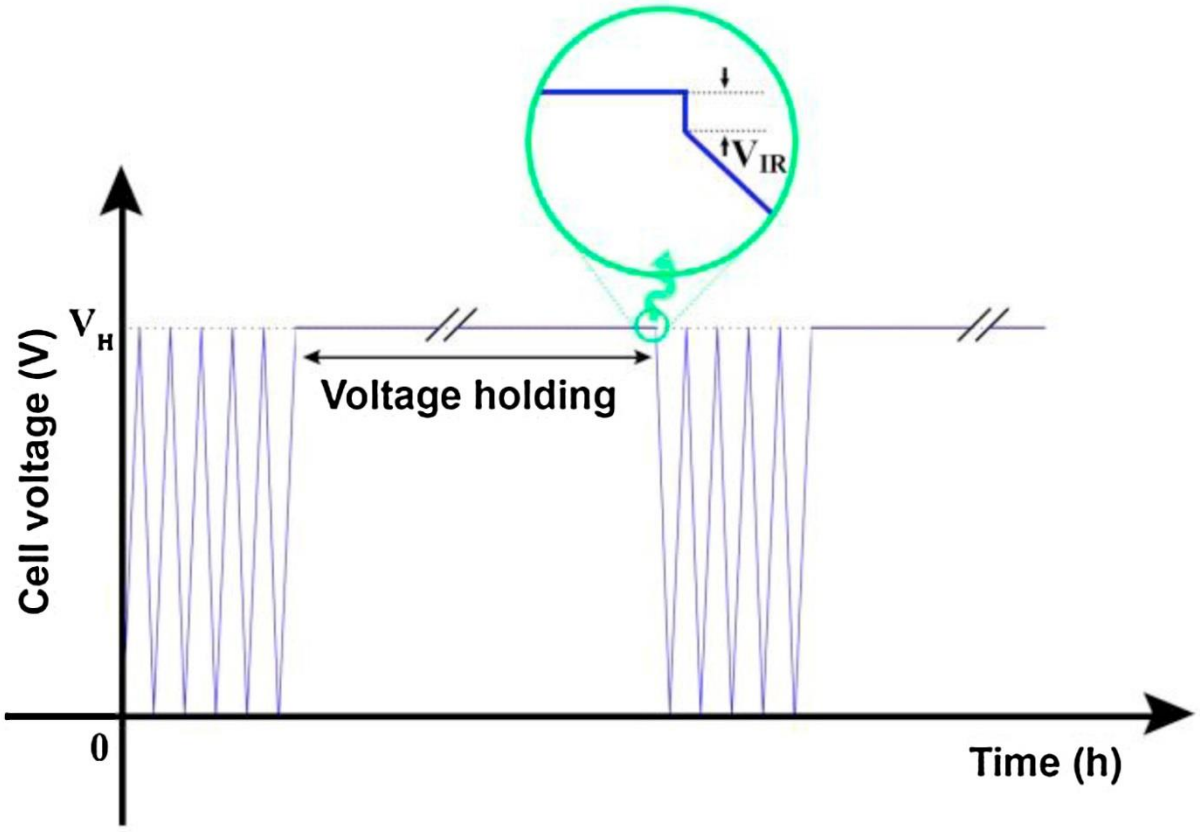

Fig. 2.13: Schematic illustration of a floating test (adapted from [90]).

2.6.4 Electrochemical impedance spectroscopy (EIS)

Electrochemical impedance spectroscopy (EIS) or alternating current (ac) impedance spectroscopy methods have seen a tremendous increase in popularity in recent years. It is a technique that measures the behavior of small potential perturbations at different frequencies (ranging from mHz to MHz) at a constant ac signal or open circuit potential. EIS is often represented by the Nyquist plot that presents the real and imaginary part of the impedance on

both the x and y-axis respectively. The Nyquist plot takes into account the different parameters (resistance, capacitance, inductance and etc.) all being contingent on the frequency. Initially applied to the determination of the double-layer capacitance [114]–[116] and in ac polarography, [114] they are now applied to the characterization of electrode processes and complex interfaces. It is a crucial technique used to further evaluate the electrical resistance of a SC material. EIS studies the system response to the application of a periodic small amplitude ac signal. The EIS measurements are carried out at different ac frequencies and, thus, the name impedance spectroscopy was later adopted. Analysis of the system response contains information about the interface, its structure and reactions taking place there. EIS analysis is mostly performed in an open circuit potential, recorded by introducing a small-amplitude alternating potential (mV) over a broad frequency (f) range, such as 10 mHz–100 kHz. The Nyquist and Bode plots are usually employed in the EIS data analysis.

Fig 2.12 shows a typical Nyquist EIS plot. The figure depicts both the imaginary ($Z(\omega)''$) and real ($Z(\omega)'$) parts of the impedance. In the plot, three regions exist namely, the low, medium and high-frequency regions [108]. In the high-frequency region, the existence of a small semicircle is attributed to the interfacial charge transfer resistance (R_{ct}) and mass transport through the material. The intersection with the real Z' axis is ascribed to the total resistances at the electrolyte-electrode-current collector interface known as the solution or equivalent series resistance (R_{Ω}), the intrinsic resistance of the active material and the contact resistance at the interface between the active electrode material and current collector. The medium frequency region (10 to 1 Hz) is an exhibition of pseudo-charge transfer resistance attributed to the material's porosity. The low-frequency region is due to the diffusion mechanism of ions in the material; the parallel line to the imaginary axis is an ideal capacitive nature.

Nonetheless, in practice, a slight shift from the ideal vertical line usually at around 45˚-90˚, is attributed to the ions diffusion process [117].

The low-frequency region also exhibits a capacitance (C(ω)) due to the sum of the imaginary (C″(ω)) and real (C′(ω)) parts of the capacitance, according to the following equations [59], [108]:

$$C(\omega) = C'(\omega) + jC''(\omega) \quad \textbf{19}$$

$$C'(\omega) = -\frac{Z''(\omega)}{\omega|Z(\omega)^2|} \quad \textbf{20}$$

$$C''(\omega) = -\frac{Z'(\omega)}{\omega|Z(\omega)^2|} \quad \textbf{21}$$

where C′(ω) relates to the stationary capacitance obtained during the steady current discharge, C″(ω) relates to energy dissipation of the electrode through a voltage (IR) drop and an irreversible Faradaic charge transfer mechanism. |Z(ω)| is the modulus of impedance, and ω is the angular frequency [59], [108], [117].

The needed time to effectively supply the stored energy known as the relaxation time (τ), can be estimated via the knee frequency in the plots of C′(ω) and C″(ω) as a function of frequency and expressed as $\tau = \frac{1}{f}$, where f is the distinctive frequency of the active material, and τ is maximum in the imaginary capacitance against frequency plot. This demonstrates the difference between the capacitive and resistive behavior of the active material.

Another important plot from the EIS measurements is the Bode plot. The Bode plot emphasizes the correlation between the frequency and the imaginary part of the impedance ((Z(ω)″), and the capacitance of the material can be deduced from the linear portion of a graph of log Z'' against log f using the equation:

$$C = \frac{1}{2\pi f|Z''|} \quad \textbf{22}$$

where C is the capacitance (F), f is the frequency (z), and Z'' is the imaginary impedance.

Unlike the Nyquist plot, the Bode plot explicitly shows frequency information. A tilted line with respect to the real axis with the angle of $45^{o} \leq \theta \leq 90^{o}$ is achieved, and this has been shown to correspond to an ion diffusion mechanism between the Warburg diffusion and ideal capacitive ion diffusion [118].

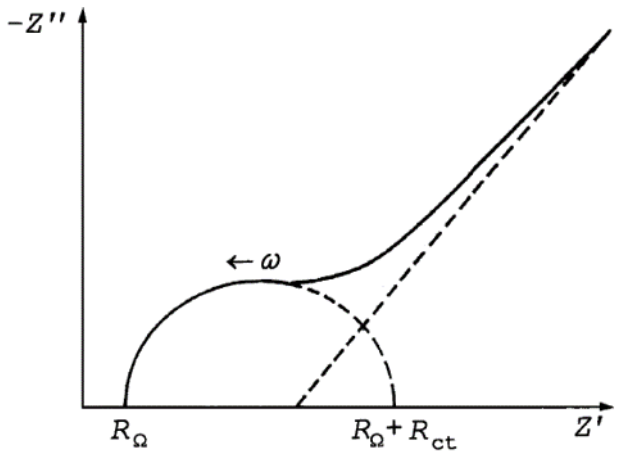

Fig. 2.14: An EIS Nyquist plot [95].

Chapter 3

3.1 Experimental details

This chapter of the thesis explains the procedures used for materials synthesis and the characterization techniques employed in this work. It also includes a brief description of some of the devices used for materials synthesis and characterization.

3.1.1 Preparation of electrode materials

3.1.1.1 The Hummers' method

The Hummers' method [119], established in 1958, is a chemical process that can be used to generate graphite oxide through the addition of potassium permanganate to a solution of graphite, sodium nitrate, and sulfuric acid. It is commonly used by engineers and lab technicians as a reliable method of producing quantities of graphite oxide. It has also been revised in the creation of a one-molecule-thick version of the substance known as graphene oxide. The method was developed as a safer, quicker and more efficient way of producing graphite oxide than other techniques such as the Staudenmeier–Hoffman–Hamdi [120] method which includes potassium chloride and however, posed more hazards and could only produce one gram of graphite oxide to ten grams of potassium chloride [120], [121]. This method involves addition of potassium permanganate to a solution containing graphite,

sodium nitrate, and sulfuric acid [121], [122]. Hummers' method came into the limelight after the discovery of graphene in 2004. The method does not require high temperatures (above 98 ˚C) and avoids most of the explosive risks associated with the Staudenmeier–Hoffman–Hamdi method [123]. This thesis presents two phases of carbon-based materials namely; graphene oxide (GO) gel and carbon nanorods obtained from the GO gel via a modified Hummer's method and a force-driven reflux process respectively, using powdered graphite as the main precursor.

3.1.1.2 The reflux system

Reflux is a technique involving the condensation of vapors and the return of this condensate to the system from which it originated. It is used in industrial and laboratory [124] distillations. It is also used in chemistry to supply energy to reactions over a long period of time. A mixture of reactants and solvent is placed in a suitable vessel, such as a round bottom flask. This vessel is connected to a water-cooled Liebig or Vigreux condenser, which is typically open to the atmosphere at the top. The reaction vessel is heated in order to boil the reaction mixture; vapours produced from the mixture are condensed by the condenser, and return to the vessel through gravity. The purpose is to thermally accelerate the reaction by conducting it at an elevated, controlled temperature (i.e. the solvent's boiling point) and ambient pressure [124].

3.1.1.3 Synthesis of graphene oxide (GO) gel

Graphene oxide gel was prepared at room temperature using a modified Hummers method [125]. Briefly, 1.0 g of graphite powder and 6.0 g of $KMnO_4$ were poured into a beaker containing 120 mL of concentrated sulphuric acid (H_2SO_4) (95-99.9%). The mixture was stirred for 15 min to secure a homogeneous dispersion of the solution which resulted in a yellowish-green dark suspension. This was then transferred into a silicone oil bath and further stirred at 50 ° C for 180 min to obtain a thick dark-grey solution which was left to cool down to room temperature. A stoichiometric volume of 30% H_2O_2 and distilled water was subsequently poured into the solution to subdue the residual permanganate and manganese (IV) oxide mixture to a colourless soluble manganese sulphate. This caused a large heat evolution due to the dehydration of the tetraoxo sulphate (VI) ions. The reacted solution became very hot with distinct agitation. The recovered solution was stirred for 1 min and then centrifuged for 10 min with the supernatant decanted away. The recovered gelatinous solution was re-dispersed in distilled water by mechanical shaking (250 oscillations/minute) for 1 h, with additional centrifugation for 30 min and thereafter was kept for 10 days in ambient conditions to solidify. The recovered solid (graphene oxide) was dried in an electric furnace under normal pressure at a temperature of 90 °C for 2 h.

3.1.1.4 Synthesis of carbon nanorods

The carbon nanorods in this work were synthesized by re-dispersing 0.3 g of the as-prepared GO gel into 45 ml of 10 M aqueous NaOH solution with continuous stirring for 5 min. The mixture

was transferred into a reflux set-up with magnetic stirring. The reflux flask was put in a silicone oil bath on a hot plate at 100 °C which is close to the boiling point of the high-concentration alkaline solution (ca. 120 °C) for 24 h at a stirring rate of 500 revolutions per minute, as shown in Fig. 3.1. This synthesis was carried out under reflux condition so that the pressure within the system during synthesis is kept constant at ambient atmospheric pressure. After the reaction, the reflux flask was taken out of the bath and allowed to cool naturally to room temperature. The resulting sample was collected via centrifugation, washed repeatedly with deionized water to obtain a pH of 7. The recovered sample was re-dispersed in water with 2 ml HCl (32%) added drop wise and heated at 100 °C for 20 min to further neutralize the solution. The supernatant was decanted away and the resulting sample was washed several times with deionized water. The recovered product was put in an oven to dry at a temperature of 80 °C.

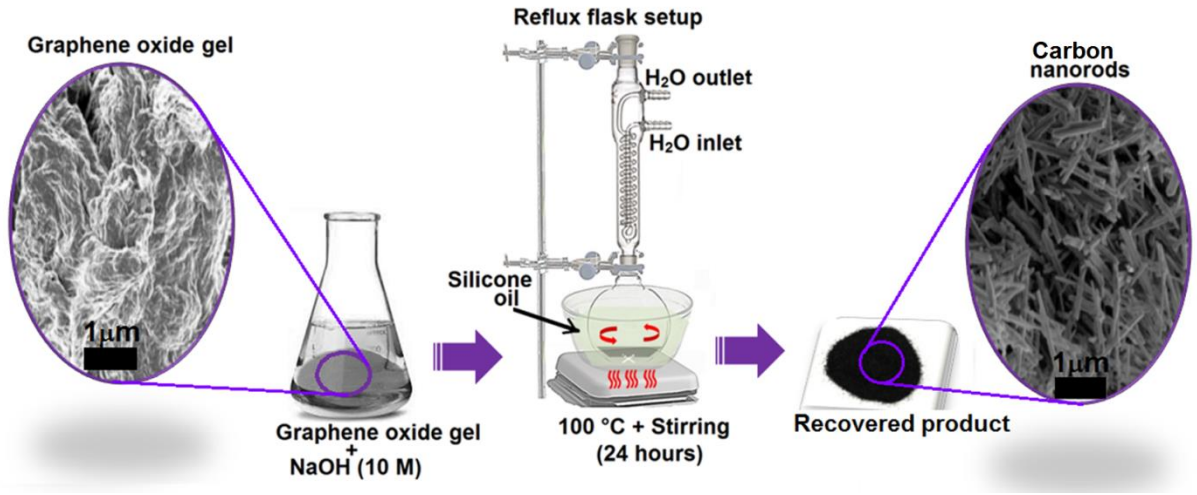

Fig. 3.1: The synthesis process of carbon nanorods from as-prepared graphene oxide gel.

3.1.1.5 Annealing

In an annealing process, a material usually a metal is subjected to a temperature above its recrystallization temperature, and maintained at that temperature for a particular time for homogenization followed by gradual cooling to enhance equilibrium structural growth within the material [126]. The process improves a material's formability, toughness and electrical conductivity among other properties. It is a means to adjust the required microstructure and characteristics in a material.

3.1.1.6 Atmospheric pressure chemical vapor deposition technique (APCVD)

The APCVD device shown in Fig. 3.2 was employed for the annealing of some samples used in this work. It was established in the early 1960s to prepare carbon fibers and carbon nanofibers. The materials are placed at the middle of the reactor chamber in a continuous gas (or a mixture of gases) flow at a particular temperature. The method is simple, cost-effective and reliable. It is suitable for the production of good quality, uniform and large-scale deposition of materials [127].

Fig.3.2: The APCVD device used for annealing in this work.

3.1.2 Preparation of NiCoMn-triple hydroxide (NiCoMn-TH) and ternary NiCo-MnO_2 composites

In the synthesis of the NiCoMn-TH sample, 0.67 g of $Mn(NO_3)_2{\cdot}4H_2O$, $Ni(NO_3)_2{\cdot}6H_2O$ and $Co(NO_3)_2{\cdot}6H_2O$ precursor salts were completely dissolved in 100 ml of deionized water whilst magnetically stirring the mixture. Subsequently, 14 ml of 1 M NaOH was added dropwise to maintain a pH of 10 for polarization, with the homogeneous mixture kept at 40 °C for 2 h upon magnetic stirring. The resulting greyish-cream mixture was left to stand for about 10 h for complete precipitation. It was then centrifuged and washed several times with deionised water and ethanol. The solid precipitate was collected and dried in an oven at 60 °C for 12 h. The interim solid ternary nickel cobalt manganese triple hydroxide (NiCoMn-TH) material was then annealed in air at 650 °C for 1 h at a ramping rate of 2 °C/min to obtain a

more stable ternary NiCo-MnO_2 composite. Fig. 3.3 shows the synthesis route used to produce the composite materials.

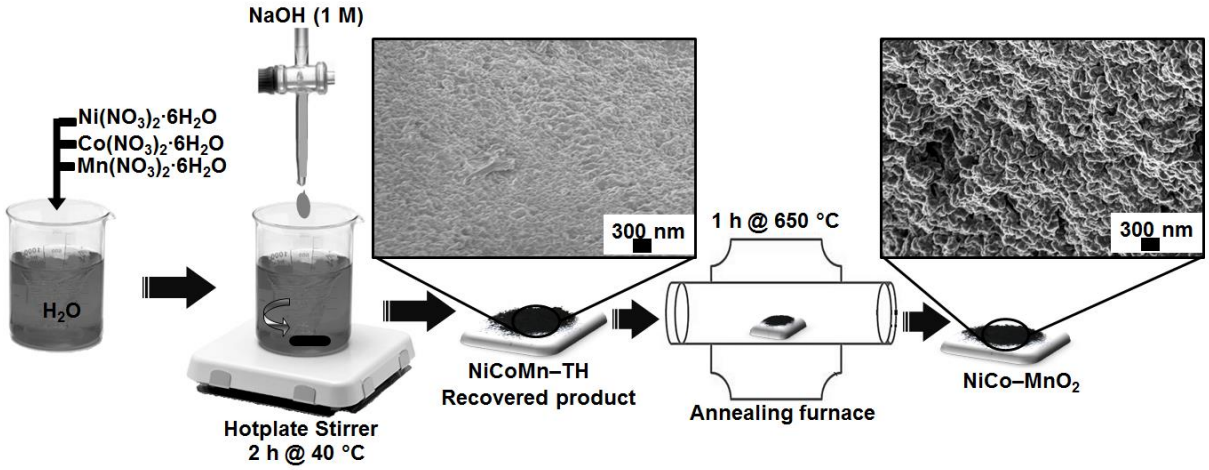

Fig. 3.3: Schematic of the synthesis route of NiCoMn-TH and NiCo-MnO_2 composites

3.1.2.1 Solvothermal process

A solvothermal process can be defined as a process in a closed reaction vessel inducing decomposition or chemical reactions between precursors in the presence of a solvent at a temperature higher than the boiling temperature of the solvent [128], [129]. The pressure can be autogeneous (in such a case the pressure value depends on the filling of the reaction vessel) or imposed (the pressure value being higher than 1 bar (105 Pa) at the starting point of the experiment through the compression of the reaction medium). Depending on the experimental conditions (pressure and temperature), the solvothermal system can be heterogeneous or homogeneous and in subcritical or supercritical conditions [129]. The word “solvothermal”

can be used whatever the chemical composition of the solvent is aqueous or non-aqueous [128]–[130]. Originally such processes were developed with water. For aqueous solutions the word “hydrothermal” is commonly used [129]. Solvothermal process allows for the precise control of the size, shape distribution, and crystallinity of metal oxide nanostructures [130]. Fig. 3.4 shows the set-up used for the solvothermal process in this research.

Fig. 3.4: Solvothermal apparatus.

3.1.3 Preparation of Mn_3O_4 nanoparticles

The Mn_3O_4 nanoparticles employed in this work were prepared by dissolving 0.768 g of $KMnO_4$ in 100 mL ethanol (99.9 %) followed by addition of 0.5 mL of 10.2 M HCl drop-wise with magnetic stirring at room temperature to achieve a homogeneous mixture. The contents

were then transferred into a Teflon-lined autoclave for a dwell time of 4 hours at a temperature of 150 ˚C. The system was allowed to cool down naturally to room temperature and the recovered sample was washed several times with deionized (DI) water to remove excess reagent. The brown precipitate was then dried for 12 h in an electric oven at 60 ˚C in air (under normal laboratory conditions).

3.1.4 Preparation of the Ti_3C_2-Mn_3O_4 nanocomposite

Briefly, 100 mg Ti_3C_2 was dispersed in 100 mL ethanol 99.9 % with magnetic stirring at room temperature. The mixture was sonicated for 1 hour to speed-up the uniform dispersion. Thereafter, 0.768 g $KMnO_4$ was added to the Ti_3C_2 mixture with a drop-wise introduction of 0.5 mL HCl (10.2 M) for homogeneity while magnetically stirring the entire reaction chamber for 20 minutes. The resulting mixture was poured into a Teflon-lined stainless steel autoclave unit and bubbled with argon gas to prevent oxidation of the sample before being sealed and heated up to 150 ˚C for a dwell time of 4 hours. After cooling to room temperature, the resulting precipitate was washed several times with deionized water until a neutral pH was recorded and then oven dried at 60 ˚C for 12 h in air to obtain the Ti_3C_2-Mn_3O_4 nanocomposite. Fig. 3.5 below shows the synthesis process of the composite material.

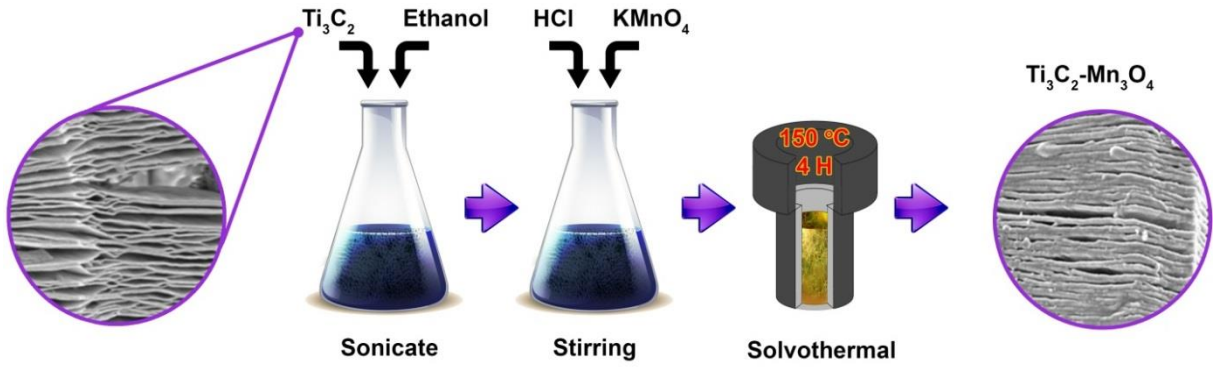

Fig 3.5: Schematic of the synthesis process to the Ti_3C_2-Mn_3O_4 nanocomposite.

3.1.5 Preparation of carbonized iron cations adsorbed onto PANI (C-FP)

Iron (III) nitrate nonahydrate (0.2 g), 0.0125 g of polyaniline (PANI) and 0.026 g each of carbon acetylene black (CB) and polyvinyldifluoride (PVDF) were completely dissolved in ethanol (50 mL, 99.9 %) whilst magnetically stirring for 5 minutes. The precursors' masses were carefully selected to ensure an approximate weight ratio of 80:10:10 for iron (III) nitrate salt and PANI (80 %), CB (10 %) and PVDF (10 %) respectively. After 5 minutes of stirring, the resulting mixture was sonicated several hours to form a slurry. The recovered slurry was then coated onto cut-to-size nickel foam (1 cm × 1 cm) which was transferred into a chemical vapour deposition (CVD) system under N_2 atmosphere at 850 °C for 2 h to obtain iron cations adsorbed onto the PANI film (C-FP) directly grown onto the nickel foam as displays in Fig. 3.6 below:

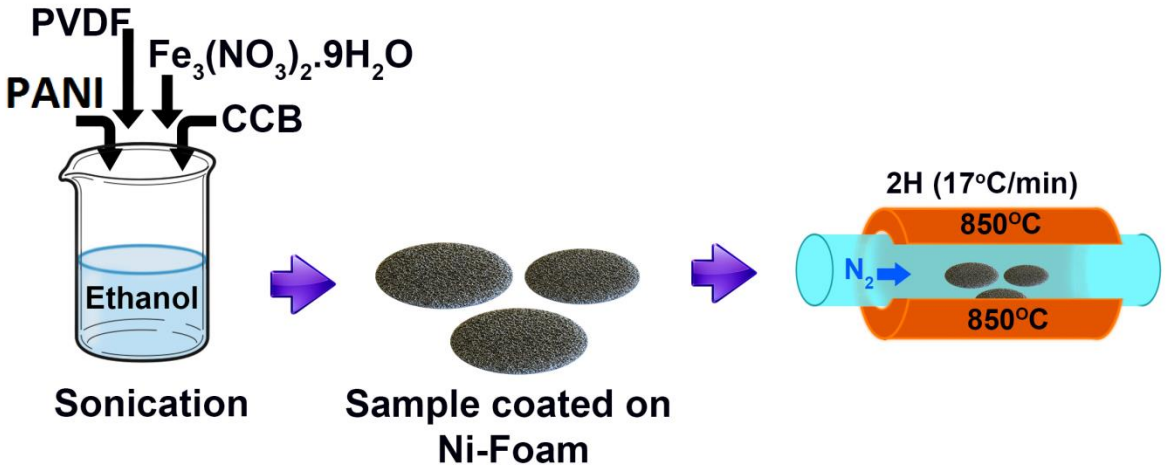

Fig. 3.6: Synthesis route of C-FP electrode material.

3.1.5.1 Preparation of polyaniline (PANI)

0.2 M of aniline hydrochloride (C_6H_8ClN) (2.59 g aniline hydrochloride in 50 ml deionized water) was added to 0.25 M of ammonium peroxydisulfate ($(NH_4)_2S_2O_8$) (5.71 g ammonium peroxysulfate in 50 ml deionized water. The mixture was stirred for 10 minutes, and then left to stand overnight to polymerize. The supernatant was decanted away and the recovered precipitate was washed several times with deionized water. The resulting sample was dried overnight in an electric oven at 60 °C under ambient condition.

3.2 Material characterization techniques

3.2.1 Scanning electron microscopy (SEM) and energy dispersive X-ray spectrometry (EDX)

The surface morphology and the composition of the samples in this thesis were visualized and examined using scanning electron microscopy. Scanning electron microscopy uses a focused beam of high-energy electrons to generate a variety of signals at the surface of the solid samples. The types of signals usually produced by a SEM include secondary electrons (SE), back-scattered electrons (BSE), characteristic X-ray, light cathodoluminescence (CL), specimen current and transmitted electrons. Secondary electron detectors are standard equipment in all SEMs, but it is rare that a single SEM would have detectors for all possible signals. The signals result from interactions of the electron beam with atoms at or near the surface of the sample. The signals that are derived reveal information about the sample such as morphology, chemical composition, thickness, porosity and orientation of the microscopic materials that make up bulk material. Due to the very narrow electron beam, SEM images have a large depth of field yielding a characteristic three-dimensional appearance useful for the understanding the surface structure and texture of the sample. In SEM, a wide range of magnifications is possible, from about 10 times (equivalent to that of a powerful hand-lens) to more than 500,000 times, about 250 times the magnification limit of the best light microscopes. In most applications, data are collected over selected areas of the surface of the sample, and a 2-dimensional image that displays spatial variations in these properties is generated. The Carl Zeiss Ultra Plus 55 scanning electron microscope, shown in Fig. 3.7, is located at the Microscopy lab, University of Pretoria. The system combines all the advantages

of an optical and electron microscopes in one integrated system without compromising on ease of use or time to result.

Energy Dispersive X-ray spectroscopy (EDS) is an analytical technique used for the elemental analysis or chemical characterization of a sample, it can serve as a complementary technique for IBA techniques such as Particle Induced X-ray Emission technique. In recent time, this technique is usually coupled with the field emission scanning electron microscopy (FESEM) using a high-resolution (Carl Zeiss, Ultra Plus 55) on SEM equipment and the analyses are usually carried out simultaneously. Information about samples is obtained from interaction of some sources of X-ray excitation and a sample. Its characterization capabilities are due in large part to the fundamental principle that each element has a unique atomic structure allowing unique set of peaks on its X-ray spectrum [131]. To stimulate the emission of characteristic X-rays from a specimen, a high-energy beam of charged particles such as electrons or protons, or a beam of X-rays, is focused into the sample being studied. An atom within the sample contains ground state (or unexcited) electrons in discrete energy levels or electron shells bound to the nucleus. The incident beam may excite an electron from inner shell, ejecting it from the shell while creating an electron hole. An electron from an outer, higher-energy shell then fills the hole, and the difference in energy between the higher-energy shell and the lower energy shell may be released in the form of an X-ray. The number and energy of the X-rays emitted from a specimen can be measured by an energy-dispersive spectrometer. As the energy of the X-rays is characteristic of the difference in energy between the two shells, and of the atomic structure of the element from which they were emitted, this allows the elemental composition of the specimen to be measured [131]. The accuracy of EDS is usually affected by various factors. For instance, many elements may have overlapping peaks. The accuracy of the spectrum can also be affected by the nature of the sample. In

addition, X-rays can be generated by any atom in the sample that is sufficiently excited by the incoming beam. These X-rays are emitted in any direction, and so they may not all escape the sample. The likelihood of an X-ray escaping the specimen, and thus being available to detect and measure depends on the energy of the X-ray and the amount and density of material it has to pass through. This can result in reduced accuracy in inhomogeneous and rough samples.

The microscopic images and elemental compositions for all samples in this thesis were examined by the field emission scanning electron microscopy (FESEM) using a high-resolution Zeiss Ultra Plus 55, operating at 2.0 kV, coupled with integrated energy dispersive X-ray spectrometer (EDX), operating at 20 kV.

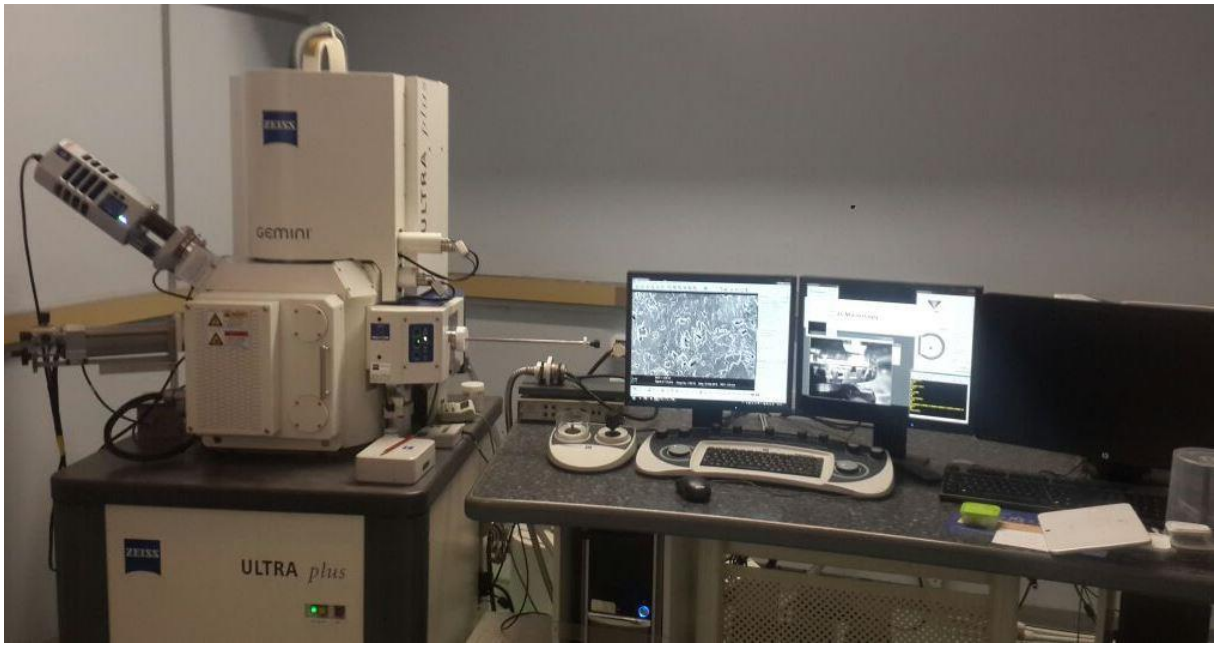

Fig. 3.7: High-resolution FESEM instrument (Carl Zeiss, Ultra Plus 55) at the University of Pretoria, South Africa.

3.2.2 Transmission electron microscopy (TEM)

Transmission electron microscopy (TEM) is a microscopy technique in which a beam of electrons is transmitted through an ultra-thin specimen, interacting with the specimen as it passes through. An image is formed from the interaction of the electrons transmitted through the specimen; the image is magnified and focused onto an imaging device, such as a fluorescent screen, on a layer of photographic film, or to be detected by a sensor such as a (charge-coupled device) CCD camera.

TEM is capable of imaging at a significantly higher resolution than light microscopes, owing to the small de Broglie wavelength of electrons. This enables the instrument's user to examine fine detail—even as small as a single column of atoms, which is thousands of times smaller than the smallest resolvable object in a light microscope. TEM forms a major analysis method in a range of scientific fields, in both physical and biological sciences. TEM finds application in cancer research, virology, materials science as well as pollution, nanotechnology, and semiconductor research. At smaller magnifications TEM image contrast is due to absorption of electrons in the material, due to the thickness and composition of the material. At higher magnifications complex wave interactions modulate the intensity of the image, requiring expert analysis of observed images. Alternate modes of use allow for the TEM to observe modulations in chemical identity, crystal orientation, electronic structure and sample induced electron phase shift as well as the regular absorption based imaging [132], [133]. Fig. 3.8 shows the high-resolution transmission electron microscopy (HR-TEM) JEOL 2100F (from Japan) equipped with LaB6 filament, a Gartan U1000 camera of 2028 x 2028 pixels and operated at 200 kV, employed to acquire electron micrographs for all samples in this thesis.

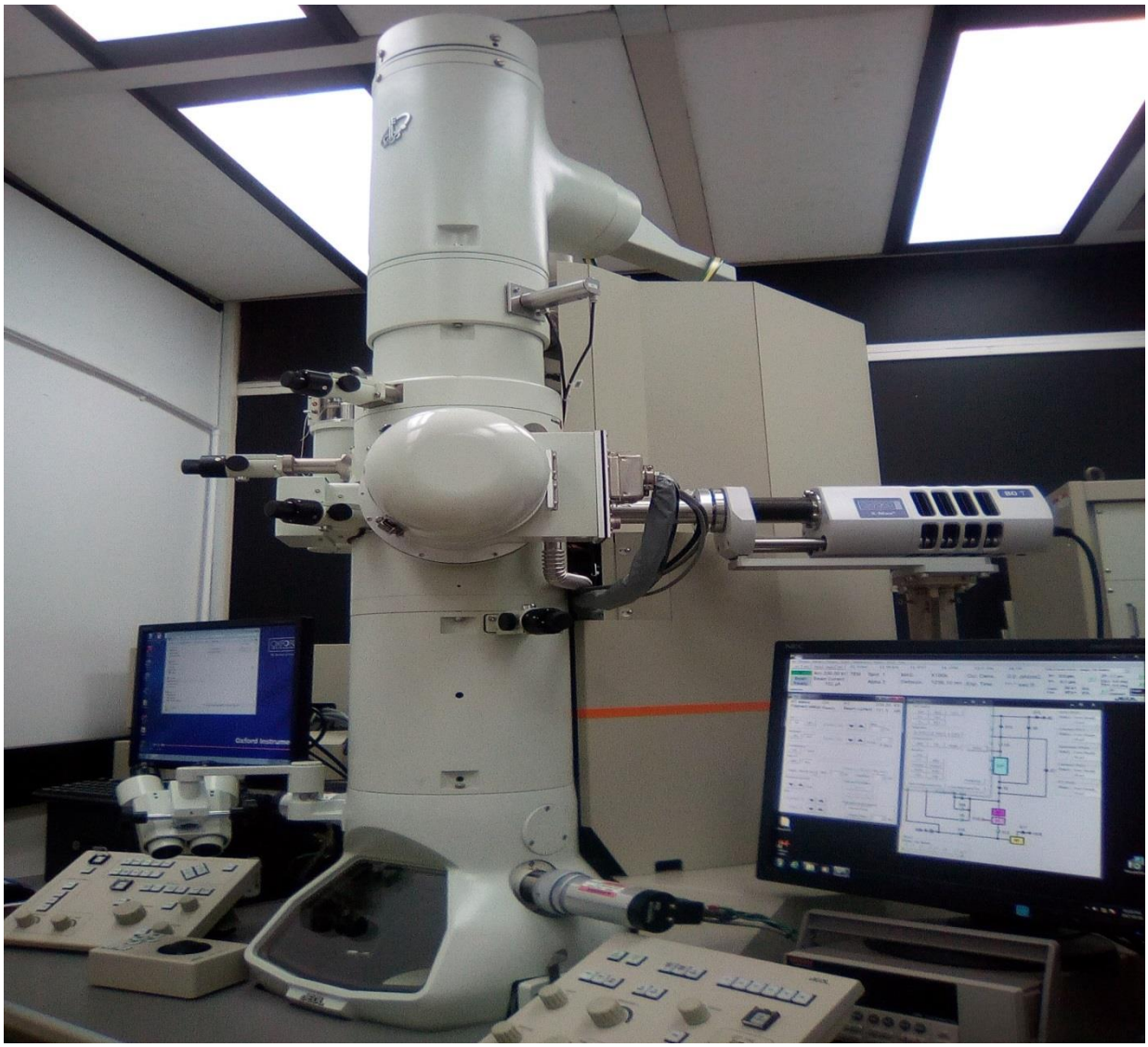

Fig: 3.8: Transmission electron microscopy instrument (HR-TEM-JEOL 2100F).

The device is equipped with an integrated scanning transmission electron microscope along with energy dispersive X-ray (STEM-EDX). Sample specimens were prepared via uniform dispersion of the powder specimen in an ethanol solvent (100%), and sonicated over an hour and subsequent drop casting on a lacey carbon-coated copper grid which was then dried before loading onto the analysis chamber.

3.2.3 X-ray powder diffraction (XRD)

XRD characterization in this thesis was done using an XPERT-PRO diffractometer in a θ/2θ configuration, with a cobalt tube at 35 kV and 50 mA (PANalytical BV, Netherlands), located at the Department of Geology, University of Pretoria, South Africa.

Powder X-ray diffraction techniques were employed for the determination of the crystallinity and phase changes in the materials as they are subjected to different physical and chemical treatments. The materials were all subjected to careful scrutiny before and after preparation to ascertain among others the effect of preparatory methods on the microstructure of the materials. XRD is a non-destructive analytical technique utilized for the investigation of the phases of crystalline materials [134], [135], as well as other parameters that include lattice parameters, crystallite sizes, and phase distribution via Rietveld confinement [134]. The device is made-up of three major components, namely an X-ray tube, a sample holder, and an X-ray detector, all assembled on the circumference of the circle called the 'focusing circle'. Electrons are emitted from a cathode ray tube by heating the filament and subsequently accelerated to the target (the anode, usually composed of copper or cobalt) where the bombardment occurs to yield X-rays in a cathode ray tube. The X-ray production is the product of the interaction of the bombarded electrons with electrons in the inner shell of the target material that results in the dislodgement of the inner shell electrons by the bombarded electrons [135], [136]. The type of the anode material used determines the type of the characteristic X-rays to be produced (for example, Cu produces X-ray with a $\lambda = 1.5406$ Å and Co with $\lambda = 1.7890$ Å). Using the X-ray interaction with the specimen, constructive interference takes place and the Bragg's law is satisfied [136]:

$$n\lambda = 2d\ sin\ \theta \quad \textbf{23}$$

where n is any integer value (1,2,3..), λ is the wavelength of the incident x-ray, d is the spacing between the diffracting planes and θ is the incident angle. The angle between the projection of the X-ray source and the detector is 2θ. In a crystalline specimen, Bragg's law gives the relation between the wavelength of an electromagnetic radiation, angle of diffraction (Bragg's angle), and lattice distance. The crystallize size of the specimen can be calculated from the XRD data via [136]:

$$G_{hkl} = \frac{k\lambda}{\beta\ Cos(\theta)} \quad \textbf{24}$$

where G_{hkl} is the average linear dimension of the crystal perpendicular to the diffracting plane (hkl) (diameter of the particles), β (radians) is the full-width at half-maximum in the 2θ scan, k is a dimensionless shape factor with a typical value of 0.89, λ is the wavelength of the X-rays and θ is the Bragg's angle.

3.2.4 Raman spectroscopy

Raman spectroscopy is an important technique used in studying vibrational, rotational, and other low-frequency modes of a material [137]. The technique operates on the inelastic scattering (Raman scattering) of monochromatic light, generally emanating from a laser in the visible, near infrared, or near ultraviolet regions. The interactions of the laser light with molecular vibrations, phonons or other excitations in a material result in the energy or frequency of the laser photons to be varied up or down with respect to the energy or frequency of the original monochromatic light, in a process called Raman Effect [137]. The energy or

frequency variations supply information on the vibrational modes in a material. The technique can be employed to investigate of solid, liquid, and gaseous materials. [138]–[141].

A T64000 micro-Raman spectrometer (HORIBA Scientific, Jobin Yvon Technology) with a 514 nm laser wavelength and spectral acquisition time of 120 s was used to characterize the as-prepared samples in this work. The Raman system laser power was set as low as 5 mW in order to minimize heating effects.

3.2.5 Fourier transforms infrared (FTIR) spectroscopy

FTIR spectroscopy is a method employed to acquire an infrared spectrum of absorption or emission by a solid, liquid or gas. The spectrometer simultaneously obtains high-spectral-resolution data over a wide spectral range. This confers a significant advantage over a dispersive spectrometer, which can only measure intensity over a narrow range of wavelengths at a time. The term "Fourier transform" originated from the fact that a mathematical process called Fourier transform is required to transform the raw data into the actual spectrum [142].

Fourier transform-infrared (FT-IR) spectra of the samples in this study were obtained using a Varian FT-IR Spectroscopy (Bruker Vertex 77 v FT-IR spectrometer) in the wavenumber range of 400 - 4000 cm^{-1}, operated with the OPUS software.

3.2.6 N_2 gas-absorption-desorption measurement

N_2-absorption-desorption is a useful technique in sample analysis. It is employed to examine the specific surface area (SSA), porosity, average pore volume, and the broad pore size distribution of powder specimen. In this work, N_2-absorption-desorption isotherms were obtained on a Micromeritics TriStar II 3020 system operated in a relative pressure (P/P_o) range of 0.01–1.0 with pre-degassing of the samples at 100 °C for 18 h under vacuum prior to the measurement. The Brunauer-Emmett-Teller (BET) and Barrett–Joyner–Halenda (BJH) models were used to determine the surface area and the pore size distribution (PSD) of the samples respectively. The procedure for acquiring the isotherms comprised degassing of the pre-weighed samples at specific temperature under vacuum to eliminate any residual moisture, then loaded onto the analysis chamber for the investigation under extremely cold environment such as N_2 gas at low pressure and 77 K. This is followed by dosing the specimens with a particular quantity of gas and subsequent evacuation of the gas to acquire the amount of gas absorbed by the specimens over a relative pressure range, P/P_0 (i.e. $0.01<P/P_0<0.2$). The type of the isotherm acquired provides information on the class of pore size in the specimen. Brunauer et al. (1940) reported five classes of adsorption isotherms [143], before the International Union of Pure and Applied Chemistry (IUPAC) (1985) [144] came up with six categories of the adsorption isotherms. Gregg and Sing [145], later gave the detailed account of the variations between the categories with a supplementary adsorption and desorption hysteresis. Fig. 3.9 shows the various adsorption-desorption isotherms and hysteresis loops.

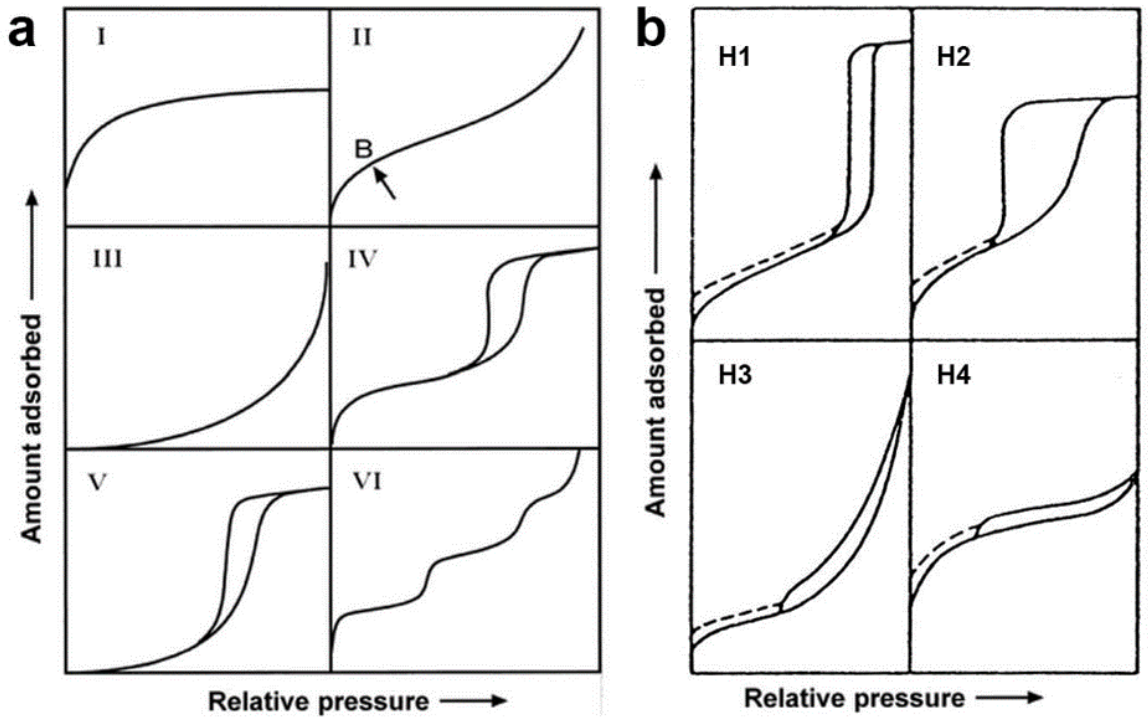

Fig. 3.9: (a) The IUPAC classification of adsorption-desorption isotherms for gas–solid equilibria [146], (b) the adsorption-desorption hysteresis [145].

Fig. 3.9a shows different types of isotherms. Type 1 isotherm is called Langmuir type, which is associated to adsorption on the microporous structure. Type II and III correspond to macroporous or non-porous adsorbents, showing strong and weak interactions respectively. Type VI and V are typical of mesoporous structure with the latter showing weak interactions. Type VI isotherm is a characteristic of stepwise, layer-by-layer adsorption on a macroporous surface [146]. The adsorption-desorption hysteresis loop is classified into four categories namely, H1, H2, H3, and H4 shown in Fig. 3.9b. H1 is attributed to slight distribution of comparatively similar cylindrical-like pores, H2 signifies a complex pore structure, while H3

and H4 corresponding to accumulations of slit-shaped pores, and complex materials consisting of both microporous and mesoporous structure respectively [145].

3.2.7 Thermal gravimetric analysis (TGA)

TGA is a technique of thermal analysis involving the mass of a sample been measured over time as the temperature varies. It provides information about physical phenomena such as phase transitions, absorption and desorption, and thermal decomposition among others. TGA also supplies information about some chemical phenomena like chemisorptions, solid-gas reactions of thermal analysis that account for variations in physical and chemical properties of materials against increase in temperature (with constant heating rate), or against time (with constant temperature and/or constant mass loss) [147], [148]. TGA is generally employed to investigate certain features of materials showing either mass loss or gain due to decomposition, oxidation, or loss of moisture [147].

In this work, thermogravimetric analysis (TGA) was carried out using a thermogravimetric analyzer (Hitachi TGA, from 20 °C to 1000 °C in air) to determine the material weight change against increase in temperature in a controlled environment over time. The results from TGA analysis were used in determining the carbon content in the hybrid sample, which is calculated from the residual mass of the pristine and hybrid samples. TGA samples in this thesis were heated from ambient temperature to 1000˚C at a ramp rate of 10˚C min-1 in nitrogen gas.

3.2.8 X-ray photoelectron spectroscopy (XPS)

The XPS, a surface-sensitive quantitative spectroscopic technique that measures the elemental composition at the parts per thousand range, empirical formula, chemical state and electronic state of the elements that exist within a material. XPS spectra are acquired by irradiating a material with a beam of X-rays whilst concurrently measuring the kinetic energy and number of elastically scattered electrons (photoelectrons) that break from the top 0 to 10 nm of atomic layers in the material being analyzed [132]. The technique requires high vacuum (P ~ 10−8 millibar) or ultra-high vacuum (UHV; P < 10−9 millibar) conditions, however, a current area of development is ambient-pressure XPS [132], [149], and material samples are analyzed at pressures of a few tens of millibar. The technique can be used to analyze the surface chemistry of a material in its as-received state, or after some treatment. A characteristic XPS spectrum is a plot of the number of detected electrons (occasionally per unit time) against the binding energy of detected electrons. Each element generates a typical set of XPS peaks at specific binding energy values that clearly distinguish each element that is in or on the surface of the analyzed sample. The characteristic spectrum peaks are related to the electron configuration within an atom, e.g., 1s, 2s, 2p, 3s, among others. Hence, the number of electrons detected in each of the distinctive peaks is proportionally linked to the quantity of elements in the XPS sampling volume [149].

X-ray photoelectron spectroscopy (XPS) measurements of the samples in this research were conducted using a Physical Electronics VersaProbe 5000 spectrometer operating with a 100 μm monochromatic Al-Kα exciting source. A 180° hemispherical electron energy analyzer collected photoelectrons, with the samples been analyzed at a 45° angle between the sample surface and the path to the analyzer. Survey spectra were taken at pass energy of 117.5 eV,

with a step size of 0.1 eV, which was used to obtain an estimate of the elemental analysis of the powders.

3.2.9 X-ray fluorescence (XRF)

XRF is the emission of characteristic "secondary" (or fluorescent) X-rays from a material that has been excited by bombarding with high-energy X-rays or gamma rays. The phenomenon is widely used for elemental analysis and chemical analysis, particularly in the investigation of metals, glass, ceramics and building materials, and for research in geochemistry, forensic science, archaeology and art objects [150], [151] such as paintings and murals.

In this thesis, XRF measurements of the pressed powder composite samples were performed using the ARL Perform'X Sequential XRF instrument with Uniquant software for analysis.

3.3 Electrochemical characterization

The capacitive performances of the nickel foam-supported electrodes in this thesis were investigated using a Bio-Logic VMP300 potentiostat (Knoxville TN 37,930, USA) controlled by the EC-Lab® V1.40 software in both the three-electrode and two-electrode configurations. The electrochemical measurements were performed with a glassy carbon counter electrode, Ag/AgCl reference electrode, and the as-prepared mixed carbon-based materials as the working electrodes. The working electrodes were prepared by mixing active material, carbon acetylene black as a conducting agent and polyvinylidenedifluoride (PVDF) as binder in a small amount of NMP solvent, in a proportionate weight ratio to make slurry, which was then

coated onto the Ni foam current collector and dried in an electric oven at a particular temperature. All the electrochemical measurements for this study were performed in a KOH aqueous electrolyte at room temperature. Fig. 3.10 displays a 16-channel Bio-Logic VMP300 potentiostat electrochemical workstation used for characterization of materials in this thesis.

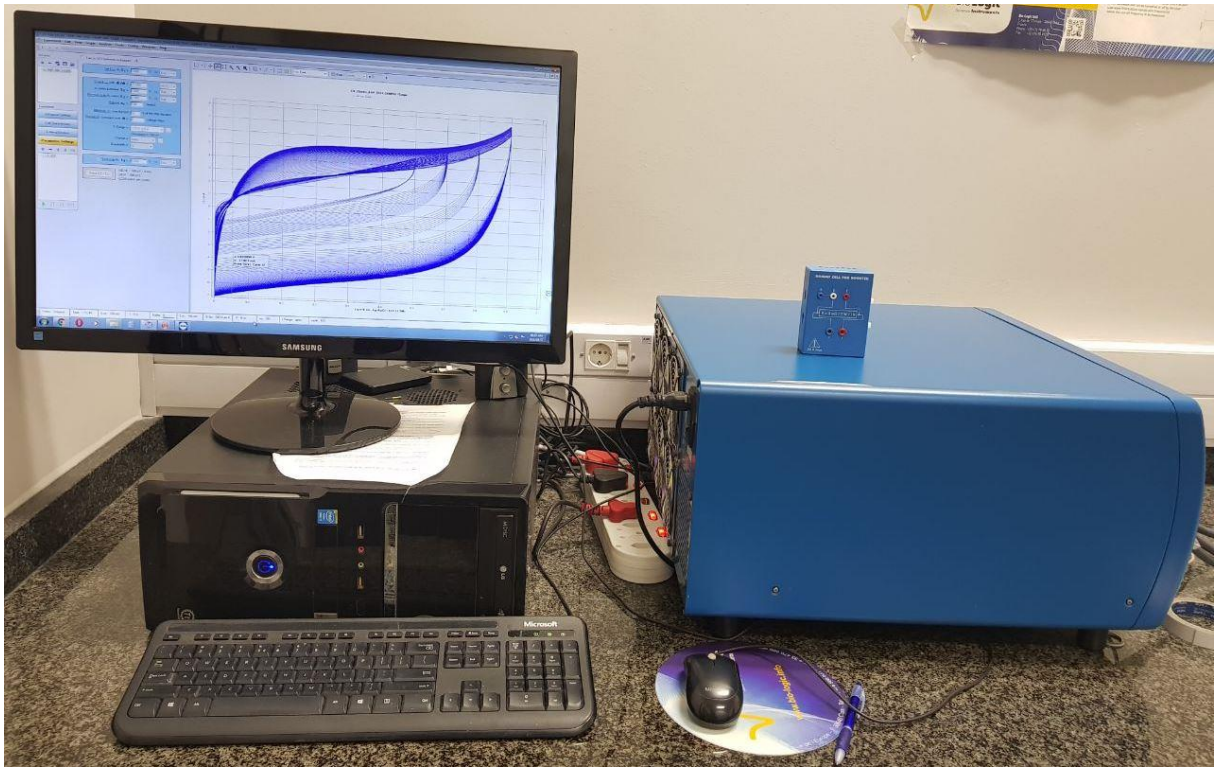

Fig. 3.10: A 16-channel Bio-Logic VMP300 potentiostat electrochemical workstation.

Chapter 4

4.1 Results and discussions

This chapter of the thesis emphasizes the successful results obtained from the synthesis, characterization and electrochemical measurements of the as-synthesized materials outlined in the previous chapter. All the results presented in this chapter are originally of the author's researches. Some of the results have been published as articles in peer-reviewed journals, while some are under review for publication.

4.1.1 Investigation of graphene oxide nanogel and carbon nanorods as electrode for electrochemical supercapacitor

4.1.1.1 Introduction

Due to high energy consumption and depleting natural resources globally, the necessity for alternative energy has never been more evident. Electrochemical energy production has been one of the focii of alternative energies as it can be designed to be environmentally friendly, suitable for both stationary and mobile systems, and more sustainable than other sources. Most of the electrical energy used in the world is currently supplied from fossil fuels. Therefore, measures are being adopted in a variety of different fields to help prevent global warming by reducing CO_2 emissions. Consequently, the automotive industry has become a

focal point when considering the impact of fossil fuel use on the environment [8], [152], [153].

In this work, the synthesized two phases of carbon-based materials; graphene oxide (GO) gel and carbon nanorods obtained from the GO gel via a modified Hummer's method and a force-driven reflux process respectively, using powdered graphite as the main precursor have demonstrated good electrochemical properties which suggest their promising contribution to the supercapacitor field.

4.1.1.2 Results and Discussion

The detailed results obtained from this work are presented in the paper below.

Electrochimica Acta 245 (2017) 268–278

Contents lists available at ScienceDirect

Electrochimica Acta

journal homepage: www.elsevier.com/locate/electacta

Investigation of graphene oxide nanogel and carbon nanorods as electrode for electrochemical supercapacitor

K.O. Oyedotun, M.J. Madito, A. Bello, D.Y. Momodu, A.A. Mirghni, N. Manyala*

Department of Physics, Institute of Applied Materials, SARCHI Chair in Carbon Technology and Materials, University of Pretoria, Pretoria 0028, South Africa

ARTICLE INFO

Article history:
Received 13 March 2017
Received in revised form 26 April 2017
Accepted 23 May 2017
Available online 25 May 2017

Keywords:
Graphene-oxide
Reflux
Gel
Nanorods
Specific capacitance/capacity
Supercapacitors
energy storage

ABSTRACT

In this study, a gel of graphene oxide (GO) and carbon nanorods obtained from the GO gel were synthesized via a modified Hummer's method and a force-driven reflux process respectively. Scanning electron microscopy (SEM) was used to analyse the morphology of the as-synthesized materials showing gelatinous and nanorods structures for the graphene oxide and carbon materials respectively. X-ray diffraction (XRD) suggests that the synthesized materials have a hexagonal crystal structure and an increased interlayer spacing due to the interlaced molecules of oxygen-containing functional groups. X-ray photoelectron spectroscopy (XPS) and energy dispersive X-ray spectroscopy (EDX) analysis were employed to confirm the presence of carbon and oxygen functionalities in the synthesized materials. Electrodes fabricated from both materials prove a limit specific capacitance of 436.5 $F g^{-1}$ and 719.5 $F g^{-1}$ corresponding to specific capacities of 48.5 $mAh g^{-1}$ and 80.8 $mAh g^{-1}$ at a current density of 0.5 $A g^{-1}$ in a three electrode system with 6 M KOH electrolyte for both the graphene oxide gel and carbon nanorods respectively. The materials show good cycle stability after 3000 cycling at a current density of 5 $A g^{-1}$, which implies a great promise as electrodes for supercapacitor applications.

1. INTRODUCTION

Due to high energy consumption and depleting natural resources globally, the necessity for alternative energy has become evident. Electrochemical energy storage (batteries and supercapacitors) have been one of the main focus of storage system for renewable and sustainable energy sources since most of these sources require a storage component [1–4]. Most of these combined systems are already being used in new advanced technologies to store power due to their sustainability and suitability for both stationary and mobile systems [5,6].

The requirement for micro-power units have increased in recent time, and this has put high demands on micro-power devices manufacturing [7]. Micro-power components are needed to become continuously smaller and operate faster to meet technological inventions but not at the expense of its reliability and price. The future requirement for energy generation and storage cannot be easily achieved without innovative design of electrode materials. Therefore, an enormous effort has to be spent on research and development of new materials in order to develop high performance and reliable energy storage devices.

Supercapacitors (SCs) are classified as emerging high power-delivery storage devices which are known to be able to hold much more electrical charge than standard parallel-plate capacitors [3,8]. They are also easily able to discharge at a very fast rate in delivering the necessary high power as compared to batteries and thus can complement batteries in many domestic, commercial and industrial applications [2,3]. SCs also work in very low temperatures; an operating condition that prevents the adoption of many types of electrochemical batteries [5]. They can be divided into three categories, specifically, (1) electric double-layer capacitors (EDLCs) which arise as a result of charge separation at an electrode/electrolyte interface (electric double-layer capacitive behaviour), (2) pseudocapacitors and redox SCs which use the charge-transfer arising from redox reactions occurring on the surface of the electrode (Faradaic behaviour) and (3) hybrid capacitors which combine both the EDLCs properties with a battery-type electrode material to form asymmetric SCs or hybrid systems [3].

Graphene is a hexagonal planar allotrope of carbon and the most representative single-atom-thick two-dimensional (2D) material which exhibits distinct properties which are radically different from its bulk three-dimensional (3D) counterpart of graphite due to its freestanding 2D nature and are suitable for diverse applications due to their fascinating properties such as superior chemical/thermal stability, excellent electrical properties, mechanical properties, high specific surface area (SSA) and good

* Corresponding author. Tel.:+ + 27 12 420 3549; fax: + 27 12 420 2516.
E-mail address: ncholu.manyala@up.ac.za (N. Manyala).

http://dx.doi.org/10.1016/j.electacta.2017.05.150
0013-4686/

flexibility [1,2,10]. The high theoretical SSA and excellent electrical conductivity has made them attractive as electrode material for energy storage, providing new possibilities for improvement in performance with high rate capability accompanied with minimal cost [3,11,12–15]. Despite these excellent properties, graphene-based electrode materials are still plagued with low energy densities when adopted in energy storage devices such as supercapacitors.

Graphene oxide (GO) or exfoliated graphene oxide has been chiefly prepared by the oxidation of graphite powder and prevalent research has been done to uncover its chemical structure or surface chemistry [16–20]. GO produced by the oxidation of graphite mainly shows sheet-like morphology and the electrochemical performance of this material has been evaluated as SC electrodes. For instance, functionalized exfoliated graphene oxide [18], electrochemically reduced graphene oxide [16], poly(ionic liquid)-modified reduced graphene oxide [21] and GO [20] show specific capacitance values in the range of 146–223.6 F g^{-1} at 5 mV s^{-1}. These specific capacitance values of GO could be enhanced by improving the surface chemistry (i.e. optimize the oxygen-containing surface functionalities) and the morphological properties of the material. Similarly, the energy density of the supercapacitor could be enhanced by either increasing the device specific capacitance by modifying the electrode material or increasing operating potential window by using organic and ionic liquids electrolytes [22,23].

In this research, we synthesized two phases of carbon-based materials namely; graphene oxide (GO) gel and carbon nanorods obtained from the GO gel via a modified Hummer's method and a force-driven reflux process respectively, using powdered graphite as the main precursor. The as-prepared electrode materials were extensively characterized using various techniques and the electrochemical performance of the materials was evaluated via a three electrode cell configuration. The prepared materials demonstrated good electrochemical properties which suggest their promising contribution to the supercapacitors field.

2. EXPERIMENTAL

2.1. Synthesis of graphene oxide (GO) gel

Graphene oxide gel was prepared at room temperature using a modified Hummers method [24]. In the preparation process, 1.0 g of graphite powder and 6.0 g of $KMnO_4$ were poured into a beaker containing 120 mL of concentrated sulphuric acid (H_2SO_4) (95–99.9%). The mixture was stirred for 15 min to secure a homogeneous dispersion of the solution which resulted in a yellowish-green dark suspension. This was then transferred into a silicone oil bath and further stirred at 50 °C for 180 min to obtain a thick dark-grey solution which was left to cool down to room temperature. A stoichiometric volume of 30% H_2O_2 and distilled water was subsequently poured into the solution to subdue residual permanganate and manganese (IV) oxide mixture to a colourless soluble manganese sulphate. This caused a large heat evolution due to the dehydration of the tetraoxo sulphate (VI) ions. The reacted solution became very hot with distinct agitation, which was then stirred for 1 min and then centrifuged for 10 min with the supernatant decanted away. The recovered gelatinous solution was re-dispersed in distilled water by mechanical shaking (250 oscillations/minute) for 1 h, with additional centrifugation for 30 min and thereafter was kept for 10 days in ambient conditions at room temperature to solidify. The recovered solid (graphene oxide) was dried in an electric furnace under normal pressure at a temperature of 90 °C for 2 h.

2.2. Synthesis of carbon nanorods

In the synthesis of carbon nanorods, 0.3 g of the as-prepared GO gel was re-dispersed into 45 ml of 10 M aqueous NaOH solution with continuous stirring for 5 min, and then transferred into reflux set-up upon magnetic stirring. The reflux flask was put in a silicone oil bath on a hot plate at 100 °C which is close to the boiling point of the high-concentration alkaline solution (ca. 120 °C) for 24 h at a stirring rate of 500 revolutions per minute, as demonstrated in Scheme 1. This synthesis was carried out under the refluxing condition so that the pressure within the system during synthesis is kept constant at ambient atmospheric pressure. After the reaction, the reflux flask was taken out of the bath and allowed to cool naturally to room temperature. The resulting sample was collected via centrifugation, washed repeatedly with deionized water to obtain a pH of 7. The recovered sample was re-dispersed in water with 2 ml HCl (32%) added drop wise and heated at 100 °C for 20 min to further neutralize the solution. The supernatant was decanted away and the resulting sample was washed several times with deionized water. The recovered product (i.e. carbon nanorods shown in Scheme 1) was put in an oven to dry at a temperature of 80 °C.

2.3. Materials characterizations

Scanning electron micrographs were obtained at 1 kV on a Zeiss Ultra Plus 55 field emission scanning electron microscope (FE-SEM) equipped with an energy-dispersive X-ray spectrometer (EDX). The X-ray diffraction (XRD) patterns were obtained by employing an XPERT-PRO diffractometer (PANalytical BV, Netherlands) with reflection geometry at 2θ values in the range

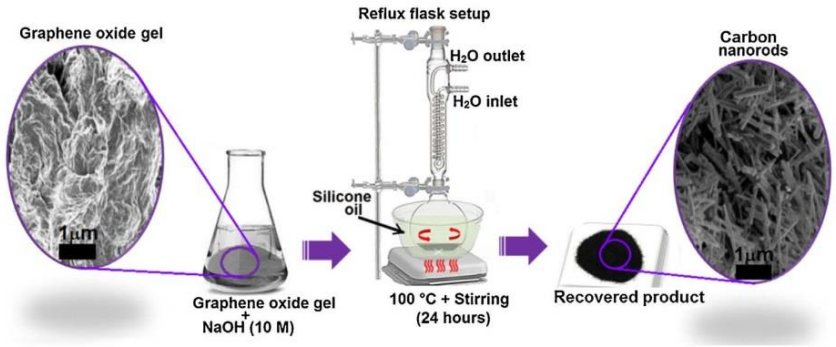

Scheme 1. Schematic of the synthesis process of carbon nanorods from as-prepared graphene oxide gel.

of 5–60° with a step size of 0.01°, operating with a Cu Kα radiation source (λ = 0.15418 nm) and at 50 kV and 30 mA. Raman spectroscopy measurements were obtained via a Jobin–Yvon Horiba TX 6400 micro-Raman spectrometer with 532 nm excitation laser and power of approximately 5 mW. X-ray photoelectron spectroscopies (XPS) of the samples were conducted using a VG Thermo ESCALAB 250 spectrometer operating with an Al-Kα exciting source.

2.4. Electrode preparation and electrochemical characterization

The electrodes were prepared by muddling the active material (80 wt %) with conductive acetylene carbon black (10 wt %) as a conducting agent and a Polyvinylidene fluoride (PVDF) (10 wt %) as a binder to make slurry, which was then coated onto nickel foam (1 cm × 1 cm) and dried at a temperature of 60 °C for 10 h. The capacitive performance of electrodes was investigated with the aid of a Bio-Logic VMP300 potentiostat (Knoxville TN 37,930, USA) controlled by the EC-Lab® V1.40 software in a three-electrode configuration. The electrochemical measurements were performed with the counter electrode made of glassy carbon, Ag/AgCl as the reference electrode, and the as-prepared graphene oxide gel and carbon nanorods electrodes as working electrodes. The measurements were conducted using a 6 M KOH aqueous solution as the electrolyte, with the mass loading of the active materials estimated to be approximately 3.0 mg and 3.8 mg for both graphene oxide gel and carbon nanorods respectively on nickel foam. The cyclic voltammetry (CV) of the as-synthesized samples were carried out at distinct scan rates ranging from 5 to 100 mV s^{-1} within a positive voltage window range of 0.0 to 0.4 V vs. Ag/AgCl as well as within a negative potential window range of −0.4 to 0.0 V vs. Ag/AgCl. The galvanostatic charge-discharge (CD) measurement was measured at distinct current densities in the range of 0.5–5.0 A g^{-1} in a potential window range of 0.0 V to 0.4 V. The electrochemical impedance spectroscopy (EIS) of the samples was performed in an open-circuit potential and in a range of 10 mHz to 100 mHz frequencies.

The specific capacitance, C_S (F g^{-1}) of the materials were evaluated via CD integration using the relation [25,26]:

$$C_S = \frac{2I}{V^2}\int V dt \tag{1}$$

The specific capacitance was converted to the equivalent specific capacity, Q (mA h g^{-1}) over a potential, V (V) according to the relations [27]:

$$Q = \frac{It}{3.6} \tag{2}$$

where $I = \frac{i}{m}$, is the current density in A g^{-1}, i is the applied current in mA, m is the mass loading of the electrode in g, V is the potential window in volts (V), and t is the time in seconds taken for

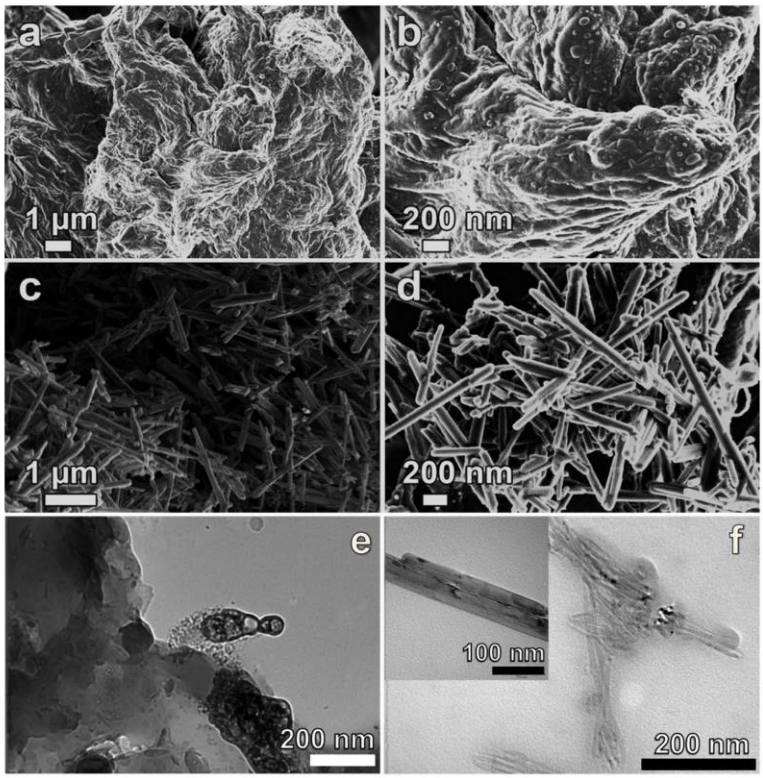

Fig. 1. (a) and (b) SEM images of the graphene oxide gel at low and high magnifications respectively. (c) and (d) SEM images of the carbon nanorods at low and high magnifications respectively. (e) and (f) TEM images of the graphene oxide gel and carbon nanorods respectively.

a complete discharge cycle.The energy efficiency of the materials was determined using the following relation [27]:

$$\eta_E = \frac{E_d}{E_c} \quad (3)$$

where η_E, E_d and E_c are energy efficiency, discharge energy from the integral of the area under the discharge curve, and charge energy from the integral of the area under the charge curve of the electrode respectively.

3. RESULTS AND DISCUSSION

3.1. Morphological and structural characterization

Fig. 1(a)–(d) and (e)–(f) show the morphology of the as-prepared samples obtained with the SEM (low and high magnifications) and TEM respectively. Fig. 1(a) and (b) show the surface morphologies of the as-prepared materials. At different magnifications, a gelatinous morphology was noticed for the graphene oxide material. The morphology of the carbon material was observed to be rod-like at low and high magnifications (Fig. 1(c) and (d)) with an overview of interconnection between the nanorods. The interconnected nanorods were observed to be closely joined to one another forming a whole conducting structure. The TEM images (Fig. 1(e) and (f)) further confirm the observations made from SEM analysis.

The overall rate of formation of the carbon nanorods is governed by the diffusion rates as well as chemical reaction between sodium hydroxide and graphene oxide gel precursor [28,29]. With the conventional hydrothermal process, nanorods with several hundreds of nanometers in length can be obtained owing to the slow dissolution-recrystallization process and low growth kinetic of nanorods at static condition [28]. To the best of our knowledge, force-driven process can provide homogeneous mix reactants in solution, increasing reaction rate whilst maintaining same reaction condition such as temperature and concentration [30]. This exited us, to development of a force-driven reflux process as shown in Scheme 1, with which the reaction was accomplished as described in the experimental section, on an ordinary hot plate magnetic stirrer which provided the heating energy and mechanical stirring simultaneously without the use of other external devices and/or apparatus. During the synthesis process, the mechanical agitation stops the dissolution-recrystallization equilibrium of nanorods growth in non-stirring conditions, expediting the under saturation of the dissolution areas on the GO surface. Besides, the mass transport of material precursors is greatly enhanced by the rigorous mechanical action induced by the high stirring rate. As a result,

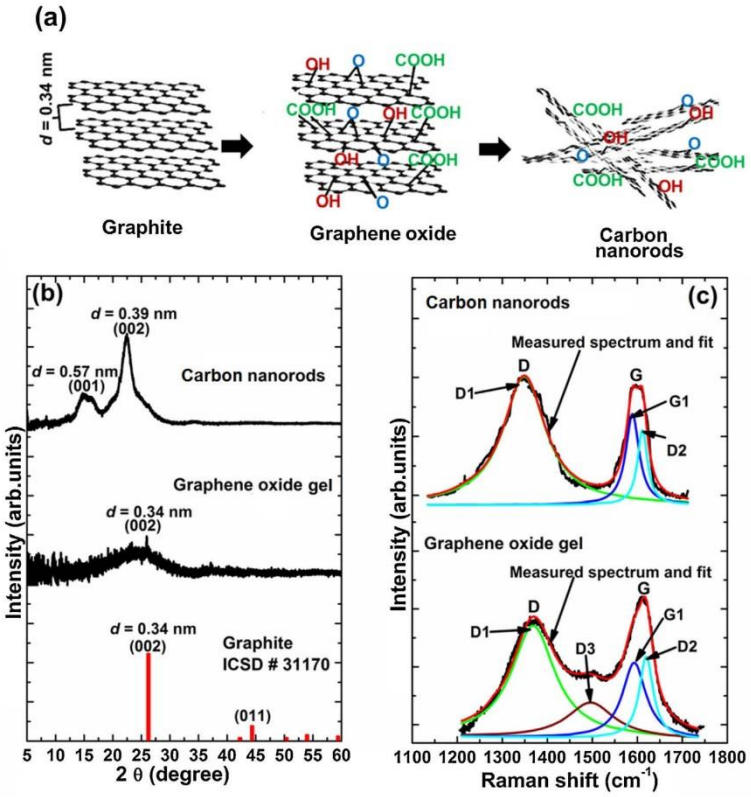

Fig. 2. (a) Schematic view of the chemical/crystal structure route from graphite powder to graphene oxide via oxidation of graphite to produce graphene oxide gel and reduction to carbon nanorods. (b) The X-ray diffraction of the graphene oxide gel, carbon nanorods and the corresponding graphite ICSD card no. 31170. (c) Raman spectra of graphene oxide and carbon nanorods (solid-lines show Lorentzian fits).

a step-by-step coalescence of the GO gel precursor enables the growth of carbon nanorods. The uniform stirring of the solution also prevents sedimentation and forces the close mixing, ensuring the occurrence of a homogeneous reaction for the growth of uniform carbon nanorods.

In summary, the constant force-driven process compels the GO gel precursor and the produced carbon nanorods to fall into line and move constantly in a particular direction with no sedimentation. The reaction temperature of 100° C has been chosen so as to preserve and/or improve the epoxide group (C_2O) in the structure of the material. This carbon-oxygen single bond has been demonstrated as energy storage device electrode material with high capability and good stability [31].

The diameters of the nanorods were estimated to range from 200 to 300 nm, with estimated length of about tens of microns. Fig. 2(a) shows a basic schematic view of the chemical/crystal structure route from graphite powder to graphene oxide via oxidation of graphite to produce a graphene oxide gel and reduction to carbon nanorods from the reflux process. XRD patterns of the graphene oxide gel, carbon nanorods, and the corresponding graphite ICSD card no. 31170 (Crystal system: hexagonal, space-group: P63mc (186), Cell parameters: $a = 0.247$ nm, $c = 0.679$ nm) are shown in Fig. 2(b). It can be noticed that the (002) peak of graphite at 26.2° is broad and has weak diffraction intensity showing poor crystalline graphene oxide gel which could be due to the interlaced molecules of oxygen-containing functional groups [28–30], as demonstrated in Fig. 2(a). In contrast to graphene oxide gel, carbon nanorods shows improved crystallinity, since the XRD pattern of carbon nanorods shows a (001) peak at ~15.6°. This peak has a smaller interlayer spacing ($d = 0.51$ nm) suggesting that the number of interlaced molecules of oxygen-containing functional groups was reduced in carbon nanorods. Based on earlier reports, the interlayer spacing in graphene oxide gel is in the range of 0.5–1.0 nm depending on the amount of interlaced molecules of oxygen-containing functional groups [32,33]. The XRD pattern of graphene oxide also shows a broad (002) peak at 22.5° which corresponds to (002) peak of graphite at 26.2°. The broadening and shift of the peak from 26.2°

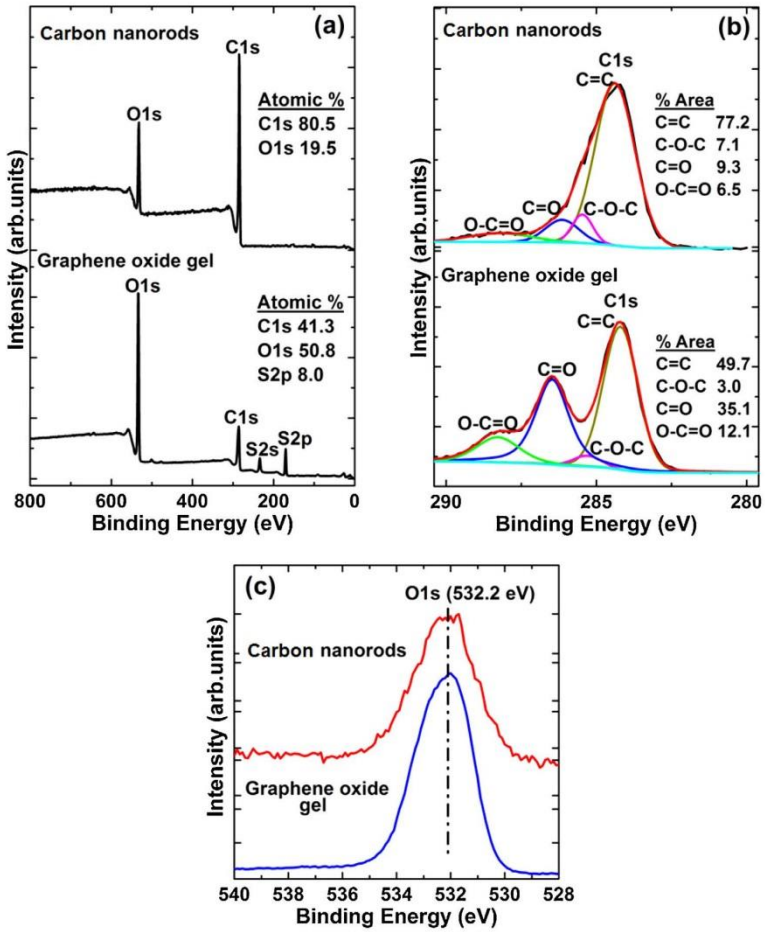

Fig. 3. XPS spectra of the graphene oxide gel and carbon nanorods (a) survey scan, and the corresponding high-resolution (b) C 1s and (c) O 1s core level spectra.

to 22.5° could be due to the short-range order in stacked of the sheets and some interlaced molecules of oxygen-containing functional groups [32].

Fig. 2(c) shows Raman spectra of GO gel and GO nanorods (solid-lines show Lorentzian fits). The fittings agree well with published Raman data for carbonaceous materials [34]. Raman spectra of GO gel and GO nanorods show both the D (defects induced) and G (carbon-carbon) vibration modes. The D band confirms the presence of functional groups in the as-prepared oxides. In contrast to graphene oxide, the Raman spectrum of carbon nanorods shows a D3 band which originates from the interstitial amorphous carbon in the disturbed graphitic lattice of carbonaceous material [34–37]. This suggests that graphene oxide gel has a distorted graphitic lattice confirming the results obtained from XRD analysis.

The XPS and EDX analysis were carried out to quantify the surface and elemental composition of the graphite and graphene oxides. The oxides surface functionalities of the samples were obtained using XPS. Fig. 3(a) shows the XPS survey spectra for graphite and graphene oxides which show the main elements of the samples (i.e. carbon and oxygen). The low concentration of sulphur observed from graphene oxide gel is due to acid used in the preparation process. Compared to the GO gel, carbon nanorods show higher carbon and lower oxygen. Fig. 3(b) exhibits the C 1 s core level spectra of the graphene oxide together with carbon nanorods.

The C=C peak (284.2 eV) confirms the sp^2 hybridization component of graphite/graphene, and C—O—C (285.6 eV), C=O (286.5 eV), O—C=O (288.4 eV) peaks confirm oxide components surface functionalities [38–41]. The O 1s spectra for both oxides show a peak at 532.2 eV assigned to oxygen. This oxygen peak position further suggests the presence of adsorbed species on the sample surface [42].

The EDX analysis (Fig. 4(a) and (b)) confirmed the presence of a high carbon concentration and low oxygen concentration in carbon nanorods compared to the GO gel, with small traces of impurities (Na, Cl, K, and Mn) having less than 0.5 at% concentrations.

3.2. Electrochemical characterization

Fig. 5(a) and (b) show the CV curves of the GO gel electrode at different scan rates in the range of 5 to 100 mV s^{-1} within the negative and positive potential window range of −0.4 to 0.0 V vs. Ag/AgCl and 0.0 to 0.4 V vs. Ag/AgCl respectively. Similarly, Fig. 5(c) and (d) also shows the CV curves of the carbon nanorods electrode at different scan rates from 5 to 100 mV s^{-1}.

In the negative potential range (Fig. 5(a) and (c)), the CV curves demonstrate a fairly rectangular shape for the both GO and carbon nanorods materials which is an indication of a high reversibility of the capacitive behaviour [43].

In the positive potential range (Fig. 5(b) and (d)), the CV curves reveal the presence of redox peaks which is ascribed to the ongoing electrochemical redox reactions arising from the high presence of oxygen functionalities which have high redox reactivity characteristics in the positive potential window [44,45]. The current response observed in the positive potential window was much higher than the negative potential range. This is due to the fact that both materials prefer to operate in the positive potential range based on the high redox reactivity characteristics and as such is depicted in the CV tests results obtained.

In general, the carbon nanorods electrode showed a better current response compared to the graphene oxide gel electrode. Apart from the morphological disparities observed earlier in both materials, the better current response recorded in the former could also be due to the reduced oxygen content compared to graphene oxide gel. This is validated by the XPS and EDX results which showed the reduction of the oxygen content in the carbon nanorods. It is worth mentioning that the current collector does not show an obvious effect on the observed behaviour of the active material (Fig. 5(e)). In Fig. 5, a pair of strong redox peaks is

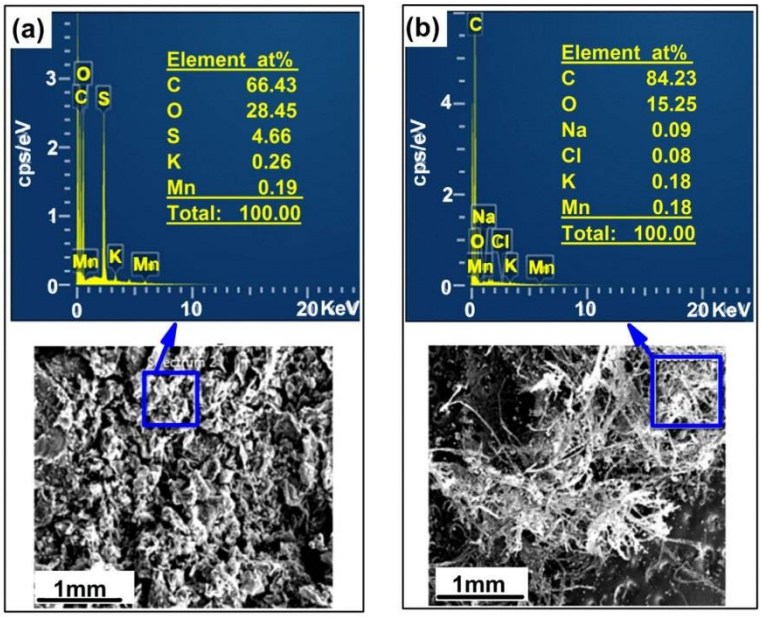

Fig. 4. EDX spectra of the (a) graphene oxide gel and (b) carbon nanorods obtained from areas shown by the boxes from secondary electron beam images.

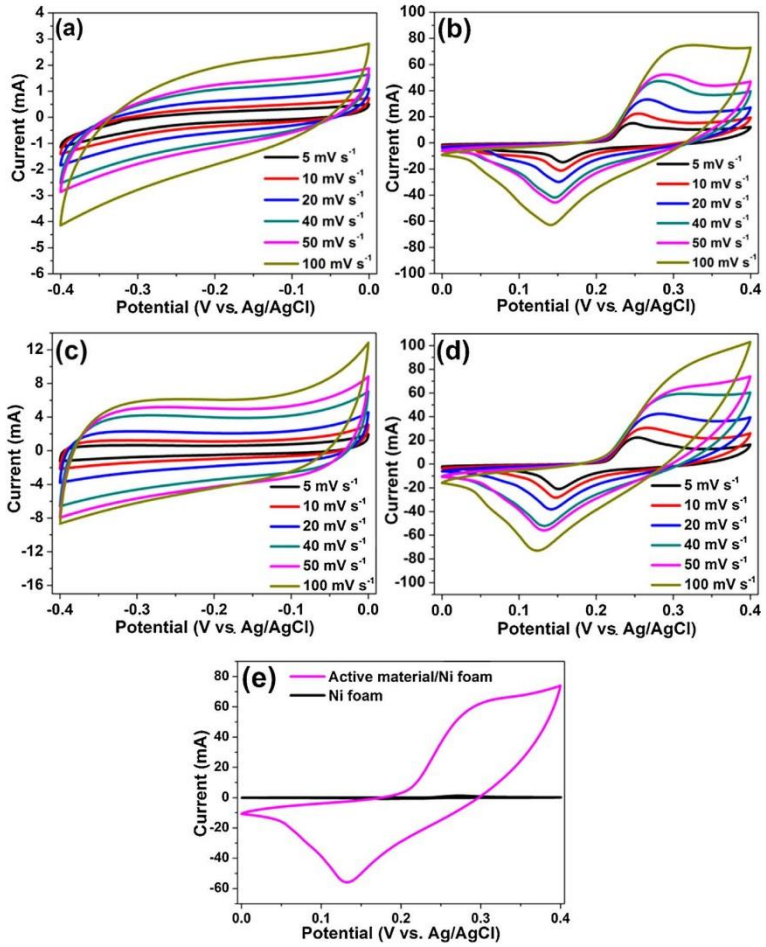

Fig. 5. (a) and (b) show the CV curves of graphene oxide gel electrode at different scan rates in both negative and positive potential windows respectively. (c) and (d) show the CV curves of carbon nanorods electrode at different scan rates in both negative and positive potential windows respectively. (e) CV curves of Ni foam and active material/Ni foam at a scan rate of 50 mV s^{-1}.

observed on each of the curves which is attributed to the pseudocapacitive behaviour of the as-prepared electrode materials [46]. The oxidation peak was observed to slightly shift from 0.23 to 0.29 V as the scan rate increases from 5 mVs^{-1} to 100 mVs^{-1} implying a proportionally low resistance of the electrodes [47]. In brief; the as-prepared electrodes show a better electrochemical performance in the positive potential window as observed from the current response discussed earlier. This observation contravenes the fact that carbonaceous materials are generally known to perform better as negative electrodes [48–50].

Fig. 6(a) and (b) show the CD curves of graphene oxide gel and carbon nanorods at current densities in the range of 0.5–5.0 A g^{-1} in a potential range of 0.0 V to 0.4 V. The discharge time of the carbon nanorods is significantly longer than that of graphene oxide gel suggesting that carbon nanorods have a better rate of discharge. The CD curves show potential steps, i.e. a swift potential drop in the range of 0.4–0.22 V and a slow potential drop in the range of 0.22–0.15 V as seen from the discharge part of CD curves which indicates the Faradaic behaviour of the electrodes. From the CD curves, the specific capacitance, C_S, of the electrode materials was evaluated by using equation 1 as 436.5 F g^{-1} and 719.5 F g^{-1} at a 0.5 A g^{-1} current density for the GO gel and carbon nanorods, respectively. The specific capacitance values were converted to the equivalent specific capacity, Q, using equation 2 and were obtained as 48.5 mA h g^{-1} and 80.8 mA h g^{-1} at a current density of 0.5 A g^{-1} for graphene oxide gel and carbon nanorods respectively. Fig. 6(c) shows the charge discharge profile of both graphene oxide gel and carbon nanorods at a current density of 0.5 A g^{-1} in a negative potential window which is a typical of EDLC materials. The observed discharge times at 0.5 A g^{-1} are very much smaller than the discharge times in the positive potential window. This further indicates the materials' preference to operate in the positive potential range. The plot of the specific capacitance and specific capacity values as a function of the current density are shown in Fig. 6(d) for both materials. It can be seen in Fig. 6(d) that carbon nanorods electrode has a higher specific capacitance/capacity as

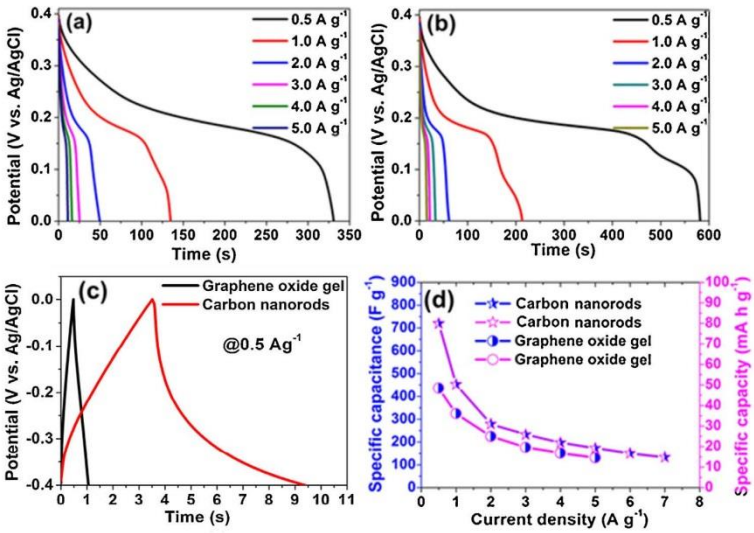

Fig. 6. The (CD) curves of (a) graphene oxide gel and (b) carbon nanorods at current densities in the range of 0.5–5.0 A g^{-1} in a potential window range of 0.0 V to 0.4 V. (c) CD curves of both graphene oxide gel and carbon nanorods at current densities 0.5 A g^{-1} in a potential range of −0.4 V to 0.0 V (d) The specific capacitance/specific capacity of graphene oxide gel and carbon nanorods as a function of the current density.

compared to the graphene oxide gel electrode. The higher C_S of the carbon nanorods is attributed to the intersected nanorods forming a network architecture of the electrode and the enhanced electrical conductivity of the electrode [51] indicating that the charge is being stored massively throughout the material coupled with at the electrolyte-electrode interface when compared with graphene oxide gel [18,47] based on reduced oxygen functionalities.

Furthermore, the electrochemical behaviour of the electrodes was evaluated using electrochemical impedance spectroscopy (EIS) and measurements were achieved at the potential of 0.0 V and the frequency range of 10 mHz to 100 mHz. Fig. 7(a) shows the Nyquist plot for the graphene oxide gel and carbon nanorods electrodes. From this plot, two distinct behaviours for each electrode can be seen at the high-frequency (the lower left

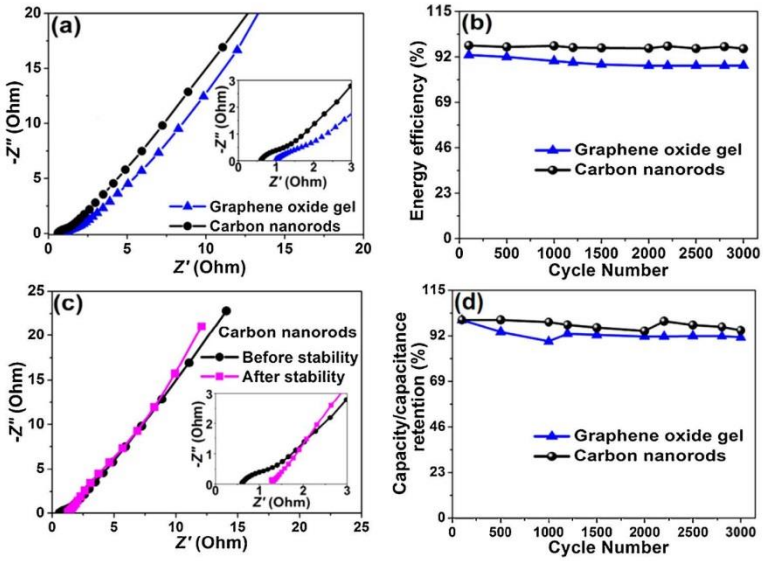

Fig. 7. (a) Nyquist plot for the graphene oxide gel and carbon nanorods electrodes (inset shows the enlarged high-frequency region of the plot); (b) The average galvanostatic cycling curves of graphene oxide gel and carbon nanorods electrodes at a current density of 5 A g^{-1} respectively. (c) Nyquist plot for the carbon nanorods electrode before and after cycling at a current density 5 A g^{-1}. (d) Cycle performance of graphene oxide gel and carbon nanorods electrodes in 6 M KOH at a current density of 5 A g^{-1} respectively.

portion of the curve) and low-frequency (the upper right portion of the curve) regions. The intercept of the EIS plot with the Z'-axis gives information about the equivalent series resistance (ESR) value of the electrode [15]. This comprises the resistance of the internal resistance of the electrode and electrolyte, plus the contact resistance at the active material/current collector interface [53]. The ESR is also commonly referred to as the solution resistance (R_S) value. From the inset to the figure, the intercept of the carbon nanorods electrode shows a smaller ESR values (0.60 Ω) as compared to that of the GO gel electrode (0.97 Ω). In addition, the inclined region of the curve (low-frequency region) should in principle be a vertical line to the y-axis, however, the inclination is due to the presence of a leakage resistance [54]. Similarly, the relatively smaller R_S value observed in the carbon nanorods electrode is an indication of improved conductivity that leads to a rapid transport mechanism when compared to graphene oxide gel electrode. The carbon nanorods also displayed much better slope as compared to the GO gel. These two factors discussed also suggest the reason for the observed enhanced capacitive behaviour of the carbon nanorod electrode.

The galvanostatic cycling curves of graphene oxide gel and carbon nanorods electrodes at a current density of 5 A g^{-1} respectively are shown in Fig. 7(b). It can be seen that the electrodes exhibited good electrochemical stability up to 3000 charge–discharge cycles with carbon nanorods electrode showing steady and higher stability than graphene oxide gel electrode at a current density of 5 A g^{-1}. After 3000 cycles, 88.7% and 96.2% initial energy retention (according to Eq. (3)) as well as 91.2% and 94.7% capacitance/capacity retention (Fig. 7(d)) were observed for both graphene oxide gel and carbon nanorods electrodes respectively. It can be observed that the carbon nanorods electrode exhibits a better long cycle life with no more than 5.3% capacitance/capacity loss after 3000 cycles. This indicates that the electrode delivers a high capacitance with exceptional rate performance compared to GO gel electrode [47]. After cycling, a little increase in the R_S value up to 1.28 Ω (see Fig. 7 (c) inset) and the diffusion path length further deviates from the ideal vertical behaviour which could be attributed to the repeated cycling effect such as polarization and less utilization or insufficient active material during redox reaction during the cycling probably due to the high current density. Furthermore, the diameter of semicircle for the electrode after cycle test is slightly higher, which indicates that there was an increase in the R_{CT} value which could be due to the formation of inactive sites caused by the collapse of some part of structures during the cycle test and this could be ascribed to the adhesion loss of some electroactive material on the current collector surface [46,53]. Besides, the deviation in the diffusion path length as well as the slope of the Nyquist plot in the low frequency region with respect to the ideal nature is due to the further interaction of the ions with initially unlocked pore sites which were unavailable but became accessible due to continuous cycling. Similar phenomena have been reported in our earlier work on activated carbon nanostructures [15]. Nonetheless, carbon nanorods exhibited a good electrochemical performance and stability as displayed in Fig. 7(d).

The outstanding capacitive performance of carbon nanorods electrode can be attributed to the combined effect of the enhanced electrical conductivity due to reduced oxygen concentration and the interconnected nanorods which forms network architecture. This results in the facilitation of the penetration of electrolyte ions into the inner parts of the electrode and reduces the ion- diffusion path during electrode operation.

Our results show significant enhancement on the specific capacitance of graphene oxide electrodes compared with erstwhile studies, as shown in Fig. 8. Herein, a comparison of the specific capacitance of graphene-oxide based electrodes was made with

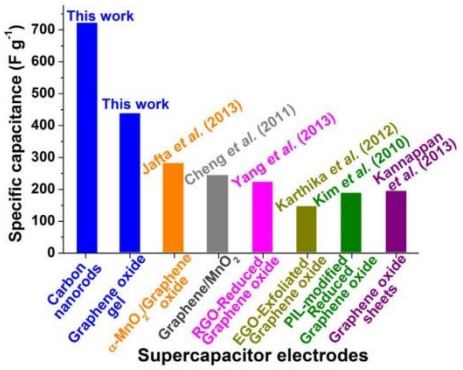

Fig. 8. A comparison of the specific capacitance of carbon nanorods and graphene oxide gel at a current density of 0.5 A g^{-1} in KOH electrolyte with other reports [16,18,21,51,52,48].

the previous published work by Jafta et al. (2013) [55], Cheng et al. (2011) [56], Yang et al. (2013) [16], Karthika et al. (2012) [18], Kim et al. (2010) [21] and Kannappan et al. (2013) [19]. In reference 46, α-MnO_2/graphene oxide composite at a current density of 0.5 A g^{-1} using KOH electrolyte was reported. Cheng et al. [56] reported graphene/MnO_2 composite at 1 mA in KCl electrolyte with maximum specific capacitance of 245 F g^{-1}. Electrochemically reduced graphene oxide (RGO)-sheets at a scan rate of 5 mV s^{-1} using KCl as the electrolyte was also reported by Yang et al. The maximum specific capacitance obtained for the material was given as 223.6 F g^{-1} [16]. Functionalized exfoliated graphene oxide (EGO) was studied by Karthika et al., at a scan rate of 5 mV s^{-1} with KOH electrolyte. A maximum specific capacitance of 146 F g^{-1} was reported for the material [18]. Kim et al. analysed poly ionic liquid (PIL)-modified reduced graphene oxide (RGO) in EMIM-NTf_2 electrolyte at a scan rate of 0.5 mV s^{-1}, and reported 187 F g^{-1} as the limit specific capacitance for material [21] Also, graphene oxide was studied at a current density of 2.5A g^{-1} in BMIM BF_4 electrolyte giving a maximum capacitance value of 195 F g^{-1} [48]. In all these studies, a higher specific capacitance value was obtained which demonstrates a progress in the research field.

4. CONCLUSIONS

In this work, we have successfully synthesized GO gel and carbon nanorods via a modified Hummer's method and a force-driven reflux process respectively. Extensive characterization of the as-prepared electrode materials showed gelatinous morphology for the gel and a rod-like morphology for the carbon nanorods. The presence of carbon, oxygen and oxygen-containing surface functionalities was also confirmed from the structural and elemental analysis done. It was observed that the carbon nanorods exhibited an improved electrochemical performance as compared to the graphene oxide gel. Electrodes fabricated from both materials exhibited a limit specific capacitance of 436.5 F g^{-1} and 719.5 F g^{-1} corresponding to specific capacities of 48.5 mAh g^{-1} and 80.8 mAh g^{-1} at a current density of 0.5 A g^{-1} in a three electrode system in a 6 M KOH electrolyte. The excellent capacitive performance of the carbon nanorods electrode can be linked to the combined effect of the interconnected nanorods and the electrical conductivity of the electrode due to reduced concentration of oxygen. This provides a shorter ion-diffusion path and less resistance to ion-transport. The as-prepared electrodes

demonstrated a good and promising electrochemical performance suitable for supercapacitor electrode applications. Our results show significant improvement and further research progress on the reports related to electrochemical performance of graphene-oxides based electrodes published previously by other studies. This study is also being considered for further testing of the electrochemical performance of the carbon nanorods electrode in other storage device technologies such as battery applications.

ACKNOWLEDGEMENTS

This work is basically upon the research supported by the South African Research Chairs Initiative of the Department of Science and Technology and National Research Foundation of South Africa (Grant No. 61056). Any opinions, results, conclusions and, or suggestions expressed in this work are those of the author(s), and the NRF does not agree to any liability on this ground. K. O. Oyedotun acknowledges the funding from the University of Pretoria and National Research Foundation (NRF) for his PhD studies.

References

[1] J.-M. Tarascon, M. Armand, Issues and challenges facing rechargeable lithium batteries, Nature. 414 (2001) 359–367, doi:http://dx.doi.org/10.1038/35104644.
[2] J.R. Miller, P. Simon, Electrochemical Capacitors for Energy Management, Science 80- (321) (2008) 651–652, doi:http://dx.doi.org/10.1126/science.1158736.
[3] P. Simon, Y. Gogotsi, Materials for electrochemical capacitors, Nat. Mater. 7 (2008) 845–854, doi:http://dx.doi.org/10.1038/nmat2297.
[4] M. Armand, J.-M. Tarascon, Building better batteries, Nature. 451 (2008) 652–657, doi:http://dx.doi.org/10.1038/451652a.
[5] I. Hadjipaschalis, A. Poullikkas, V. Efthimiou, Overview of current and future energy storage technologies for electric power applications, Renew. Sustain. Energy Rev. 13 (2009) 1513–1522, doi:http://dx.doi.org/10.1016/j.rser.2008.09.028.
[6] I. Dincer, Renewable energy and sustainable development: a crucial review, Renew. Sustain. Energy Rev. 4 (2000) 157–175, doi:http://dx.doi.org/10.1016/S1364-0321(99)00011-8.
[7] J.R. Miller, R.A. Outlaw, B.C. Holloway, Graphene Double-Layer Capacitor with ac Line-Filtering Performance, Science 329 (80-) (2010).
[8] G. Feng, S. Li, V. Presser, P.T. Cummings, Molecular Insights into Carbon Supercapacitors Based on Room-Temperature Ionic Liquids, J. Phys. Chem. Lett. 4 (2013) 3367–3376, doi:http://dx.doi.org/10.1021/jz4014163.
[10] W. Lv, Z. Li, Y. Deng, Q.-H. Yang, F. Kang, Graphene-based materials for electrochemical energy storage devices: Opportunities and challenges, Energy Storage Mater. 2 (2016) 107–138, doi:http://dx.doi.org/10.1016/j.ensm.2015.10.002.
[11] C. Liu, Z. Yu, D. Neff, A. Zhamu, B.Z. Jang, Graphene-Based Supercapacitor with an Ultrahigh Energy Density, Nano Lett. 10 (2010) 4863–4868, doi:http://dx.doi.org/10.1021/nl102661q.
[12] M. Zhang, D. Lei, X. Yin, L. Chen, Q. Li, Y. Wang, et al., Magnetite/graphene composites: microwave irradiation synthesis and enhanced cycling and rate performances for lithium ion batteries, J. Mater. Chem. 20 (2010) 5538, doi:http://dx.doi.org/10.1039/c0jm00638f.
[13] Z.-S. Wu, W. Ren, L. Wen, L. Gao, J. Zhao, Z. Chen, et al., Graphene Anchored with Co_3O_4 Nanoparticles as Anode of Lithium Ion Batteries with Enhanced Reversible Capacity and Cyclic Performance, ACS Nano. 4 (2010) 3187–3194, doi:http://dx.doi.org/10.1021/nn100740x.
[14] Y.J. Mai, D. Zhang, Y.Q. Qiao, C.D. Gu, X.L. Wang, J.P. Tu, MnO/reduced graphene oxide sheet hybrid as an anode for Li-ion batteries with enhanced lithium storage performance, J. Power Sources. 216 (2012) 201–207, doi:http://dx.doi.org/10.1016/j.jpowsour.2012.05.084.
[15] F. Barzegar, A. Bello, O.O. Fashedemi, J.K. Dangbegnon, D.Y. Momodu, F. Taghizadeh, et al., Synthesis of 3D porous carbon based on cheap polymers and graphene foam for high-performance electrochemical capacitors, Electrochim. Acta. 180 (2015) 442–450, doi:http://dx.doi.org/10.1016/j.electacta.2015.08.148.
[16] J. Yang, S. Gunasekaran, Electrochemically reduced graphene oxide sheets for use in high performance supercapacitors, Carbon. 51 (2013) 36–44, doi:http://dx.doi.org/10.1016/j.carbon.2012.08.003.
[17] W. Hummers Jr, R. Offeman, Preparation of graphitic oxide, J. Am. Chem. 80 (1958) 1339-1339.
[18] P. Karthika, N. Rajalakshmi, K.S. Dhathathreyan, Functionalized Exfoliated Graphene Oxide as Supercapacitor Electrodes, 2012(2012), doi:http://dx.doi.org/10.4236/SNL.2012.24011.
[19] S. Kannappan, K. Kaliyappan, R.K. Manian, A.S. Pandian, H. Yang, Y.S. Lee et al., Graphene based Supercapacitors with Improved Specific Capacitance and Fast Charging Time at High Current Density, arXiv preprint arXiv:1311.1548 (2013).
[20] L. Zhang, K.N. Hui, K. San Hui, H. Lee, High-performance hybrid supercapacitor with 3D hierarchical porous flower-like layered double hydroxide grown on nickel foam as binder-free electrode, J. Power Sources. 318 (2016) 76–85, doi:http://dx.doi.org/10.1016/j.jpowsour.2016.04.010.
[21] T.Y. Kim, H.W. Lee, M. Stoller, D.R. Dreyer, C.W. Bielawski, R.S. Ruoff, et al., High-Performance Supercapacitors Based on Poly(ionic liquid)-Modified Graphene Electrodes, (2010), doi:http://dx.doi.org/10.1021/NN101968P.
[22] E. Frackowiak, Carbon materials for supercapacitor application, Phys. Chem. Chem. Phys. 9 (2007) 1774–17785, doi:http://dx.doi.org/10.1039/b618139m.
[23] C. Liu, F. Li, L.P. Ma, H.M. Cheng, Advanced Materials for Energy Storage, Adv. Mater. 22 (2010) E28–E62, doi:http://dx.doi.org/10.1002/adma.200903328.
[24] D.-W. Wang, C. Sun, G. Zhou, F. Li, L. Wen, B.C. Donose, et al., The examination of graphene oxide for rechargeable lithium storage as a novel cathode material, J. Mater. Chem. A. 1 (2013) 3607, doi:http://dx.doi.org/10.1039/c3ta01658g.
[25] B. Akinwolemiwa, C. Peng, G.Z. Chen, Redox Electrolytes in Supercapacitors, J. Electrochem. Soc. 162 (2015) A5054–A5059, doi:http://dx.doi.org/10.1149/2.0111505jes.
[26] A. Laheaar, P. Przygocki, Q. Abbas, F. B??guin, A. Laheäär, P. Przygocki, et al., Appropriate methods for evaluating the efficiency and capacitive behavior of different types of supercapacitors, Electrochem. Commun. 60 (2015) 21–25, doi:http://dx.doi.org/10.1016/j.elecom.2015.07.022.
[27] G. Godillot, L. Guerlou-Demourgues, P.-L. Taberna, P. Simon, C. Delmas, Original Conductive Nano-Co3O4 Investigated as Electrode Material for Hybrid Supercapacitors, Electrochem. Solid-State Lett. 14 (2011) A139, doi:http://dx.doi.org/10.1149/1.3609259.
[28] L. Torrente-Murciano, A.A. Lapkin, D. Chadwick, Synthesis of high aspect ratio titanate nanotubes, J. Mater. Chem. 20 (2010) 6484, doi:http://dx.doi.org/10.1039/c0jm01212b.
[29] T. Kijima, Inorganic and Metallic Nanotubular Materials: Recent Technologies and Applications, Top. Appl. Phys. 117 (2010) 17–32, doi:http://dx.doi.org/10.1007/978-3-642-03622-4.
[30] Y. Tang, Y. Zhang, J. Deng, J. Wei, H. Le Tam, B.K. Chandran, et al., Mechanical force-driven growth of elongated bending TiO2 –based nanotubular materials for ultrafast rechargeable lithium ion batteries, Adv. Mater. 26 (2014) 6111–6118, doi:http://dx.doi.org/10.1002/adma.201402000.
[31] D.-W. Wang, C. Sun, G. Zhou, F. Li, L. Wen, B.C. Donose, et al., The examination of graphene oxide for rechargeable lithium storage as a novel cathode material, J. Mater. Chem. A. 1 (2013) 3607, doi:http://dx.doi.org/10.1039/c3ta01658g.
[32] P. Ramesh, S. Bhagyalakshmi, S. Sampath, Preparation and physicochemical and electrochemical characterization of exfoliated graphite oxide, J. Colloid Interface Sci. 274 (2004) 95–102, doi:http://dx.doi.org/10.1016/j.jcis.2003.11.030.
[33] J. Li, X. Zeng, T. Ren, E. van der Heide, The Preparation of Graphene Oxide and Its Derivatives and Their Application in Bio-Tribological Systems, Lubricants. 2 (2014) 137–161, doi:http://dx.doi.org/10.3390/lubricants2030137.
[34] A. Sadezky, H. Muckenhuber, H. Grothe, R. Niessner, U. Poschl, Raman microspectroscopy of soot and related carbonaceous materials: Spectral analysis and structural information, Carbon. 43 (2005) 1731–1742, doi:http://dx.doi.org/10.1016/j.carbon.2005.02.018.
[35] T. Jawhari, A. Roid, J. Casado, Raman spectroscopic characterization of some commercially available carbon black materials, Carbon. 33 (1995) 1561–1565, doi:http://dx.doi.org/10.1016/0008-6223(95)00117-V.
[36] S.K. Sze, N. Siddique, J.J. Sloan, R. Escribano, Raman spectroscopic characterization of carbonaceous aerosols, Atmos. Environ. 35 (2001) 561–568, doi:http://dx.doi.org/10.1016/S1352-2310(00)00325-3.
[37] B. Dippel, H. Jander, J. Heintzenberg, NIR FT Raman spectroscopic study of flame soot, Phys. Chem. Chem. Phys. 1 (1999) 4707–4712, doi:http://dx.doi.org/10.1039/a904529e.
[38] S. Ogawa, T. Yamada, S. Ishidzuka, A. Yoshigoe, M. Hasegawa, Y. Teraoka, et al., Graphene Growth and Carbon Diffusion Process during Vacuum Heating on Cu (111)/Al 2 O 3 Substrates, Jpn. J. Appl. Phys. 52 (2013) 110122.
[39] T. Ando, Physics of Graphene, Hyomen Kagaku. 29 (2008) 296–303, doi:http://dx.doi.org/10.1380/jsssj.29.296.
[40] Y.V. Butenko, S. Krishnamurthy, A.K. Chakraborty, V.L. Kuznetsov, V.R. Dhanak, M.R.C. Hunt, et al., Photoemission study of onionlike carbons produced by annealing nanodiamonds, Phys. Rev. B. 71 (2005) 75420.
[41] M. Hsiao, S. Liao, M. Yen, C. Teng, S. Lee, N. Pu, et al., Preparation and properties of a graphene reinforced nanocomposite conducting plate, J. Mater. Chem. 20 (2010) 8496.
[42] J.-C. Dupin, D. Gonbeau, P. Vinatier, A. Levasseur, Systematic XPS studies of metal oxides, hydroxides and peroxides, Phys. Chem. Chem. Phys. 2 (2000) 1319–1324, doi:http://dx.doi.org/10.1039/a908800h.
[43] Y. Gao, L. Wang, Z. Li, Y. Zhang, B. Xing, C. Zhang, et al., Electrochemical performance of Ti3C2 supercapacitors in KOH electrolyte, J. Adv. Ceram. 4 (2015) 130–134, doi:http://dx.doi.org/10.1007/s40145-015-0143-3.
[44] C. Zhao, Q. Wang, H. Zhang, S. Passerini, X. Qian, Two-Dimensional Titanium Carbide/RGO Composite for High-Performance Supercapacitors, ACS Appl Mater. Interfaces. 8 (2016) 15661–15667, doi:http://dx.doi.org/10.1021/acsami.6b04767.
[45] A. Singh, A. Chandra, Enhancing Specific Energy and Power in Asymmetric Supercapacitors – A Synergetic Strategy based on the Use of Redox Additive Electrolytes, Sci. Rep. 6 (2016) 25793, doi:http://dx.doi.org/10.1038/srep25793.

[46] D. Cai, B. Liu, D. Wang, Y. Liu, L. Wang, H. Li, et al., Facile hydrothermal synthesis of hierarchical ultrathin mesoporous NiMoO4 nanosheets for high performance supercapacitors, Electrochim. Acta. 115 (2014) 358–363, doi: http://dx.doi.org/10.1016/j.electacta.2013.10.154.
[47] J. Yan, Z. Fan, W. Sun, G. Ning, T. Wei, Q. Zhang, et al., Advanced Asymmetric Supercapacitors Based on Ni(OH)2/Graphene and Porous Graphene Electrodes with High Energy Density, Adv. Funct. Mater. 22 (2012) 2632–2641, doi:http://dx.doi.org/10.1002/adfm.201102839.
[48] L. Sui, S. Tang, Y. Chen, Z. Dai, H. Huangfu, Z. Zhu, et al., An asymmetric supercapacitor with good electrochemical performances based on Ni (OH) 2/AC/CNT and AC, Electrochim. Acta. 182 (2015) 1159–1165.
[49] M. Jana, J.S. Kumar, P. Khanra, P. Samanta, H. Koo, N.C. Murmu, et al., Superior performance of asymmetric supercapacitor based on reduced graphene oxide-manganese carbonate as positive and sono-chemically reduced graphene oxide as negative electrode materials, J. Power Sources 303 (2016) 222–233.
[50] F. Barzegar, A. Bello, O. Guellati, D.Y. Momodu, A. Harat, J.K. Dangbegnon, et al., Effect of addition of different carbon materials on hydrogel derived carbon material for high performance electrochemical capacitors, Electrochim. Acta. (2015), doi:http://dx.doi.org/10.1016/j.electacta.2015.10.189.
[51] D. Yu, K. Goh, H. Wang, L. Wei, W. Jiang, L.D. Qiang Zhang, et al., Scalable synthesis of hierarchically structured carbon nanotube-graphene fibres for capacitive energy storage, Nat. Nanotechnol. 9 (2014) 555–562, doi:http://dx.doi.org/10.1038/NNANO.2014.93.
[52] W. Yang, Z. Gao, J. Wang, J. Ma, M. Zhang, L. Liu, Solvothermal one-step synthesis of Ni-Al layered double hydroxide/carbon nanotube/reduced graphene oxide sheet ternary nanocomposite with ultrahigh capacitance for supercapacitors, ACS Appl Mater. Interfaces. 5 (2013) 5443–5454, doi:http://dx.doi.org/10.1021/am4003843.
[53] Z. Fan, J. Yan, T. Wei, L. Zhi, G. Ning, T. Li, et al., Asymmetric Supercapacitors Based on Graphene/MnO2 and Activated Carbon Nanofiber Electrodes with High Power and Energy Density, Adv. Funct. Mater. 21 (2011) 2366–2375, doi: http://dx.doi.org/10.1002/adfm.201100058.
[54] D. Momodu, M. Madito, F. Barzegar, A. Bello, A. Khaleed, O. Olaniyan, et al., Activated carbon derived from tree bark biomass with promising material properties for supercapacitors, J. Solid State Electrochem. (2016) 1–14, doi: http://dx.doi.org/10.1007/s10008-016-3432-z.
[55] C.J. Jafta, F. Nkosi, L. le Roux, M.K. Mathe, M. Kebede, K. Makgopa, et al., Manganese oxide/graphene oxide composites for high-energy aqueous asymmetric electrochemical capacitors, Electrochim. Acta 110 (2013) 228–233, doi:http://dx.doi.org/10.1016/j.electacta.2013.06.096.
[56] Q. Cheng, J. Tang, J. Ma, H. Zhang, N. Shinya, L.C. Qin, Graphene and nanostructured MnO2 composite electrodes for supercapacitors, Carbon 49 (2011) 2917–2925, doi:http://dx.doi.org/10.1016/j.carbon.2011.02.068.

4.1.1.3 Concluding Remarks

GO gel and carbon nanorods have been successfully synthesized via a modified Hummer's method and a force-driven reflux process respectively. Extensive characterization of the as-prepared electrode materials showed gelatinous morphology for the gel and a rod-like morphology for the carbon nanorods. The presence of carbon, oxygen and oxygen-containing surface functionalities was also confirmed from the structural and elemental analysis done. It was observed that the carbon nanorods exhibited an improved electrochemical performance as compared to the graphene oxide gel. Electrodes fabricated from both materials exhibited a limit specific capacitance of 436.5 F g^{-1} and 719.5 F g^{-1} corresponding to specific capacities of 48.5 mAh g^{-1} and 80.8 mAh g^{-1} at a current density of 0.5 A g^{-1} in a three electrode system in a 6 M KOH electrolyte. The excellent capacitive performance of the carbon nanorods electrode can be linked to the combined effect of the interconnected nanorods and the electrical conductivity of the electrode due to reduced concentration of oxygen. This provides a shorter ion-diffusion path and less resistance to ion-transport. The as-prepared electrodes demonstrated a good and promising electrochemical performance suitable for supercapacitor

electrode applications. Our results show significant improvement and further research progress on the reports related to electrochemical performance of graphene-oxides based electrodes published previously by other studies. This study is also being considered for further testing of the electrochemical performance of the carbon nanorods electrode in other storage device technologies such as battery applications.

4.2 Synthesis of ternary NiCo-MnO_2 nanocomposite and its application as a novel high energy supercapattery device

4.2.1 Introduction

As a result of the shortcomings of the conventional EDLC materials, such as low specific capacitance (usually < 300 F g^{-1}), low energy density among others [154], transition metal oxides/hydroxides such as MnO_2, TiO_2, RuO_2, NiO, $Ni(OH)_2$ and $Co(OH)_2$ with high theoretical specific capacities among other potentials, have been employed as an alternative electrode materials [155]–[158]. Besides being semi-conductive, transition metal oxides/hydroxides have been used as electrode materials for supercapacitors due to their cost effectiveness, natural abundance cum adequate electrochemical performance [20], [88]. However, they are plagued with low electrical conductivity, poor rate capability as well as poor cycle life due to their characteristics redox reactions [15,16,40]. Carbon materials such as graphene and reduced graphene oxide, carbon nanotubes, and activated carbon proved to have high electrical conductivity, excellent cycle life with a high theoretical surface area, have been selected as optimal supporting materials to enhance the electrochemical performances of transition metal oxides/hydroxides-based materials [159]–[161].

4.2.2 Results and Discussions

The below paper presents the detailed results obtained from the synthesized ternary NiCo-MnO_2 nanocomposite.

Chemical Engineering Journal 335 (2018) 416–433

Contents lists available at ScienceDirect

Chemical Engineering Journal

journal homepage: www.elsevier.com/locate/cej

Synthesis of ternary NiCo-MnO_2 nanocomposite and its application as a novel high energy supercapattery device

Kabir O. Oyedotun, Moshawe J. Madito, Damilola Y. Momodu, Abdulmajid A. Mirghni, Tshifhiwa M. Masikhwa, Ncholu Manyala*

Department of Physics, Institute of Applied Materials, SARCHI Chair in Carbon Technology and Materials, University of Pretoria, Pretoria 0028, South Africa

GRAPHICAL ABSTRACT

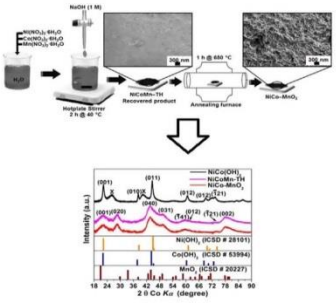

ARTICLE INFO

Keywords:
Mixed hydroxides
NiCo-MnO_2
Carbonized iron cations (C-FP)
Electrochemical performance
Supercapattery
Energy density

ABSTRACT

NiCo /NiCoMn-mixed hydroxides and ternary NiCo-MnO_2 electrode materials were successfully synthesised by a force-driven hydrolysis of hydrated nickel, cobalt and manganese nitrate salts at 40 °C for 2 h with an additional annealing step adopted in producing the NiCo-MnO_2 sample. The morphological, structural, compositional and textural characterization of the samples were obtained using scanning electron microscopy (SEM), transmission electron microscopy (TEM), X-ray powder diffraction (XRD), Raman spectroscopy, X-ray photoelectron spectroscopy (XPS), and N_2 physisorption respectively. The initial sample characterization confirmed bigger material agglomeration of the as-prepared mixed hydroxides compared to the NiCo-MnO_2 sample which had small stacked sheet-like and porous morphology. Further sample analysis also confirmed a high degree of crystallinity in both the mixed hydroxides and NiCo-MnO_2 samples with the elemental constituents existing in different oxidation states. One of the mixed hydroxides sample namely, $NiCo(OH)_2$ exhibited a specific surface area (SSA) of approximately 3.40 $m^2 g^{-1}$ as compared to the ternary NiCo-MnO_2 material which exhibited a higher SSA of 153.94 $m^2 g^{-1}$. The ternary NiCo-MnO_2 electrode exhibited the highest specific capacity of 132.1 mAh g^{-1}, compared to $NiCo(OH)_2$ and NiCoMn-triple hydroxide (NiCoMn-TH) electrodes which exhibited a specific ca-

* Corresponding author.
E-mail address: ncholu.manyala@up.ac.za (N. Manyala).

http://dx.doi.org/10.1016/j.cej.2017.10.169
Received 28 August 2017; Received in revised form 26 October 2017; Accepted 30 October 2017
Available online 31 October 2017
1385-8947/

pacities of 110.3 and 64.36 mAh g $^{-1}$ respectively at a current density of 0.5 A g $^{-1}$. In addition, the ternary NiCo-MnO_2 electrode exhibited a better cycling stability compared to $NiCo(OH)_2$ electrode. Notably, an assembled NiCo-MnO_2//C-FP hybrid asymmetric supercapattery, displayed a specific capacitance of 130.67 F g $^{-1}$, high energy and power densities of 48.83 Wh kg $^{-1}$ and 896.88 W kg $^{-1}$ at 1 A g $^{-1}$ respectively. An excellent cycling stability with a coulombic efficiency of 99.98% and capacitance retention of 96.78% was recorded for up to 10,000 cycles within an operating voltage of 1.5 V, at a 3 A g $^{-1}$ current density.

1. Introduction

High-performance energy storage devices are in great demand in modern society due to the development of numerous portable electronic devices and the emergence of hybrid electric vehicles. However, most of these new inventions require high-performance energy storage units with both high energy and power densities [1–4]. Among common electrical energy storage devices in use are lead–acid batteries, nickel–metal hydride batteries, lithium ion batteries (LIBs) and supercapacitors. Batteries with high energy density and supercapacitors (SCs) with excellent power density are currently considered to meet the needs of increasing energy demand [5]. LIBs can store a large amount of energy as high as 150–200 Wh kg^{-1}, but are confined to their low power density (below 1000 W kg^{-1}) and poor cycle life (usually less than 1000 cycles) [6,7].

Supercapacitors also known as electrochemical capacitors are a class of energy storage devices with the capability of giving off high power with capability of delivering energy in short period of time unlike batteries. Their low cost, low maintenance, relative safety and long cycle life makes them even more desirable for high-power delivery applications. Supercapacitors are used mainly as the power source in electric/hybrid electric vehicles, backup memories, airplane emergency doors, micro-devices and portable electronics [8]. Nevertheless, they are disadvantageous from the perspective of their poor energy density when compared to lithium ion batteries [9,10].

An assessment of various research studies related to energy storage device technology has shown an extensive efforts by many experts in the field to produce materials with desirable properties [11]. This led to the emergence of various syntheses techniques of new materials, most of which require high temperature reaction environments and a continuous power supply to obtain the final products. Presently, materials for energy storage devices with controlled morphology and properties are prepared using simple and low-temperature stirring technique [12–14]. The preparation technique is relatively simple, cost effective and relatively environmentally benign.

Generally, transition metal hydroxides are plagued with a low electrical conductivity but high specific capacitance due to their characteristic redox reaction. As such, they do not yield a high performance under high-rate current densities [15,16]. On the other hand, transition metal hydroxides/oxides have been intensely studied with a view to overcome the above limitation and refine their properties to fit the desired use [17,18]. Transition metal hydroxides/oxides are semi-conductive materials among which Ni based oxides have been taken into account as a promising candidate as electrode materials for electrochemical capacitors owing to its cost effectiveness, natural abundance as well as adequate electrochemical performance [16,19]. The latest progress of NiCo-based application for supercapacitor and battery have been reported in the literature [20–22]. Nevertheless, the demonstrated electrochemical performances of the so called supercapacitor electrodes are nonetheless not enough, particularly in terms of energy density.

In this work, we report the synthesis of mixed transition metal hydroxides $NiCo(OH)_2$, NiCoMn-triple hydroxide (NiCoMn-TH) and ternary metal oxide (NiCo-MnO_2) materials via a facile low temperature process and the characterization/electrochemical testing as potential *SC* electrode materials with a view to highlighting some unique features which make them useful in this regard. The electrode materials were synthesized by force-driven hydrolysis of hydrated nitrate salts of nickel, cobalt and manganese salt at 40 °C for 2 h. The electrochemical performance of the electrode materials were analyzed in a three-electrode cell configuration using 1 M KOH electrolyte. The ternary NiCo-MnO_2 electrode exhibited the highest specific capacity of 132.1 mAh g^{-1}, compared to $NiCo(OH)_2$ and NiCoMn-TH electrodes which exhibited a specific capacities of 110.3 and 64.36 mAh g^{-1} respectively at a current density of 0.5 A g^{-1}. The complete asymmetrical cell displayed a specific capacitance of 130.67 F g^{-1}, high energy and power densities of 48.83 Wh kg^{-1} and 896.88 W kg^{-1} at 1 A g^{-1} respectively. An excellent cycling stability with a coulombic efficiency of 99.98% was recorded for up to 10,000 cycles at a current density of 3 A g^{-1}.

2. Experimental details

2.1. Preparation of materials

2.1.1. Preparation of $NiCo(OH)_2$

All the reagents used in this work were of analytical grade and used as received without further purification. The $NiCo(OH)_2$ sample was synthesized via a chemical precipitation process. Briefly, 1 g of Ni $(NO_3)_2{\cdot}6H_2O$ together with 1 g of $Co(NO_3)_2{\cdot}6H_2O$ were dissolved in 100 ml of deionised water. The solution was then stirred for 30 min to obtain a homogeneous mixture. Thereafter, 14 ml of 1 M NaOH aqueous solution was added dropwise to maintain a pH of 10 for polarization, which changed the colour of the homogeneous mixture kept at 40 °C from brown to bluish dark while magnetically stirring for 2 h. The resulting greenish dark precipitate was collected by centrifugation, washed several times with deionised water and ethanol, with the recovered solid particle put in an oven to dry at 60 °C overnight.

The following Eq. (1) below summarizes the reaction route to obtain $NiCo(OH)_2$.

$$\boldsymbol{Ni(NO_3)_{2(s)} + Co(NO_3)_{2(s)} + 2N_a OH_{(aq)} + H_2O_{(l)} \rightarrow NiCo(OH)_{2(s)} + 2Na(NO_3)_{2(aq)} + H_2O_{(l)}} \quad (1)$$

2.1.2. Preparation of NiCoMn-triple hydroxide (NiCoMn-TH) and ternary NiCo-MnO_2 composites

Using the same procedure as in 2.1.1., 0.67 g of $Mn(NO_3)_2{\cdot}4H_2O$, Ni $(NO_3)_2{\cdot}6H_2O$ and $Co(NO_3)_2{\cdot}6H_2O$ precursor salts were completely dissolved in 100 ml of deionised water whilst magnetically stirring the mixture. Subsequently, 14 ml of 1 M NaOH was added dropwise the homogeneous mixture kept at 40 °C for 2 h upon magnetic stirring. The resulting greyish-cream mixture was left to stand for about 10 h for complete precipitation. It was then centrifuged and washed several times with deionised water and ethanol. The solid precipitate was collected and dried in an oven at 60 °C for 12 h. The interim solid ternary nickel cobalt manganese triple hydroxide (NiCoMn-TH)

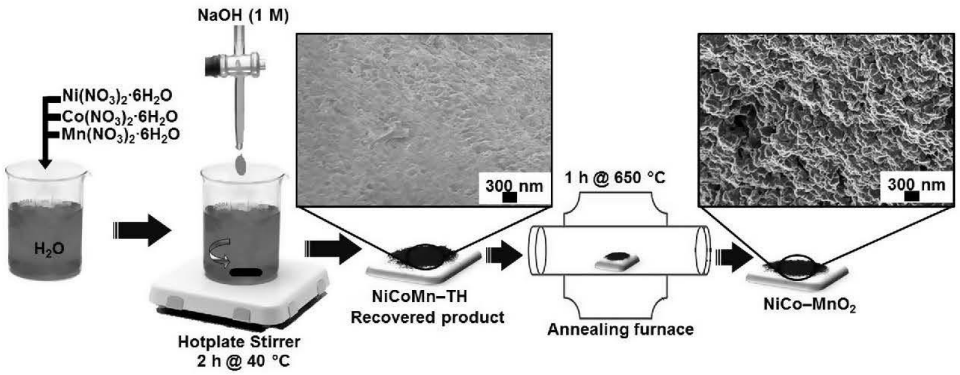

Scheme 1.

material was then annealed in air at 650 °C for 1 h at a ramping rate of 2 °C/min to obtain a more stable ternary NiCo-MnO_2 composite as shown in Scheme 1 above:

2.1.3. Preparation of C-FP negative electrode material

Pyrolysis of the iron-containing mixture, denoted as C-FP was achieved by complete dissolution of iron (III) nitrate nonahydrate salt in ethanol, and mixed with PANI. The resulting mixture was sonicated for several hours to have slurry which was then coated onto nickel foam. The coated nickel foam was then transferred into a Quartz tube under N_2 atmosphere at 850 °C to enhance the adsorption of iron cations (Fe^{3+}) onto the PANI film (C-FP) which was deposited on a nickel foam template (*see Supplementary information for more details*).

2.2. Characterization of the samples

Scanning electron microscope (SEM) micrographs, energy dispersive X-ray (EDX) spectra and the transmission electron microscopy (TEM) micrographs of the as-prepared samples were obtained on a Zeiss Ultra Plus 55 field emission scanning electron microscope (FE-SEM) operated at 1.0 kV and a JEOL-2100F high-resolution transmission electron microscope (HRTEM FEI Tecnai-F30) alongside 200 kV acceleration voltage respectively. The structural analysis (X-ray diffraction (XRD)) was carried out using an XPERT-PRO diffractometer (PANalytical BV, Netherlands) with reflection geometry at 2θ values (18–90°) with a step size of 0.01°, operating with a Co $K\alpha$ radiation source (λ = 0.178901 nm) at 50 kV and 30 mA. A T64000 micro-Raman spectrometer (HORIBA Scientific, Jobin Yvon Technology) with a 514 nm laser wavelength and spectral acquisition time of 120 s was used to characterize the as-prepared samples. The Raman system laser power was set as low as 5 mW in order to minimize heating effects. Fourier transform-infrared (FT-IR) spectra of the samples were obtained using a Varian FT-IR Spectroscopy in the wavenumber range of 400–4000 cm^{-1}. X-ray photoelectron spectroscopy (XPS) measurements of the samples were conducted using a Physical Electronics VersaProbe 5000 spectrometer operating with a 100 µm monochromatic Al-Kα exciting source. N_2-absorption/desorption isotherms were obtained on a Micromeritics TriStar II 3020 system operated in a relative pressure (P/P_o) range of 0.01–1.0 with pre-degassing of the samples at 100 °C for 18 h under vacuum prior to the measurement. The Brunauer-Emmett-Teller (BET) and Barrett–Joyner–Halenda (BJH) models were used to determine the surface area and the pore size distribution (PSD) of the samples respectively. XRF measurement of the pressed powder composite sample was performed using the ARL Perform'X Sequential XRF instrument with Uniquant software for analysis.

2.3. Electrochemical measurements

The electrodes were prepared by mixing the active material (80 wt %) with conductive acetylene carbon black (10 wt%) as a conducting agent and a PVDF binder (10 wt%), with a small amount of N-methyl-2-pyrrolidone (NMP) solvent added to the mixture with low-speed stirring to form a uniform slurry. The slurry was then coated onto nickel foam and dried at a temperature of 60 °C for 10 h. The capacitive performance of nickel foam-supported electrodes was investigated using a Bio-Logic VMP300 potentiostat (Knoxville TN 37,930, USA) controlled by the EC-Lab® V1.40 software in a three-electrode configuration. The electrochemical measurements were performed with a glassy carbon counter electrode, Ag/AgCl reference electrode, and the as-prepared mixed hydroxide materials as the working electrodes. All the electrochemical measurements for this study were performed in a 1 M KOH electrolyte at room temperature. The mass loading of the active material was estimated to be ca. 2.5 mg, 2.34 and 2.3 mg for the NiCo$(OH)_2$, NiCoMn-TH and NiCo-MnO_2 electrodes respectively. The cyclic voltammetry (CV) of the as-prepared samples were carried out at different scan rates from 1 to 50 mV s^{-1} within a potential window range of −0.1 to 0.4 V vs. Ag/AgCl. The galvanostatic charge-discharge (GCD) measurement was carried out at different current densities in the range of 0.5–5.0 A g^{-1} in a potential window range of −0.1 V to 0.4 V. The electrochemical impedance spectroscopy (EIS) of the samples was conducted in an open-circuit potential and in a frequency range of 10 mHz–100 kHz.

The gravimetric specific capacitance, C_s (F g^{-1}) of the half-cell was derived from the CV curves according to the formula stated in Eq. (2) below [23]:

$$C_s = \frac{1}{mS_c \cdot V}\int_{v_1}^{v_2} IdV_s \tag{2}$$

where, v_1 and v_2 are the vertex potential of the potential range, I is the current response (mA), ΔV is the cell voltage (V) for the single electrode, S_c is the scan rate (mV s^{-1}) and m is the loading mass (g) of the single electrode.

The specific capacity, Q_s (mAh g^{-1}), energy efficiency of the materials using GCD curves were calculated according to the following relations [8,9] [11,24]:

$$Q_s = \frac{It}{3.6m} \tag{3}$$

$$\eta_E = \frac{E_d}{E_c} \times 100 \tag{4}$$

where I is the discharge current in mA, m is the mass loading of the

electrode in mg, and t is the time in seconds taken for a complete discharge cycle. η_E, E_d and E_c are energy efficiency, discharge energy and charge energy from the integral of the area under the charge-discharge curve of the electrode respectively.

The specific capacitance, C_s, energy and power densities of the full hybrid asymmetric supercapattery (composed of the ternary NiCo-MnO_2 and C-FP selected as both positive and negative electrode respectively), with respect to the current density of the device were evaluated from the slope of the discharge curve according to following equations:

$$C_s = \frac{I \times \Delta t}{m \times \Delta V} [\mathrm{Fg^{-1}}] \tag{5}$$

$$E_d = I/3.6m \int^{V} dt \, [\mathrm{Whkg^{-1}}] \tag{6}$$

$$P_d = 3.6 \times E_d/\Delta t \, [\mathrm{kWkg^{-1}}] \tag{7}$$

where .C_s is the specific capacitance of the electrode based on the mass of the active material, I is the discharge current in Amperes (A), m is the mass loading of the active material in grams (g). ΔV is the operating potential window in volts (V), Δt in seconds is the electrode discharge time respectively, E_d & P_d, are the energy and power densities respectively with their specified units.

The maximum constant-current discharge power density, P_{max} of the hybrid cell was predicted using the effective solution resistance, R_s (ohm) determined from the Z'-intercept of the Nyquist plots of frequency analysis according to the following equation [26,27]

$$P_{max} = \frac{V^2}{4mR_s} \tag{8}$$

where V (V) and m (g) are the potential window as well as the mass loading of the active material respectively.

The fabricated hybrid asymmetry SC could operate in a wider potential window, *ca.* 1.50 V. For optimal performance of the hybrid asymmetry device, the mass on each electrode was balanced using the charge balance equation,

$$Q_+ = Q_-$$

,with the charge stored on each electrode expressed as [28]:

$$Q = C_s \times m\Delta V \tag{9}$$

where Q (C) is the stored charge on the electrode, C_S (F g^{-1}) is the specific capacitance of the electrode based on the mass of active material, m (g) is the mass of active material, and ΔV (V) is the potential window.

The mass balancing between the positive and negative electrodes was accurately determined by further considering [29]:

$$\frac{m_+}{m_-} = \frac{C_{s-}\Delta V_-}{C_{s+}\Delta V_+} \tag{10}$$

3. Results and discussion

3.1. Morphological, structural and composition characterization

Fig. 1 shows the SEM and TEM morphologies of the as-prepared materials. Fig. 1(a) and (b) represent low and high magnifications SEM images of $NiCo(OH)_2$. It can be seen that the as-prepared $NiCo(OH)_2$ has an agglomerated larger flake-like morphology compared to the NiCo-MnO_2 sample which shows a singly stacked porous sheet-like as shown in Fig. 1(c and d). The morphology of the samples was further analyzed by TEM technique as shown in Fig. 1(e and f). The TEM micrographs clearly show the agglomerated flake-like particles of $NiCo(OH)_2$ (Fig. 1(e)) and the singly stacked porous sheet-like structures of the NiCo-MnO_2 (Fig. 1(f)) in accordance with SEM results.

Fig. S1 in the supporting information displays the SEM micrographs of the NiCoMn-TH electrode material at low and high magnifications and the TEM micrograph to further observe the material morphology. It can be seen from the microscopy images that NiCoMn-TH material is composed of stacked flake-like nano structures which is further confirmed by the TEM image as shown in Fig. S1 (c). Visible flakes are clearly seen in the TEM micrograph overlapping each other in different orientations.

Fig. S2 shows the SEM and TEM micrographs of the as-synthesized C-FP negative electrode material of the hybrid NiCo-MnO_2//C-FP supercapattery. It can be observed that the material mainly composed of orthorhombic nano grains at low and high magnifications respectively. These microstructures were further confirmed by TEM as shown in Fig. S2 (c–d). The TEM micrographs clearly show the nano sized particles of the material.

The purity and phase structure of the as-prepared materials were observed using X-ray diffraction (XRD). Fig. 2(a) shows the powder XRD spectrum of the samples with the matching inorganic crystal structure database (ICSD) card No. 28101 for $Ni(OH)_2$ crystal system: (trigonal; space-group: *P-3m1*; cell parameters: a = 3.1300 Å, c = 4.6300, b = 3.1299 Å), ICSD card No. 88940 for $Co(OH)_2$ crystal system: (trigonal; space-group: *P-3m1*; cell parameters: a = 3.186 Å, c = 4.653 Å, b = 3.1859 Å), and ICSD card No. 20227 for MnO_2 crystal system: (tetragonal; space-group: *I4/m*; cell parameters: a = 9.8151 Å, c = 2.8471 Å, b = 9.8154 Å). The XRD spectrum of $NiCo(OH)_2$ sample shows the typical diffraction of the transition metal hydroxide phases and matches well with the patterns of the $Ni(OH)_2$, ICSD card No. 28101 and $Co(OH)_2$, ICSD card No. 88940 standards, except, for peaks indicated by X which could be possibly due to defects. Using equation ES2 (*see Supplementary Information*), the NiCo-MnO_2 electrode material has an average crystallite size of 8.62 nm compared to 15.45 nm observed for $NiCo(OH)_2$ material, suggesting that the NiCo-MnO_2 with smaller particle size is more nanocrystalline in nature, which accounts for the material's enhanced electrochemical results. Fig. 2(b) is a 2 × 2 × 2 cell of $Ni(OH)_2$, $Co(OH)_2$ and MnO_2 viewed along y-axis based on Crystallographic Information Files (CIF) of above-mentioned ICSD cards. The $Ni(OH)_2$ has an O—H distance of 1.06 Å, with Ni^{2+} ion-ion interaction taking place via the oxygen ions since the Ni-Ni distance (4.63 A) is much greater than the sum of ionic radii of Ni-Ni [30]. These indirect interactions, including interaction via Ni-OH-OH-Ni ions could be responsible for the magnetic nature often seen in $Ni(OH)_2$ as well as in $Co(OH)_2$ [30,31]. Also, Fig. 2(a) shows the XRD spectrum of NiCo-MnO_2 with broader diffraction peaks matching well the MnO_2 (ICSD 20227) standard. The peak broadening can be attributed to the sample's reduced crystallites size, which agrees well with SEM and TEM results. This can be attributed to the high surface area-to-volume ratio of the material which would lead to an increase in the amount of interfaces and enhanced electron and mass transport yielding electrode with much higher electrochemical performance. The MnO_2 structure is composed of more oxygen atoms with most manganese atoms located in the center of the structure (Fig. 2(b)). Hence, XRD results affirm further the synthesis of the materials.

A representative XRD spectrum and the matching ICSD card of the as-prepared C-FP material indexed using the matching Inorganic Crystal Structure Data-base (ICSD) card No. 16593 with chemical formula Fe_3C is displayed in S3 (a) of the Supplementary information, with well-defined diffraction peaks and identified crystal planes of Fe_3C phase respectively. The expected broad but weak diffraction peak around 30° corresponding to the (0 0 2) plane of graphitic carbon is observed, indicating presence of particular graphitic structures. A diffraction (3 2 0) peak around 52.5° is due to presence of metallic Fe and Ni. The two peaks at around 44.2° and 64.3° can be attributed to the (1 1 0) and (2 0 0) reflections of α-Fe, respectively (JCPDS, No. 870722). The other diffraction peaks present are characteristic of the crystalline planes of Fe_3C species (JCPDS, No. 892867). A further description of the nature of the peaks is discussed in the Supplementary Information.

It is observed that the NiCoMn-TH and NiCo-MnO_2 exhibited similar

crystal structure as shown in Fig. 2(a). However, further sample characterization were focused on the $NiCo(OH)_2$ and $NiCoMnO_2$ due to the poor electrochemical performance recorded for the NiCoMn-TH sample since the main focus area of this present study is related to the electrochemical performance. This will be discussed at a later stage in Fig. 8 where the three electrode materials are compared.

Fig. 3(a) shows the Raman spectra of the as-prepared $NiCo(OH)_2$ and $NiCo\text{-}MnO_2$ samples which were fitted to a combination of Lorentzian and Gaussian modes. In Fig. 3(a), the Raman spectrum of the as-prepared $NiCo(OH)_2$ sample shows modes at 310, 458, 558 and 649 cm^{-1}. These modes were compared to those reported in earlier studies [32,33] for $Ni(OH)_2$ and $Co(OH)_2$. It is worth mentioning that a group theory analysis of the phonon modes in brucite-type hydroxides (e.g., $Ni(OH)_2$ and $Co(OH)_2$) predicts that four Raman active modes are allowed, three of which are lattice modes in the range of 310–530 cm^{-1}, and one is a symmetric OH stretching vibration at about 3581 cm^{-1} [34,35]. In addition, $Co(OH)_2$ and cobalt oxyhydroxide, CoO(OH), show Raman active modes at 557 and 641 cm^{-1} respectively [36,37]. Therefore, the observed Raman modes of $NiCo(OH)_2$ sample reveals the major vibrational features of the $Ni(OH)_2$, $Co(OH)_2$ and CoO(OH). The $NiCo\text{-}MnO_2$ sample also displayed Raman active modes at 502, 584 and 625 cm^{-1} wavenumber, as shown in Fig. 3(a). These modes agree well with the three major vibrational features of the MnO_2 previously reported at 500, 585, and 625 cm^{-1} on

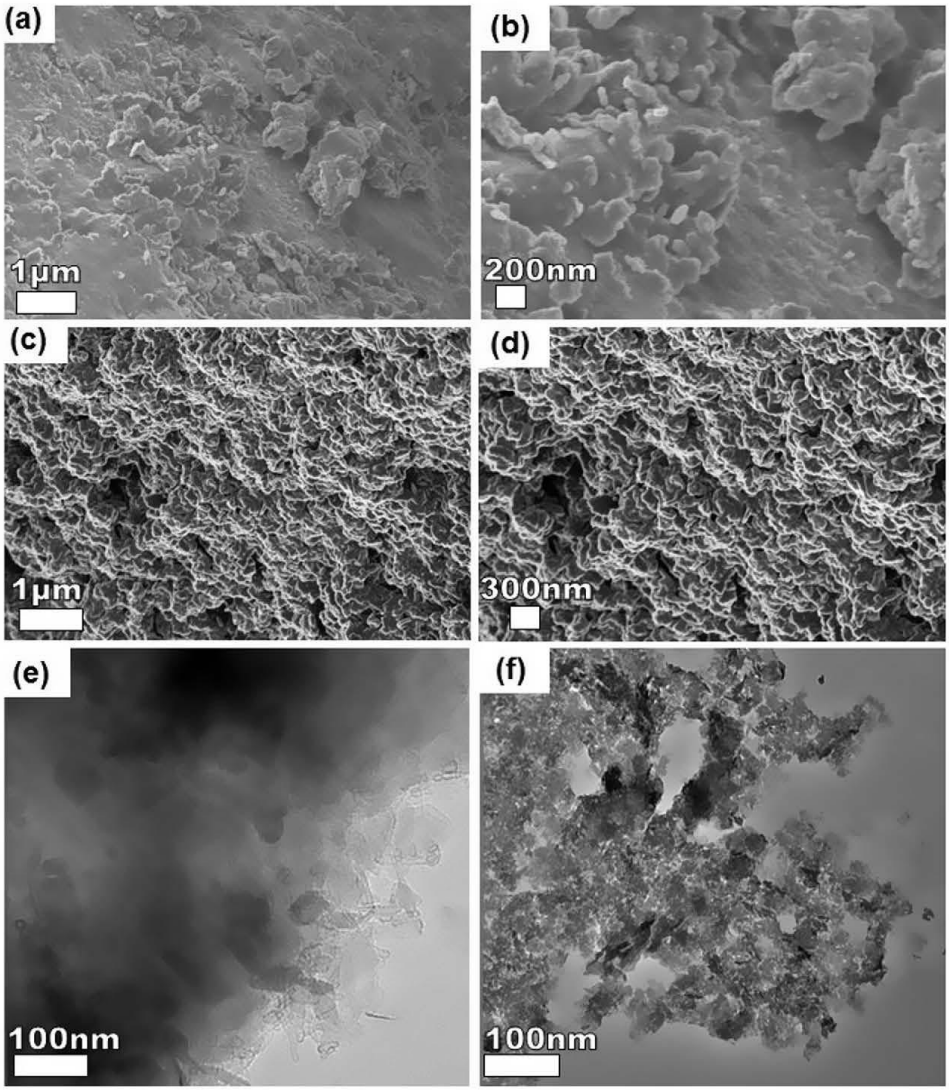

Fig. 1. (a, b) SEM images of the as-prepared $NiCo(OH)_2$ at low and high magnifications respectively. (c, d) SEM images of the as-prepared $NiCo\text{-}MnO_2$ at low and high magnifications respectively. (e, f) TEM images of the $NiCo(OH)_2$ and $NiCo\text{-}MnO_2$ respectively.

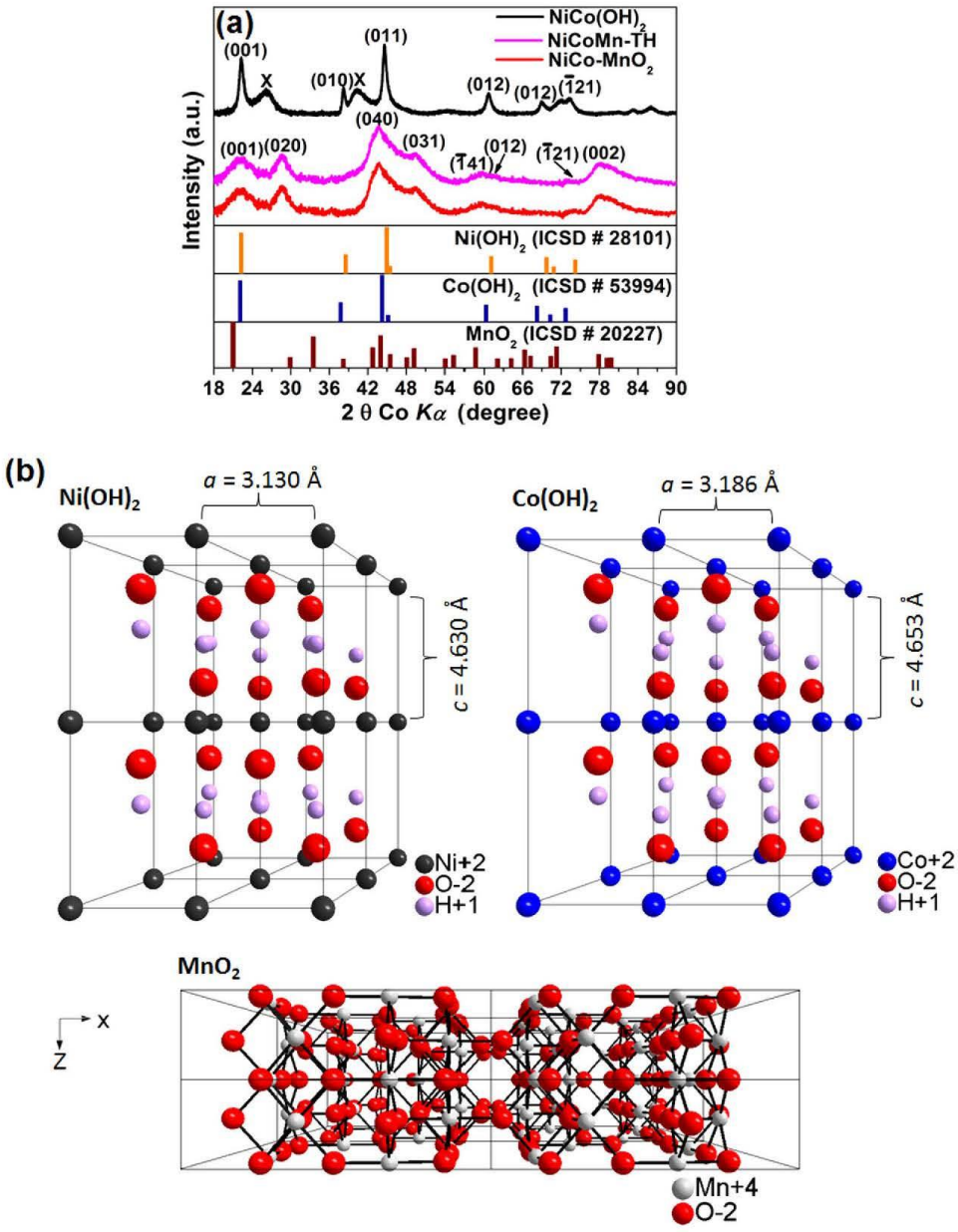

Fig. 2. (a) The X-ray diffraction of the as-prepared $NiCo(OH)_2$, NiCoMn-TH and $NiCo\text{-}MnO_2$ samples, and the matching ICSD cards for $Ni(OH)_2$, $Co(OH)_2$ and MnO_2. (b) $2 \times 2 \times 2$ cells of $Ni(OH)_2$,$Co(OH)_2$ and MnO_2 viewed along y-axis.

similar materials [38,39]. Thus, this confirms MnO_2 compound in the sample and the relatively high intensity of these modes suggest that a relatively high MnO_2 content is present in the $NiCo\text{-}MnO_2$ sample.

Fig. 3(b) shows the FT-IR spectra of the as-prepared materials. As depicted in Fig. 3(b), the band at about 3480 cm^{-1} is assigned to O—H stretching vibrations and that at 1600 cm^{-1} is assigned to O—H bending vibrations, and both bands can be predominantly due to the complexation of metal-hydroxyl groups [40–42]. In fact, the IR band at ~1600 cm^{-1} is usually ascribed to H_2O bending vibration features. The band at 2980 cm^{-1} is ascribed to the –C—H vibration mode of $-CH_2$ [41]. The IR band at 1350 cm^{-1} is assigned to CO_3^{2-} asymmetrical stretching vibrations, while a band at 830 cm^{-1} is assigned to the

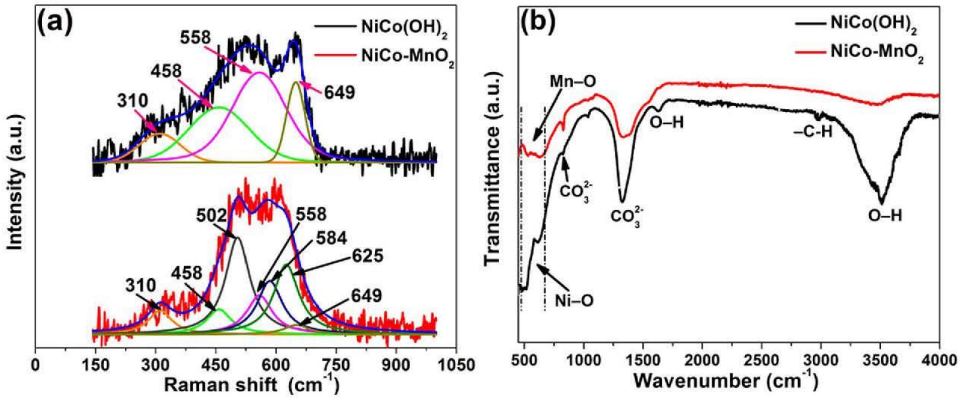

Fig. 3. (a) The Raman spectra and (b) The FT-IR spectra of the as-prepared $NiCo(OH)_2$ and $NiCo\text{-}MnO_2$. Raman spectra were fitted to a combination of Lorentzian and Gaussian modes.

bending vibrations of CO_3^{2-} [40–42]. The bands in the range of 500–640 cm^{-1} can be assigned to the M–O, O–M–O, and M–O–M (M = Co, Ni and Mn) lattice vibrations [42,43]. In comparison between $NiCo(OH)_2$ and $NiCoMnO_2$, it can be seen that the broadband at 3480 cm^{-1} belonging to the O—H vibrations disappears confirming the transformation of $NiCo(OH)_2$ to $NiCo\text{-}MnO_2$.

Fig. 4(a) and (b) show the EDX spectra of the as-prepared $NiCo(OH)_2$ and $NiCo\text{-}MnO_2$ respectively. In the figures, it is seen that both the $NiCo(OH)_2$ and $NiCo\text{-}MnO_2$ materials are composed of Ni, Co and O with an additional Mn peak in the $NiCo\text{-}MnO_2$ spectrum. Both samples reveal traces of chlorine (Cl) which could be linked to the sample preparation, while the high C content arose from the carbon coating step adopted for measurements carried out by EDX-SEM system.

The elemental and structural clarification analysis of the C-FP negative electrode material are shown in Fig. S3 (b). The analysis shows iron (Fe) and carbon (C) as the major elements with high content. The Sulphur (S) and Nitrogen (N) are linked to the PANI composition. A detailed description of the percentage weight of these elements is described in the Supplementary Information.

In addition to the bulk elemental composition of the samples, the surface elemental composition of the as-prepared $NiCo(OH)_2$ and $NiCo\text{-}MnO_2$ samples was analyzed by XPS. Fig. 5(a) shows the wide scan XPS spectra of the as-synthesized $NiCo(OH)_2$ which displays the main elements (Ni, Co, and O) of the composition of the sample with fractional concentrations of 17.65 at.% Ni 2p, 20.90 at.% Co 2p and 52.61at% O 1 s. The sample shows traces of 6.24 at.% C 1 s and 2.60 at.% Cl 2 s which could be due to sample preparation and handling through air.

Fig. 5(b) shows the core level spectrum of Co 2p of the $NiCo(OH)_2$ sample which reveals the binding energy peaks at 780.4 eV and 785.5 eV which were fitted to Co $2p_{3/2}$, and other binding energy peaks at 795.9 eV and 802.5 eV which correspond to Co $2p_{1/2}$ core level. The fitted Co $2p_{3/2}$ peaks suggests that the Co oxidation state of the as-synthesized $NiCo(OH)_2$ is predominantly Co(II) (2 + valence state) with a fitted peak at 780.1 eV corresponding to CoO $2p_{3/2}$ core level with a binding energy of 780.2 eV. The core level spectrum of Ni 2p of a $NiCo(OH)_2$ sample reveals the binding energy peaks at 854.4, 861.0 corresponding to Ni $2p_{3/2}$ core level, and 872.1 and 879.3 eV which correspond to Ni $2p_{1/2}$ core level. Similar to the fitted Co $2p_{3/2}$ peaks, the fitted Ni $2p_{3/2}$ peaks suggests that the Ni oxidation state of the sample is predominantly Ni^{2+} [44–46]. Additionally, a binding energy peak at about 854.1 eV suggests the presence of CoNi bond since the CoNi $2p_{3/2}$ core level has a binding energy peak at 853.09 eV.

Furthermore, Fig. 5(d) shows the core level spectrum of O 1 s with fitted peaks at 529.6 and 531.4 eV which could be ascribed to O 1 s in Ni-O and Co-O compounds. The XPS of the as-synthesized $NiCo(OH)_2$ reveals two mixed oxidation states. The two states, Ni^{2+}/Ni^{3+} and Co^{2+}/Co^{3+} are mixed in the materials since there is no obvious difference in the diffraction patterns of the hydroxides (Fig. 2). Both $Ni^{2+}/$

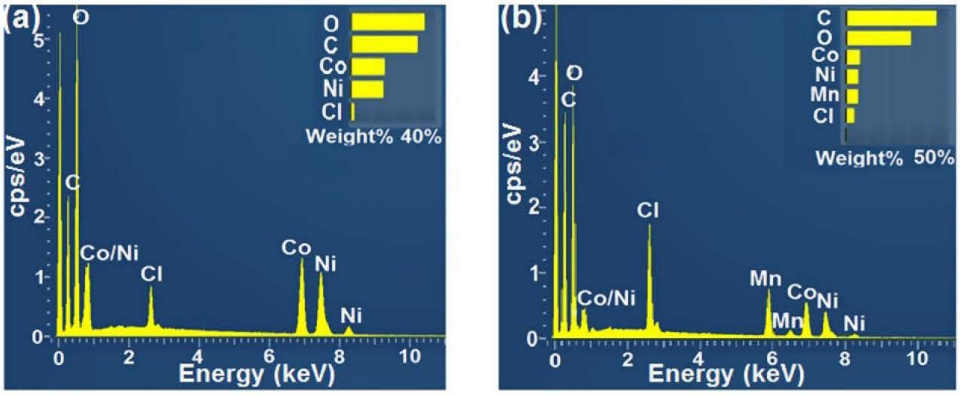

Fig. 4. EDX spectra of the as-prepared (a) $NiCo(OH)_2$ and (b) $NiCo\text{-}MnO_2$ samples.

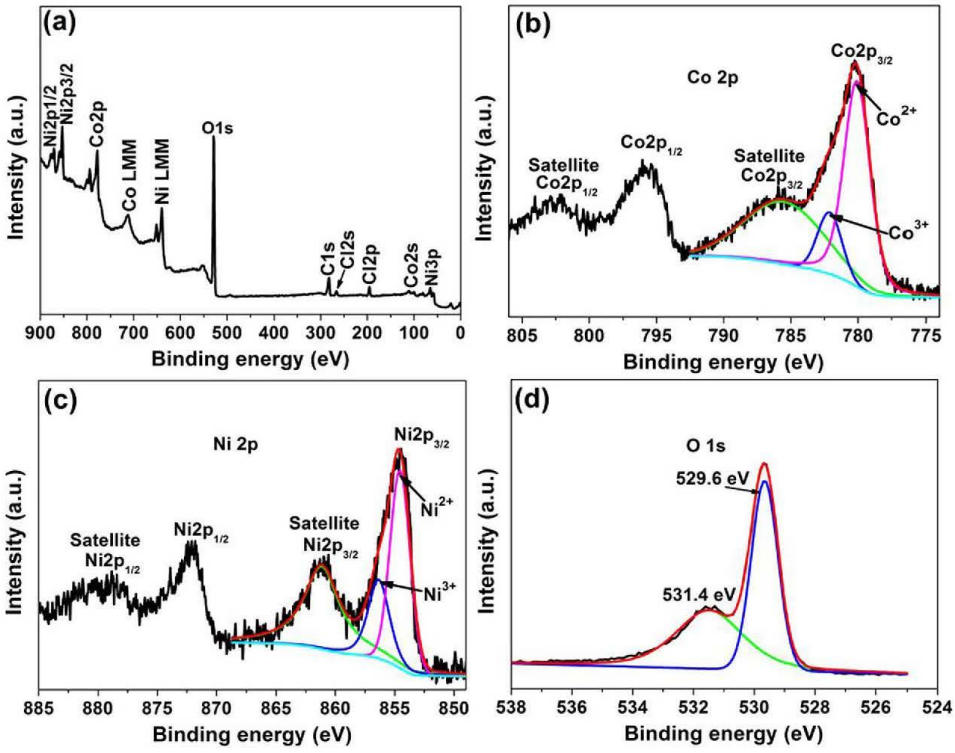

Fig. 5. (a) The wide scan XPS spectra of the as-received $NiCo(OH)_2$ sample. The core level spectrum of (b) Co 2p, (c) Ni 2p and (d) O 1s of a $NiCo(OH)_2$ sample.

Ni^{3+} and Co^{2+}/Co^{3+} redox couples ensure a major electrocatalytic effectiveness [47] based on the synergistic redox reaction involving the changes in oxidation states with OH^- present in KOH electrolyte.

The wide scan XPS spectra of the annealed NiCo-MnO_2 (as shown in Fig. 6(a)), displays the main elements (Ni, Co, Mn and O) of the composition of the sample with fractional concentrations of 10.10 at.% Ni 2p, 13.30 at.% Co 2p, 21.15 at.% Mn 2p and 50.60 at.% O 1 s. This sample also shows traces of 3.24 at.% C 1 s, 1.30 at.% Cl 2 s and 0.31 at. % N 1 s. The core level spectrum of Mn 2p of the NiCo-MnO_2 sample reveals the binding energy peaks at 639.4 and 651.0 eV which agree with Mn $2p_{3/2}$ and Mn $2p_{1/2}$ core levels, respectively, shown in Fig. 6(b). The fitted Mn $2p_{3/2}$ peaks suggests that the Mn oxidation state of the sample is composed of both Mn^{3+} and Mn^{4+} [48].

Similar to the core level spectra of Co 2p and Ni 2p of a $NiCo(OH)_2$ sample, the core level spectra of Co 2p and Ni 2p of the NiCo-MnO_2 sample reveal the oxidation states of Co and Ni (see Fig. 6(c) and (d)). However, the observed peaks are slightly shifted suggesting a change in the binding energy of a core electron of these elements predominantly due to a change in the chemical bonding of these elements (i.e., chemical change from $NiCo(OH)_2$ to NiCo-MnO_2). Fig. 6(e) shows the core level spectrum of O 1s with fitted peaks at 526.9, 528.4 and 529.7 eV which could be ascribed to O 1s in Ni-O, Co-O and Mn-O compounds.

Fig. 7(a) shows the pore-size distribution curves of the as-prepared material, showing the presence of a mesoporous structure within the as-prepared material. The higher pore volume recorded is an order of magnitude higher for the NiCo-MnO_2 sample as compared to the $NiCo(OH)_2$ sample. The PSD results also confirms the observed enhancement in the SSA recorded with the $NiCoMnO_2$ sample exhibiting a high BET specific surface area of 153.94 m^2g^{-1} compared to the $NiCo(OH)_2$ which exhibited 3.40 m^2g^{-1} as shown from the absorption-desorption isotherm in Fig. 7(b). The textural properties could also be linked to the morphological characterization (TEM) results earlier discussed where an agglomerated flake-like sample morphology was seen for the $NiCo(OH)_2$ material as compared to the porous non-agglomerated stacked sheet-like particles morphology for the NiCo-MnO_2 sample.

The molar ratio of Ni: Co: Mn in the ternary metal oxide was given by the XRF measurement as 0.85:1:0.89 respectively as shown in Table S2 in the supplementary information. These measured Ni: Co: Mn ratios are in agreement with what was determined by the EDX analysis (Fig. 4(b)). The ARL Perform'X Sequential XRF instrument with Uniquant software is used to analyze all elements in the periodic table between Na and U, but only elements found above the detection limits are reported.

3.2. Electrochemical characterization

3.2.1. Three-electrode electrochemical measurements of half-cell electrodes

To investigate the electrochemical performance of the as-prepared electrode materials, initial three-electrode measurements were carried out in 1 M KOH electrolyte. Fig. 8(a) shows the charge-discharge (CD) curves of the $NiCo(OH)_2$, NiCoMn-TH and NiCo-MnO_2 at a current density of 0.5 A g^{-1} in a potential window range of −0.1–0.4 V. In comparison to the $NiCo(OH)_2$ and NiCoMn-TH electrodes, the NiCo-MnO_2 electrode exhibited a longer discharge time. Therefore, the CD curves clearly show that the addition of manganese to the nickel cobalt hydroxide with further annealing step significantly improves the capacity of the material. In addition, the nonlinear CD curves of the electrodes show potential steps, corresponding to a fast drop in the

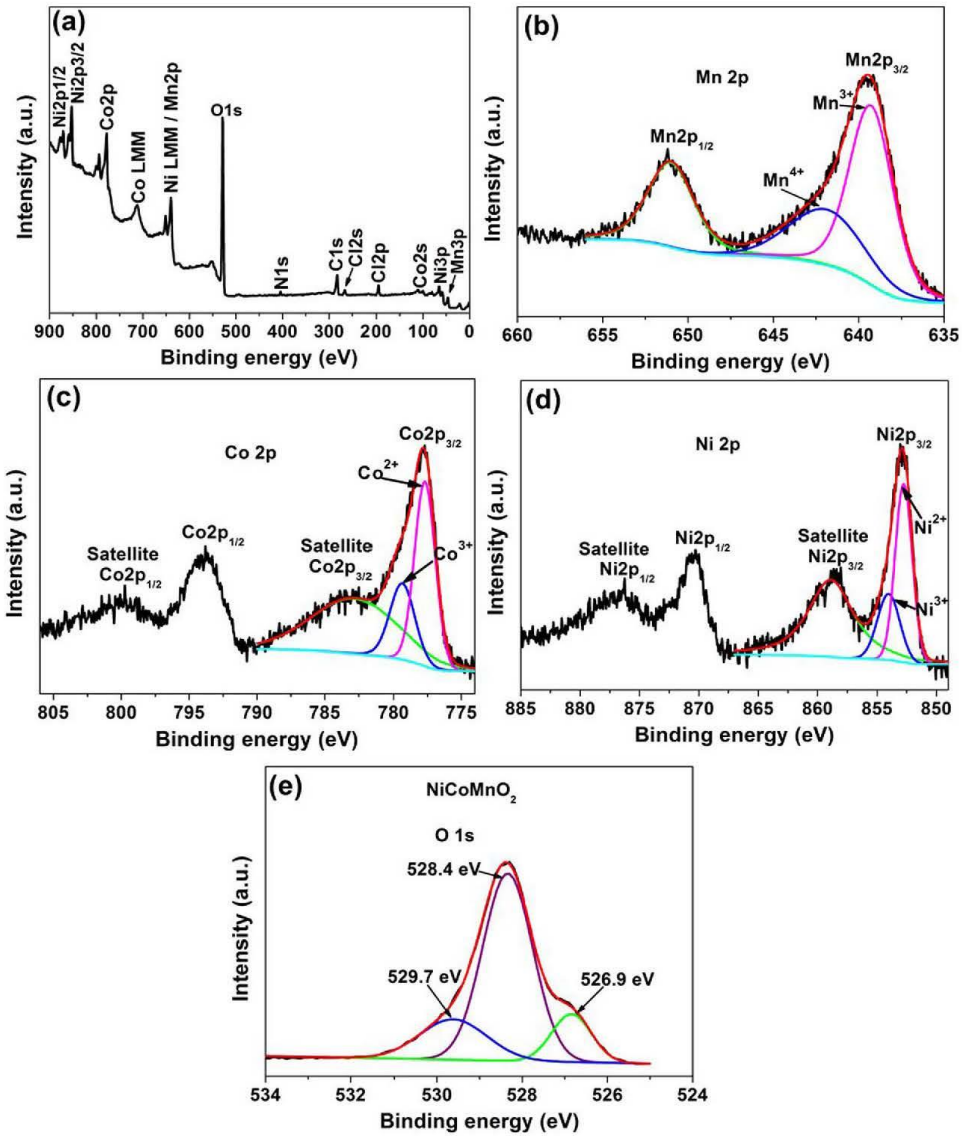

Fig. 6. (a) The wide scan XPS spectra of the as-received NiCo-MnO_2 sample. The core level spectrum of (b) Mn 2p, (c) Co 2p, (d) Ni 2p and (e) O 1 s of a NiCo-MnO_2 sample.

potential range of about 0.4–0.3 V and a slow drop in the potential range of about 0.3–0.2 V, suggesting faradic behavior of the electrode materials. Similarly, Fig. 8(b) shows the associated CV curves of NiCo $(OH)_2$, NiCoMn-TH and NiCo-MnO_2 electrodes at a scan rate of 20 mV s^{-1} in a potential window range of −0.1–0.4 V which reveals that the NiCo-MnO_2 electrode has a high current response suggesting a high specific capacity. Thus, as hinted earlier, there was no further need to analyze the intermediate NiCoMn-TH but rather focus on the annealed NiCo-MnO_2 material electrode. Fig. 8(c) shows the CV curves of NiCo-MnO_2 and nickel foam taken at a scan rate of 1 mV s^{-1} in the potential range of −0.1–0.4 V. It can be observed that the redox peaks of Ni-foam are negligible in comparison with that of as-synthesized ternary transition metal oxide. Nevertheless, it is believed that the redox peaks are substantively ascribed to electrode materials [25,49]. The two redox peaks can be ascribed to the electrochemical reactions of Ni-Co-Mn species according to the equations below:

$$NiO + OH^- = NiOOH + e^- \quad (11)$$

$$C_{03}O_4 + H_2O + OH^- = 3C_0OOH + e^- \quad (12)$$

$$M_nO + OH^- = M_nOOH + e^- \quad (13)$$

$$N_iC_oM_nO_4 + OH^- + H_2O = N_iOOH + C_oOOH + M_nOOH + e^- \quad (14)$$

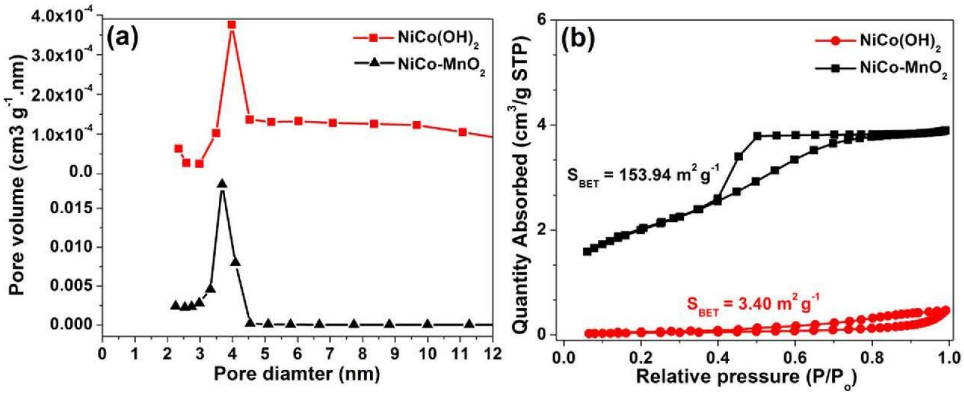

Fig. 7. (a) Pore size distribution and (b) N_2 isotherms of $NiCo(OH)_2$ and $NiCo\text{-}MnO_2$ samples.

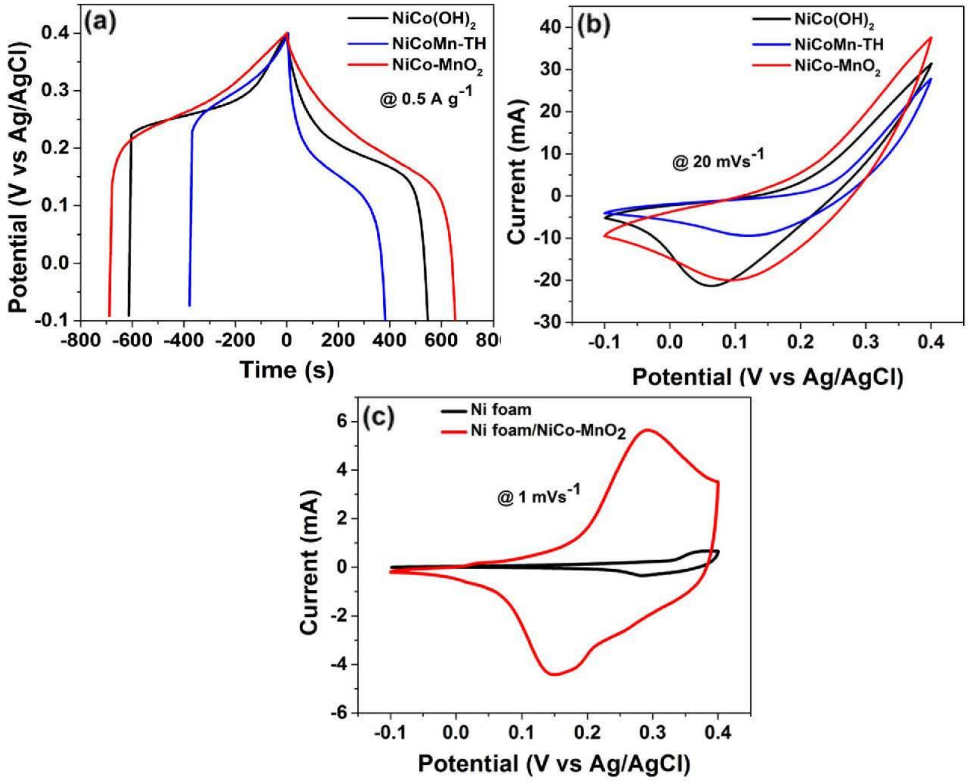

Fig. 8. (a) CD curves of $NiCo(OH)_2$, NiCoMn-TH and $NiCo\text{-}MnO_2$ at a current density of 0.5 A g^{-1}, (b) the CV curves of $NiCo(OH)_2$, NiCoMn-TH and $NiCo\text{-}MnO_2$ at a scan rate of 20 mVs^{-1} and (c) CV curves of ternary metal oxides ($NiCo\text{-}MnO_2$) and nickel foam at a scan rate of 1 mVs^{-1}.

$$M_nOOH + OH^- = M_nO_2 + H_2O + e^- \quad (15)$$

Besides, the peak current of the $NiCo\text{-}MnO_2$ is much higher than those of $NiCo(OH)_2$ and NiCoMn-TH at the same scan rate. Also, it has been proven that the area under the CV curve reflects the electrochemical performance of the electrode materials. The higher the response current density is, the larger the specific capacitance of the material is delivered [50]. We can infer that the $NiCo\text{-}MnO_2$ proved a better capacitance/capacity than those of $NiCo(OH)_2$ and NiCoMn-TH.

To further investigate the electrochemical performance of $NiCo\text{-}MnO_2$ electrode material, the CD curves were obtained at different current densities (Fig. 9(a)), while the CV curves were obtained at

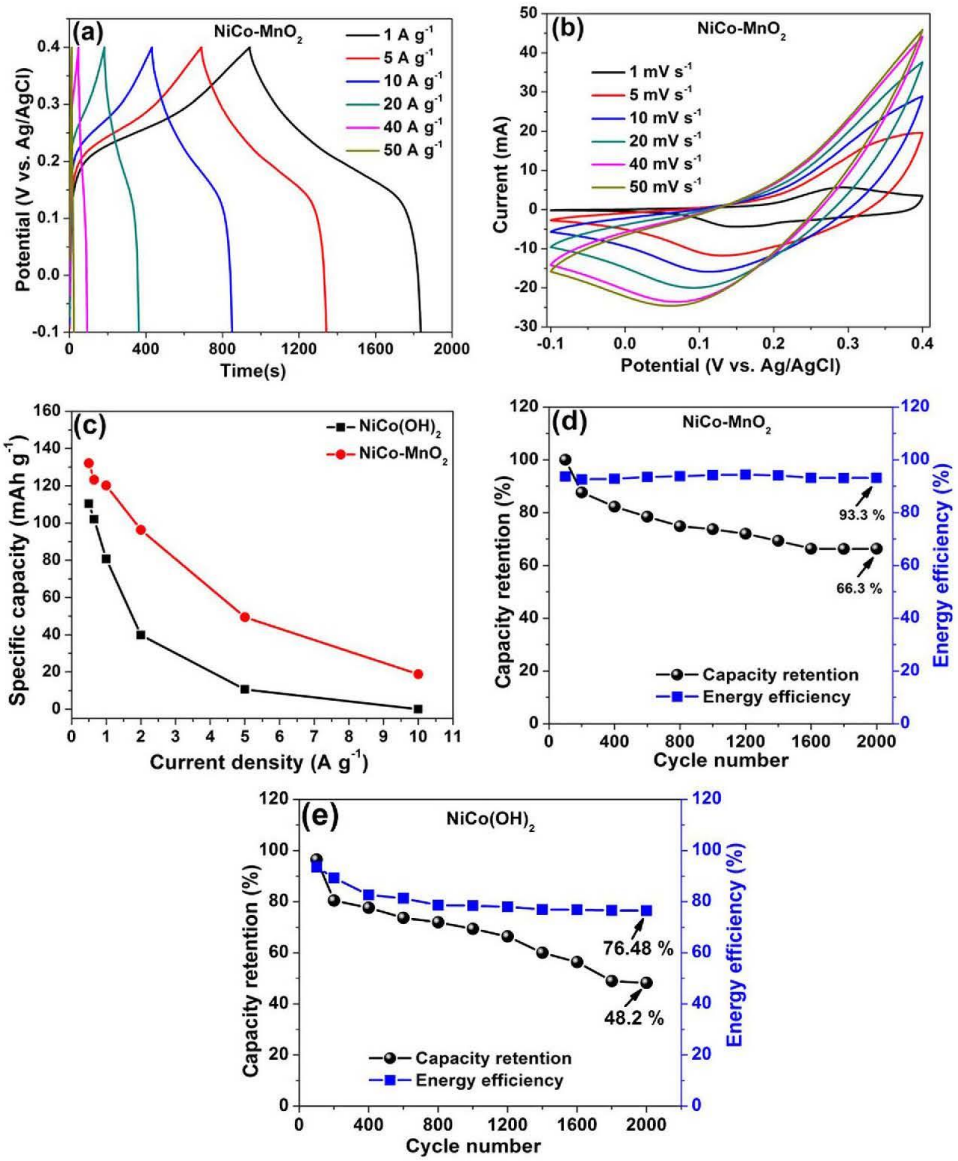

Fig. 9. (a) CD curves of NiCo-MnO_2 at different current densities, (b) the CV curves of NiCo-MnO_2 at various scan rates. (c) A plot of specific capacity against current densities for both $NiCo(OH)_2$ and NiCo-MnO_2. (d and e) Variations of specific capacity and energy efficiency of NiCo-MnO_2 and $NiCo(OH)_2$ electrodes as a function of cycle number measured at 5 A g^{-1} in 1 M KOH aqueous solution respectively.

different scan rates (Fig. 9(b)), in a potential window range of −0.1–0.4 V. The nonlinear CD curves and the CV curves show oxidation and reduction peaks at approximately 0.1 V and 0.3 V corresponding to anodic and cathodic peaks respectively. This is as a result of the reversible redox faradaic reaction of a mixed composition, containing Ni^{2+},Ni^{3+}, Co^{2+}, Co^{3+}, Mn^{2+} and Mn^{3+} [51–53] confirming the faradic property of the NiCo-MnO_2 electrode material. According to equation 2, the NiCo-MnO_2 electrode has a maximum specific capacitance of 1205.1 Fg^{-1} compared to 991.85 and 231.69 Fg^{-1} for the $NiCo(OH)_2$ and NiCoMn-TH electrodes all at a scan rate of 5 mVs^{-1} respectively. Using equation 3, the specific capacities of the NiCo-MnO_2 electrode material were calculated and plotted as a function of current densities as shown in Fig. 9(c).For further comparison, the specific capacity of the $NiCo(OH)_2$ electrode is shown in Fig. 9(c) which is smaller compared to that of the NiCo-MnO_2 electrode. In Fig. 9(c), it can be seen that the specific capacity decreases with the increasing current

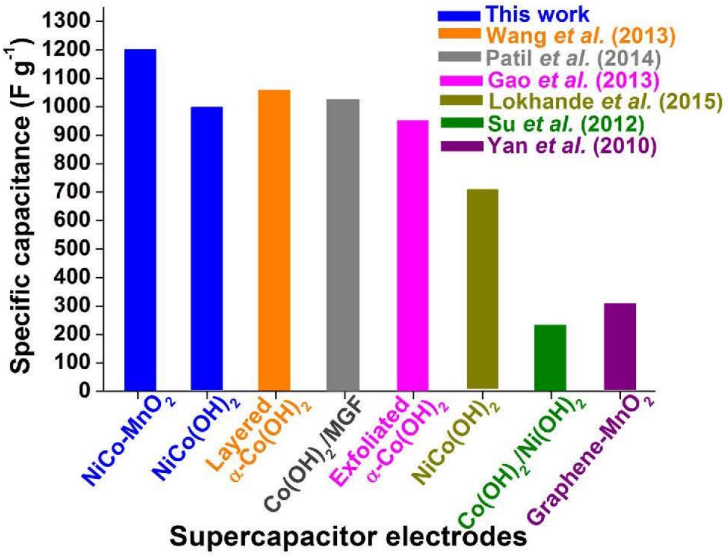

Fig. 10. A comparison of the specific capacitance of transition metal hydroxides-based electrodes and manganese oxide electrode evaluated in a three-electrode cell configuration found in this work and previously published results.

density and this could be attributed to the ion exchange mechanism [54,55]. In this case, if the current density is low, the OH^- has enough time to interact with the surface of electrode which will be intercalated/extracted into/out of the electrode when charging/discharging occurs and hence a high specific capacity/capacitance is obtained. However, if the current density is high, less charge is transferred between electrolyte and the surface of electrode and hence a low specific capacity/capacitance is obtained.

Fig. 9(d) shows the specific capacity retention and energy efficiency of a NiCo-MnO_2 electrode as a function of cycle number over 2000 charge-discharge cycles. The discharge capacity of approximately 66.3 mAh g^{-1} was retained for the half-cell electrode over 2000 charge-discharge cycles with an energy efficiency of about 93.3% compared to 48.2 % and 76.48 % respectively, for $NiCo(OH)_2$ electrode as shown in Fig. 9(e). The high capacity retention of 66.3% could be ascribed to the higher electronic conductivity, due to the low R_s value (0.98 Ω). Besides, the particular porous and stacked sheet-like structure of NiCo-MnO_2 electrode makes the material much more accessible for ion diffusion in the interlayer sheets [56]. In addition, the electrochemical reactions usually depend on the insertion-extraction of OH^- from the electrolyte, while the porous structure is beneficial for the ions to diffuse into the electrode holes [57].

Moreover, compared with the previous studies available on the electrochemical performances of transition metal hydroxides-based electrodes and some manganese oxide-based electrodes evaluated in a three-electrode cell configuration [8,58,59], the NiCo-MnO_2 electrode displays the highest specific capacitance as shown in bar chat in Fig. 10.

To further evaluate the electrical resistance of the $NiCo(OH)_2$ and NiCo-MnO_2 electrodes, the electrochemical impedance spectroscopy (EIS) at the potential of 0.0 V and the frequency range of 10 mHz–100 kHz was carried out. Fig. 11(a) shows the Nyquist impedance plot of both $NiCo(OH)_2$ and NiCo-MnO_2. It can be observed that the Nyquist plots for both electrodes have distinct semicircle in the high frequency region which is attributed to the interfacial charge transfer resistance and mass transport through the material and is denoted by R_1, R_2 and R_3 respectively. In the Nyquist plot, the intersection with the real Z′ axis is ascribed to the total resistance of the ionic resistance of electrolyte, the intrinsic resistance of the active materials and the contact resistance at the interface between the active electrode material and current collector [60], denoted as R_S. From the Fig. 11(a), the R_S values for both $NiCo(OH)_2$ and NiCo-MnO_2 electrodes are 5.0 Ω and 0.98 Ω respectively.

Interestingly, the low R_S value of the NiCo-MnO_2 electrode suggests high electrical conductivity, which results in the good capacitive performance of the electrode material. Furthermore, the Nyquist plot for NiCo-MnO_2 electrode was fitted (Fig. 11(b)) using a ZFIT fitting program v11.02 with the equivalent circuit shown as inset to Fig. 11(b). In the equivalent circuit, the R_S is connected in series with three units within the circuit, namely; the constant phase element, Q_1, which is connected in parallel with the charge transfer resistance, R_1. The transition from high-low frequency region is modeled by Warburg diffusion element and represented by W which is in series with R_1. The second and third branch composed of another constant phase elements Q_2 and Q_3 which are non-intuitive circuit elements used in place of a capacitance in the series circuit with the resistance, and are connected in parallel with single resistance, R_2 and R_3 respectively. These two final branches represent the middle and low frequency region respectively. The incorporation of constant phase elements in the circuit can be ascribed to a distribution of the relaxation times owing to inhomogeneity occurring at the electrode/electrolyte interface, as well as the porous nature of the electrode material. Fig. 11(c) shows the CV curves of NiCo-MnO_2 electrode before and after 2000 charge-discharge cycles at a scan rate of 20 mV s^{-1}. It can be seen that the current response of the NiCo-MnO_2 electrode after stability slightly decreased and this can be correlated to the increased resistance (i.e., semicircle in the high frequency region) as suggested by Fig. 11(d).

The electrochemical properties of the as-synthesized C-FP were as well investigated for its use as a negative electrode in the hybrid asymmetric NiCo-MnO_2//C-FP supercapattery. The C-FP electrode was adopted as a potential negative electrode due to its ability to function effectively in the negative potential window. Fig. S4 displays the electrochemical performance of the C-FP electrode in 1 M KOH aqueous electrolyte at different scan rates in a three-electrode configuration. The C-FP -based negative electrode displayed no noticeable peaks in its curves, with an ideal rectangular CV curves, showing the material's double-layer capacitive characteristics with good reversibility. The EIS deduction has been one of the requisite techniques in probing the electrochemical behavior of electrode materials for supercapacitor.

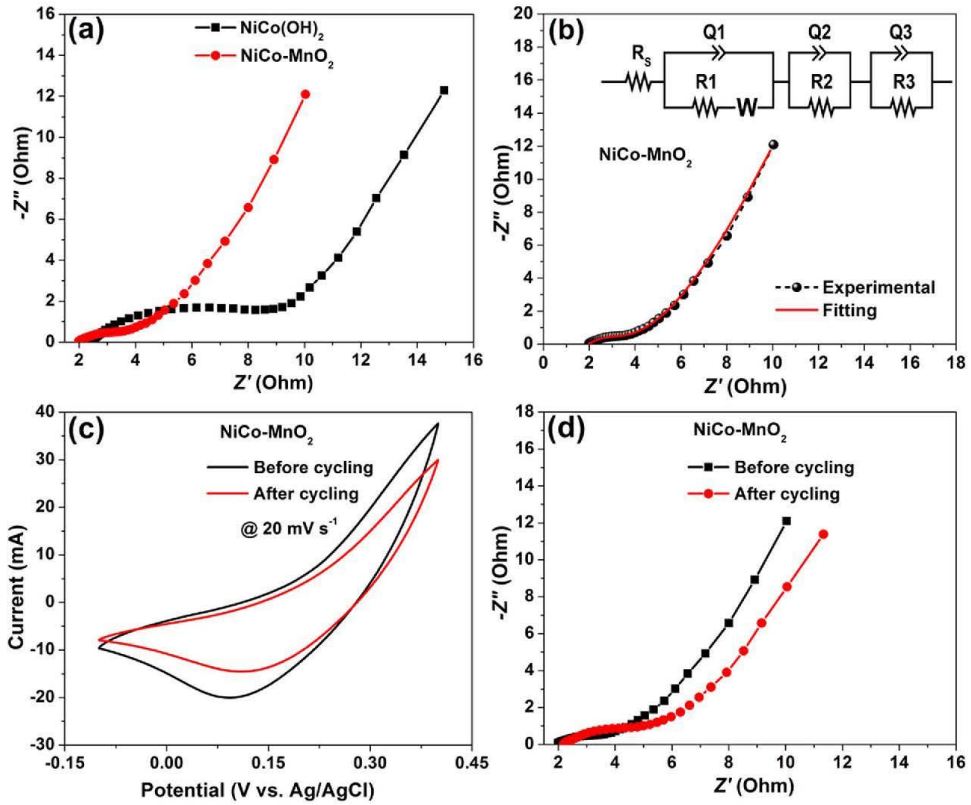

Fig. 11. (a) Nyquist impedance plot of both $NiCo(OH)_2$ and NiCo-MnO_2 electrodes. (b) The fitted Nyquist plot of NiCo-MnO_2 electrode and the equivalent circuit (insert). (c) CV curves of NiCo-MnO_2 electrode before and after 2000 charge-discharge cycles at a scan rate of 20 mVs^{-1} and (d) Nyquist plots of NiCo-MnO_2 electrode before and after 2000 charge-discharge cycles at a current density of 5 A g^{-1}.

Fig. S4 (c) in the supplementary information shows the Nyquist plot of C-FP negative electrode used for the *SC*. The inset to the figure shows a low equivalent series resistance, R_s value of 0.92 Ω which is the intercept of the plot with the real *Z'*-axis at the high frequency region.

Fig. S4 (d) displays the specific capacitance values as a function of varying gravimetric current densities. Different C_S-values of 264.1, 224.1, 173.3, 155.0, 143.3, and 133.3 F g^{-1} at current densities of 0.5, 1.0, 2.0, 3.0, 4.0 and 5.0 A g^{-1} respectively (see Fig. S4 (d)) were recorded for the C-FP negative electrode between −1.2 V and 0 V potential range.

The unique coulombic efficiency improvement (102.6%) after being subjected to cyclic stability test shown in Fig. S4 (e) could be ascribed to a good electronic conductivity and the crystalline nature of the C-FP material. This is confirmed from the observed nanostructured morphology of the C-FP from the SEM micrograph (Fig. S2 (a–b)), the sample TEM micrographs (Fig. S2 (c–d)), as well as the XRD analysis result of the carbon-based material (Fig. S3 (a)). The C-FP electrode also displayed good electrical conductivity as implied from EIS results (Fig. S4 (c)).

3.2.2. Two-electrode electrochemical measurements of the hybrid asymmetric NiCo-MnO_2//C-FP supercapattery

As a result of the remarkable electrochemical performances of both the positive and negative materials in Section 3.2.1., a hybrid asymmetric supercapattery, *SC* was fabricated and designated as NiCo-MnO_2//C-FP with mass balance ratio estimated according to equation 9, as 2.0: 3.34 corresponding to a loading mass of approximately 2.2 and 3.6 mg cm^{-2} for both NiCo-MnO_2 and C-FP selected as positive and negative electrode materials respectively, since the heightened sensitivity of a three-electrode configuration could over-project the storage capability of an electrode material for practical supercapacitor use. The NiCo-MnO_2 positive working electrode was prepared by mixing active material, carbon acetylene black as a conducting agent and polyvinylidenedifluoride (PVDF) as binder in a small amount of NMP solvent, in a weight ratio of 80:10:10 and was then coated onto the Ni foam current collector and dried overnight at 60 °C under ambient environment. The total mass loading of both NiCo-MnO_2 and C-FP active materials in the hybrid asymmetric *SC* electrodes was estimated to be approximately 5.8 mg/cm^{-2}, with the electrode thickness of about 96 μm by means of micro balance. The electrochemical testing of the asymmetric supercapacitor was carried out in two-electrode configurations using 1 M KOH aqueous electrolyte.

Fig. 12(a) displays the individual CV profiles of the ternary NiCo-MnO_2 and C-FP electrodes at a scan rate of 20 mVs^{-1} in a three electrode configurations. The C-FP electrode exhibits a quasi-rectangular CV curve, which is quite close to the electric double-layer capacitive properties. It can be observed that the fabricated hybrid asymmetry *SC* could operate in a much wider potential window ~1.5 V based on the synergy of their respective operating potential limits. Fig. 12(b) shows the associated CD profiles of NiCo-MnO_2 and C-FP at a 1 A g^{-1} current

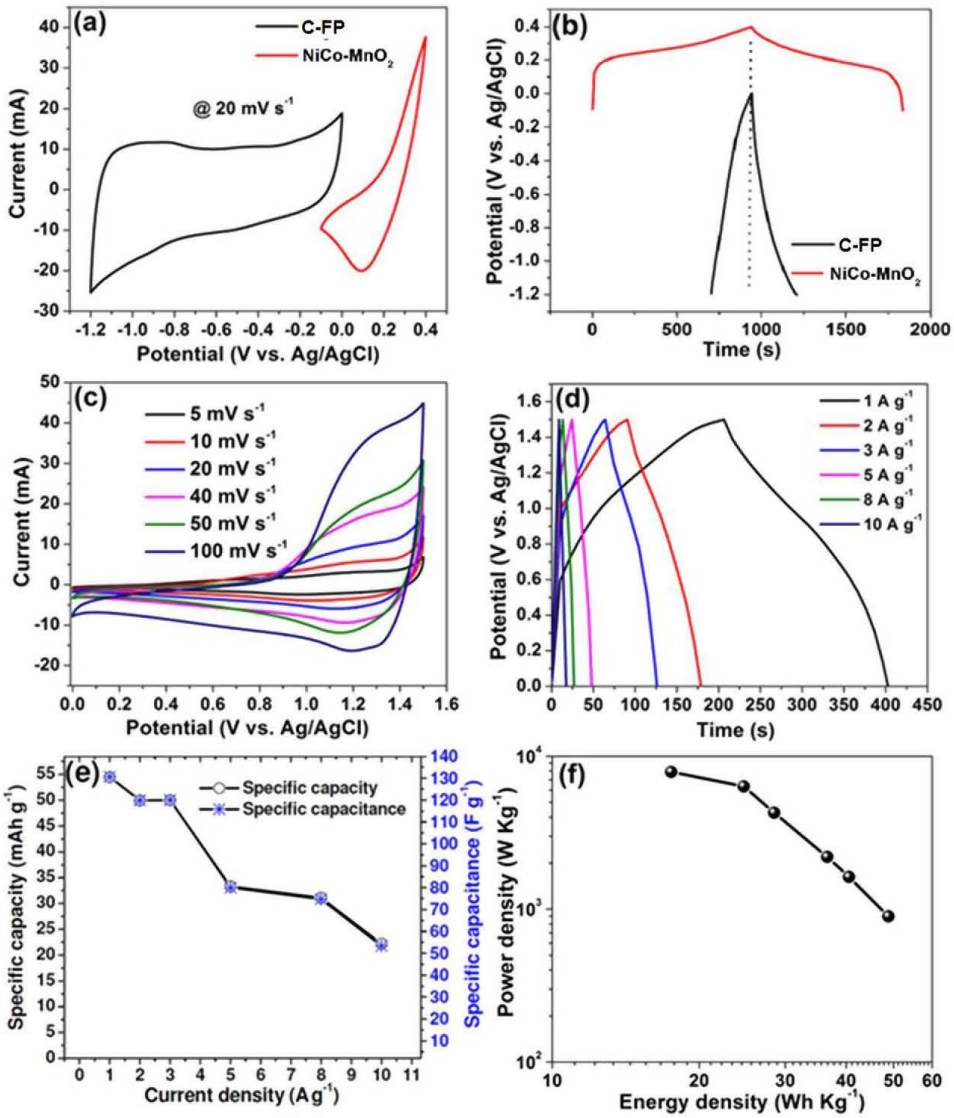

Fig. 12. (a) CV curves of NiCo-MnO_2 and C-FP at 20 mVs^{-1}, (b) CD profiles of NiCo-MnO_2 and C-FP at 1 Ag^{-1}, (c) CV curves of NiCo-MnO_2//C-FP at various scan rates, (e) specific capacity/capacitance of NiCo-MnO_2//C-FP determined at various current densities and (f) Ragone plots of the asymmetric device.

density. As expected, the CD profile for the ternary oxide is faradic in nature while the C-FP electrode displayed a much linear discharge characteristic confirming the double-layer capacitive trend.

Fig. 12(c) shows the CV curves of the hybrid NiCo-MnO_2//C-FP asymmetric cell measured at various scan rates from 5 to 100 mV s^{-1}. It can be observed that the CV curves at various scan rates displayed a mixed electric-double layer capacitance and faradic behaviors which is typical of hybrid asymmetric *SC* [29]. Fig. 12(d) displays the charge–-discharge profiles of the hybrid asymmetric *SC* at various current densities. The triangular profiles are considerably non-symmetrical, indicating the contribution from the hybrid NiCo-MnO_2//C-FP *SC* redox reaction [29,56]. This is in accordance with the CV curves of the hybrid asymmetric device (Fig. 12(c)).

Fig. 12(e) displays the hybrid asymmetric cell specific capacitance calculated using Eq. (5) and plotted as a function of current density. At a current density of 1 A g^{-1}, the hybrid cell was observed to deliver specific capacitance of 130.67 F g^{-1} corresponding to specific capacity of 54.45 mA h g^{-1}. Fig. 12(f) displays the Ragone plot for both energy density and power density as two crucial parameters to determining the electrochemical behavior of the hybrid *SC*. The corresponding energy and power densities of the device were determined according to equations 6 and 7. The energy density of the hybrid *SC* was observed to

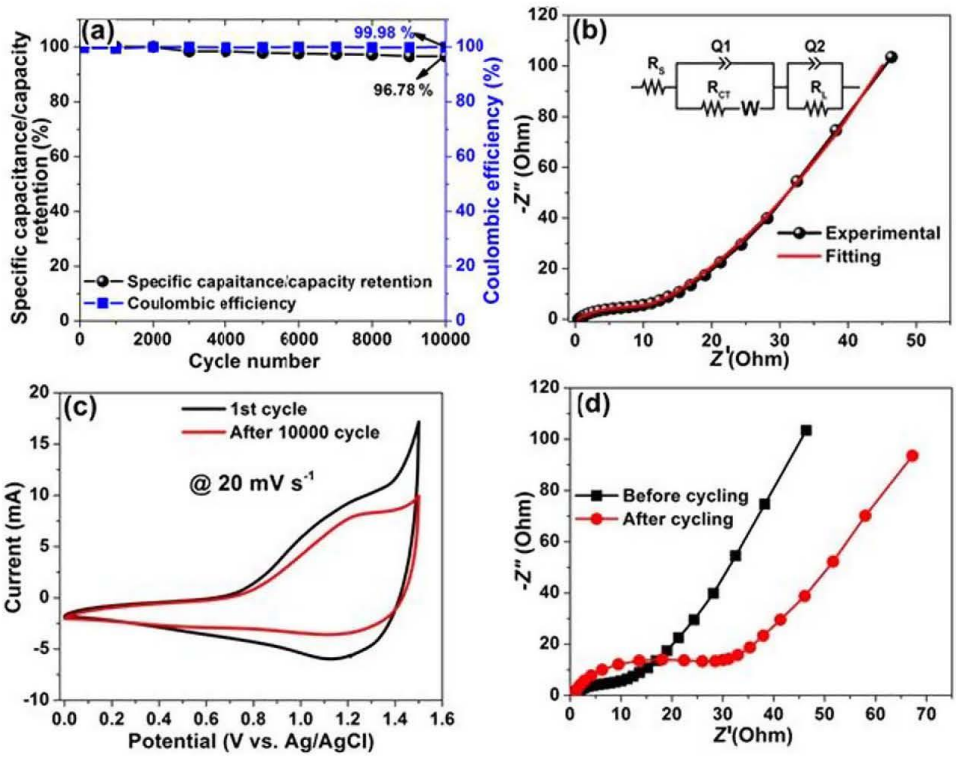

Fig. 13. (a) cyclic performance, (b) EIS plot and fitting curve, (c) CV curves before and after cycling for the hybrid asymmetric *SC* respectively and (d) EIS before and after 10,000 cycling of the hybrid NiCo-MnO_2//C-FP asymmetric device at a current density of 3 Ag^{-1}.

reach as high as 48.83 Wh kg^{-1} corresponding to a power density of 896.88 W kg^{-1} at a current density of 1 A g^{-1}. Interestingly, at a power density of 6345 W kg^{-1}, the energy density remained as high as 24.675 Wh kg^{-1} at a current density of 8 A g^{-1}. This hints that the fabricated asymmetric *SC* could dispense a high power density devoid of a considerable loss in the stored energy. This point addresses the important fact that as much as the goal in the supercapacitor research is improve its energy density to match that of batteries, this is not supposed to be done at the expense of a compromised power density of the SC.

The energy densities recorded by the hybrid *SC* showed considerable improvement when compared to other asymmetric *SCs* in aqueous electrolyte. Such as, FeOOH//MnO_2; 24 Wh kg^{-1} at power density of 3700 W kg^{-1}, at 0.5 A g^{-1}[61], MnO_x//graphene; 23.02 Wh kg^{-1} at power density of 947 W kg^{-1}, at 1 A g^{-1}[62], MnS//EDAC; 37.6 Wh kg^{-1} at power density of 181.2 W kg^{-1}, at 1 A g^{-1}[56], C7N3//AC; 34.9 Wh kg^{-}1 at power density of 875 W g^{-1}, at 1 A g^{-1}[49]; AEG//PAC; 24.6 Wh kg^{-1} at power density of 400 W kg^{-1}, at 0.5 A g^{-1}[63] and AC//RGO-CoO; 35.7 Wh kg^{-1} at power density of 225 W kg^{-1}, at 0.5 A g^{-1}[64]. A maximum constant-current discharge power density of 440.83 kW kg^{-1} was recorded as determined according to equation 8 for the hybrid asymmetric *SC*.

From Fig. 13(a), it could be observed that the hybrid *SC* records an excellent coulombic efficiency of 99.98 % (using ES1) and as well preserves 96.78% of its incipient capacitance up to a 10000 constant charge–discharge cycle at a current density of 3 A g^{-1}. Such impressive stability is mostly seen for EDLC and not supercapattery-type devices. This unique behavior is due to the mesoporous structure that could play an important role in heightening the effective electrode surface area, facilitating electrolyte permeation, and shortening the electron pathway in the active materials [56]. The mesoporous structure of the ternary NiCo-MnO_2 nanocrystal is better accessible for the reactant molecules cum cations via the interlayer space [65]. Moreover, the particular mesoporous structure could accommodate well the solvated ions (OH^-), thereby contributing to capacitance enhancement owing to compact layers of ions residing on both adjacent hole walls [56,66].

The mesoporous structure could bring about ion and electron transfer, restraining the volumetric alteration of the electrode in the charge-discharge process [49].

Electrochemical impedance spectroscopy (EIS) analysis was used to further confirm the electrochemical behavior of the device (Fig. 13(b & d)). Fig. 13(b) is a display of the Nyquist plot with a fit using the equivalent circuit inset to the Figure. The solution resistance, R_s and charge transfer resistance, R_{CT} were estimated to be 0.22 Ω and 1.94 Ω, respectively, which are significantly smaller compared with what is obtainable in the literature [56,63], indicating the desirable electrical properties of the materials used in the hybrid *SC*. The R_{CT} of NiCo-MnO_2 electrode portrays charge-transfer resistance, while the R_{CT} of C-FP is liable for the self-discharge process [13,56]. At the high frequency, the equivalent series resistance, R_s which is the intercept to the *Z'*-axis, includes the total resistance comprising the electrolyte resistance, and the resistance between the contact and the electrode materials. The calculated values of R_s, R_{CT}, and Q using ZFIT program software are summarized in Table S1 in the supplementary information.

At the mid-frequency region, a small semicircle, designated as R_{CT} is noticed owing to the charge transfer resistance and mass transport

across the framework of the material. At the low-frequency region, the curve portrays a line fairly perpendicular to the *Z*'-axis marking an ideal behavior of the hybrid *SC*. The device nevertheless, shows a divergence from this ideal behavior owing to a resistive element, R_L (leakage current resistance) associated and in parallel with constant phase element, Q_2.

The deviation from the perfect line perpendicular to the *Z*'-axis is as a result of a diffusion process which occurs at the electrode-electrolyte interface, mainly indicated by the existence of a Warburg impedance element, *W* [67]. By standard, the phase angle of the Warburg impedance is −45°, being a representation of a vector of equal real and imaginary amplitudes. In practice, a deviation from that phase angle is noticed and is attributed to porous nature of the electrode materials with different pore dimensions which play an important role in the impedance analysis [68]. The transition from high to low frequency is represented by Warburg element (*W*) which is in series with R_{ct}. In principle, an ideal cell will give a vertical line parallel to the y-axis at a low frequency which is represented by constant phase element, Q_1 in the circuit diagram.

Fig. 13(c) shows the CV curves of the hybrid *SC* before and after 10000 cycling at a scan rate of 20 mVs^{-1}. It can be seen that even after a very large number of cycles, the current response of the NiCo-MnO_2//C-FP hybrid *SC* after stability slightly decreased while the shape is still preserved which shows the relative stability of cell for potential practical application. Fig. 13(d) shows the Nyquist plot of the device before and after 10,000 cycles. After cycling, the diffusion path length is observed to further deviate from the ideal vertical nature which can be ascribed to the repeated cycling effects such as polarization and less utilization or insufficient active material during redox reaction, probably owing to the high current density [11].

Fig. S4 (f) displays the self-discharge (SD) profile of the hybrid NiCo-MnO_2//C-FP symmetric *SC* carried out at room temperature in 1 M KOH electrolyte. The cell was charged to its peak voltage of 1.50 V at 0.5 A g^{-1} and then held at that voltage for about 1 h and later kept at open circuit potential to undergo self-discharge for more than 50 h with the *SC*'s terminals' voltage being monitored. The *SC* was observed to maintain a substantial voltage of 1.11 V (over 74% of its operating voltage) which indicates a good practical application of the hybrid *SC*. The sudden fall of the hybrid *SC* voltage at the incipient stage of the self-discharge is perhaps as a result of the decomposition of water used as the solvent, as previously explained [69,70]. Concisely, when the cell is fully charged, the solvent could be abridged on the cathode, a reduction that could continue even after current cut-off, resulting in a sharp decrease in the cathode potential [63]. This procedure is influenced by the surface property of the electrode and is not diffusion controlled neither due to current leakage. Accordingly, any investigation of the self-discharge mechanism will exclude the potential drop [63,69].

4. Conclusion

Mixed transition meta hydroxides $NiCo(OH)_2$, NiCoMn-triple hydroxide (NiCoMn-TH) and a ternary NiCo-MnO_2 electrode materials were successfully synthesized by force-driven hydrolysis of hydrated nitrates of nickel, cobalt and manganese salt at a low temperature while C-FP electrode was synthesized via a complete dissolution of iron (III) nitrate and PANI in ethanol. The characterization of the samples confirmed that the as-prepared mixed hydroxides electrode materials have agglomerated flake-like particles which exhibited a small specific surface area compared to the NiCo-MnO_2 with porous and stacked sheet-like morphology. It was also confirmed that the prepared samples are crystalline, and composed of Ni, Co, O (or O−H bond in $NiCo(OH)_2$ sample) and Mn in NiCo-MnO_2 sample with Ni, Co and Mn existing in different oxidation states. The C-FP on the other hand, is composed of nano grains with some level of crystallinity. The electrochemical performance of the electrode materials evaluated in a three-electrode cell configuration using 1 M KOH electrolyte showed a significant improvement on specific capacity of 132.1 mAh g^{-1} for NiCo-MnO_2 compared to 110.3 and 64.36 mAh g^{-1} for $NiCo(OH)_2$ and the unstable NiCoMn-TH at a current density of 0.5 A g^{-1} respectively. The C-FP electrode showed a good and consistent capacitive performance with relatively high specific capacitance of 264.17 Fg^{-1} at a current density of 0.5 A g^{-1} in KOH aqueous electrolyte. A cost-effective high-performance hybrid NiCo-MnO_2//C-FP supercapattery in 1 M KOH electrolyte delivered a high energy density of 48.83 Wh kg^{-1} with a corresponding high power density of 896.88 W kg^{-1} as well as excellent stability with 97.78% capacity retention up to 10,000 cycles similar to what is observed in classic EDLC devices. Even at high current density of 8 A g^{-1} the device maintained a high energy density of 25 Wh kg^{-1} with corresponding power density of 6344 W kg^{-1} which shows that these are excellent materials for supercapacitor applications.

Acknowledgements

This work is based on the research supported by the South African Research Chairs Initiative of the Department of Science and Technology and National Research Foundation of South Africa (Grant No. 61056). Any opinion, finding, and conclusion expressed in this material are that of the author(s), and the NRF does not accept any liability in this regard. K. O. Oyedotun acknowledges financial support from the University of Pretoria and National Research Foundation (NRF) for his PhD studies.

Appendix A. Supplementary data

Supplementary data associated with this article can be found, in the online version, at http://dx.doi.org/10.1016/j.cej.2017.10.169.

References

[1] R.R. Salunkhe, J. Lin, V. Malgras, S.X. Dou, J.H. Kim, Y. Yamauchi, Large-scale synthesis of coaxial carbon nanotube/Ni(OH)2 composites for asymmetric supercapacitor application, Nano Energy 11 (2015) 211–218, http://dx.doi.org/10.1016/j.nanoen.2014.09.030.
[2] R.R. Salunkhe, C. Young, J. Tang, T. Takei, Y. Ide, N. Kobayashi, Y. Yamauchi, A high-performance supercapacitor cell based on ZIF-8-derived nanoporous carbon using an organic electrolyte, Chem. Commun. 52 (2016) 4764–4767, http://dx.doi.org/10.1039/C6CC00413J.
[3] N.L. Torad, R.R. Salunkhe, Y. Li, H. Hamoudi, M. Imura, Y. Sakka, C.C. Hu, Y. Yamauchi, Electric double-layer capacitors based on highly graphitized nanoporous carbons derived from ZIF-67, Chem. A Eur. J. 20 (2014) 7895–7900, http://dx.doi.org/10.1002/chem.201400089.
[4] R.R. Salunkhe, Y.V. Kaneti, J. Kim, J.H. Kim, Y. Yamauchi, Nanoarchitectures for Metal-Organic Framework-Derived Nanoporous Carbons toward Supercapacitor Applications, Acc. Chem. Res. 49 (2016) 2796–2806, http://dx.doi.org/10.1021/acs.accounts.6b00460.
[5] M. Armand, J.-M. Tarascon, Building better batteries, Nature 451 (2008) 652–657, http://dx.doi.org/10.1038/451652a.
[6] F. Zhang, T. Zhang, X. Yang, L. Zhang, K. Leng, Y. Huang, Y. Chen, A high-performance supercapacitor-battery hybrid energy storage device based on graphene-enhanced electrode materials with ultrahigh energy density, Energy Environ. Sci. 6 (2013) 1623, http://dx.doi.org/10.1039/c3ee40509e.
[7] J. Xu, S. Dou, H. Liu, L. Dai, Cathode materials for next generation lithium ion batteries 2 (4) (2013) 439–442, http://dx.doi.org/10.1016/j.nanoen.2013.05.013.
[8] P.E. Lokhande, Synthesis and characterization of Ni.Co(OH) 2 material for supercapacitor application, Int. Adv Res. J. Sci Eng. Technol. 2 (9) (2015) 10–13, http://dx.doi.org/10.17148/IARJSET.2015.2903.
[9] X. Wang, X. Fan, G. Li, M. Li, X. Xiao, A. Yu, Z. Chen, Composites of MnO2 nanocrystals and partially graphitized hierarchically porous carbon spheres with improved rate capability for high-performance supercapacitors, Carbon N. Y. 93 (2015) 258–265, http://dx.doi.org/10.1016/j.carbon.2015.05.072.
[10] H.D. Abruna, Y. Kiya, J.C. Henderson, Batteries and electrochemical capacitors, Phys. Today. 61 (12) (2008) 43–47, http://dx.doi.org/10.1063/1.3047681.
[11] K.O. Oyedotun, M.J. Madito, A. Bello, D.Y. Momodu, A.A. Mirghni, N. Manyala, Investigation of graphene oxide nanogel and carbon nanorods as electrode for electrochemical supercapacitor, Electrochim. Acta. 245 (2017) 268–278, http://dx.doi.org/10.1016/j.electacta.2017.05.150.
[12] P.U. Asogwa, S.C. Ezugwu, F.I. Ezema, Variation of optical and solid state properties with post deposition annealing in PVA-Capped MnO_2 thin films, Superf. Y Vacío. 23 (2010) 18–22 http://smcsyv.fis.cinvestav.mx/supyvac/23_1/SV2311810.
[13] P. Simon, Y. Gogotsi, Materials for electrochemical capacitors, Nat. Mater. 7 (2008)

845–854, http://dx.doi.org/10.1038/nmat2297.
[14] I. Hadjipaschalis, A. Poullikkas, V. Efthimiou, Overview of current and future energy storage technologies for electric power applications, Renew. Sustain. Energy Rev. 13 (2009) 1513–1522, http://dx.doi.org/10.1016/j.rser.2008.09.028.
[15] J.P. Cheng, J. Zhang, F. Liu, Recent development of metal hydroxides as electrode material of electrochemical capacitors, RSC Adv. 4 (2014) 38893–38917, http://dx.doi.org/10.1039/C4RA06738J.
[16] W. Zhang, F. Liu, Q. Li, Q. Shou, J. Cheng, L. Zhang, B.J. Nelson, X. Zhang, Transition metal oxide and graphene nanocomposites for high-performance electrochemical capacitors, Phys. Chem. Chem. Phys. 14 (2012) 16331–16337, http://dx.doi.org/10.1039/C2CP43673F.
[17] G. Wang, L. Zhang, J. Zhang, A review of electrode materials for electrochemical supercapacitors, Chem. Soc. Rev. 41 (2012) 797–828, http://dx.doi.org/10.1039/C1cs15060j.
[18] H. Chen, L. Hu, Y. Yan, R. Che, M. Chen, L. Wu, One-step fabrication of ultrathin porous nickel hydroxide-manganese dioxide hybrid nanosheets for supercapacitor electrodes with excellent capacitive performance, Adv. Energy Mater. 3 (2013) 1636–1646, http://dx.doi.org/10.1002/aenm.201300580.
[19] L. Feng, Y. Zhu, H. Ding, C. Ni, Recent progress in nickel based materials for high performance pseudocapacitor electrodes, J. Power Sources. 267 (2014) 430–444, http://dx.doi.org/10.1016/j.jpowsour.2014.05.092.
[20] T. Deng, W. Zhang, O. Arcelus, J.-G. Kim, J. Carrasco, S.J. Yoo, W. Zheng, J. Wang, H. Tian, H. Zhang, X. Cui, T. Rojo, Atomic-level energy storage mechanism of cobalt hydroxide electrode for pseudocapacitors, Nat. Commun. 8 (2017) 15194, http://dx.doi.org/10.1038/ncomms15194.
[21] Z. Pan, Y. Qiu, J. Yang, F. Ye, Y. Xu, X. Zhang, M. Liu, Y. Zhang, Ultra-endurance flexible all-solid-state asymmetric supercapacitors based on three-dimensionally coated MnOx nanosheets on nanoporous current collectors, Nano Energy 26 (2016) 610–619, http://dx.doi.org/10.1016/j.nanoen.2016.05.053.
[22] H.X. Wang, W. Zhang, N.E. Drewett, H.B. Zhang, K.K. Huang, S.H. Feng, X.L. Li, J. Kim, S. Yoo, T. Deng, S.J. Liu, D. Wang, W.T. Zheng, Unifying miscellaneous performance criteria for a prototype supercapacitor via Co(OH)2 active material and current collector interactions, J. Microsc. 267 (2017) 34–48, http://dx.doi.org/10.1111/jmi.12545.
[23] C. Zhang, K.B. Hatzell, M. Boota, B. Dyatkin, M. Beidaghi, D. Long, W. Qiao, E.C. Kumbur, Y. Gogotsi, Highly porous carbon spheres for electrochemical capacitors and capacitive flowable suspension electrodes, Carbon N. Y. 77 (2014) 155–164, http://dx.doi.org/10.1016/j.carbon.2014.05.017.
[24] G. Godillot, L. Guerlou-Demourgues, P.-L. Taberna, P. Simon, C. Delmas, Original conductive nano-Co3O4 investigated as electrode material for hybrid supercapacitors, Electrochem. Solid-State Lett. 14 (2011) A139, http://dx.doi.org/10.1149/1.3609259.
[25] B. Akinwolemiwa, C. Peng, G.Z. Chen, Redox electrolytes in supercapacitors, J. Electrochem. Soc. 162 (2015) A5054–A5059, http://dx.doi.org/10.1149/2.0111505jes.
[26] B.E. Conway, Electrochemical supercapacitors: scientific fundamentals and technological applications, Springer Science & Business Media (2013), http://dx.doi.org/10.1007/978-1-4757-3058-6.
[27] A. Burke, Ultracapacitors: why, how, and where is the technology, J. Power Sour. 91 (2000) 37–50, http://dx.doi.org/10.1016/S0378-7753(00)00485-7.
[28] J. Zhang, J.P. Cheng, M. Li, L. Liu, F. Liu, X.B. Zhang, Flower-like nickel-cobalt binary hydroxides with high specific capacitance: tuning the composition and asymmetric capacitor application, J. Electroanal. Chem. 743 (2015) 38–45, http://dx.doi.org/10.1016/j.jelechem.2015.02.021.
[29] T.M. Masikhwa, M.J. Madito, D.Y. Momodu, J.K. Dangbegnon, O. Guellati, A. Harat, M. Guerioune, F. Barzegar, N. Manyala, High performance asymmetric supercapacitor based on CoAl-LDH/GF and activated carbon from expanded graphite, RSC Adv. 6 (2016) 46723–46732, http://dx.doi.org/10.1039/C6RA07419G.
[30] A. Szytula, A. Murasik, M. Balanda, Neutron diffraction study of Ni(OH)2, Phys. Status Solidi. 43 (1971) 125–128, http://dx.doi.org/10.1002/pssb.2220430113.
[31] T. Takada, Y. Bando, M. Kiyama, H. Miyamoto, T. Sato, The magnetic property of β-Co(OH) $_2$, 2726 2726, J. Phys. Soc. Jpn. 21 (1966), http://dx.doi.org/10.1143/JPSJ.21.2726.
[32] C. Zhao, X. Wang, S. Wang, Y. Wang, Y. Zhao, W. Zheng, Synthesis of Co(OH) 2/graphene/Ni foam nano-electrodes with excellent pseudocapacitive behavior and high cycling stability for supercapacitors, Int. J. Hydrogen Energy 37 (2012) 11846–11852, http://dx.doi.org/10.1016/j.ijhydene.2012.05.138.
[33] W. Zhou, X. Cao, Z. Zeng, W. Shi, Y. Zhu, Q. Yan, H. Liu, J. Wang, H. Zhang, One-step synthesis of Ni $_3$ $_S$ 2 nanorod@Ni(OH$_)$ 2 nanosheet core–shell nanostructures on a three-dimensional graphene network for high-performance supercapacitors, Energy Environ. Sci. 6 (2013) 2216–2221, http://dx.doi.org/10.1039/C3EE40155C.
[34] S.R. Shieh, T.S. Duffy, Raman spectroscopy of Co (OH) 2 at high pressures: Implications for amorphization and hydrogen repulsion, Phys. Rev. B 66 (2002) 134301, http://dx.doi.org/10.1103/PhysRevB.66.134301.
[35] H.D. Lutz, H. Möller, M. Schmidt, Lattice vibration spectra. Part LXXXII. Brucite-type hydroxides M(OH)2 (M = Ca, Mn Co, Fe, Cd) — IR and Raman spectra, neutron diffraction of Fe(OH)2, J. Mol. Struct. 328 (1994) 121–132, http://dx.doi.org/10.1016/0022-2860(94)08355-X.
[36] J. Yang, H. Liu, W.N. Martens, R.L. Frost, Synthesis and characterization of cobalt hydroxide, cobalt oxyhydroxide, and cobalt oxide nanodiscs, J. Phys. Chem. C 114 (2010) 111–119, http://dx.doi.org/10.1021/jp908548f.
[37] T. Pauporté, L. Mendoza, M. Cassir, M.C. Bernard, J. Chivot, Direct low-temperature deposition of crystallized CoOOH films by potentiostatic electrolysis, J. Electrochem. Soc. 152 (2005) C49, http://dx.doi.org/10.1149/1.1842044.
[38] H. Xia, Y. Wang, J. Lin, L. Lu, Hydrothermal synthesis of MnO_2 /CNT nanocomposite with a CNT core/porous MnO_2 sheath hierarchy architecture for supercapacitors, Nanoscale Res. Lett. 7 (1) (2012) 33, http://dx.doi.org/10.1186/1556-276X-7-33.
[39] A. Ogata, S. Komaba, R. Baddour-Hadjean, J.-P. Pereira-Ramos, N. Kumagai, Doping effects on structure and electrode performance of K-birnessite-type manganese dioxides for rechargeable lithium battery, Electrochim. Acta. 53 (2008) 3084–3093, http://dx.doi.org/10.1016/j.electacta.2007.11.038.
[40] Y. Ren, N. Yan, J. Feng, J. Ma, Q. Wen, N. Li, Q. Dong, Adsorption mechanism of copper and lead ions onto graphene nanosheet/δ-MnO2, Mater. Chem. Phys. 136 (2012) 538–544, http://dx.doi.org/10.1016/j.matchemphys.2012.07.023.
[41] Y. Zhao, H. Ma, S. Huang, X. Zhang, M. Xia, Y. Tang, Z.-F. Ma, Monolayer nickel cobalt hydroxyl carbonate for high performance all-solid-state asymmetric supercapacitors, ACS Appl. Mater. Interfaces 8 (2016) 22997–23005, http://dx.doi.org/10.1021/acsami.6b05496.
[42] R. Li, Z. Hu, X. Shao, P. Cheng, S. Li, W. Yu, W. Lin, D. Yuan, Large scale synthesis of nico layered double hydroxides for superior asymmetric electrochemical capacitor, Sci. Rep. 6 (2016) 18737, http://dx.doi.org/10.1038/srep18737.
[43] J. Pérez-Ramírez, G. Mul, F. Kapteijn, J.A. Moulijn, In situ investigation of the thermal decomposition of Co–Al hydrotalcite in different atmospheres, J. Mater. Chem. 11 (2001) 821–830, http://dx.doi.org/10.1039/b009320n.
[44] P.R. Jothi, K. Shanthi, R.R. Salunkhe, M. Pramanik, V. Malgras, S.M. Alshehri, Y. Yamauchi, Synthesis and characterization of α-NiMoO $_4$ nanorods for supercapacitor application, Eur. J. Inorg. Chem. 2015 (2015) 3694–3699, http://dx.doi.org/10.1002/ejic.201500410.
[45] Y. Gao, L. Mi, W. Wei, S. Cui, Z. Zheng, H. Hou, W. Chen, Double metal ions synergistic effect in hierarchical multiple sulfide microflowers for enhanced supercapacitor performance 7 (7) (2015) 4311–4319, http://dx.doi.org/10.1021/am508747m.
[46] X. Lu, X. Huang, S. Xie, T. Zhai, C. Wang, P. Zhang, M. Yu, W. Li, C. Liang, Y. Tong, Controllable synthesis of porous nickel–cobalt oxide nanosheets for supercapacitors, J. Mater. Chem. 22 (2012) 13357, http://dx.doi.org/10.1039/c2jm30927k.
[47] H. Cheng, Y.-Z. Su, P.-Y. Kuang, G.-F. Chen, Z.-Q. Liu, Hierarchical NiCo $_2$ $_O$ 4 nanosheet-decorated carbon nanotubes towards highly efficient electrocatalyst for water oxidation, J. Mater. Chem. A. (2015) 1–8, http://dx.doi.org/10.1039/C5TA03985A.
[48] S. Hu, Y. Li, F. Lai, X. Zhang, Q. Li, Y. Huang, X. Yuan, J. Chen, H. Wang, Enhanced electrochemical performance of LiMn $_2$ O $_4$ cathode with a Li $_{0.34}$ La $_{0.51}$ TiO $_3$ -coated layer, RSC Adv. 5 (2015) 17592–17600, http://dx.doi.org/10.1039/C4RA15374J.
[49] J. Zhang, F. Liu, J.P. Cheng, X.B. Zhang, Binary Nickel-Cobalt Oxides Electrode Materials for High-Performance Supercapacitors: Influence of its Composition and Porous Nature, ACS Appl. Mater. Interfaces 7 (2015) 17630–17640, http://dx.doi.org/10.1021/acsami.5b04463.
[50] M. Li, J.P. Cheng, J.H. Fang, Y. Yang, F. Liu, X.B. Zhang, NiAl-layered double hydroxide/reduced graphene oxide composite: microwave-assisted synthesis and supercapacitive properties, Electrochim. Acta. 134 (2014) 309–318, http://dx.doi.org/10.1016/j.electacta.2014.04.141.
[51] D. Cai, B. Liu, D. Wang, Y. Liu, L. Wang, H. Li, Y. Wang, C. Wang, Q. Li, T. Wang, Facile hydrothermal synthesis of hierarchical ultrathin mesoporous NiMoO4 nanosheets for high performance supercapacitors, Electrochim. Acta. 115 (2014) 358–363, http://dx.doi.org/10.1016/j.electacta.2013.10.154.
[52] M.-C. Liu, L. Kang, L.-B. Kong, C. Lu, X.-J. Ma, X.-M. Li, Y.C. Luo, Facile synthesis of $NiMoO_4$ xH 2 O nanorods as a positive electrode material for supercapacitors, RSC Adv. 3 (18) (2013) 6472–6478, http://dx.doi.org/10.1039/c3ra22993a.
[53] J.F. Marco, J.R. Gancedo, M. Gracia, J.L. Gautier, E.I. Ríos, H.M. Palmer, C. Greaves, F.J. Berry, Cation distribution and magnetic structure of the ferrimagnetic spinel NiCo2O4, J. Mater. Chem. 11 (2001) 3087–3093, http://dx.doi.org/10.1039/B103135J.
[54] S. Xiong, C. Yuan, X. Zhang, B. Xi, Y. Qian, Controllable synthesis of mesoporous Co3O4 nanostructures with tunable morphology for application in supercapacitors, Chem. A Eur. J. 15 (2009) 5320–5326, http://dx.doi.org/10.1002/chem.200802671.
[55] C. Yuan, X. Zhang, L. Su, B. Gao, L. Shen, Facile synthesis and self-assembly of hierarchical porous NiO nano/micro spherical superstructures for high performance supercapacitors, J. Mater. Chem. 19 (2009) 5772–5777, http://dx.doi.org/10.1039/B902221J.
[56] T. Chen, Y. Tang, Y. Qiao, Z. Liu, W. Guo, J. Song, S. Mu, S. Yu, Y. Zhao, F. Gao, All-solid-state high performance asymmetric supercapacitors based on novel MnS nanocrystal and activated carbon materials, Sci. Rep. 6 (2016) 23289, http://dx.doi.org/10.1038/srep23289.
[57] Y. Zhang, M. Ma, J. Yang, H. Su, W. Huang, X. Dong, Selective synthesis of hierarchical mesoporous spinel NiCo(2)O(4) for high-performance supercapacitors, Nanoscale 6 (2014) 4303–4308, http://dx.doi.org/10.1039/c3nr06564b.
[58] L. Wang, Z.H. Dong, Z.G. Wang, F.X. Zhang, J. Jin, Layered α-Co(OH) $_2$ nanocones as electrode materials for pseudocapacitors: understanding the effect of interlayer space on electrochemical activity, Adv. Funct. Mater. 23 (2013) 2758–2764, http://dx.doi.org/10.1002/adfm.201202786.
[59] U.M. Patil, M.S. Nam, J.S. Sohn, S.B. Kulkarni, R. Shin, S. Kang, S. Lee, J.H. Kim, S.C. Jun, Controlled electrochemical growth of Co(OH)$_2$ flakes on 3D multilayered graphene foam for high performance supercapacitors, J. Mater. Chem. A 2 (2014) 19075–19083, http://dx.doi.org/10.1039/C4TA03953J.
[60] X.Y. Liu, Y.Q. Zhang, X.H. Xia, S.J. Shi, Y. Lu, X.L. Wang, C.D. Gu, J.P. Tu, Self-assembled porous $NiCo_2O_4$ hetero-structure array for electrochemical capacitor, J.

Power Sour. 239 (2013) 157–163, http://dx.doi.org/10.1016/j.jpowsour.2013.03.106.
[61] W.H. Jin, G.T. Cao, J.Y. Sun, Hybrid supercapacitor based on MnO_2 and columned FeOOH using Li_2SO_4 electrolyte solution, J. Power Sour. 175 (2008) 686–691, http://dx.doi.org/10.1016/j.jpowsour.2007.08.115.
[62] J. Yang, G. Li, Z. Pan, M. Liu, Y. Hou, Y. Xu, H. Deng, L. Sheng, X. Zhao, Y. Qiu, Y. Zhang, All-solid-state high-energy asymmetric supercapacitors enabled by three-dimensional mixed-valent MnOx nanospike and graphene electrodes, ACS Appl. Mater. Interfaces 7 (2015) 22172–22180, http://dx.doi.org/10.1021/acsami.5b07849.
[63] F. Barzegar, A. Bello, J.K. Dangbegnon, N. Manyala, X. Xia, Asymmetric carbon supercapacitor with activated expanded graphite as cathode and Pinecone tree activated carbon as anode materials, Appl. Energy. (2016), http://dx.doi.org/10.1016/j.apenergy.2017.05.110.
[64] L.J. Xie, J.F. Wu, C.M. Chen, C.M. Zhang, L. Wan, J.L. Wang, Q.Q. Kong, C.X. Lv, K.X. Li, G.H. Sun, A novel asymmetric supercapacitor with an activated carbon cathode and a reduced graphene oxide-cobalt oxide nanocomposite anode, J. Power Sources. 242 (2013) 148–156, http://dx.doi.org/10.1016/j.jpowsour.2013.05.081.
[65] A. Bergmann, I. Zaharieva, H. Dau, P. Strasser, Electrochemical water splitting by layered and 3D cross-linked manganese oxides: correlating structural motifs and catalytic activity, Energy Environ. Sci. 6 (2013) 2745, http://dx.doi.org/10.1039/c3ee41194j.
[66] E. Raymundo-Pinero, P. Azais, T. Cacciaguerra, D. Cazorla-Amorós, A. Linares-Solano, F. Béguin, KOH and NaOH activation mechanisms of multiwalled carbon nanotubes with different structural organisation, Carbon 43 (4) (2005) 786–795, http://dx.doi.org/10.1016/j.carbon.2004.11.005.
[67] H. Li, J. Wang, Q. Chu, Z. Wang, F. Zhang, S. Wang, Theoretical and experimental specific capacitance of polyaniline in sulfuric acid, J. Power Sour. 190 (2009) 578–586, http://dx.doi.org/10.1016/j.jpowsour.2009.01.052.
[68] H. Song, H. Song, Y. Jung, Y. Jung, K. Lee, K. Lee, L.H. Dao, L.H. Dao, Electrochemical impedance spectroscopy of porous electrodes: the effect of pore size distribution, Electrochim. Acta. 44 (1999) 3513–3519, http://dx.doi.org/10.1016/S0013-4686(99)00121-8.
[69] F. Barzegar, A.A. Khaleed, F.U. Ugbo, K.O. Oyeniran, D.Y. Momodu, A. Bello, J.K. Dangbegnon, N. Manyala, Cycling and floating performance of symmetric supercapacitor derived from coconut shell biomass, AIP Adv. 6 (11) (2016), http://dx.doi.org/10.1063/1.4967348.
[70] L. Chen, H. Bai, Z. Huang, L. Li, Mechanism investigation and suppression of self-discharge in active electrolyte enhanced supercapacitors, Energy Environ. Sci. 7 (2014) 1750–1759, http://dx.doi.org/10.1039/C4EE00002A.

SUPPLEMENTARY INFORMATION

Synthesis of ternary NiCo-MnO_2 nanocomposite and its application as a novel high energy supercapattery device

Kabir O. Oyedotun, Moshawe J. Madito, Damilola Y. Momodu, Abdulmajid A. Mirghni, Tshifhiwa M. Masikhwa and Ncholu Manyala*

Department of Physics, Institute of Applied Materials, SARCHI Chair in Carbon Technology and Materials, University of Pretoria, Pretoria 0028, South Africa.

*Corresponding author's email: ncholu.manyala@up.ac.za, Tel.: + (27)12 420 3549

EXPERIMENTAL

Preparation of Polyaniline (PANI)

0.2 M of aniline hydrochloride (C_6H_8ClN) (2.59 g aniline hydrochloride in 50 ml deionized water) was added to 0.25 M of ammonium peroxydisulfate ($(NH_4)_2S_2O_8$) (5.71 g ammonium peroxysulfate in 50 ml deionized water. The mixture was stirred for 10 minutes, and then left to stand overnight for polymerization. The supernatant was decanted away and the recovered precipitate was washed several times with deionized. The resulting sample was dried overnight in an electric oven at 60 °C under ambient condition.

Preparation of carbonized iron cations adsorbed onto PANI (C-FP)

0.2 g iron (III) nitrate nonahydrate, 0.0125 g of polyaniline (PANI) and 0.026 g each of carbon acetylene black (CB) and PVDF were completely dissolved in ethanol (50 mL, 99.9 %) whilst magnetically stirring for 5 minutes. The precursors' masses were carefully selected to ensure an approximate weight ratio of 80:10:10 for iron (III) nitrate salt and PANI, CB and PVDF respectively. After 5 minutes of stirring, the resulting mixture was sonicated for several hours until slurry. The recovered slurry was then coated onto cut-to-size nickel foam (1 cm × 1 cm) which was transferred into a chemical vapour deposition

(CVD) system under N_2 atmosphere at 850 °C for 2 h to obtain iron cations adsorbed onto the PANI film (C-FP) directly grown onto the nickel foam.

The loading mass of the prepared the negative electrode was estimated to be approximately 4.0 mg cm^{-2} for the active material. The electrochemical impedance spectroscopy (EIS) of the samples was conducted in an open-circuit potential and in a range of 10 mHz to 100 kHz frequency at 0.0V potential.

The columbic efficiency, C_E as well as the specific capacitance, C_s (Fg^{-1}) (calculated according to equation 5) over a potential, V (V), of the nickel foam-supported negative electrode was estimated using the following relations:

$$C_E = \frac{t_D}{t_c} \times 100\% \qquad \text{ES1}$$

where C_s (F g^{-1}), I (A), Δt (s), ΔV (V), m (g), t_c and t_D, and C_E (%) are the specific capacitance, discharge current, discharge time, discharge potential window, active material mass, the times for charging and discharging with the same current, as well as the columbic efficiency respectively.

The average crystallite size of the as-synthesized samples was determined by the X-ray line broadening method via the Scherrer equation [1,7]:

$$L = \frac{k\lambda}{\beta Cos\theta} \qquad \text{ES2}$$

Where λ is the wavelength of the radiation used, CoKα in this case, k is the Scherrer constant, β $(radian)$ is the full width at half maximum (FWHM) intensity of the diffraction peak for which the size is to be determined, θ is the diffraction angle of the particular peak, and L is the crystallite size.

RESULTS

Morphological, structural and elemental analyses

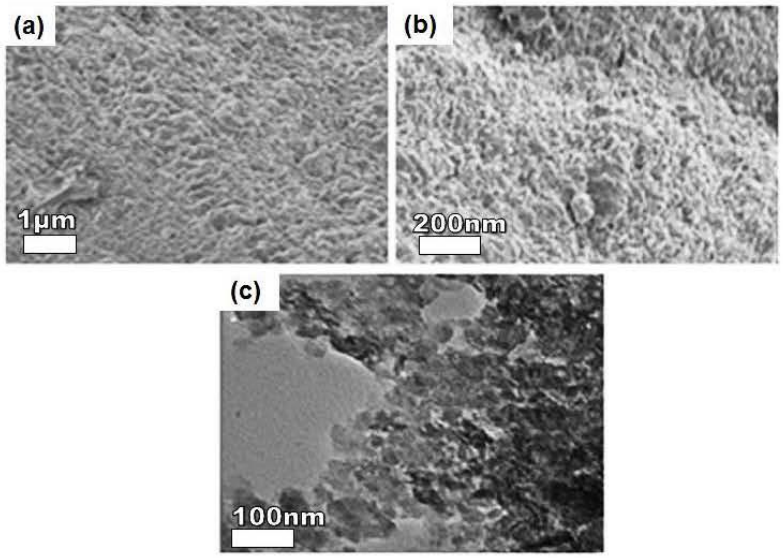

Fig. S1. (a) and (b) SEM images of the NiCoMn-TH at low and high magnifications respectively. (c) TEM image of the NiCoMn-TH.

Fig. S1 and S2 display the electron microscopy images at low and high magnifications of the NiCoMn-TH and as-synthesized C-FP electrodes respectively.

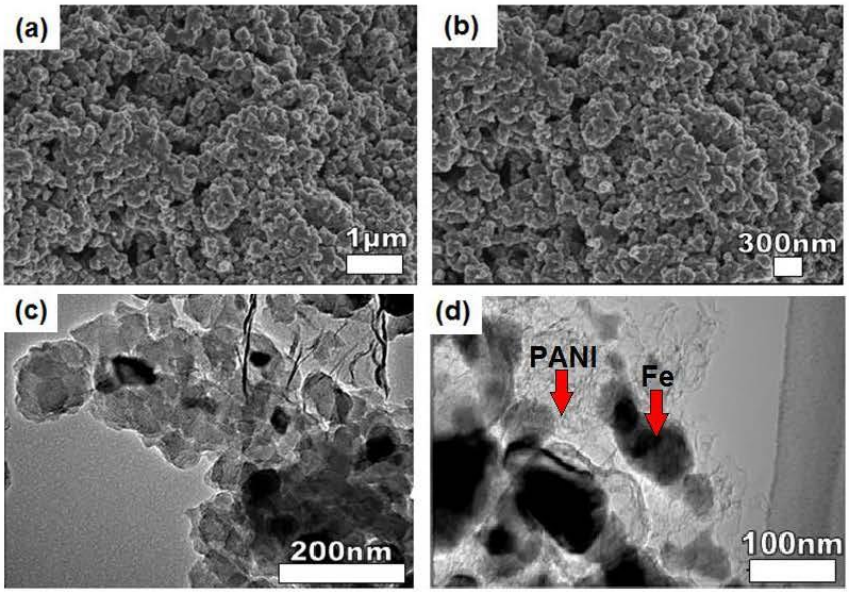

Fig. S2. (a) and (b) SEM images of the C-FP at low and high magnifications respectively. (c) and (d) TEM images of the C-FP at low and high magnifications respectively.

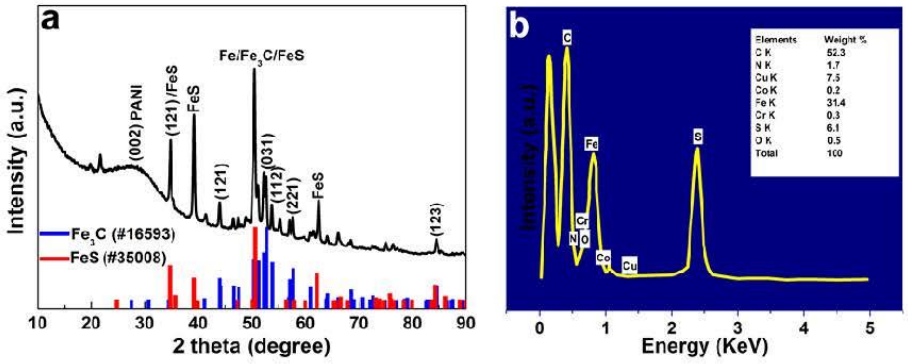

Fig. S3. (a) XRD spectrum and the matching ICSD card (b) EDX spectrum of the as-synthesized C-FP material respectively.

Fig. S3(a) shows the powder X-ray diffraction spectrum of the sample, and the best matching Inorganic Crystal Structure Database (ICSD) card no. 16593 with chemical formula Fe_3C (crystal system: orthorhombic and space-group: *Pnma*) and ICSD card no.

35008 with chemical formula FeS (crystal system: orthorhombic; space-group: *Pnma*) [2]. The XRD pattern shows a significant amount of orthorhombic Fe_3C predominantly due to the dissolution of carbon atoms into Fe lattices during pyrolysis at a high temperature of about 850 °C. In addition, the FeS diffraction peaks suggest that during the pyrolysis process the degradation of ammonium persulphate generated iron sulfide. The diffraction peak at about 52° could also be due to metallic Fe, in addition to Fe_3C and FeS diffraction. The XRD spectrum shows a broad peak for graphitic carbon; around 2θ = 30°, i.e. a (002) reflection [3]. Besides, the small size of the carbon nanoparticles could as well gives rise to peak broadening, an idea supported by the TEM micrographs results of the as-prepared C-FP sample (Fig. S2 (c-d)). The small peak at 2θ = 22.5 ° could be attributed to the presence of polyvinylidene fluoride (PVDF) used as the binder [4] .

The elemental analysis of the C-FP is as shown in Fig. S3 (b). The EDX spectra show that iron (31.4 wt. %) and carbon (52.3 wt. %) are the major elements present in the sample. The presence of sulphur (6.1 wt. %) and nitrogen (1.7 wt. %) in the EDX spectrum could be ascribed to the PANI composition. The elements Cu and other trace elements recorded in the spectra are portrayed owing to the grid sample holder for EDX analysis.

Electrochemical measurements of the C-FP

Fig. S4 displays the electrochemical performance of the C-FP electrode at different scan rates in a three-electrode configuration. The negative electrode material displayed no noticeable peaks in its curves, S4 (a), with an ideal rectangular CV curves, showing the material's double-layer capacitive characteristics with good reversibility.

Fig. S4 (b) shows the CD profiles of the as-synthesized C-FP negative electrode at various current densities. The C-FP electrode specific capacitance is shown as function of current

density in Fig. S4 (d). The cycling stability of C-FP was measured up to 1000 cycles at a charging–discharging current density of 5 A g^{-1} (S4 (e)). A coulombic efficiency of 102.6 % is observed for the electrode over 1000 cycling. The uniquely good cycling performance with relatively high specific capacitance is responsible for the material's good electrochemical performance. Fig. S4(c) displays Nyquist plot of C-FP electrode. The plot is observed to be composed of a nearly vertical line (Warburg line) within the low frequency region and a semicircle within the high frequency region indicating a typical capacitive behavior of EDLCs electrode [5,6].

Fig. S4 (f) shows the self-discharge (SD) curve of the hybrid NiCo-MnO_2//C-FP symmetric *SC* carried out at room temperature. From S4 (f), the *SC* was observed to maintain a substantial voltage of 1.11 V which indicates a good practical application of the hybrid *SC*.

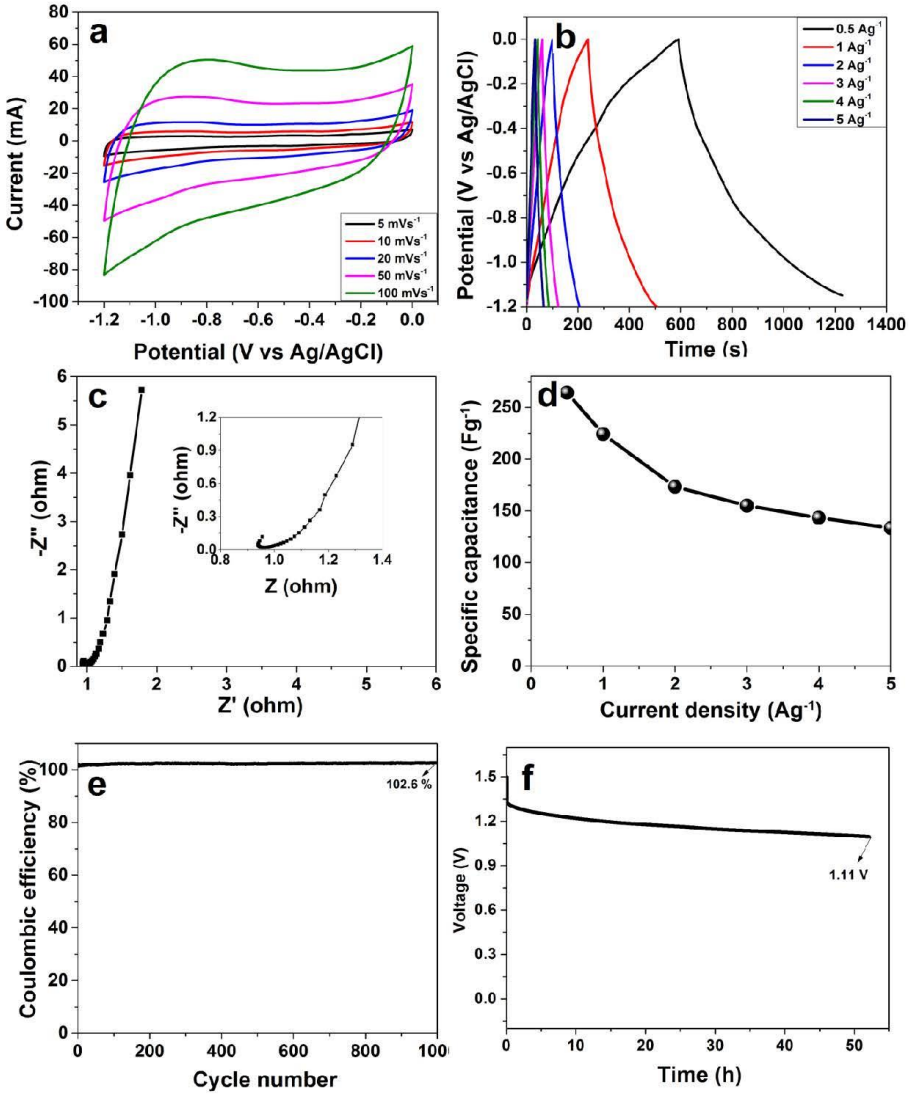

Fig. S4. (a) CV curves at various scan rates (b) CD profiles at various current densities (c) EIS Nyquist plot (d) Plot showing specific capacitance values against the current densities (e) plot showing efficiency against the cycle number for the as-prepared C-FP material respectively. (f) Self-discharge curve of the hybrid NiCo-MnO_2//C-FP asymmetric *SC*.

Table S1: Calculated values of R_s, R_{CT}, and Qs fitted parameters through ZFIT fitting of the experimental impedance spectra based on equivalent circuit shown in the inset to figure 13b.

Electrode	R_s (Ω)	R_{CT} (Ω)	Q_1 ($F.s^{(a-1)}$)	Q_2 ($F.s^{(a-1)}$)
NiCo-MnO_2//Fe_3C	0.22	1.94	0.03201	0.3274

Where R_s is the solution resistance, R_{CT} is the charge-transfer resistance, and Qs are the constant phase elements respectively.

Table S2: XRF data analysis of NiCo-MnO_2 as-prepared electrode material prepared as pressed powder.

Compounds	Weight %
Co	34.52
Mn	30.70
Ni	29.27
Cl	4.06
Na_2O	1.01
MgO	0.25
Eu_2O_3	0.08
SiO2	0.03
Tm_2O_3	0.03
MoO_3	0.02
CuO	0.02
Total	99.99

Loss on ignition = 0.01 Weight %.

REFERENCES

[1] S. Patra, P. Mitra, S.K. Pradhan, Preparation of nanodimensional CdS by chemical dipping technique and their characterization, Mater. Res. 14 (2011) 17–20. doi:10.1590/S1516-14392011005000015.

[2] R.T. Downs, M. Hall-Wallace, The American Mineralogist crystal structure database, Am. Mineral. 88 (2003) 247–250.

[3] K. W. Andrews, The structure of cementite, Acta Metall. 11 (1963) 939–946.

[4] J.P. Cheng, L. Liu, J. Zhang, F. Liu, X.B. Zhang, Influences of anion exchange and phase transformation on the supercapacitive properties of α-Co(OH)2, J. Electroanal. Chem. 722–723 (2014) 23–31. doi:10.1016/j.jelechem.2014.03.019.

[5] M. Yan, Y. Yao, J. Wen, W. Fu, L. Long, M. Wang, X. Liao, G. Yin, Z. Huang, X. Chen, A facile method to synthesize Fe<inf>x</inf>C<inf>y</inf>/C composite as negative electrode with high capacitance for supercapacitor, J. Alloys Compd. 641 (2015) 170–175. doi:10.1016/j.jallcom.2015.04.024.

[6] Y. Wang, G. Zhang, G. Liu, W. Liu, H. Chen, J. Yang, Facile synthesis of highly porous N-doped CNTs/Fe $_3$ C and its electrochemical properties, RSC Adv. 6 (2016) 44013–44018. doi:10.1039/C6RA07101E.

[7] H. P. Klug, & L. E. Alexander, X-Ray Diffraction Procedures: For Polycrystalline and Amorphous Materials, Wiley-VCH, May (1974) 992, ISBN 0-471-49369-4.

4.2.3 Concluding Remarks

Mixed transition meta hydroxides $NiCo(OH)_2$, NiCoMn-triple hydroxide (NiCoMn-TH) and a ternary NiCo-MnO_2 electrode materials were successfully synthesised by force-driven hydrolysis of hydrated nitrates of nickel, cobalt and manganese salt at a low temperature while C-FP electrode was synthesized via a complete dissolution of iron (III) nitrate and PANI in ethanol. The characterization of the samples confirmed that the as-prepared mixed hydroxides electrode materials have agglomerated flake-like particles which exhibited a small specific surface area compared to the NiCo-MnO_2 with porous and stacked sheet-like morphology. It was also confirmed that the prepared samples are crystalline, and composed of Ni, Co, O (or O–H bond in $NiCo(OH)_2$ sample) and Mn in NiCo-MnO_2 sample with Ni, Co and Mn existing in different oxidation states. The C-FP on the other hand, is composed of

nano grains with some level of crystallinity. The electrochemical performance of the electrode materials evaluated in a three-electrode cell configuration using 1 M KOH electrolyte showed a significant improvement on specific capacity of 132.1 mAh g^{-1} for NiCo-MnO_2 compared to 110.3 and 64.36 mAh g^{-1} for $NiCo(OH)_2$ and the unstable NiCoMn-TH at a current density of 0.5 A g^{-1} respectively. The C-FP electrode showed a good and consistent capacitive performance with relatively high specific capacitance of 264.17 Fg^{-1} at a current density of 0.5 A g^{-1} in KOH aqueous electrolyte. A cost-effective high-performance hybrid NiCo-MnO_2//C-FP supercapattery in 1 M KOH electrolyte delivered a high energy density of 48.83 Wh kg^{-1} with a corresponding high power density of 896.88 W kg^{-1} as well as excellent stability with 97.78% capacity retention up to 10,000 cycles similar to what is observed in classic EDLC devices. Even at high current density of 8 A g^{-1} the device maintained a high energy density of 25 Wh kg^{-1} with corresponding power density of 6344 W kg^{-1} which shows that these are excellent materials for supercapacitor applications.

4.3 Electrochemical performance of two-dimensional Ti_3C_2-Mn_3O_4 nanocomposites and carbonized iron cations for hybrid supercapattery electrodes

4.3.1 Introduction

Hybrid supercapacitors have attracted great research attentions as renewable energy storage systems due to their potential for use in hybrid electric vehicles among others. More importantly, advances in environmental technology, such as the emergence of hybrid electric vehicles in the 1990's, have brought innovation to an era when vehicles have been traditionally powered by gasoline [54]. The latest progress of electrode materials application for supercapacitors and batteries have been reported in the literature [22], [23], [162]. Nevertheless, the demonstrated electrochemical performances of the so called supercapacitor electrodes are not enough, particularly in terms of energy density.

In this work, a binder-free Ti_3C_2-Mn_3O_4 nanocomposite electrode has been fabricated via a green solvothermal process which allows for the precise control of the size, shape distribution, and crystallinity of metal oxide nanostructures. A synergy of the individual electrochemical features of these materials is achieved by integrating the Mn_3O_4 into the Ti_3C_2 network.

4.3.2 Results and Discussions

A detail summary of the results of the electrochemical performance of solvothermal synthesized two-dimensional Ti_3C_2-Mn_3O_4 nanocomposites and its application as hybrid supercapattery electrodes is presented in the paper below (under review for publication).

Electrochemical performance of two-dimensional Ti_3C_2-Mn_3O_4 nanocomposites and carbonized iron cations for hybrid supercapacitor electrodes

Kabir O. Oyedotun[1], Damilola Y. Momodu[1], Michael Naguib[2], Abdulmajid A. Mirghni[1], Tshifhiwa M. Masikhwa[1], Abubakar A. Khaleed[1], Mesfin Kebede[3], and Ncholu Manyala[1]*

[1]Department of Physics, Institute of Applied Materials, SARCHI Chair in Carbon Technology and Materials, University of Pretoria, Pretoria 0028, South Africa.
[2]Department of Physics and Engineering Physics, Tulane University, New Orleans, LA 70118, USA.
[3]Energy Materials, Materials Science and Manufacturing, Council for Scientific and Industrial Research (CSIR), Pretoria, 0001, South Africa
*Corresponding author's email: ncholu.manyala@up.ac.za, Tel.: + (27)12 420 3549.

Abstract

In this work, we present a simple two-step synthesis route to develop a cost effective high performance Ti_3C_2-Mn_3O_4 nanocomposite via a solvothermal process at 150 °C. The characterization of the composite material was obtained via various techniques. Electrochemical performance study of the material as a potential supercapacitor electrode demonstrated a maximum specific capacitance and specific capacity of 1010 F g^{-1} and 128 mAh g^{-1} at 5 mV s^{-1} and 1 A g^{-1} respectively in a 6 M KOH aqueous electrolyte. A capacity retention of 77.7% of the initial value was recorded after over 2,000 galvanostatic cycles at 10 A g^{-1} for the single electrode. More so, the as-prepared nanocomposite sample electrode also showed a relatively stable property with an energy efficiency of 83.5 % after cycling tests. Interestingly, an assembled hybrid supercapacitor device with carbonized iron cations (C-FP) and the Ti_3C_2-Mn_3O_4 composite delivered a specific capacity of 78.9 mAh g^{-1}. The device yielded a high energy of 28.3 Wh kg^{-1} with an equivalent 463.4 W kg^{-1} power densityat 1 A g^{-1}. A good cycling stability performance with an energy efficiency of 90.2% in addition to a 92.6% capacitance retention was observed for over 10,000 cycles at specific current of 3 A g^{-1} over a voltage window of 1.5 V.

KEYWORDS: MXene, Ti_3C_2-Mn_3O_4, nanocomposites, specific capacitance/capacity, supercapacitor electrodes, carbonized iron cations.

1. Introduction

As a result of higher demand for cleaner energy being witnessed globally, there is an urgent need to further explore novel clean energy sources and associated energy storage systems to work efficiently in storing the as-generated energy [1,2]. Electrochemical capacitors, the recent innovative energy storage components has gained much research attention due to their demonstrated potential to not only be used in combination with the much older battery technology framework but also additional merits such as its environmentally friendliness, high power densities (fast charge/discharge abilities) and long cycle life [2,3].

Various materials have been examined as electrodes for energy storage devices, such as activated carbon, metal hydroxides/oxides, metal sulfides and conducting polymers with efforts being focused on the exploration of novel composite electrode materials to enhance electrochemical performance of the supercapacitor device via exploitation of the individual material storage capability [4,5].

Until the separation of mono layer graphene in 2004 [6], two-dimensional (2D) materials have caught great research attention owing to their characteristic attributes connected to their bulk form. There are currently numerous new 2D materials, some of which are transition metal dichalcogenides, transition metal sulphides, and transition metal oxides, among others [7–10]. MXenes are a new class of 2D materials, which were recently discovered to be applicable in most dynamic and technologically advancing applications. It mainly exists as transitional metal nitrides and/or carbides having a common formula $M_{n+1}X_nT_z$, where M, X, and T_z are the early transition metal elements, nitrogen and/or carbon , and surface limiting groups (mainly OH, O, and F), respectively, with n = 1, 2, or 3 [11,12].

The 2D materials have hydrophilic surfaces [13] with high metallic conductivities usually around6000 to 8000 Scm^{-1} [14], which confirms its suitable accomplishment in energy storage devices applications, catalysis, water desalination, electromagnetic interference shielding, and conducting thin films [14–18] among others [13]. The materials have attracted significance attention basically for their enormous potential in applications such as energy storage devices which include electrochemical capacitors and metal-ion batteries [12,19,20].

Till to date, the significance of MXenes, viz., early transition metal carbides and/or carbonitrides, is currently vastly investigated by researchers globally for further energy storage applications, which is obtainable based on its good electrical conductivities and surface terminations which makes it electrochemically active [1,13,21].

Manganese oxide (Mn_3O_4) in the form of hausmannite is a black mineral. It is composed of a spinel structure, having tetragonal distortion arising from a Jahn-Teller effect on the Mn^{+2} ion. The tetrahedral and octahedral sites of the Mn^{+2} $(Mn^{+3})_2O_4$ structure are occupied by the Mn^{+2} and Mn^{+3} ions respectively. The hausmannite material in its tetragonal crystal structure has lattice parameters a = 0.5762 nm, b = 0.5762 nm, and c = 0.9470 nm with space group $I4_1/amd$ [22]. Manganese oxides of different structures have also been widely adopted as electrode materials, soft magnetic materials, and catalysts [23–27], of which Mn_3O_4 is popular as a top catalyst material for redox reactions in general. For instance, the material is known for its use as a catalyst in selective reduction of nitrobenzene and methane and carbon monoxide oxidation process the [24]. Mn_3O_4 is mainly produced by calcination of manganese hydroxides, hydroxyoxides, or oxysalts at a temperature usually above

800 °C. Its nanowires could be produced via the hydroxide powder calcination at 850 °C using the micro-emulsion technique [24,28]. Generally, Mn_3O_4 particles synthesized using these traditional methods possess low surface area and with random shape thereby limiting their specific uses. The materials specific physical and chemical attributes account for their suitability in catalysis and energy storage devices applications among others [24]. Nevertheless, Mn_3O_4 is intrinsically poor in electrical conductivity hence incorporating nanostructured Mn_3O_4 into conductive 2D carbon-based materials has been recently explored by other researchers [29],[30–32].

Based on the available reports involving the incorporation of these pseudocapacitive oxide materials with other electrically conductive carbon-based materials, it is expected that Mn_3O_4 insertion into the electrically conductive $Ti_3C_2T_z$ layers will generally be considered as a promising approach to further solve the poor electrical conductivity property. By maximizing the conductive and flexible characteristic of the $Ti_3C_2T_z$ layers as the scaffold material, Mn_3O_4 nanoparticles could be uniformly dispersed between the $Ti_3C_2T_z$ layers to facilitate ionic and electronic transport. The issue of restacking of the nanolayers could also be limited with the presence of the embedded Mn_3O_4 nanoparticles.

In this work, a binder-free $Ti_3C_2T_z$-Mn_3O_4 nanocomposite electrode has been fabricated via a green solvothermal process. This process permits for an exact influence on the magnitude, form, as well as crystallinity of metal oxide nanostructures. A synergy of the individual electrochemical features of these materials is achieved by integrating the Mn_3O_4 into the Ti_3C_2 network. Besides, the nature of the composites assembled was a free-standing film without the use of

binders which further increased the rate kinetics and system stability [30]. The Mn_3O_4 lying on the surface of the $Ti_3C_2T_z$ layers could improve the active material-electrode surface contact which will in turn smoothen the process of electrons transfer to the current collector, thereby remarkably improving the electrochemical accomplishment of the entire composite material as electrode.

2. Experimental

2.1. Materials preparation

2.1.1. Preparation of the $Ti_3C_2T_z$ (MXene) material

The $Ti_3C_2T_z$ utilized for the synthesis of the $Ti_3C_2T_z$-Mn_3O_4 nanocomposite material was synthesized as reported in earlier work [21,33]. Briefly, the Ti_3AlC_2 powder was synthesized by ball-milling equal molar ratio of Ti_2AlC and TiC powders for 4 h with the aid of zirconia balls, With the resulting mixture been heated to 1350 °C for 2 h in argon gas flow. The recovered sample was crushed with a pestle, in a mortar. About 10 g of Ti_3AlC_2 powder (-325 mesh) was then dispersed in 100 mL of a 48% concentrated HF aqueous solution at 25 °C for 18 h. The recovered suspension was washed severally with fresh deionized (DI) water, centrifuged to remove the etching products and remaining acids until the pH reached values > 4. Then the powders were separated from the liquid using vacuum-assisted filtration device.

2.1.2. Preparation of Mn_3O_4 nanoparticles

$KMnO_4$ (0.768 g) was dispersed in 100 mL ethanol (99.9 %) and 0.5 mL of 10.2 M HCl was added drop-wise with magnetic stirring at 25 °C to achieve a uniform mixture. The contents were then transferred into a Teflon-lined autoclave for a dwell time of 4 hours at a temperature of 150 ˚C. The system was left to cool down

naturally, and the recovered sample was washed severally with DI water to be free of excess reagent. The brown precipitate was then dried for 12 h in an electric oven at 60 ˚C in air (under normal laboratory conditions).

2.1.3. Preparation of $Ti_3C_2T_z$-Mn_3O_4 nanocomposite

100 mg $Ti_3C_2T_z$ was dispersed in 100 mL ethanol 99.9 % upon magnetic stirring at room temperature with subsequent sonication for 1 h to speed-up uniform dispersion. Thereafter, 0.768 g $KMnO_4$ was added to the $Ti_3C_2T_z$ mixture with a drop-wise introduction of 0.5 mL HCl (10.2 M) for homogeneity while magnetically stirring the entire reaction chamber for nearly 30 minutes. The resulting mixture was poured into a Teflon-lined stainless steel autoclave unit, bubbled with argon gas to prevent oxidation of the sample before being sealed and heated up to 150 ˚C for a dwelling time of 4 h. After been left to cool down naturally, the precipitated sample was washed severally with DI water until a pH 7 was recorded and then oven dried at 60 ˚C for 12 h in air to obtain the $Ti_3C_2T_z$-Mn_3O_4 nanocomposite (see scheme 1).

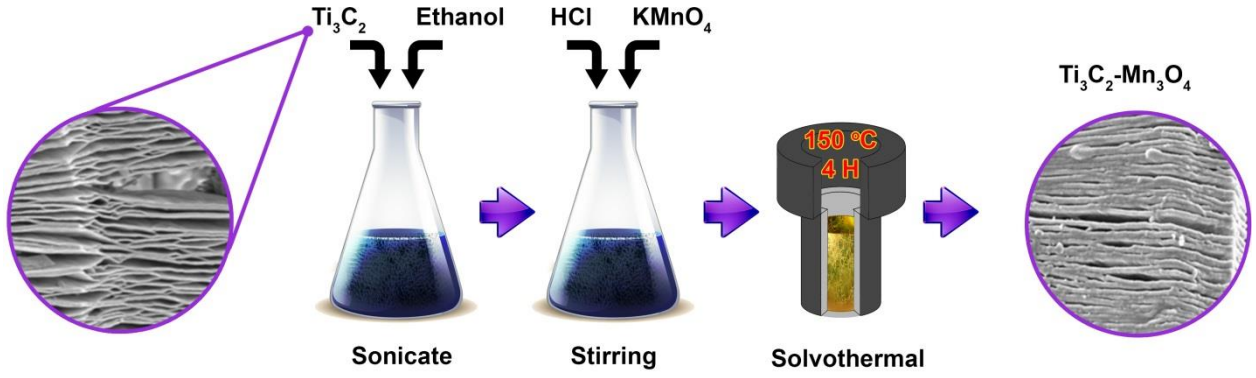

Scheme 1: Diagram of the synthesis process of $Ti_3C_2T_z$-Mn_3O_4 nanocomposite.

2.1.4. Preparation of carbonized iron cations (C-FP) electrode

The carbonized Iron cations used as the negative electrode in the fabrication of the Ti_3C_2-Mn_3O_4//C-FP hybrid supercapattery device was prepared as depicted in our earlier work [34,35]. Briefly, the iron-containing mixture, C-FP was pyrolysed by entirely dissolving $Fe(NO_3)_2$. $9H_2O$ salt in ethanol, with subsequent addition of Polyaniline (PANI) already reported in our earlier work [34]. The resulting mixture was put into sonication until slurry that was pasted onto nickel foam template. The prepared sample was later moved into a Quartz tube and annealed at 850 °C for 2 h under N_2 atmosphere for the iron cations (Fe^{3+}) to be adsorbed onto the PANI film directly grown onto the nickel foam template.

2.2. Materials characterization

The as-synthesized samples micrographs and energy dispersive X-ray (EDX) spectrum were acquired using a Zeiss Ultra Plus 55 field emission scanning electron microscope (FE-SEM) actuated at 1.0 kV, alongside with a JEOL JEM 2100F high-resolution transmission electron microscope (HRTEM FEI Tecnai-F30) operated with a 200 KV acceleration voltage. X-ray diffraction (XRD) analysis was achieved by using an XPERT-PRO diffractometer (PANalytical BV, Netherlands) having a reflection geometry at 2θ values of 9–90° and a step size of 0.01°, actuating with a Co Kα radiation source (λ = 0.178901 nm). An alpha 300 RAS+ Confocal micro-Raman spectrometer (WiTec Focus Innovations, Germany) set on the 532 nm laser wavelength was employed to analyze the as-prepared samples with a spectral acquisition time of 150 s and laser power of 5 mW. Fourier transform-infrared (FT-IR) analysis was achieved via a Varian FT-IR spectroscopy in a range of 500-4000 cm^{-1} in wavenumber, while the X-ray photoelectron spectroscopy (XPS) analysis was

achieved with the help of a Physical Electronics Versa Probe 5000 spectrometer activated with a 100 µm monochromatic Al-Kα exciting source. The textural properties of the samples were acquired by using a Micrometrics TriStar II 3020 pore analyzer run in the range 0.01–1.0 of relative pressure (P/Po), with a pre-degassing done under vacuum for 18 h at 100 °C. Brunauer-Emmett-Teller (BET) and Barrett–Joyner–Halenda (BJH) models were utilized to ascertain the specific surface area (SSA) as well as pore size distribution (PSD) of the samples respectively. Thermogravimetry analysis (TGA) measurements of the as-prepared samples were done by using a thermogravimetric analyzer, TGA-STA 449C between 20 °C and 1000 °C at 20 °C/min in air. XRF analysis of the compacted powder nanocomposite was carried out by using the ARL Perform'X Sequential XRF instrument with Uniquant software for examination.

2.3. Electrochemical measurements

The electrode materials were fabricated by muddling the active material (90 wt. %) with conductive carbon (10 wt. %) and N-methyl-2-pyrrolidone (NMP) to make slurry. The prepared slurry was pasted onto a 1.0 X 1.0 cm^2 area of the annealed nickel foam template serving as the current collector with subsequent drying at 60 °C overnight. Afterwards, the as-synthesized electrodes were subjected to a pressure of 20 MPa for about 20 seconds. A Bio-Logic VMP300 potentiostat (Knoxville TN 37930, USA) was employed to measure the capacitive performance of the nickel foam-supported electrodes via a three-electrode electrochemical set-up. The performance assessments were carried out using a counter electrode made of glassy carbon, an Ag/AgCl/3 M KCl reference electrode, and the active materials on nickel foam stubs serving as the working electrodes in 6 M KOH at 25 °C. The areal loading

mass of each of the active materials was estimated to be nearly 2.5, 2.1, 2.1 and 2.6 mg cm^{-2} for the $Ti_3C_2T_z$-Mn_3O_4, $Ti_3C_2T_z$, Mn_3O_4 and C-FP electrodes correspondingly. Cyclic voltammetry (CV) tests of the as-synthesized $Ti_3C_2T_z$, Mn_3O_4, $Ti_3C_2T_z$-Mn_3O_4 samples were performed at distinct scan rates ranging from 5 to 100 mV s^{-1} within a negative and a positive operating potential windows of -0.4 to -0.9 V and 0.0 to 0.35 V vs. Ag/AgCl correspondingly. The galvanostatic charge-discharge (GCD) measurement was done at various increasing specific currents from 1 to 10 A g^{-1}. The electrochemical impedance spectroscopy (EIS) was carefully measured in an open-circuit potential, in a frequency range of 10 mHz to 100 kHz.

The single electrode specific capacitance, C_s (F g^{-1}) was obtained via the CV profiles using the relation depicted in equation 1 below [36]:

$$C_s = \frac{1}{mS_c\Delta V}\int_{v_1}^{v_2} IdV \quad (1)$$

where, v_1 and v_2 are the peak potentials, I (mA) is the current response, ΔV (V) is the electrode potential, S_c (mV s^{-1}) as the scan rate and m (g) is the mass of the active material.

The specific capacity, Q_s(mAh g^{-1}) and energy efficiency, η_E (%) of the materials were estimated via the GCD curves in line with the following relations expressed as [37]:

$$Q_s = \frac{I\Delta t}{3.6m} \quad (2)$$

$$\eta_E = \frac{E_d}{E_c} \times 100 \quad (3)$$

From equations 2 and 3 above, *I* (mA) typifies the discharge current, *t* measured in seconds is the time taken for a complete discharge cycle, and *m* measured in grams

accounts for the mass of the electrode. η_{E} is the energy efficiency, E_{d} represents the discharge energy, while E_{c} is the charge energy obtained by integrating the area under the CD profiles respectively.

Equations 4 and 5 stated below were adopted for the estimation of both energy and power densities for the hybrid supercapattery, (Ti_3C_2-Mn_3O_4//C-FP) from the area under the discharge curve:

$$E_d = I/3.6m \int V dt \quad [\text{Wh kg}^{-1}] \tag{4}$$

$$P_d = 3600 \times E_d/\Delta t \ [\text{W kg}^{-1}] \tag{5}$$

I describes the discharge current (A), *m* (g) represents mass of active material. Δ*V* in volts (V) and Δ*t* in seconds are the potential window as well as electrode discharge time respectively, and $E_d \ and P_d$, are energy and power densities sequentially.

To our notice, the assembled hybrid asymmetry supercapacitor (SC) operates well in a larger potential window, *c.a.* 1.50 Volts. For best output, respective mass of each electrode in the device was balanced according to the law, $Q_+ = Q_-$, and the charge stored on each electrode depicted as:

$$Q = C_s \times m \, \Delta V \tag{6}$$

In equation 6, *Q* measured in coulombs (C) represents the charge stored on the electrode, while C_S *in* F g^{-1} typifies the specific capacitance estimated on the basis of mass of the active material. Δ*V* (V) is the electrode potential, and *m* (g) as the mass of active material.

The precise mass equilibrium between the two (positive and negative) electrodes was calculated using a more expression of $Q_+ = Q_-$ as:

$$\frac{m_+}{m_-} = \frac{C_{s-}\ \Delta V_-}{C_{s+}\ \Delta V_+} \quad (7)$$

3. Results and discussions

3.1. Morphological, structural and compositional analysis

Fig. 1 demonstrates the FESEM images of the as-prepared materials. Fig. 1 (a-b) presents the surface morphology of the Ti_3C_2 sample at both low and high magnifications respectively. It is evident that the as-prepared Ti_3C_2 is made up of stacked sheet-like structure similar to that of exfoliated graphite or transition metal oxides [38]. The as-observed image confirms the successful removal of the aluminum layer through the HF treatment resulting in a stacked Ti_3C_2 accordion-like morphology which could enhance the electrode/electrolyte contact thereby resulting in efficient ionic transport and pseudo-capacitance performance [1].

Fig. 1 (c-d) displays the FESEM micrographs of Mn_3O_4 material at low and high magnifications accordingly. It could be noticed that the material is composed majorly of tiny, agglomerated irregular nanoparticles that have probably been constituted by the aggregation of smaller Mn_3O_4 nanostructures [39].

Fig. 1 (e-f) displays the FESEM images of Ti_3C_2-Mn_3O_4 composite at various magnifications. It can be observed that the addition of Mn_3O_4 leads to its integration in-between the Ti_3C_2 sheets giving the Ti_3C_2-Mn_3O_4 nanocomposite mix. In addition, the Ti_3C_2 nanosheets function as a conductive support base for the aggregated Mn_3O_4 nanostructures which will likely serves as a nanoscale collector for electron transfer [1,40].

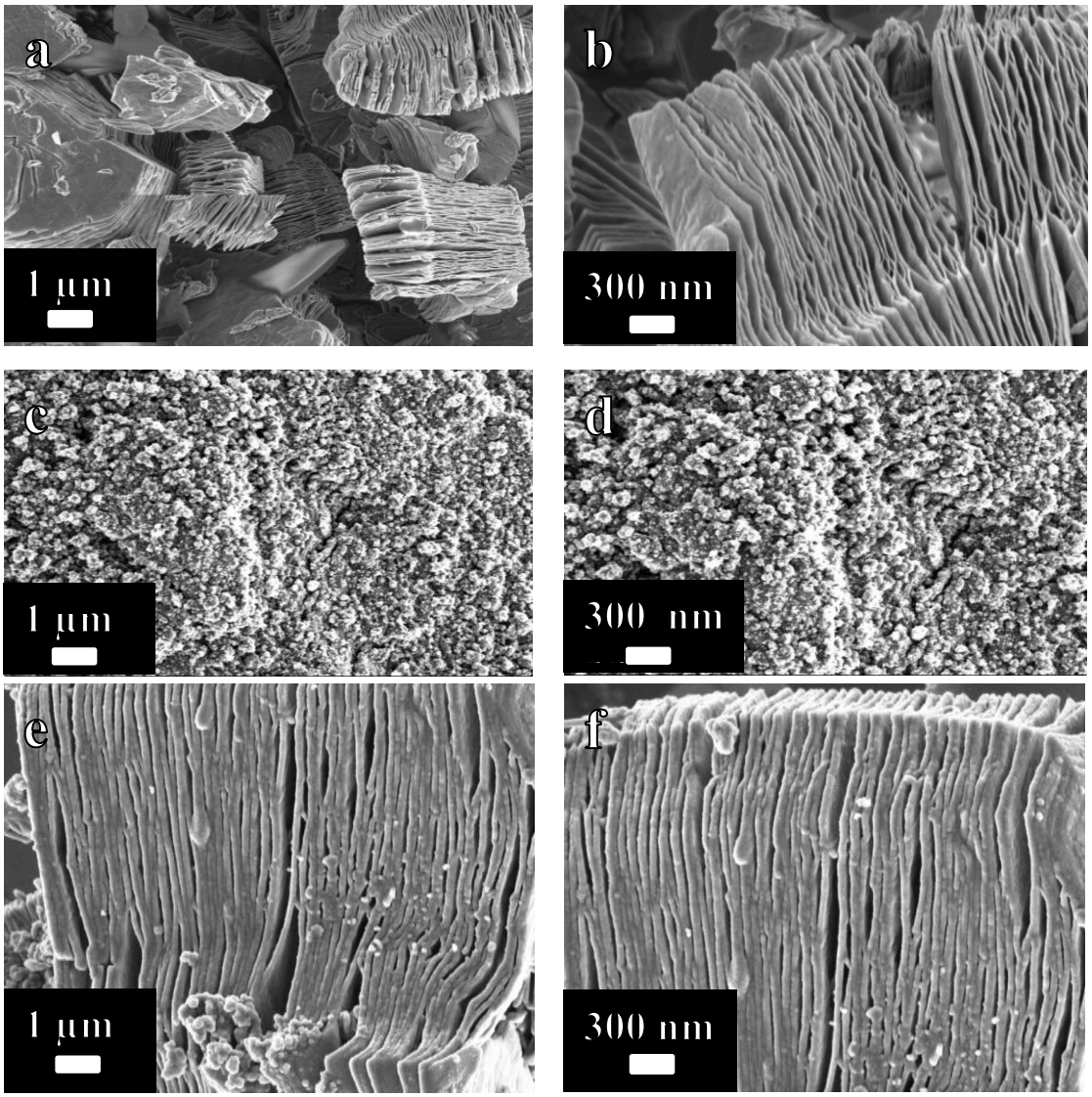

Fig. 1. SEM images of (a-b) the pristine Ti_3C_2, (c-d) the pristine Mn_3O_4 and (e-f) Ti_3C_2-Mn_3O_4 hybrid at low and high magnifications respectively.

Fig. 2 (a-b) indicates the HRTEM images of the Mn_3O_4 sample portraying uniformly distributed irregular nanoparticles which agrees well with SEM results from Fig. 1(c–d). Fig. 2 (c-d) demonstrates a characteristic HRTEM micrograph of the Ti_3C_2-Mn_3O_4 nanocomposite electrode material indicating the fine layered structure of the material. The interlayer spacing of the material was estimated to be ~ 12.51-18.64 nm as shown in Fig. 2(c). The Mn_2O_3 nanostructures are obviously seen located in the

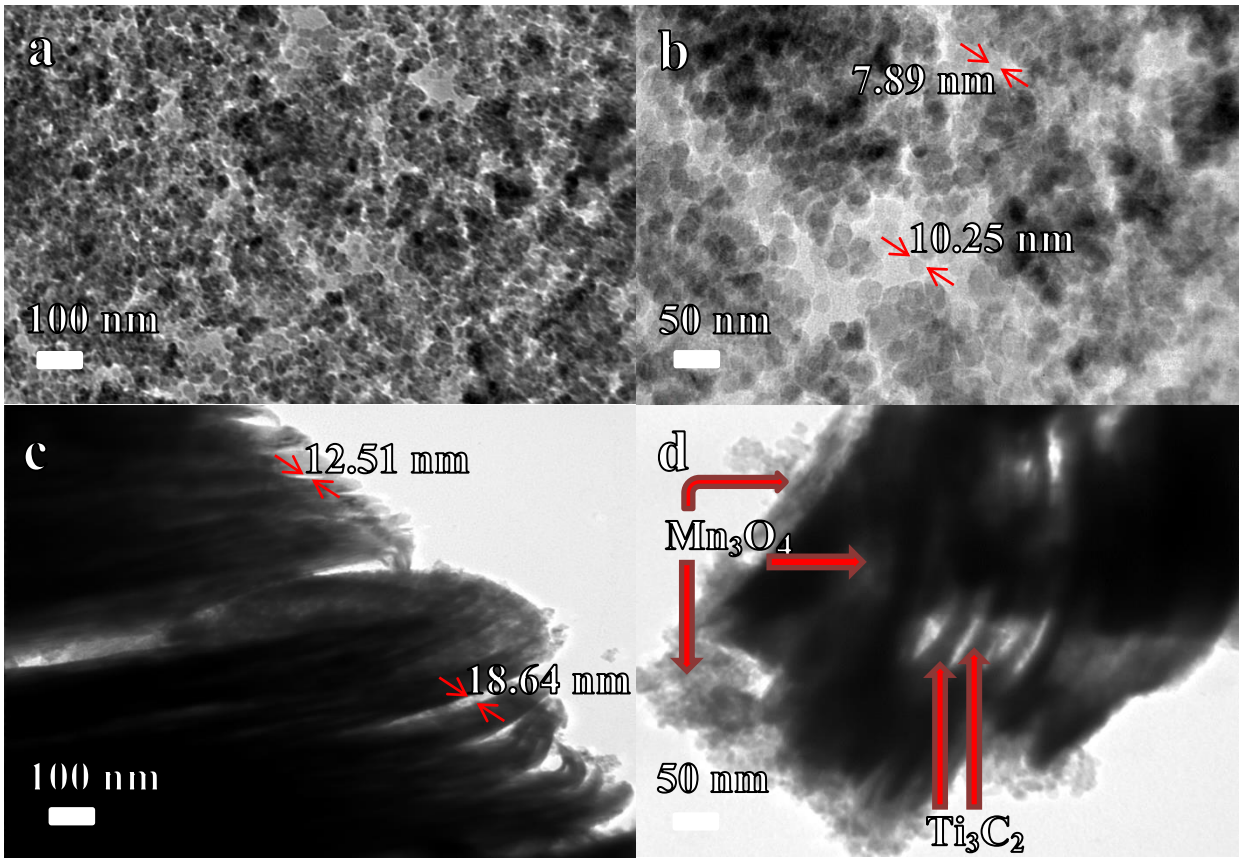

Fig. 2. HRTEM images of (a-b) Mn_3O_4 and (c-d) Ti_3C_2-Mn_3O_4 nanocomposite at low and high magnifications respectively.

interlayer spacing of the MXene sheets along with some located on the surfaces as indicated with the arrows in Fig. 2 (d). It can also be noticed that the Ti_3C_2 nanosheets are evenly loaded with numerous Mn_3O_4 nanoparticles as shown in Fig. 2d with an approximate thickness of ~ 7.89-10.25 nm.

Fig. 3 (a) shows the XRD spectra of Ti_3C_2, Mn_3O_4, and Ti_3C_2-Mn_3O_4 composite. There exist peaks at 2θ values of about 10° (d-spacing; 5.15201 Å), 20.8° (d-spacing; 4.91807 Å) and 32° (d-spacing; 3.08401 Å) which correspond to (002), (006) and (008) planes of a pure Ti_3C_2 material earlier reported by other researchers [3,21,41].

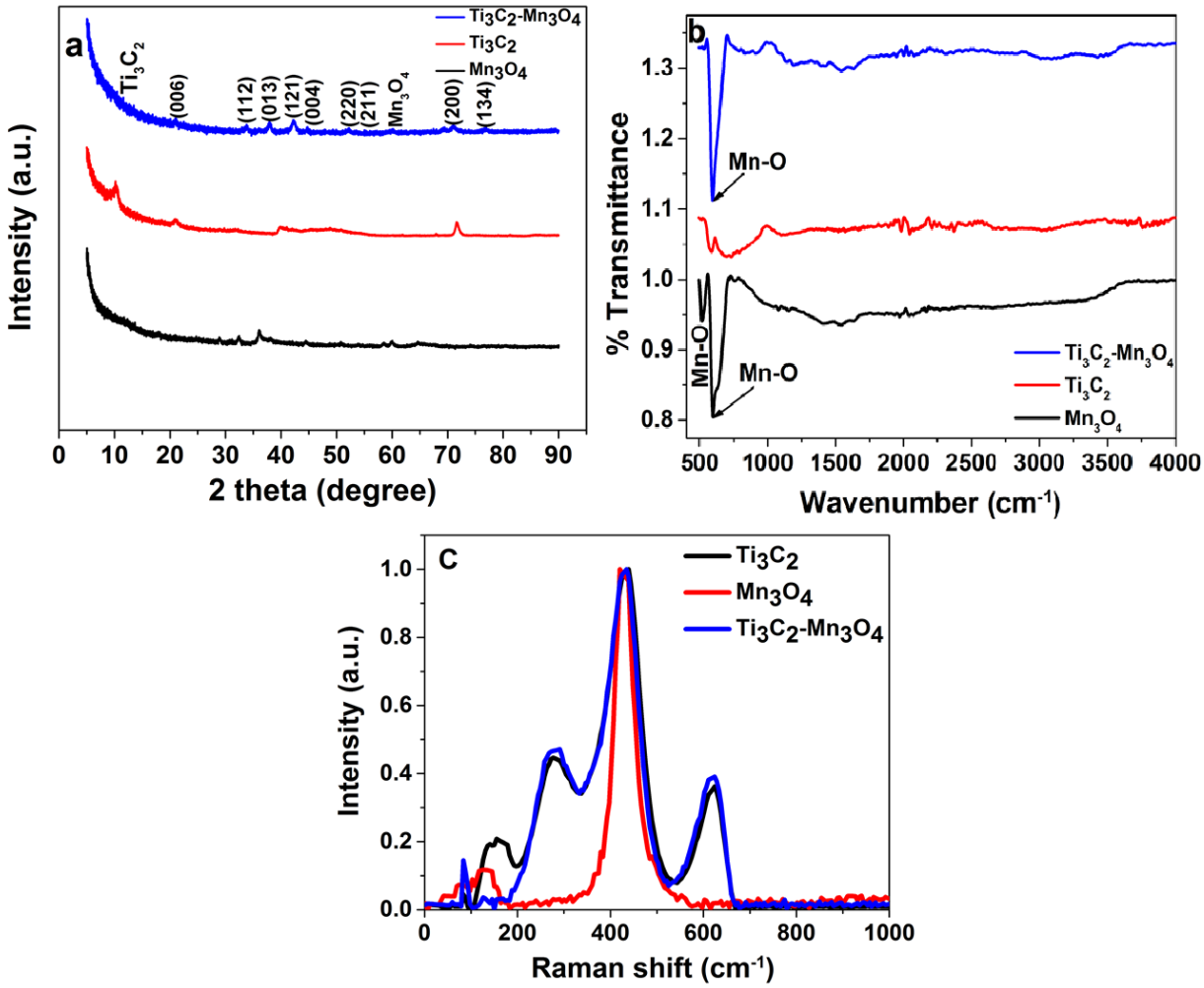

Fig.3. (a) XRD patterns, (b) FTIR spectra and (c) Raman spectra of the as-prepared Ti_3C_2 pristine, Mn_3O_4 pristine and Ti_3C_2-Mn_3O_4 nanocomposite respectively.

The broad and low intensity (002) peak at 2θ = 10° arises from the larger *d*-spacing due to the structural expansion from HF etching as well as Al substitution with -F and the -OH/=O bonding groups. The broad peak observed at approx. 39.6° (104) is typical of the 2D $Ti_3C_2T_x$ MXene materials [42]. The diffraction pattern of Mn_3O_4 shows strong peaks corresponding to (101), (112), (211), (220), (204), (015) and (400) planes ascribed to the hausmannite Mn_3O_4 tetragonal structure indexed according to JCPDS card No. 00-24-0734. The intense peaks from the XRD pattern

of the Ti_3C_2-Mn_3O_4 nanocomposite corresponding to both Ti_3C_2 and Mn_3O_4 indicated that the Ti_3C_2-Mn_3O_4 nanocomposite was properly synthesized.

Fourier transform infrared spectroscopy (FTIR) was performed to examine the surface functional groups. The FTIR spectra of the Ti_3C_2, Mn_3O_4 and Ti_3C_2-Mn_3O_4 are shown in Fig. 3 (b). The two strong transmission peaks around 601 and 520 cm^{-1} can be designated to the combined mode connecting Mn-O stretching modes of tetrahedral and octahedral sites in Mn_3O_4. However, in the Mn_3O_4 spectrum, the bands around 1630 and 1400 cm^{-1} are characteristics of resonances of the surface adsorbed O-H molecules and carbonate ions that are present with Mn atoms proportionally in atmosphere. In addition, the spectrum for the nanocomposite material recorded peaks around 596 and 515 cm^{-1} which can also be observed for Mn_3O_4 spectrum, indicating the presence of Mn_3O_4 in the nanocomposite. For all the samples, the peaks around 3400 and 1520 cm^{-1} are known to be an attribute of strongly hydrogen-bonded (–OH) groups or external water molecules been absorbed on the surface. Therefore, the accomplished coating of Mn_3O_4 nanoparticles on the Ti_3C_2 sheets is further confirmed by the FTIR results.

Fig. 3 (c) demonstrates the Raman spectra of Ti_3C_2, Mn_3O_4, and Ti_3C_2-Mn_3O_4 nanocomposites in the 100–2000 cm^{-1} region. Raman spectroscopy peaks of the as-prepared Ti_3C_2 samples at around 150, 275, 435, and 623 cm^{-1} are consistent with that of the reported data in the literature [39,43]. The observed peaks at around 275, 360, and the strong peak centered at 655 cm^{-1} are characteristic features of the tetragonal Mn_3O_4 structure [39], which conform with the XRD analysis in Fig. 3 (a). The Ti_3C_2-Mn_3O_4 nanocomposite Raman spectrum shows strong peaks at around

275, 434, and 623 cm^{-1} indicating the successful synthesis of Ti_3C_2-Mn_3O_4 nanocomposite.

Fig. S1 (*see supporting information*) shows the elemental and chemical analysis of Ti_3C_2-Mn_3O_4 nanocomposite. Fig. S1 (a) shows the EDX spectrum, while Fig. S1 (b) depicts a table of the chemical analysis for the as-synthesized Ti_3C_2-Mn_3O_4 nanocomposite respectively. From the Fig., it is evident that the nanocomposite material is mainly made up of C, O, Ti and Mn. The material reveals traces of Cl and Si which could be linked to the resin used in the EDX substrate sample preparation, and the F contents is ascribed to the HF etching step employed in the Ti_3C_2 MXenes preparation.

Fig. S2 displays the nitrogen adsorption–desorption isotherms obtained from the analysis and used in evaluating the BET surface area alongside with the pore size distribution of Ti_3C_2-Mn_3O_4 nanocomposite. The results indicate an increase in the SSA after deposition of the Mn_3O_4 material (*see Fig. S2 (a) in the supporting information*).

A BET SSA of 37.0 $m^2\,g^{-1}$ was recorded for the synthesized nanocomposite material compared to that of the pristine Ti_3C_2 sample (5.5 $m^2\,g^{-1}$). The improved SSA was ascribed to the integration of numerous Mn_3O_4 nanoparticles into the interlayer spaces between the Ti_3C_2 sheets resulting in an enlargement of pore sites after the solvothermal process. Fig. S2 (b) displays the corresponding pore-size distribution (PSD) plots of the pristine MXene material and the Ti_3C_2-Mn_3O_4 composite confirming the presence of mesopores within structure of the material [1]. From the PSD plots, the presence of both micropores and mesopores is confirmed within both materials with a peak centered at ca. 2.0 nm and a higher volume of mesopores

recorded between 3.0 – 4.5 nm. Furthermore, the introduction of Mn_3O_4 nanoparticles into the Ti_3C_2 nanosheets provides larger SSA and more mesopores for cation intercalation which is also indicated with the higher pore volume displayed for the Ti_3C_2-Mn_3O_4 nanocomposite. This unique layered pore structure in the composites could improve the material's charge storage performance when applied as supercapacitor electrodes [44].

The thermal stability of the Ti_2C_3, Mn_3O_4 and the Ti_2C_3-Mn_3O_4 samples was evaluated by thermogravimetric analysis (TGA) performed in air between 20 °C and 1000 °C as shown in Fig. S2 (c) in the supporting information. From the TGA profile, a very slight weight loss close to a 100 °C temperature point was observed which was related to the loss of interfacial-adsorbed moisture in both Mn_3O_4 and Ti_2C_3-Mn_3O_4 samples. The weight loss just below 300 °C was asserted to the evaporation of adsorbed water molecules [45,46]. The TGA profile of the oxidized Ti_3C_2 was observed to depict two processes which contribute to the weight change. The weight gains at around 420 ˚C is attributed to the Ti_3C_2 (MXene) oxidation, forming titanium dioxide and carbon [47]. The corresponding weight loss is due to the carbon combustion with further heating [47,48]. From the residual weights of the two samples (90.10% (Mn_3O_4) and 57.23% (Ti_3C_2-Mn_3O_4)) at 994 °C, the Mn_3O_4 contents in the composites materials was estimated to be ~32.87 wt%.

Fig. S3 (*see supporting information*) portrays the surface elemental composition of the as-synthesized Ti_3C_2-Mn_3O_4 sample analyzed further using the XPS technique. The high resolution XPS survey scans exhibited the presence of Mn, Ti, O and C atoms.

Fig. S3 (a) shows the Mn*2p* core level peaks with a $2p_{3/2}$–$2p_{1/2}$ doublet at 639.2 eV and 650.8 eV coupled with a spin-splitting width of 11.626 eV in the Mn 2*p* spectrum which is in accordance with the spectrum for Mn_3O_4 [49,50]. The peaks observed at 639.2 eV and 650.8 eV are ascribed to Mn $2p_{3/2}$ and Mn $2p_{1/2}$, correspondingly. This binding energy corresponds to the oxidation state of Mn(II) and Mn(III).

Fig. S3 (b) shows the Ti 2p core levels with doublets (Ti 2p3/2 and Ti 2p1/2) at 455.770 and 461.5 eV respectively coupled with a splitting width of 5.7 eV which agrees well with earlier studies reported in the literature [51,52].

Fig. S3 (c) shows the deconvoluted C*1s* peaks with the main C-C bond recorded at a binding energy of 282.0 eV, and other associated bonds like the C-O bonds and the C=O bonds observed at 283.2 eV and 286.0 eV binding energies respectively [53].

Fig. S3 (d) shows the deconvoluted O*1s* core level peaks. The peak conprises two components at 529.2 eV (a characteristic of metal-oxygen bonds) and at 527.3 eV which could be linked to the lattice oxygen in the material and the oxygen of the hydroxide ions respectively [54,55].

A molar ratio of 5:1 was obtained for the Mn_3O_4:Ti_2C_3 in the composite material using XRF method and is depicted in Table S1 in the supporting document. The ARL Perform'X Sequential XRF instrument with Uniquant software was employed for the analysis of elements in the periodic table in interval of Na and U, with just the elements discovered over the detection bounds been described. Carbon (C) falls outside the detection ability of XRF but the program adopted in this study was used to calculate semi-quantitatively values for specific compounds such as Ti_3C_2. The values were normalized, as no loss of ignition (LOI) was done to determine crystal water and oxidation state changes. The presence of Al_2O_3 in significant quantity (2.4

wt. %) could be ascribed to the sample preparation [33] in the laboratory; since small amount of Al_2O_3 are expected in the parent MAX phases, also another source of Al could be the presence of some residual Al from the parent MAX phase material during the etching process to produce the Ti_3C_2. Other trace elements/compounds recorded are portrayed owing to the impurities from chemicals used in sample preparation.

3.2 Electrochemical characterization

3.2.1 Electrochemical measurements of single electrodes in a three-electrode set-up

The electrochemical evaluation of the as-synthesized electrode materials was investigated via a three-electrode measurement configuration done in 6 M KOH aqueous electrolyte. The associated CV curves of the Ti_3C_2, Mn_3O_4 and Ti_3C_2-Mn_3O_4 electrodes at 50 mV s^{-1} scan rate in both negative and positive operating potentials are shown in Fig. 4(a-b). The different plots reveal that the Ti_3C_2-Mn_3O_4 composite electrode has a higher current response in the positive potential indicating a higher specific capacity. The CV curve of the Ti_3C_2 material compared to that of Mn_3O_4 and Ti_3C_2-Mn_3O_4 exhibits a quasi-rectangular shapes, showing a contribution of both faradic nature and electrical double layer capcitance (EDLC). The inset to Fig. 4(a) is the zoomed-in section of the CV curves of the three different materials showing clearly the overshadowed curve for the Mn_3O_4. This signifies the ability of the material to be charged and discharged at a pseudoconstant rate over the entire voltammetric cycle in the negative potential range [56].

Fig. 4 (b) displays the CV profile of the Ti_3C_2-Mn_3O_4 composite and its constituents, with that of Ni-foam pristine in the positive potential window range. It is noticed from

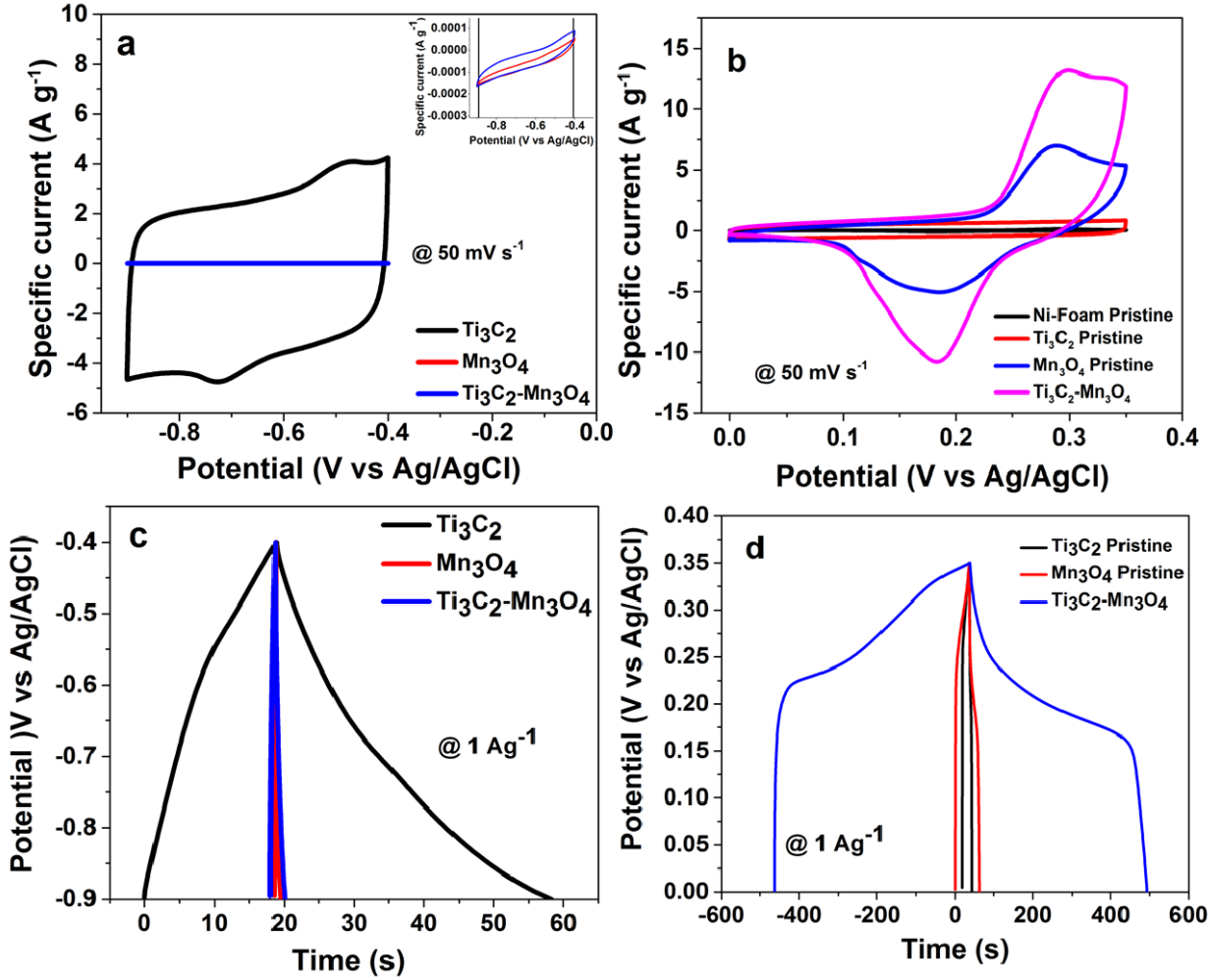

Fig. 4. CV curves of the Ti_3C_2 pristine, Mn_3O_4 pristine and Ti_3C_2-Mn_3O_4 composites (a) in the negative potential window, inset to (a) is the zoomed-in CV curves of the samples and (b) including that of pristine Ni-foam in the positive potential window at a scan rate of 50 mV s^{-1} respectively, (c) and (d) GCD curves of all the three materials in both negative and positive potentials at a specific current of 1 A g^{-1} respectively.

the Fig., that the redox peaks from the Ni-foam are negligible compared to those from the as-synthesized Mn_3O_4 and Ti_3C_2-Mn_3O_4 materials which clearly depicts no contribution of capacitance. An indication that the redox peaks are essentially attributed to the electrode materials.

Additionally, the peak specific current of the Ti_3C_2-Mn_3O_4 nanocomposite is much higher than that of Ti_3C_2 and Mn_3O_4 at the same 50 mV s^{-1} scan rate implying a larger

specific capacity/capacitance of the material is obtainable [57]. However, it is considered that the redox peaks are essentially assigned to the Ti_3C_2-Mn_3O_4 electrode material [37].

Fig. 4 (c-d) shows a plot comparing the CD profiles of the as-synthesized electrode materials in both negative and positive potential windows indicating an improved electrochemical charge storage capability which is faraidic in nature in the positive operating potential range.

To further examine the electrochemical properties of Ti_3C_2-Mn_3O_4 nanocomposite electrode material, the CV curves at varying scan rates in a potential range of 0.0 – 0.35 V are displayed in Fig. 5 (a). The curves at distinct scanning rates show a pair of well-defined redox peaks associated with the reversible transformation of Ti^{3+}/Ti^{4+} and Mn^{3+}/Mn^{4+}.

Fig. 5 (b) shows the CD curves at different specific currents. The nonlinear CV and CD curves demonstrate oxidation and reduction peaks owing to the reversible redox faradic reaction of a mixed proportion, comprising Ti^{2+}, Ti^{3+}, Mn^{2+} and Mn^{3+} affirming the faradic property of the Ti_3C_2-Mn_3O_4 electrode. The nonlinear CD curves and the voltage plateau observed corresponds well to the peaks displayed by the CV curves [58], a further confirmation of the material's faradic behavior.

A shift of the anodic and cathodic peaks potentials in the positive and negative directions is observed with increasing scan rate (Fig. 5(a)), owing to the aggravated polarization [59,60], emanating from the inadequacy of ion diffusion rate to fulfil electronic neutralization in the redox process [61]. The redox peaks intensities are

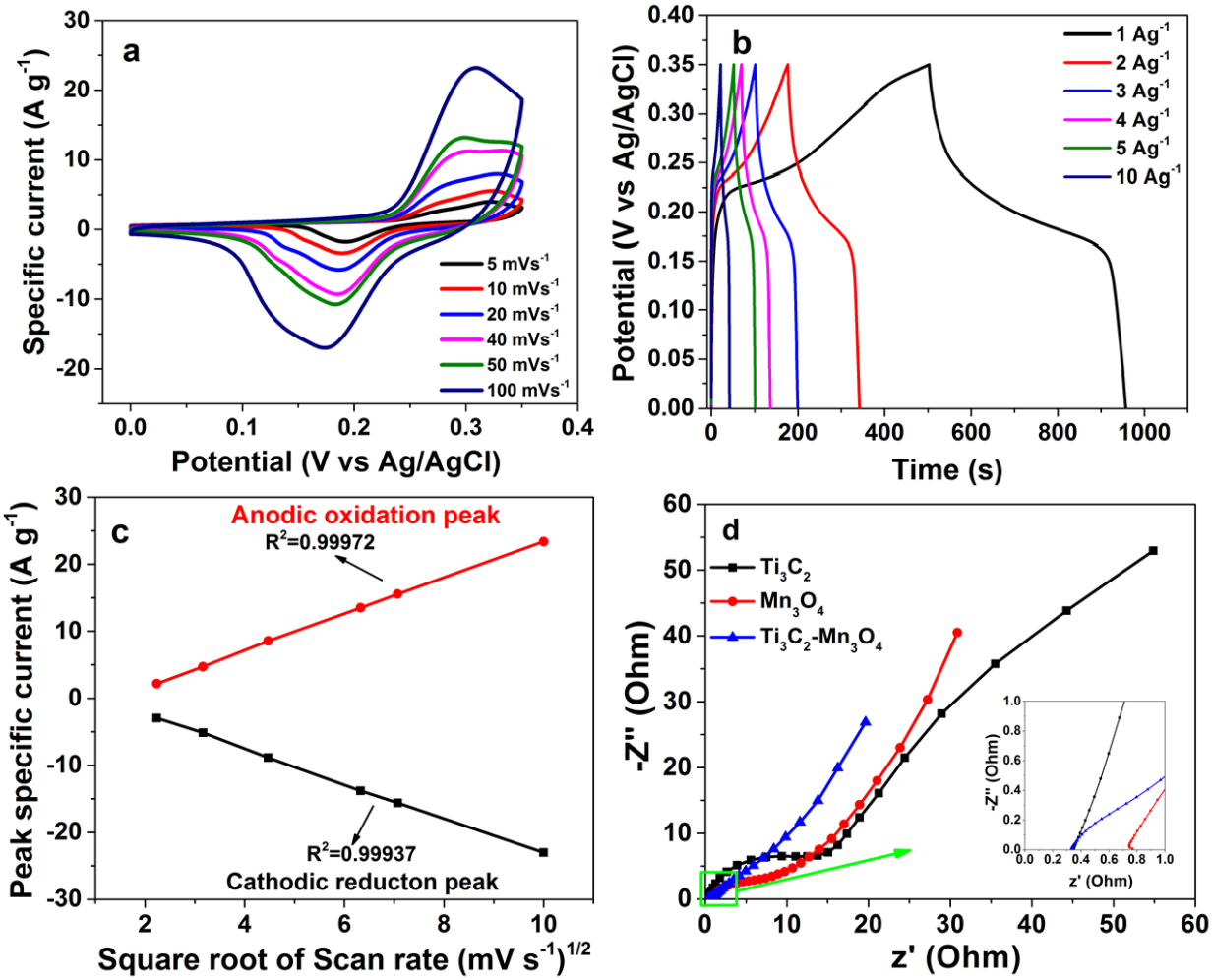

Fig. 5. (a) CV curves of the Ti_3C_2-Mn_3O_4 composite at distinct scan rates, (b) CD curves of the Ti_3C_2-Mn_3O_4 composite at various specific currents, (c) anodic and cathodic peak specific current plotted as function of square root of scan rate for Ti_3C_2-Mn_3O_4 composite and (d) EIS Niquist plots comparison of the Ti_3C_2, Mn_3O_4 and Ti_3C_2-Mn_3O_4 with an enlarged high-frequency region as the inset respectively.

improved relative to increasing scanning rate [60]. Fig. 5 (c) displays a linear relationship of the peak specific current as a function of the square roots of scan rate. The linearity of the plots confirmed that the electrochemical reaction is diffusion controlled, and further affirms the swift faradaic charge storage process within the Ti_3C_2-Mn_3O_4 nanocomposite electrode [62].

The electrical resistance of the electrode materials was further evaluated through the EIS technique at an open circuit potential, 0.0 V with frequencies ranging from 10 mHz to100 kHz. A demonstration of the Nyquist impedance plots of the Ti_3C_2, Mn_3O_4 and Ti_3C_2-Mn_3O_4 nanocomposite is shown in Fig. 5 (d).

From the EIS plots for all three electrodes (Fig. 5(d)), a semicircle was noticed in the high frequency region, displaying the interfacial charge transfer resistance, R_{ct} and mass transport via the material [34]. The inset to Fig. 5(d) portrays a zoomed-in high frequency region of the plots. The intersection to the real Z' axis is attributed to the electrode series resistance, R_S that involves the electrolyte ionic resistance, the intrinsic resistance of the active materials together with the contact resistance at the electrode material/current collector interface [34].

From the Fig., the R_S values for the Ti_3C_2, Mn_3O_4 and Ti_3C_2-Mn_3O_4 nanocomposite electrodes were recorded as 0.35 Ω, 0.73 Ω as well as 0.31 Ω respectively. Remarkably, the low R_S of the synthesized Ti_3C_2-Mn_3O_4 electrode material implies a high electrical conductivity, resulting in a satisfying capacitive behaviour of the electrode material based on the successful integration of the metal oxide into the MXene framework.

The specific capacitance, together with specific capacity values plotted against the scan rate and specific current are shown in Fig. 6 (a-b) for Ti_3C_2-Mn_3O_4 electrode material respectively. The evaluated specific capacitance values evaluated from CV profiles at increasing scan rates in a range of 5–100 mV s^{-1} was 1010.0–335.0 F g^{-1}

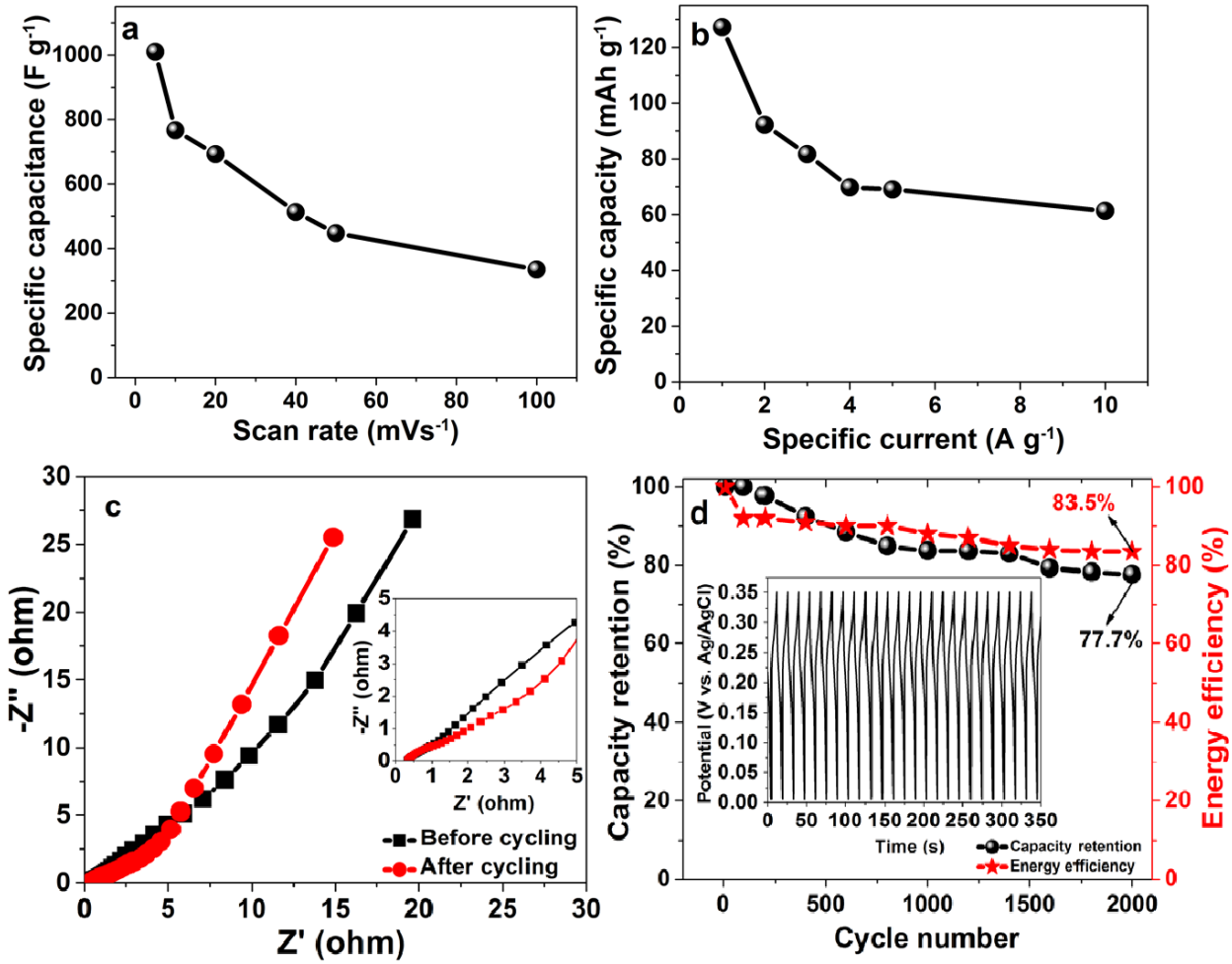

Fig. 6. Plots of (a) specific capacitance vs. scan rate and (b) specific capacity vs. specific current of the Ti_3C_2-Mn_3O_4 composite, (c) EIS Niquist plot Ti_3C_2-Mn_3O_4 composite before and after 2000 cycling, with the zoomed-in high-frequency region of the plot in the inset and (d) cycling performance of Ti_3C_2-Mn_3O_4 composite up to 2000 cycles at 10 A g^{-1}, and the corresponding few cycles of the CD profiles in the inset respectively.

while the specific capacities evaluated from the CD curves at increasing specific currents of 1–10 A g^{-1} ranged from 128.0–61.5 mA h g^{-1}. It is obvious that the material displayed a higher specific capacitance/capacity (1010 F g^{-1}/128 mA h g^{-1}) compared to some other similar Ti_3C_2, and Mn_3O_4-based composites materials earlier reported in the literature [1,38,43,46,58-61]. The high performance is ascribed

to the presence of an optimized orientation of the MXene material in combination with the metal oxide material which synergistically improved the individual properties of both material to provide a combined improved conductivity, swift electron transportation, and larger SSA for more access to aqueous electrolyte to the electrodes [52].

The higher capacitance/capacity values could be attributed to the introduction of Mn_3O_4 nanoparticles, which further modifies the morphology and structure of the Ti_3C_2-Mn_3O_4 nanocomposite sample. Besides, Mn_3O_4 nanoparticles may act like a template for mitigating potential volume changes from cations insertion, and as well as a secondary current collector providing supports for electronic conductivity in the composite reflecting the massive charge being stocked everywhere in the material as well as at the electrolyte-electrode interface compared to Ti_3C_2 electrode [37,65]. Also, the Ti_3C_2 nanosheets in the composite sample perform as conductive span as well as nanoscale collector for electron transfer [1,40].

Fig. 6 (c) demonstrates the EIS graphs of Ti_3C_2-Mn_3O_4 electrode before, and over 2000 charge and discharge cycling at 10 A g^{-1}. The semicircle in the high frequency region shows that resistance of the composite electrode material slightly increased after 2000 cycles as indicated by the inset to Fig. 6 (c).

Fig. 6 (d) is the specific capacity retention and energy efficiency of the Ti_3C_2-Mn_3O_4 composite electrode plotted the cycle number. A discharge capacity of about 77.7% was retained for the single electrode, with a corresponding energy efficiency of about 83.5% for over 2000 cycles at 10 A g^{-1}. The high capacity retention could be ascribed to the material's higher electronic conductivity and the particular pore and perfect separated layered nanosheets structure of Ti_3C_2-Mn_3O_4 material. Moreover, the Ti_3C_2

nanosheets in Ti_3C_2-Mn_3O_4 nanocomposite electrode supply good adhesion to the Mn_3O_4 nanomaterial with a π-π bonding energy which keeps the material intact. This bonding helps to stabilize the Ti_3C_2-Mn_3O_4 nanocomposite mechanically, preventing loss of electrode material while cycling against the prevalent trend of dissolution of Manganese into the electrolyte solution and improves the cycle life of Mn_3O_4-based material electrodes [66,67].

3.2.2. Electrochemical evaluations of the hybrid Ti_3C_2-Mn_3O_4//C-FP supercapattery

Owing to the remarkable performance of Ti_3C_2-Mn_3O_4 nanocomposite electrode material, a hybrid supercapattery was assembled and named as Ti_3C_2-Mn_3O_4//C-FP, with Ti_3C_2-Mn_3O_4: C-FP mass balancing ratio, evaluated using equation 7, as 1.00: 0.74 corresponding to an aerial mass loading of approximately 1.9 and 1.47 mg/cm^2 for Ti_3C_2-Mn_3O_4 and C-FP chosen as positive and negative electrodes accordingly. The Ti_3C_2-Mn_3O_4 nanocomposite electrode was obtained by mixing up the active material with conductive carbon black at a weight ratio of 90:10 for slurry, which was pasted on a nickel foam current collector and dried at 60 $^{\circ}$C overnight in air. The overall area mass loading of both Ti_3C_2-Mn_3O_4 and C-FP active material components in the hybrid device was calculated to be nearly 3.37 mg/cm^2, with an electrode thickness of around 91 µm estimated via microbalance. Performance evaluation of the asymmetric device was performed in a two-electrode configuration using 6 M KOH aqueous electrolyte.

Fig. 7 (a) indicates the CV curves of Ti_3C_2-Mn_3O_4 and C-FP tested as single electrodes at a scan rate of 20 mV s^{-1}. The C-FP material electrode displayed a quasi-rectangular CV curve that is truly comparable to double-layer capacitive

properties. The assembled hybrid device as observed in Fig. 7 (c), could operate in a much larger potential window up to 1.5 V.

Fig. 7 (b) depicts the potential profiles of Ti_3C_2-Mn_3O_4 and C-FP, at a specific current of 1 A g^{-1}. The C-FP negative electrode delivers a specific capacitance of 235 F g^{-1} at 1 A g^{-1} within -1.2 V to 0 V potential ranges. Fig. 7 (c) displays the CV curves of the hybrid Ti_3C_2-Mn_3O_4//C-FP device performed at distinct scan rates in the range of 5 to 100 mV s^{-1}. To our notice, the CV profiles at distinct scan rates portrays a mix of faradic and that of electric-double layer capacitance behaviors, a characteristic feature associated with hybrid SCs [34,36].

Fig. 7 (d) exhibits the CD profiles of the assembled device at various specific currents. The non-symmetric CD profiles indicates the faradaic contribution via redox reactions to the hybrid Ti_3C_2-Mn_3O_4//C-FP device [34,36,68]. This also confirms the assertion made earlier regarding the results from the CV plots demonstrated in Fig. 7 (c).

Fig. 8 (a) demonstrates the estimated specific capacities of the Ti_3C_2-Mn_3O_4//C-FP device using equation 2 and plotted against different specific currents. At specific current of 1 A g^{-1}, the device was noticed to produce maximum a specific capacity of 78.9 mA h g^{-1}. Fig. 8 (b) is a display of the Ragone chart of energy and power densities as two key parameters used to ascertain the applicability of a device. The equivalent energy density together with power density of the assembled device were calculated using equations 4 and 5. A high energy density of 28.3 Wh kg^{-1}, equivalent to a power density of 463.4 W kg^{-1} at a specific current of 1 A g^{-1} was recorded. Remarkably, the device retained a notably high energy density of 22.2 Wh kg^{-1} that is equal to a power density of 2285.5 W kg^{-1} at 5 A g^{-1} specific current.

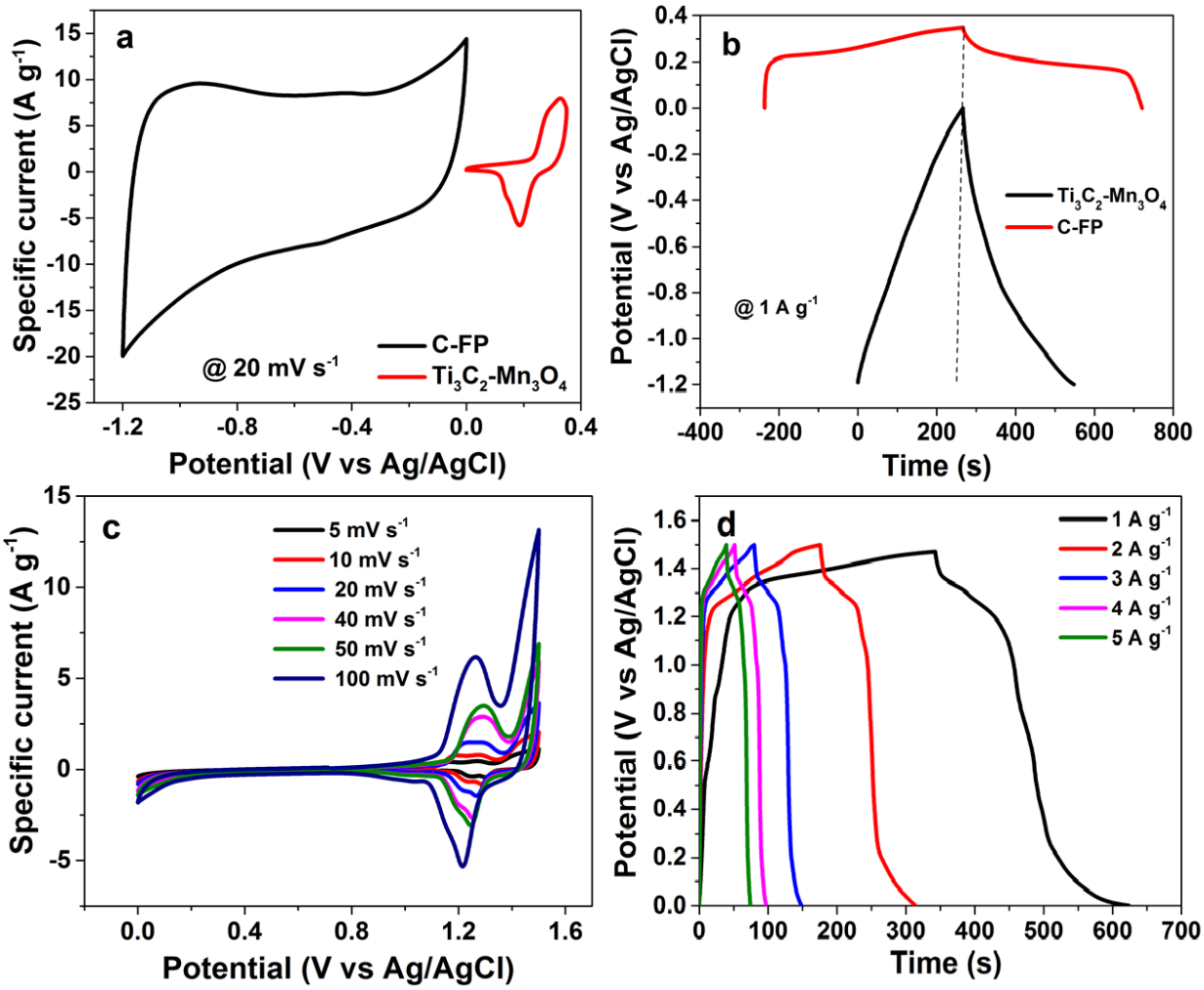

Fig. 7. (a) CV curves of Ti_3C_2-Mn_3O_4 and C-FP, (b) CD curves of Ti_3C_2-Mn_3O_4 and C-FP, (c) CV curves of Ti_3C_2-Mn_3O_4//C-FP at distinct scan rates, and (d) CD profiles of Ti_3C_2-Mn_3O_4//C-FP at various specific currents of the asymmetric device.

This is an indication that the assembled hybrid *SC* is able to deliver a large power density without a significant loss of the stored energy [34]. This indication resolves the importance of the point that as greatly as the hope in the study of supercapacitor is to enhance its energy capability to contend with that of battery, but not expected to be accomplished at the cost of compromising its power density [34]. The energy density obtained for asymmetric device in this work compares well with some other recently published asymmetric devices in the literature [69–72].

From Fig. 8 (c), it could be noticed that the device showcased a superior energy efficiency of 90.2 % determined using equation 3. The device also preserved 92.6 % of the initial capacity after continuously cycling for up to a 10000 cycles at a specific current of 3 A g^{-1}. This demonstrates an excellent long-term electrochemical stability of the asymmetric device. Such remarkable stability is mostly uncommon for supercapattery-type devices but EDLC. The unmatched behavior is ascribed to the mesoporous nature of the Ti_3C_2-Mn_3O_4 nanocomposite material that plays a crucial part in raising the efficient electrode surface area, easing electrolyte permeability, thereby narrowing electron pathway in the active materials [34,73]. The mesopores in the Ti_3C_2-Mn_3O_4 nanocomposite structure provide improved accessibility towards the reactant molecules cations through the interlayer space [74]. Furthermore, the distinguished mesoporous structure could suit well the OH^- ions, thus promoting electrochemical improvement as a result of closely packed ionic layers lying on both adjoining hole walls [73,75]. This mesoporous nature could as well contribute to ion and electron flow, repressing any modification of electrode volume in the charge-discharge process [76].

In Fig. 8(d) the EIS analysis employed to further assess the properties of the device is shown. From the plots, the solution resistances, R_s before and after 10000 cycles were estimated to be 0.86 Ω and 0.89 Ω, respectively, showing the suitability of electrical behaviours of the material adopted in fabricating the hybrid *SC*. The R_s which occurs at the intercept to the Z'-axis in the high frequency region, is a summed up of resistance in the electrolyte together with that between the contact and the material electrode.

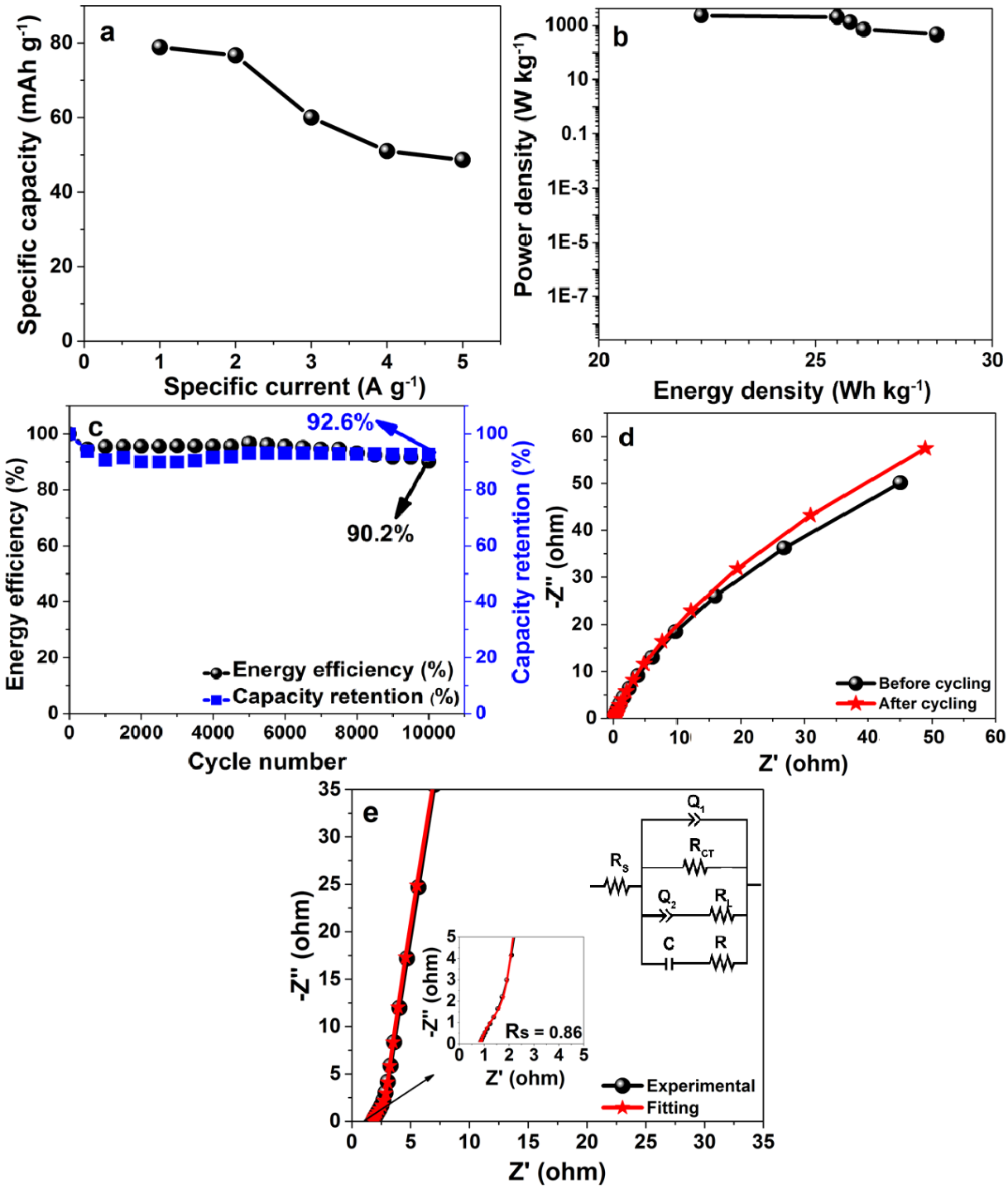

Fig. 8. (a) Specific capacity vs. specific current and (b) Ragone plot, (c) cyclic performance, (d) EIS before and over 10000 cycles at a specific current of 3 A g^{-1}, and (e) the fitted Nyquist plot by using equivalent circuit (inset) of the Ti_3C_2-Mn_3O_4//C-FP asymmetric device.

Following cycling, the diffusion path length was noticed to have drifted towards the optimal perpendicular nature, and is attributed to the optimum use or sufficient active material during redox reaction [34], irrespective of the high specific current.

Moreover, the Nyquist plot for Ti_3C_2-Mn_3O_4//C-FP asymmetric device was fitted as shown in Fig. 8(e) with aid of a ZFIT fitting program v11.02, with its corresponding electrical circuit displayed in the inset. From the circuit, the R_S is joined in series with a constant phase element (CPE) Q_1, that is parallely connected to the charge transfer resistance, R_{CT}. The leakage current resistance, R_L is in series with another CPE, Q_2. The mass capacitance indicated as C is joined parallel to load resistance, R_L, all of which are in series with the R_S.

Conclusion

Ti_3C_2-Mn_3O_4 nanocomposite electrode materials were successfully synthesized by a solvothermal process which permits for the exact influence on the magnitude, form, as well as crystallinity of the metal oxide nanostructures, by introducing Mn_3O_4 into the Ti_3C_2 layers with the aim of taking advantage of the surface functionalities on the MXene sheets. The characterization of the composite electrode material confirmed that the as-synthesized material is composed of a layered structure of nanosheets which are clearly delaminated with the integration of the metal oxide nanoparticles into the interlayer spaces. The material demonstrated an enhanced electrochemical performance with a recorded specific capacity value of 128 mAh g^{-1} at specific current of 1 A g^{-1}. The great performance was illustrated by the Ti_3C_2-Mn_3O_4 composite material capacitance/capacity, satisfactory cycling stability as well as the 77.65 %

capacity retention for up to 2000 constant CD cycles at 10 A g^{-1}. An assembled low cost hybrid Ti_3C_2-Mn_3O_4//C-FP SC device in 6 M KOH electrolyte yielded a comparable energy density of 28.32 Wh kg^{-1} with an equivalent high power density of 463.42 W kg^{-1} at a specific current of 1 A g^{-1}, and a 92.6% capacity retention for over 10000 cycling test. The device was observed to maintain a considerably high energy density of 22.22 Wh kg^{-1} with corresponding power density of 2285.49 W kg^{-1} at a high specific current of 5 A g^{-1}. The research provides an addition to the knowledge of 2D MXene-based composites and is useful in designing novel high-performance hybrid electrode materials with promising device efficiency for supercapacitors applications.

Acknowledgements

This study is supported by the South African Research Chairs Initiative of the Department of Science and Technology and National Research Foundation of South Africa (Grant No. 61056). All observations and results put forward in this material are those of the authors, and the NRF does not take a liability regarding this. The authors are grateful for the invaluable inputs by Prof. Yury Gogotsi of the Department of Materials Science & Engineering, Drexel University, 3141 Chestnut Street, Philadelphia 19104, USA. And Dr. Farshad Barzegar from University of Pretoria for valuable discussions. K. O. appreciates the financial assistance from the University of Pretoria and National Research Foundation (NRF) for studentship grants.

References

[1] C. Zhao, Q. Wang, H. Zhang, S. Passerini, X. Qian, Two-Dimensional Titanium Carbide/RGO Composite for High-Performance Supercapacitors, ACS Appl. Mater. Interfaces. 8 (2016) 15661–15667. doi:10.1021/acsami.6b04767.

[2] G. Yu, X. Xie, L. Pan, Z. Bao, Y. Cui, Hybrid nanostructured materials for high-performance electrochemical capacitors, Nano Energy. 2 (2013) 213–234. doi:10.1016/j.nanoen.2012.10.006.

[3] F. Wang, M. Cao, Y. Qin, J. Zhu, L. Wang, Y. Tang, ZnO nanoparticle-decorated two-dimensional titanium carbide with enhanced supercapacitive performance, RSC Adv. 6 (2016) 88934–88942. doi:10.1039/C6RA15384D.

[4] P. Liu, M. Verbrugge, S. Soukiazian, Influence of temperature and electrolyte on the performance of activated-carbon supercapacitors, J. Power Sources. 156 (2006) 712–718. doi:10.1016/j.jpowsour.2005.05.055.

[5] Z. Zhang, Q. Wang, C. Zhao, S. Min, X. Qian, One-Step Hydrothermal Synthesis of 3D Petal-like Co 9 S 8 /RGO/Ni 3 S 2 Composite on Nickel Foam for High-Performance Supercapacitors, *ACS appl. mater. interfaces*. **7** (2015) 4861-4868. doi:10.1021/am5088192.

[6] K.S. Novoselov, A.K. Geim, S. V. Morozov, D. Jiang, Y. Zhang, S. V. Dubonos, I. V. Grigorieva, A.A. Firsov, Electric Field Effect in Atomically Thin Carbon Films, Science (80-.). 306 (2004) 666-669. doi: 10.1126/science.1102896.

[7] H. Zhang, Ultrathin Two-Dimensional Nanomaterials, ACS Nano Lecturesh. Award. 9 (2015) 9451–9469. doi:10.1021/acsnano.5b05040.

[8] Y. Liu, X. Peng, Recent advances of supercapacitors based on two-dimensional materials, Appl. Mater. Today. 7 (2017) 1–12. doi:10.1016/j.apmt.2017.01.004.

[9] T. Palaniselvam, J.-B. Baek, Graphene based 2D-materials for supercapacitors, 2D Mater. 2 (2015) 032002. doi:10.1088/2053-1583/2/3/032002.

[10] X. Peng, L. Peng, C. Wu, Y. Xie, Two dimensional nanomaterials for flexible supercapacitors, Chem. Soc. Rev. 43 (2014) 3303. doi:10.1039/c3cs60407a.

[11] M. Naguib, V.N. Mochalin, M.W. Barsoum, Y. Gogotsi, 25th anniversary article: MXenes: A new family of two-dimensional materials, Adv. Mater. 26 (2014) 992–1005. doi:10.1002/adma.201304138.

[12] L. Dong, H. Kumar, B. Anasori, Y. Gogotsi, V.B. Shenoy, Rational Design of Two-Dimensional Metallic and Semiconducting Spintronic Materials Based on Ordered Double-Transition-Metal MXenes, J. Phys. Chem. Lett. 8 (2017) 422-428. doi:10.1021/acs.jpclett.6b02751.

[13] B. Anasori, M.R. Lukatskaya, Y. Gogotsi, 2D metal carbides and nitrides (MXenes) for energy storage, Nat. Rev. Mater. 2 (2017) 16098. doi:10.1038/natrevmats.2016.98.

[14] A.D. Dillon, M.J. Ghidiu, A.L. Krick, J. Griggs, S.J. May, Y. Gogotsi, M.W. Barsoum, A.T. Fafarman, Highly Conductive Optical Quality Solution-Processed Films of 2D Titanium Carbide, Adv. Funct. Mater. 26 (2016) 4162–4168. doi:10.1002/adfm.201600357.

[15] X. Liang, A. Garsuch, L.F. Nazar, Sulfur Cathodes Based on Conductive MXene Nanosheets for High-Performance Lithium-Sulfur Batteries, Angew. Chemie Int. Ed. 54 (2015) 3907–3911. doi:10.1002/anie.201410174.

[16] C.E. Ren, K.B. Hatzell, M. Alhabeb, Z. Ling, K.A. Mahmoud, Y. Gogotsi, Charge- and Size-Selective Ion Sieving Through $Ti_3C_2T_x$ MXene Membranes, J. Phys. Chem. Lett. 6 (2015) 4026–4031. doi:10.1021/acs.jpclett.5b01895.

[17] Z.W. Seh, K.D. Fredrickson, B. Anasori, J. Kibsgaard, A.L. Strickler, M.R. Lukatskaya, Y. Gogotsi, T.F. Jaramillo, A. Vojvodic, Two-Dimensional Molybdenum Carbide (MXene) as an Efficient Electrocatalyst for Hydrogen Evolution, ACS Energy Lett. 1 (2016) 589–594. doi:10.1021/acsenergylett.6b00247.

[18] F. Shahzad, M. Alhabeb, C.B. Hatter, B. Anasori, S. Man Hong, C.M. Koo, Y. Gogotsi, Electromagnetic interference shielding with 2D transition metal carbides (MXenes), Science. 353 (2016) 1137-1140. doi: 10.1126/science.aag2421.

[19] M. Naguib, J. Halim, J. Lu, K.M. Cook, L. Hultman, Y. Gogotsi, M.W. Barsoum, New two-dimensional niobium and vanadium carbides as promising materials for li-ion batteries, J. Am. Chem. Soc. 135 (2013) 15966-15969. doi:10.1021/ja405735d.

[20] C. Eames, M.S. Islam, Ion intercalation into two-dimensional transition-metal carbides: Global screening for new high-capacity battery materials, J. Am. Chem. Soc. 136 (2014) 16270-16276. doi:10.1021/ja508154e.

[21] M. Naguib, O. Mashtalir, J. Carle, V. Presser, J. Lu, L. Hultman, Y. Gogotsi, M.W. Barsoum, Two-Dimensional Transition Metal Carbides Herein we report on the synthesis of two-dimensional transition metal carbides, *ACS nano.* 6 (2012) 1322-1331. doi:10.1021/nn204153h.

[22] J. Pike, J. Hanson, L. Zhang, S. Chan, Synthesis and Redox Behavior of Nanocrystalline Hausmannite (Mn_3O_4), Chem. Mater. 19 (2007) 5609–5616. doi:10.1021/cm071704b.

[23] J.C. Nardi, Characterization of the Li/MnO[sub 2] Multistep Discharge, J. Electrochem. Soc. 132 (1985) 1787. doi:10.1149/1.2114218.

[24] X. Li, L. Zhou, J. Gao, H. Miao, H. Zhang, J. Xu, Synthesis of Mn_3O_4 nanoparticles and their catalytic applications in hydrocarbon oxidation, Powder Technol. 190 (2009) 324–326. doi:10.1016/j.powtec.2008.08.010.

[25] C.J. Jafta, F. Nkosi, L. le Roux, M.K. Mathe, M. Kebede, K. Makgopa, Y. Song, D. Tong, M. Oyama, N. Manyala, S. Chen, K.I. Ozoemena, Manganese oxide/graphene oxide composites for high-energy aqueous asymmetric electrochemical capacitors, Electrochim. Acta. 110 (2013) 228–233. doi:10.1016/j.electacta.2013.06.096.

[26] K. Makgopa, P.M. Ejikeme, C.J. Jafta, K. Raju, M. Zeiger, V. Presser, K.I. Ozoemena, A high-rate aqueous symmetric pseudocapacitor based on highly graphitized onion-like carbon/birnessite-type manganese oxide nanohybrids, J. Mater. Chem. A. 3 (2015) 3480–3490. doi:10.1039/C4TA06715K.

[27] A. Bello, O.O. Fashedemi, J.N. Lekitima, M. Fabiane, D. Dodoo-Arhin, K.I. Ozoemena, Y. Gogotsi, A.T. Charlie Johnson, N. Manyala, High-performance symmetric electrochemical capacitor based on graphene foam and nanostructured manganese oxide, AIP Adv. 3 (2013) 082118. doi:10.1063/1.4819270.

[28] Y. Hu, J. Chen, X. Xue, T. Li, Synthesis of monodispersed single-crystal compass-shaped Mn3O4 via gamma-ray irradiation, Mater. Lett. 60 (2006) 383–385. doi:10.1016/j.matlet.2005.08.056.

[29] K.I. Ozoemena, K. Raju, P.M. Ejikeme, K.I. Ozoemena, High-performance Mn_3O_4/onion-like carbon (OLC) nanohybrid pseudocapacitor: Unravelling the intrinsic properties of OLC against other carbon supports, Carbon N. Y. 117 (2017) 20–32. doi:10.1016/j.carbon.2017.02.050.

[30] T. Xiong, W.S.V. Lee, X. Huang, J.M. Xue, Mn_3O_4 /reduced graphene oxide based supercapacitor with ultra-long cycling performance, J. Mater. Chem. A. 5 (2017) 12762–12768. doi:10.1039/C7TA03319B.

[31] C.-L. Liu, K.-H. Chang, C.-C. Hu, W.-C. Wen, Microwave-assisted hydrothermal synthesis of Mn3O4/reduced graphene oxide composites for high power supercapacitors, J. Power Sources. 217 (2012) 184–192. doi:10.1016/j.jpowsour.2012.05.109.

[32] Q. Jiangying, G. Feng, Z. Quan, W. Zhiyu, H. Han, L. Beibei, W. Wubo, W. Xuzhen, Q. Jieshan, Highly atom-economic synthesis of graphene/Mn3O4 hybrid composites for electrochemical supercapacitors, Nanoscale. 5 (2013) 2999. doi:10.1039/c3nr33700f.

[33] M. Naguib, M. Kurtoglu, V. Presser, J. Lu, J. Niu, M. Heon, L. Hultman, Y. Gogotsi, M.W. Barsoum, Two-dimensional nanocrystals produced by exfoliation of Ti 3AlC 2, Adv. Mater. 23 (2011) 4248–4253. doi:10.1002/adma.201102306.

[34] K.O. Oyedotun, M.J. Madito, D.Y. Momodu, A.A. Mirghni, T.M. Masikhwa, N. Manyala, Synthesis of ternary NiCo-MnO 2 nanocomposite and its application as a novel high energy supercapattery device, Chem. Eng. J. 335 (2018) 416–433. doi:10.1016/j.cej.2017.10.169.

[35] M.N. Rantho, M.J. Madito, F.O. Ochai-Ejeh, N. Manyala, an Asymmetric supercapacitor based on vanadium disulfide nanosheets as a cathode and carbonized iron cations adsorbed onto polyaniline as node, Electrochim. Acta. 260 (2017) 11–23. doi:10.1016/j.electacta.2017.11.074.

[36] C. Zhang, K.B. Hatzell, M. Boota, B. Dyatkin, M. Beidaghi, D. Long, W. Qiao, E.C. Kumbur, Y. Gogotsi, Highly porous carbon spheres for electrochemical capacitors and capacitive flowable suspension electrodes, Carbon N. Y. 77 (2014) 155–164. doi:10.1016/j.carbon.2014.05.017.

[37] K.O. Oyedotun, M.J. Madito, A. Bello, D.Y. Momodu, A.A. Mirghni, N. Manyala, Investigation of graphene oxide nanogel and carbon nanorods as electrode for electrochemical supercapacitor, Electrochim. Acta. 245 (2017) 268–278. doi:10.1016/j.electacta.2017.05.150.

[38] R.B. Rakhi, B. Ahmed, M.N. Hedhili, D.H. Anjum, H.N. Alshareef, Effect of post-etch annealing gas composition on the structural and electrochemical properties of Ti2CTx MXene electrodes for supercapacitor applications, Chem. Mater. 27 (2015) 5314-5323. doi:10.1021/acs.chemmater.5b01623.

[39] F. Davar, M. Salavati-Niasari, N. Mir, K. Saberyan, M. Monemzadeh, E. Ahmadi, Thermal decomposition route for synthesis of Mn3O4 nanoparticles in presence of a novel precursor, Polyhedron. 29 (2010) 1747–1753. doi:10.1016/j.poly.2010.02.026.

[40] K. Wang, C. Zhao, S. Min, X. Qian, Facile synthesis of Cu2O/RGO/Ni(OH)2 nanocomposite and its double synergistic effect on supercapacitor performance, Electrochim. Acta. 165 (2015) 314-322. doi:10.1016/j.electacta.2015.03.029.

[41] M. Ghidiu, J. Halim, S. Kota, D. Bish, Y. Gogotsi, M.W. Barsoum, Ion-Exchange and Cation Solvation Reactions in Ti3C2 MXene, Chem. Mater. 28 (2016) 3507–3514. doi:10.1021/acs.chemmater.6b01275.

[42] Y. Li, X. Zhou, J. Wang, Q. Deng, M. Li, S. Du, Y.-H. Han, J. Lee, Q. Huang, Facile preparation of in situ coated $Ti_3C_2T_x$ /$Ni_{0.5}Zn_{0.5}Fe_2O_4$ composites and their electromagnetic performance, RSC Adv. 7 (2017) 24698–24708. doi:10.1039/C7RA03402D.

[43] M. Naguib, O. Mashtalir, M.R. Lukatskaya, B. Dyatkin, C. Zhang, V. Presser, Y. Gogotsi, M.W. Barsoum, One-step synthesis of nanocrystalline transition metal oxides on thin sheets of disordered graphitic carbon by oxidation of MXenes, Chem. Commun. 50 (2014) 7420–7423. doi:10.1039/C4CC01646G.

[44] J. Zhu, Y. Tang, C. Yang, F. Wang, M. Cao, Composites of TiO_2 Nanoparticles Deposited on Ti_3C_2 MXene Nanosheets with Enhanced Electrochemical Performance, J. Electrochem. Soc. 163 (2016) A785–A791. doi:10.1149/2.0981605jes.

[45] A.A. Khaleed, A. Bello, J.K. Dangbegnon, M.J. Madito, O. Olaniyan, F. Barzegar, K. Makgopa, K.O. Oyedotun, B.W. Mwakikunga, S.C. Ray, N. Manyala, Solvothermal synthesis of surfactant free spherical nickel hydroxide/graphene oxide composite for supercapacitor application, J. Alloys Compd. 721 (2017) 80–91. http://dx.doi.org/10.1016/j.jallcom.2017.05.310.

[46] Y. Liu, R. Wang, X. Yan, Synergistic Effect between Ultra-Small Nickel Hydroxide Nanoparticles and Reduced Graphene Oxide sheets for the Application in High-Performance Asymmetric Supercapacitor, Sci. Rep. 5 (2015) 11095. doi:10.1038/srep11095.

[47] M. Naguib, T. Saito, S. Lai, M.S. Rager, T. Aytug, M. Parans Paranthaman, M.-Q. Zhao, Y. Gogotsi, $Ti_3C_2T_x$ (MXene)–polyacrylamide nanocomposite films, RSC Adv. 6 (2016) 72069–72073. doi:10.1039/C6RA10384G.

[48] C. Zhang, M. Beidaghi, M. Naguib, M.R. Lukatskaya, M.Q. Zhao, B. Dyatkin, K.M. Cook, S.J. Kim, B. Eng, X. Xiao, D. Long, W. Qiao, B. Dunn, Y. Gogotsi, Synthesis and Charge Storage Properties of Hierarchical Niobium

Pentoxide/Carbon/Niobium Carbide (MXene) Hybrid Materials, Chem. Mater. 28 (2016) 3937–3943. doi:10.1021/acs.chemmater.6b01244.

[49] Y. Tang, J. Zhu, C. Yang, F. Wang, Enhanced supercapacitive performance of manganese oxides doped two-dimensional titanium carbide nanocomposite in alkaline electrolyte, J. Alloys Compd. 685 (2016) 194–201. doi:10.1016/j.jallcom.2016.05.221.

[50] Y. Qiao, Q. Sun, H. Cui, D. Wang, F. Yang, X. Wang, Synthesis of micro/nano-structured Mn3O4 for supercapacitor electrode with excellent rate performance, RSC Adv. 5 (2015) 31942–31946. doi:10.1039/c5ra02395e.

[51] J. Xiang, Y. Ding, L. Du, J. Li, Growth mechanism of atomic-layer-deposited TiAlC metal gate based on TiCl4 and TMA precursors, Chinese Phys. B. 25 (2016) 1–4. doi:10.1088/1674-1056/25/3/037308.

[52] Y. Tang, J. Zhu, C. Yang, F. Wang, Enhanced Capacitive Performance Based on Diverse Layered Structure of Two-Dimensional Ti_3C_2 MXene with Long Etching Time, J. Electrochem. Soc. 163 (2016) A1975–A1982. doi:10.1149/2.0921609jes.

[53] J. Duan, S. Chen, S. Dai, S.Z. Qiao, Shape control of Mn3O4 nanoparticles on nitrogen-doped graphene for enhanced oxygen reduction activity, Adv. Funct. Mater. 24 (2014) 2072–2078. doi:10.1002/adfm.201302940.

[54] F. Zheng, D. Zhu, X. Shi, Q. Chen, Metal–organic framework-derived porous $Mn_{1.8}Fe_{1.2}O_4$ nanocubes with an interconnected channel structure as high-performance anodes for lithium ion batteries, J. Mater. Chem. A. 3 (2015) 2815–2824. doi:10.1039/C4TA06150K.

[55] C. Yuan, J. Li, L. Hou, X. Zhang, L. Shen, X.W. Lou, Ultrathin mesoporous NiCo 2O 4 nanosheets supported on Ni foam as advanced electrodes for supercapacitors, Adv. Funct. Mater. 22 (2012) 4592–4597. doi:10.1002/adfm.201200994.

[56] M.R. Lukatskaya, S.-M. Bak, X. Yu, X.-Q. Yang, M.W. Barsoum, Y. Gogotsi, Probing the Mechanism of High Capacitance in 2D Titanium Carbide Using In Situ X-Ray Absorption Spectroscopy, Adv. Energy Mater. 5 (2015) 1500589. doi:10.1002/aenm.201500589.

[57] M. Li, J.P. Cheng, J.H. Fang, Y. Yang, F. Liu, X.B. Zhang, NiAl-layered Double Hydroxide/Reduced Graphene Oxide Composite: Microwave-assisted Synthesis and Supercapacitive Properties, Electrochim. Acta. 134 (2014) 309–318. doi:10.1016/j.electacta.2014.04.141.

[58] X. Xiao, B. Han, G. Chen, L. Wang, Y. Wang, Preparation and electrochemical performances of carbon sphere@ZnO core-shell nanocomposites for supercapacitor applications, Sci. Rep. 7 (2017) 40167. doi:10.1038/srep40167.

[59] J. Li, X. Cao, A. Pan, Y. Zhao, H. Yang, G. Cao, S. Liang, Nanoflake-assembled three-dimensional Na3V2(PO4)3/C cathode for high performance sodium ion batteries, Chem. Eng. J. 335 (2018) 301–308. doi:10.1016/j.cej.2017.10.164.

[60] X. Cao, A. Pan, Y. Zhang, J. Li, Z. Luo, X. Yang, S. Liang, G. Cao, Nanorod-Nanoflake Interconnected $LiMnPO_4 \cdot Li3V2(PO_4)_3$/C Composite for High-Rate and Long-Life Lithium-Ion Batteries, ACS Appl. Mater. Interfaces. 8 (2016) 27632–27641. doi:10.1021/acsami.6b06456.

[61] Nanosheets based mesoporous NiO microspherical structures via facile and template-free method for high performance supercapacitors, Electrochim. Acta. 56 (2011) 4849–4857. doi:10.1016/J.ELECTACTA.2011.02.116.

[62] A.G. Dylla, G. Henkelman, K.J. Stevenson, Lithium insertion in nanostructured TiO2(B) architectures, Acc. Chem. Res. 46 (2013) 1104–1112. doi:10.1021/ar300176y.

[63] M.Q. Zhao, C.E. Ren, Z. Ling, M.R. Lukatskaya, C. Zhang, K.L. Van Aken, M.W. Barsoum, Y. Gogotsi, Flexible MXene/carbon nanotube composite paper with high volumetric capacitance, Adv. Mater. 27 (2015) 339–345. doi:10.1002/adma.201404140.

[64] R.B. Rakhi, B. Ahmed, D. Anjum, H.N. Alshareef, Direct Chemical Synthesis of MnO2 Nanowhiskers on Transition-Metal Carbide Surfaces for Supercapacitor Applications, ACS Appl. Mater. Interfaces. 8 (2016) 18806–18814. doi:10.1021/acsami.6b04481.

[65] P. Karthika, N. Rajalakshmi, K.S. Dhathathreyan, Functionalized Exfoliated Graphene Oxide as Supercapacitor Electrodes, 2 (2012) 59. doi:10.4236/SNL.2012.24011.

[66] G. Yu, L. Hu, N. Liu, H. Wang, M. Vosgueritchian, Y. Yang, Y. Cui, Z. Bao, Enhancing the supercapacitor performance of graphene/MnO2 nanostructured electrodes by conductive wrapping, Nano Lett. 11 (2011) 4438–4442. doi:10.1021/nl2026635.

[67] G.S. Gund, D.P. Dubal, B.H. Patil, S.S. Shinde, C.D. Lokhande, Enhanced activity of chemically synthesized hybrid graphene oxide/Mn 3O4 composite for high performance supercapacitors, Electrochim. Acta. 92 (2013) 205–215. doi:10.1016/j.electacta.2012.12.120.

[68] J.F. Marco, J.R. Gancedo, M. Gracia, J.L. Gautier, E.I. Rios, H.M. Palmer, C. Greaves, F.J. Berry, Cation distribution and magnetic structure of the ferrimagnetic spinel NiCo2O4, J. Mater. Chem. 11 (2001) 3087–3093. doi:10.1039/B103135J.

[69] Z.S. Wu, D.W. Wang, W. Ren, J. Zhao, G. Zhou, F. Li, H.M. Cheng, Anchoring hydrous RuO2 on graphene sheets for high-performance electrochemical capacitors, Adv. Funct. Mater. 20 (2010) 3595–3602. doi:10.1002/adfm.201001054.

[70] Z.-S. Wu, W. Ren, D.-W. Wang, F. Li, B. Liu, H.-M. Cheng, High-Energy MnO_2 Nanowire/Graphene and Graphene Asymmetric Electrochemical Capacitors, ACS Nano. 4 (2010) 5835–5842. doi:10.1021/nn101754k.

[71] Q. Jiang, N. Kurra, M. Alhabeb, Y. Gogotsi, and H. N. Alshareef, All Pseudocapacitive MXene-RuO2 Asymmetric Supercapacitors, Adv. Energy Mater. 8

(2018) 1703043. doi: 10.1002/aenm.201703043.

[72] H. Chen, L. Hu, Y. Yan, R. Che, M. Chen, L. Wu, One-step fabrication of ultrathin porous nickel hydroxide-manganese dioxide hybrid nanosheets for supercapacitor electrodes with excellent capacitive performance, Adv. Energy Mater. 3 (2013) 1636–1646. doi:10.1002/aenm.201300580.

[73] T. Chen, Y. Tang, Y. Qiao, Z. Liu, W. Guo, J. Song, S. Mu, S. Yu, Y. Zhao, F. Gao, All-solid-state high performance asymmetric supercapacitors based on novel MnS nanocrystal and activated carbon materials, Sci. Rep. 6 (2016) 23289. doi:10.1038/srep23289.

[74] A. Bergmann, I. Zaharieva, H. Dau, P. Strasser, Electrochemical water splitting by layered and 3D cross-linked manganese oxides: correlating structural motifs and catalytic activity, Energy Environ. Sci. 6 (2013) 2745. doi:10.1039/c3ee41194j.

[75] E. Raymundo-Piñero, P. Azaïs, T. Cacciaguerra, D. Cazorla-Amorós, A. Linares-Solano, F. Béguin, KOH and NaOH activation mechanisms of multiwalled carbon nanotubes with different structural organisation, Carbon N. Y. 43 (2005) 786–795. doi:10.1016/j.carbon.2004.11.005.

[76] J. Zhang, F. Liu, J.P. Cheng, X.B. Zhang, Binary Nickel-Cobalt Oxides Electrode Materials for High-Performance Supercapacitors: Influence of its Composition and Porous Nature, ACS Appl. Mater. Interfaces. 7 (2015) 17630–17640. doi:10.1021/acsami.5b04463.

Electrochemical performance of two-dimensional Ti_3C_2-Mn_3O_4 nanocomposites and carbonized iron cations for hybrid supercapacitor electrodes

Kabir O. Oyedotun[1], Damilola Y. Momodu[1], Michael Naguib[2], Abdulmajid A. Mirghni[1], Tshifhiwa M. Masikhwa[1], Abubakar A. Khaleed[1], Mesfin Kebede[3], and Ncholu Manyala[1]*

[1]Department of Physics, Institute of Applied Materials, SARCHI Chair in Carbon Technology and Materials, University of Pretoria, Pretoria 0028, South Africa.
[2]Department of Physics and Engineering Physics, Tulane University, New Orleans, LA 70118, USA.
[3]Energy Materials, Materials Science and Manufacturing, Council for Scientific and Industrial Research (CSIR), Pretoria, 0001, South Africa
*Corresponding author's email: ncholu.manyala@up.ac.za, Tel.: + (27)12 420 3549.

SUPPORTING INFORMATION

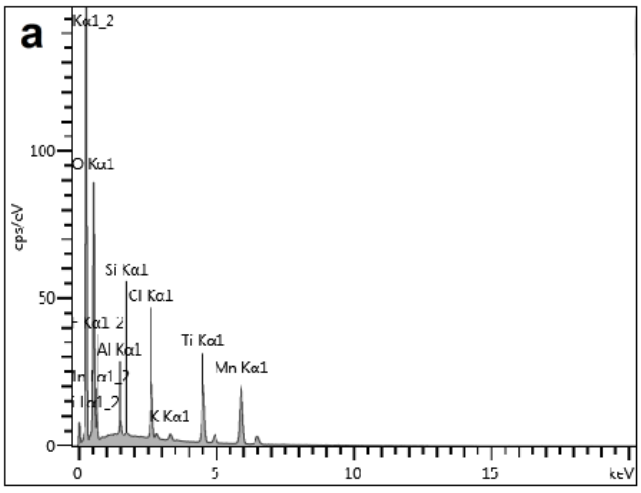

b

Element	Line Type	Apparent Concentration	k Ratio	Wt%	Wt% Sigma	Standard Label
C	K series	19.61	0.19609	39.63	0.16	C Vit
O	K series	21.19	0.07132	17.40	0.10	SiO_2
F	K series	1.85	0.00362	1.07	0.05	CaF_2
Al	K series	0.58	0.00413	0.65	0.02	Al_2O_3
Si	K series	0.14	0.00115	0.17	0.02	SiO_2
Cl	K series	3.81	0.03333	4.61	0.05	NaCl
K	K series	0.56	0.00473	0.64	0.03	KBr
Ti	K series	8.61	0.08610	12.07	0.09	Ti
Mn	K series	15.73	0.15730	23.75	0.14	Mn
Total:				100.00		

Fig. S1. (a) EDX spectrum, and (b) table of chemical analysis of Ti_3C_2-Mn_3O_4 nanocomposite respectively.

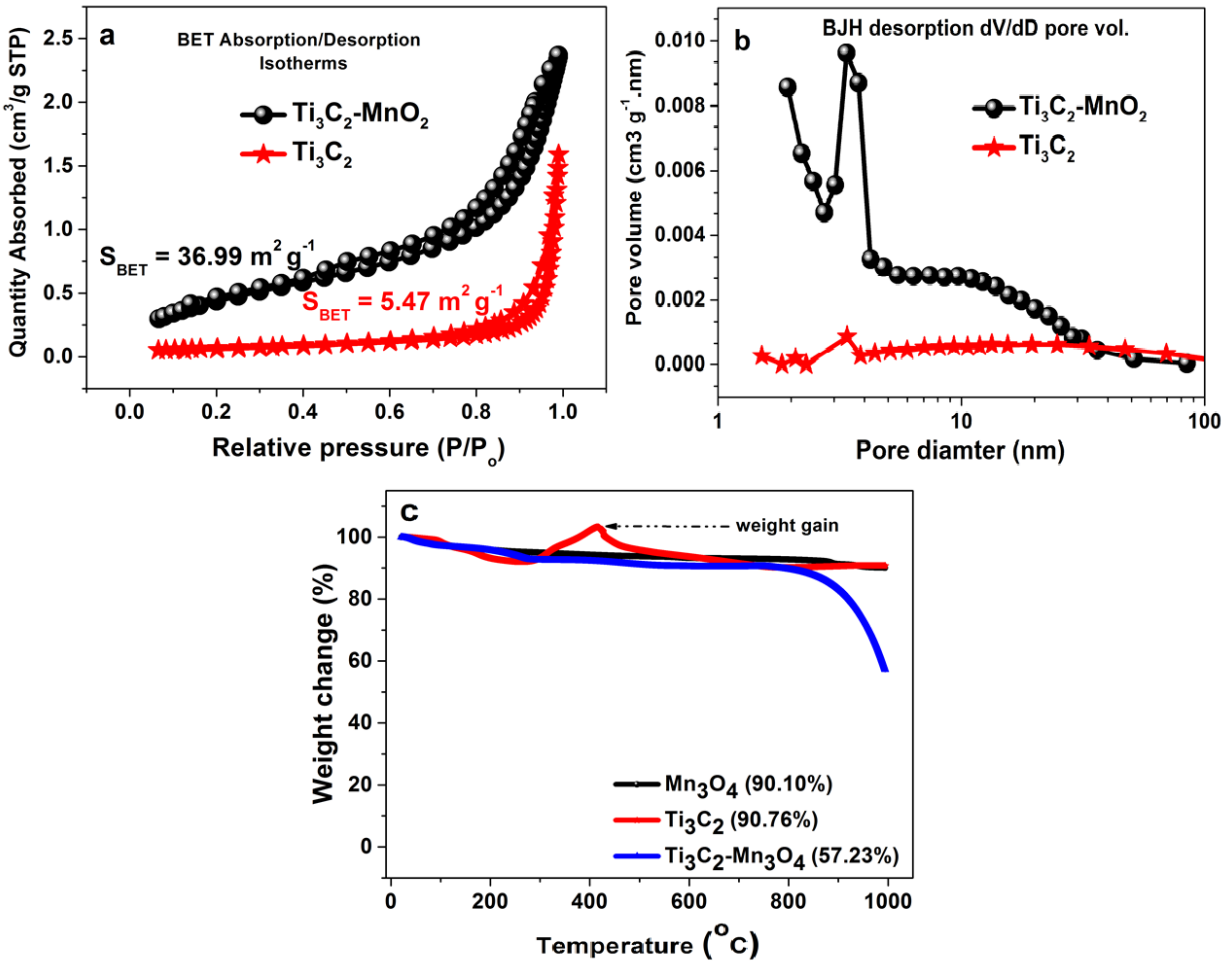

Fig. S2. (a) N_2 isotherms and (b) pore size distribution of Ti_3C_2-Mn_3O_4, and (c) Thermogravimetric analysis curves of Ti_3C_2, Mn_3O_4 and Ti_3C_2-Mn_3O_4 nanocomposite.

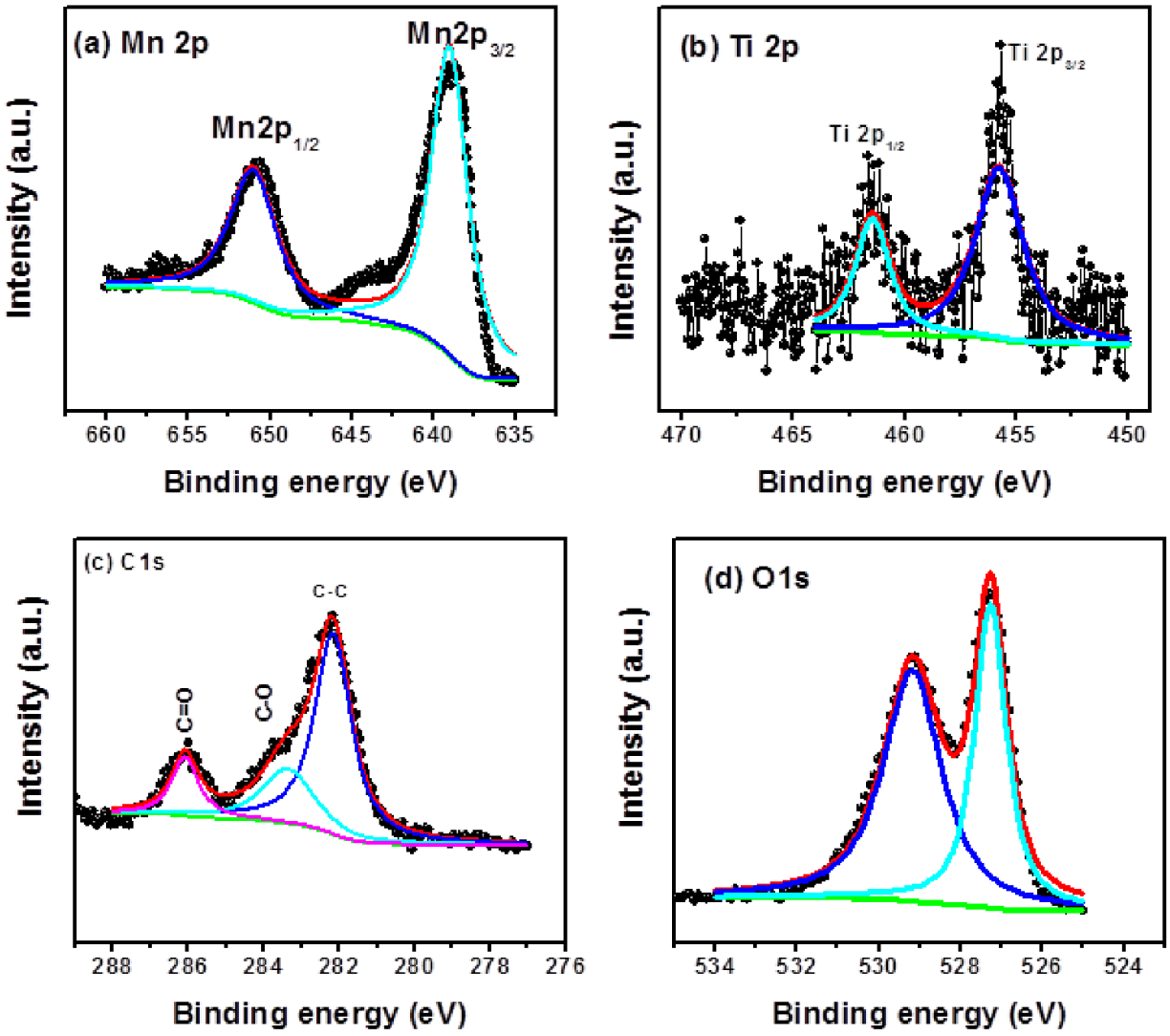

Fig. S3. The core level spectrum of (a) Mn 2p, (b) Ti 2p, (c) C 1s and (d) O 1s of a Ti3C2-Mn3O4 nanocomposite respectively.

Table S1: Showing XRF analysis of as-synthesized Ti_2C_3-Mn_3O_4 nanocomposite.

Compound	**Weight %**
Al_2O_3	2.41
K_2O	0.80
Na_2O	0.67
MgO	0.23
Sm_2O_3	0.13
Tb_4O_7	0.10
SiO_2	0.07
V_2O_5	0.05
Gd_2O_3	0.03
Cl	0.03
Co_3O_4	0.03
CaO	0.02
P	0.02
Au	0.01
MoO_3	0.01
La_2O_3	0.01
PtO_2	0.01
% Mn_3O_4	79.83
Remaining % Ti_3C_2	15.56
TOTAL	**100.00**

4.3.3 Concluding Remarks

Ti_3C_2-Mn_3O_4 nanocomposite electrode materials were successfully synthesized by a solvothermal process which allows for the precise control of the size, shape distribution, and crystallinity of the metal oxide nanostructures, by introducing Mn_3O_4 into the Ti_3C_2 layers with the aim of taking advantage of the surface functionalities on the MXene sheets. The material demonstrated an enhanced electrochemical performance with a recorded specific capacity value of 128 mAh g^{-1} at specific current of 1 A g^{-1}. An assembled low cost hybrid Ti_3C_2-Mn_3O_4//C-FP SC device in 6 M KOH electrolyte delivered a comparable energy density of 28.32 Wh kg^{-1} with a corresponding high power density of 463.42 W kg^{-1} at a specific current of 1 A g^{-1}, as well as excellent stability with 92.6% capacity retention up to 10000 cycles. The device was observed to maintain a considerably high energy density of 22.22 Wh kg^{-1} with corresponding power density of 2285.49 W kg^{-1} at a high specific current of 5 A g^{-1}. The research provides an addition to the knowledge of 2D MXene-based composites and is useful in designing novel high-performance hybrid electrode materials with promising device efficiency for supercapacitors applications.

Chapter 5

5.1 Conclusions and future work

Graphene oxide, carbon nanorods as well as high quality carbon-based transition metal oxides/hydroxides composite materials have been successfully synthesized using various techniques. Electrochemical performance measurements and other characterizations indicated the as-synthesized materials as novel active electrode materials for hybrid supercapacitor applications. The morphological, structural and compositional characterization of the as-synthesized materials were carried out by using field emission scanning electron microscope (FE-SEM) equipped with an energy-dispersive X-ray spectrometer, transmission electron microscopy (TEM), X-ray powder diffraction (XRD), Raman spectroscopy, Fourier transform infrared (FTIR) spectroscopy, thermal gravimetric analysis (TGA), X-ray photoelectron spectroscopy (XPS) and X-ray fluorescence (XRF) spectroscopic analysis.

Graphene oxide (GO) gel and carbon nanorods obtained from the GO gel via a modified Hummers' method and a force-driven reflux process respectively, with improved morphological properties and surface chemistry via optimized oxygen-containing surface functionalities in this study has shown significant enhancement on the electrochemical performances of GO based electrode materials previously published in other studies.

In section 4.2, nanosheets of a ternary NiCo-MnO_2 composite electrode material were successfully synthesized by force-driven hydrolysis of hydrated transition metals nitrate salts. The ternary composite material was observed to display improved electrochemical properties

as compared to the intermediate nickel cobalt manganese triple hydroxide (NiCoMn-TH) and the initial NiCo(OH) materials synthesized via the same process. The NiCo-MnO_2 exhibited a specific capacity of 132.1 mAh g^{-1} at a current density of 0.5 A g^{-1}, with good stability over 2000 charge-discharge cycles. The complete asymmetrical cell displayed a specific capacitance of 130.67 F g^{-1}, high energy and power densities of 48.83 Wh kg^{-1} and 896.88 W kg^{-1} at 1 A g^{-1} respectively. An excellent cycling stability with a coulombic efficiency of 99.98% was recorded for up to 10,000 cycles at a current density of 3 A g^{-1}.

Section 4.3 depicted the results obtained from the Ti_3C_2-Mn_3O_4 nanocomposite electrode successfully synthesized by a solvothermal process. The material demonstrated an enhanced electrochemical performance with a maximum specific capacity of 128 mAh g^{-1} at a specific current of 1 A g^{-1}. The Ti_3C_2-Mn_3O_4 composite material illustrated satisfactory cycling stability as well as 77.65 % capacity retention for up to 2000 constant GCD cycles at 10 A g^{-1}. An assembled low cost hybrid Ti_3C_2-Mn_3O_4//C-FP SC device in 6 M KOH electrolyte delivered a comparable energy density of 28.32 Wh kg^{-1} with a corresponding high power density of 463.42 W kg^{-1} at a specific current of 1 A g^{-1}, as well as excellent stability with 92.6% capacity retention up to 10,000 cycles. The research provided an addition to the knowledge of two dimensional (2D) MXene-based composites, which is helpful in designing novel high-performance hybrid electrode materials with promising device efficiency for supercapacitors applications.

Generally, the outcomes of this study have provided the possibility of adopting carbon/carbon-based nanocomposite materials as novel electrode materials for energy storage devices applications such as supercapacitors and batteries. This study has also added to the research of energy storage devices with a focus on hybrid supercapacitor devices, by integrating the excellence of a supercapacitor with that of a rechargeable battery.

5.2 Future work

As a next step, the carbon nanorods electrode will be subjected to further testing of the electrochemical performance in other storage device technologies such as in lithium ion battery applications. Besides, all the materials in this study will be considered for further electrochemical testing in other electrolytes such as organic and ionic liquid electrolytes. The merits and demerits in using various electrolytes will be compared and analyzed, with a view to determining the best suitable electrolyte for hybrid supercapacitor applications.

Bibliography

[1] H. Sun, L. Cao, and L. Lu, "Bacteria promoted hierarchical carbon materials for high-performance supercapacitor," *Energy Environ. Sci.*, vol. 5, no. 3, p. 6206, 2012.

[2] P. Anastas and N. Eghbali, "Green Chemistry: Principles and Practice," *Chem. Soc. Rev.*, vol. 39, no. 1, pp. 301–312, 2010.

[3] A. G. Pandolfo and A. F. Hollenkamp, "Carbon properties and their role in supercapacitors," *J. Power Sources*, vol. 157, no. 1, pp. 11–27, 2006.

[4] L. L. Zhang and X. S. Zhao, "Carbon-based materials as supercapacitor electrodes," *Chem. Soc. Rev.*, vol. 38, no. 9, p. 2520, 2009.

[5] E. Frackowiak and F. Béguin, "Electrochemical storage of energy in carbon nanotubes and nanostructured carbons," *Carbon N. Y.*, vol. 40, no. 10, pp. 1775–1787, 2002.

[6] Y. P. Wu, E. Rahm, and R. Holze, "Carbon anode materials for lithium ion batteries," *J. Power Sources*, vol. 114, no. 2, pp. 228–236, 2003.

[7] B. J. Landi, M. J. Ganter, C. D. Cress, R. A. DiLeo, and R. P. Raffaelle, "Carbon nanotubes for lithium ion batteries," *Energy Environ. Sci.*, vol. 2, no. 6, p. 638, 2009.

[8] P. Simon and Y. Gogotsi, "Materials for electrochemical capacitors," *Nat. Mater.*, vol. 7, no. 11, pp. 845–854, Nov. 2008.

[9] B. E. Conway, "Electrochemical Supercapacitors - Scientific Fundamentals and | B. E. Conway | Springer." 1999.

[10] A. Nishino, "Capacitors: Operating principles, current market and technical trends," *J. Power Sources*, vol. 60, no. 2, pp. 137–147, 1996.

[11] G. Kickelbick, “Hybrid Materials – Past, Present and Future.,” *Hybrid Mater.*, vol. 1, no. 1, 2014.

[12] K. Naoi, “‘Nanohybrid capacitor’: The next generation electrochemical capacitors,” *Fuel Cells*, vol. 10, no. 5, pp. 825–833, 2010.

[13] A. Yoshino *et al.*, “Development of a Lithium-Type Advanced Energy Storage Device,” *J. Electrochem. Soc.*, vol. 151, no. 12, p. A2180, 2004.

[14] R. Kötz, R. Kötz, M. Carlen, and M. Carlen, “Principles and applications of electrochemical capacitors,” *Electrochim. Acta*, vol. 45, pp. 2483–2498, May 2000.

[15] D. P. Dubal, O. Ayyad, V. Ruiz, and P. Gómez-Romero, “Hybrid energy storage: the merging of battery and supercapacitor chemistries,” *Chem. Soc. Rev.*, vol. 44, no. 7, pp. 1777–1790, 2015.

[16] G. Wang, L. Zhang, and J. Zhang, “A review of electrode materials for electrochemical supercapacitors,” *Chem. Soc. Rev.*, vol. 41, pp. 797–828, 2012.

[17] K. O. Oyedotun, M. J. Madito, A. Bello, D. Y. Momodu, A. A. Mirghni, and N. Manyala, “Investigation of graphene oxide nanogel and carbon nanorods as electrode for electrochemical supercapacitor,” *Electrochim. Acta*, vol. 245, pp. 268–278, 2017.

[18] P. Simon and Y. Gogotsi, “Materials for electrochemical capacitors,” *Nat. Mater.*, vol. 7, no. 11, pp. 845–854, Nov. 2008.

[19] J. P. Cheng, J. Zhang, and F. Liu, “Recent development of metal hydroxides as electrode material of electrochemical capacitors,” *RSC Adv.*, vol. 4, no. 73, pp. 38893–38917, 2014.

[20] W. Zhang *et al.*, “Transition metal oxide and graphene nanocomposites for high-

performance electrochemical capacitors," *Phys. Chem. Chem. Phys.*, vol. 14, no. 47, pp. 16331–16337, 2012.

[21] H. Chen, L. Hu, Y. Yan, R. Che, M. Chen, and L. Wu, "One-step fabrication of ultrathin porous nickel hydroxide-manganese dioxide hybrid nanosheets for supercapacitor electrodes with excellent capacitive performance," *Adv. Energy Mater.*, vol. 3, no. 12, pp. 1636–1646, 2013.

[22] T. Deng *et al.*, "Atomic-level energy storage mechanism of cobalt hydroxide electrode for pseudocapacitors," *Nat. Commun.*, vol. 8, no. May, p. 15194, 2017.

[23] Z. Pan *et al.*, "Ultra-endurance flexible all-solid-state asymmetric supercapacitors based on three-dimensionally coated MnOx nanosheets on nanoporous current collectors," *Nano Energy*, vol. 26, pp. 610–619, 2016.

[24] H. X. Wang *et al.*, "Unifying miscellaneous performance criteria for a prototype supercapacitor via Co(OH)2active material and current collector interactions," *J. Microsc.*, vol. 267, no. 1, pp. 34–48, 2017.

[25] M. D. Stoller, S. Park, Z. Yanwu, J. An, and R. S. Ruoff, "Graphene-Based ultracapacitors," *Nano Lett.*, vol. 8, no. 10, pp. 3498–3502, Oct. 2008.

[26] H. Pan, J. Li, and Y. P. Feng, "Carbon nanotubes for supercapacitor," *Nanoscale Res. Lett.*, vol. 5, no. 3, pp. 654–668, 2010.

[27] M. Armand and J.-M. Tarascon, "Building better batteries," *Nature*, vol. 451, no. 7179, pp. 652–657, Feb. 2008.

[28] F. Zhang *et al.*, "A high-performance supercapacitor-battery hybrid energy storage device based on graphene-enhanced electrode materials with ultrahigh energy density,"

Energy Environ. Sci., vol. 6, no. 5, p. 1623, 2013.

[29] D. Institute of Fuel (Great Britain) and Elsevier Science Ltd., *Fuel and energy abstracts.*, vol. 4, no. 36. [Published on behalf of the Institute of Fuel by IPC Science and Technology Press], 1995.

[30] Thomas L. Floyd and David Buchla, *Electronics Fundamentals: Circuits, Devices & Applications*, 2009th ed. Upper Saddle River, NJ, USA: Prentice Hall Press , 2009.

[31] H. D. Abruna, Y. Kiya, and J. C. Henderson, "Batteries and Electrochemical Capacitors," *Phys. Today*, vol. 61, no. 12, pp. 43–47, 2008.

[32] G. Z. Chen, "Supercapacitor and supercapattery as emerging electrochemical energy stores," *International Materials Reviews*, vol. 62, no. 4. pp. 173–202, 2017.

[33] E. Frackowiak, "Electrode Materials with Pseudocapacitive Properties," in *Supercapacitors*, Weinheim, Germany: Wiley-VCH Verlag GmbH & Co. KGaA, 2013, pp. 207–237.

[34] Y. M. Vol'fkovich and T. M. Serdyuk, "Electrochemical capacitors," *Russian Journal of Electrochemistry*, vol. 38, no. 9. pp. 935–958, 2002.

[35] L. Yuan *et al.*, "Paper-Based Supercapacitors for Self-Powered Nanosystems," *Angew. Chemie Int. Ed.*, vol. 51, no. 20, pp. 4934–4938, May 2012.

[36] A. Lahyani, P. Venet, A. Guermazi, and A. Troudi, "Battery/Supercapacitors Combination in Uninterruptible Power Supply (UPS)," *IEEE Trans. Power Electron.*, vol. 28, no. 4, pp. 1509–1522, Apr. 2013.

[37] Y. Bin Tan and J.-M. Lee, "Graphene for supercapacitor applications," *J. Mater. Chem.*

A, vol. 1, no. 47, p. 14814, 2013.

[38] F. Béguin, E. Raymundo-Piñero, and E. Frackowiak, *Electrical Double-Layer Capacitors and Pseudocapacitors*. CRC Press, 2009.

[39] A. Bard, L. Faulkner, J. Leddy, and C. Zoski, *Electrochemical methods: fundamentals and applications*. 1980.

[40] F. Béguin, V. Presser, A. Balducci, and E. Frackowiak, "Carbons and electrolytes for advanced supercapacitors," *Adv. Mater.*, vol. 26, no. 14, pp. 2219–2251, 2014.

[41] M. A. Brown *et al.*, "Determination of Surface Potential and Electrical Double-Layer Structure at the Aqueous Electrolyte-Nanoparticle Interface," *Phys. Rev. X*, vol. 6, no. 1, p. 11007, Jan. 2016.

[42] B. F. F. Frackowiak E., "Carbon materials for the electrochemical storage of energy in capacitors ," *Carbon N. Y.*, vol. 39, pp. 937–950, 2001.

[43] G. G. Amatucci, F. Badway, A. Du Pasquier, and T. Zheng, "An Asymmetric Hybrid Nonaqueous Energy Storage Cell," *J. Electrochem. Soc.*, vol. 148, no. 8, p. A930, Aug. 2001.

[44] V. Khomenko, E. Raymundo-Piñero, and F. Béguin, "High-energy density graphite/AC capacitor in organic electrolyte," *J. Power Sources*, vol. 177, no. 2, pp. 643–651, Mar. 2008.

[45] T. Brousse, M. Toupin, and D. Bélanger, "A Hybrid Activated Carbon-Manganese Dioxide Capacitor using a Mild Aqueous Electrolyte," *J. Electrochem. Soc.*, vol. 151, no. 4, p. A614, Apr. 2004.

[46] M. M. Thackeray, C. Wolverton, and E. D. Isaacs, "Electrical energy storage for

transportation—approaching the limits of, and going beyond, lithium-ion batteries," *Energy Environ. Sci.*, vol. 5, no. 7, p. 7854, 2012.

[47] J. Xu, S. Dou, H. Liu, and L. Dai, "Cathode materials for next generation lithium ion batteries," 2013.

[48] A. J. Chmiola, G. Yushin, Y. Gogotsi, C. Portet, P. Simon, and P. L. Taberna, "Anomalous Capacitance Less Than Increase in Carbon at Pore Sizes," vol. 313, no. 5794, pp. 1760–1763, 2015.

[49] X. Zhang, X. Wang, L. Jiang, H. Wu, C. Wu, and J. Su, "Effect of aqueous electrolytes on the electrochemical behaviors of supercapacitors based on hierarchically porous carbons," *J. Power Sources*, vol. 216, pp. 290–296, Oct. 2012.

[50] Q. Pan, W. Tu, L. Ding, and G. Mi, "Characteristics of electric double layer in different aqueous electrolyte solutions for supercapacitors," *Wuhan Univ. J. Nat. Sci.*, vol. 17, no. 3, pp. 200–204, Jun. 2012.

[51] K. Fic, G. Lota, and E. Frackowiak, "Electrochemical properties of supercapacitors operating in aqueous electrolyte with surfactants," *Electrochim. Acta*, vol. 55, no. 25, pp. 7484–7488, 2010.

[52] K. Fic, G. Lota, and E. Frackowiak, "Effect of surfactants on capacitance properties of carbon electrodes," *Electrochim. Acta*, vol. 60, pp. 206–212, 2012.

[53] P. W. Ruch, D. Cericola, A. Foelske-Schmitz, R. Kötz, and A. Wokaun, "Aging of electrochemical double layer capacitors with acetonitrile-based electrolyte at elevated voltages," *Electrochim. Acta*, vol. 55, no. 15, pp. 4412–4420, Jun. 2010.

[54] E. Raymundo-Piñero, K. Kierzek, J. Machnikowski, and F. Béguin, "Relationship

between the nanoporous texture of activated carbons and their capacitance properties in different electrolytes," *Carbon N. Y.*, vol. 44, no. 12, pp. 2498–2507, Oct. 2006.

[55] T. Abdallah, D. Lemordant, and B. Claude-Montigny, "Are room temperature ionic liquids able to improve the safety of supercapacitors organic electrolytes without degrading the performances?," *J. Power Sources*, vol. 201, pp. 353–359, Mar. 2012.

[56] T. Sato, G. Masuda, and K. Takagi, "Electrochemical properties of novel ionic liquids for electric double layer capacitor applications," *Electrochim. Acta*, vol. 49, no. 21, pp. 3603–3611, Sep. 2004.

[57] C. Austen Angell, Y. Ansari, and Z. Zhao, "Ionic Liquids: Past, present and future," *Faraday Discuss.*, vol. 154, no. 0, pp. 9–27, Nov. 2012.

[58] M. Galiński, A. Lewandowski, and I. Stępniak, "Ionic liquids as electrolytes," *Electrochim. Acta*, vol. 51, no. 26, pp. 5567–5580, Aug. 2006.

[59] A. Lewandowski and A. Świderska-Mocek, "Ionic liquids as electrolytes for Li-ion batteries—An overview of electrochemical studies," *J. Power Sources*, vol. 194, no. 2, pp. 601–609, 2009.

[60] A. S. Aricò, P. Bruce, B. Scrosati, J.-M. Tarascon, and W. van Schalkwijk, "Nanostructured materials for advanced energy conversion and storage devices," *Nat. Mater.*, vol. 4, no. 5, pp. 366–377, May 2005.

[61] O. Barbieri, M. Hahn, A. Herzog, and R. Kötz, "Capacitance limits of high surface area activated carbons for double layer capacitors," *Carbon N. Y.*, vol. 43, no. 6, pp. 1303–1310, May 2005.

[62] B. E. Conway, *Electrochemical Supercapacitors*. Boston, MA: Springer US, 1999.

[63] H. Lee, M. S. Cho, I. H. Kim, J. Do Nam, and Y. Lee, "RuOx/polypyrrole nanocomposite electrode for electrochemical capacitors," *Synth. Met.*, vol. 160, no. 9–10, pp. 1055–1059, May 2010.

[64] E. Frackowiak and F. Béguin, "Carbon materials for the electrochemical storage of energy in capacitors," *Carbon N. Y.*, vol. 39, no. 6, pp. 937–950, May 2001.

[65] H. Zhang, G. Cao, and Y. Yang, "Carbon nanotube arrays and their composites for electrochemical capacitors and lithium-ion batteries," 2009.

[66] Y. Gogotsi *et al.*, "Nanoporous carbide-derived carbon with tunable pore size," *Nat. Mater.*, vol. 2, no. 9, pp. 591–594, Sep. 2003.

[67] V. Presser, M. Heon, and Y. Gogotsi, "Carbide-Derived Carbons - From Porous Networks to Nanotubes and Graphene," *Adv. Funct. Mater.*, vol. 21, no. 5, pp. 810–833, Mar. 2011.

[68] G. N. Yushin, E. N. Hoffman, A. Nikitin, H. Ye, M. W. Barsoum, and Y. Gogotsi, "Synthesis of nanoporous carbide-derived carbon by chlorination of titanium silicon carbide," *Carbon N. Y.*, vol. 43, no. 10, pp. 2075–2082, Aug. 2005.

[69] A. Bianco *et al.*, "All in the graphene family – A recommended nomenclature for two-dimensional carbon materials," *Carbon N. Y.*, vol. 65, pp. 1–6, Dec. 2013.

[70] K. S. Novoselov *et al.*, "Two-dimensional gas of massless Dirac fermions in graphene," *Nature*, vol. 438, no. 7065, pp. 197–200, Nov. 2005.

[71] K. S. Novoselov *et al.*, "Electric field effect in atomically thin carbon films.," *Science*, vol. 306, no. 5696, pp. 666–9, Oct. 2004.

[72] A. K. Geim and K. S. Novoselov, "The rise of graphene," *Nat. Mater.*, vol. 6, no. 3, pp.

183–191, Mar. 2007.

[73] A. Kumar and C. Huei, “Synthesis and Biomedical Applications of Graphene: Present and Future Trends,” in *Advances in Graphene Science*, InTech, 2013.

[74] C. Peng, J. Jin, and G. Z. Chen, “A comparative study on electrochemical co-deposition and capacitance of composite films of conducting polymers and carbon nanotubes,” *Electrochim. Acta*, vol. 53, no. 2, pp. 525–537, Dec. 2007.

[75] C. Arbizzani, M. Mastragostino, and L. Meneghello~, “POLYMER-BASED REDOX SUPERCAPACITORS: A COMPARATIVE STUDY,” *Electrochim. Acta*, vol. 41, no. 1, pp. 21–26, 1996.

[76] M. Kalaji, P. J. Murphy, and G. O. Williams, “The study of conducting polymers for use as redox supercapacitors,” *Synth. Met.*, vol. 102, no. 1–3, pp. 1360–1361, Jun. 1999.

[77] W. Li, J. Chen, J. Zhao, J. Zhang, and J. Zhu, “Application of ultrasonic irradiation in preparing conducting polymer as active materials for supercapacitor,” *Mater. Lett.*, vol. 59, no. 7, pp. 800–803, Mar. 2005.

[78] H. Li, J. Wang, Q. Chu, Z. Wang, F. Zhang, and S. Wang, “Theoretical and experimental specific capacitance of polyaniline in sulfuric acid,” *J. Power Sources*, vol. 190, no. 2, pp. 578–586, May 2009.

[79] M. Deschamps *et al.*, “Exploring electrolyte organization in supercapacitor electrodes with solid-state NMR,” *Nat. Mater.*, vol. 12, no. 4, pp. 351–358, Apr. 2013.

[80] J. P. Zheng, “The Limitations of Energy Density for Electrochemical Capacitors,” *J. Electrochem. Soc.*, vol. 144, no. 6, p. 2026, Jun. 1997.

[81] T. Liu, W. G. Pell, and B. E. Conway, “Self-discharge and potential recovery phenomena at thermally and electrochemically prepared RuO2 supercapacitor electrodes,” *Electrochim. Acta*, vol. 42, no. 23–24, pp. 3541–3552, Jan. 1997.

[82] Y. R. Ahn, M. Y. Song, S. M. Jo, C. R. Park, and D. Y. Kim, “Electrochemical capacitors based on electrodeposited ruthenium oxide on nanofibre substrates,” *Nanotechnology*, vol. 17, no. 12, pp. 2865–2869, Jun. 2006.

[83] M. Toupin, T. Brousse, and D. Bélanger, “Charge storage mechanism of MnO2 electrode used in aqueous electrochemical capacitor,” *Chem. Mater.*, vol. 16, no. 16, pp. 3184–3190, 2004.

[84] K.-C. Liu, “Porous Nickel Oxide/Nickel Films for Electrochemical Capacitors,” *J. Electrochem. Soc.*, vol. 143, no. 1, p. 124, Jan. 1996.

[85] Y. Gao, S. Chen, D. Cao, G. Wang, and J. Yin, “Electrochemical capacitance of Co3O4 nanowire arrays supported on nickel foam,” *J. Power Sources*, vol. 195, no. 6, pp. 1757–1760, Mar. 2010.

[86] N. Miura, S. Oonishi, and K. Rajendra Prasad, “Indium Tin Oxide/Carbon Composite Electrode Material for Electrochemical Supercapacitors,” *Electrochem. Solid-State Lett.*, vol. 7, no. 8, p. A247, Aug. 2004.

[87] X. Zhou, H. Chen, D. Shu, C. He, J. N.-J. of P. and C. of, and undefined 2009, “Study on the electrochemical behavior of vanadium nitride as a promising supercapacitor material,” *Elsevier*.

[88] L. Feng, Y. Zhu, H. Ding, and C. Ni, “Recent progress in nickel based materials for high performance pseudocapacitor electrodes,” *J. Power Sources*, vol. 267, pp. 430–

444, 2014.

[89] A. A. . Grupioni, E. Arashiro, and T. A. . Lassali, “Voltammetric characterization of an iridium oxide-based system: the pseudocapacitive nature of the Ir0.3Mn0.7O2 electrode,” *Electrochim. Acta*, vol. 48, no. 4, pp. 407–418, Dec. 2002.

[90] A. Bello *et al.*, “Stability studies of polypyrole- derived carbon based symmetric supercapacitor via potentiostatic floating test,” *Electrochim. Acta*, vol. 213, pp. 107–114, Sep. 2016.

[91] A. Bello, K. Makgopa, M. Fabiane, D. Dodoo-Ahrin, K. I. Ozoemena, and N. Manyala, “Chemical adsorption of NiO nanostructures on nickel foam-graphene for supercapacitor applications,” *J. Mater. Sci.*, vol. 48, no. 19, pp. 6707–6712, Oct. 2013.

[92] M. Inagaki, H. Konno, and O. Tanaike, “Carbon materials for electrochemical capacitors,” *J. Power Sources*, vol. 195, no. 24, pp. 7880–7903, Dec. 2010.

[93] D. Weingarth, A. Foelske-Schmitz, A. Wokaun, and R. Kötz, “PTFE bound activated carbon - A quasi-reference electrode for ionic liquids,” *Electrochem. commun.*, vol. 18, no. 1, pp. 116–118, Jan. 2012.

[94] D. Weingarth, A. Foelske-Schmitz, A. Wokaun, and R. Kotz, “PTFE Bound Activated Carbon - A Quasi Reference Electrode for Ionic Liquids and Its Application,” *ECS Trans.*, vol. 50, no. 11, pp. 111–117, Mar. 2013.

[95] D. Y. Momodu, Investigation of metal hydroxides graphene composites as electrode materials for supercapacitor applications. Diss. University of Pretoria, 2015.

[96] K. O. Oyedotun, M. J. Madito, D. Y. Momodu, A. A. Mirghni, T. M. Masikhwa, and N. Manyala, “Synthesis of ternary NiCo-MnO 2 nanocomposite and its application as a

novel high energy supercapattery device," *Chem. Eng. J.*, vol. 335, pp. 416–433, 2018.

[97] J. R. Miller and A. F. Burke, "Electric vehicle capacitor test procedures manual," *Idaho Natl. Eng. Lab. ...*, 1994.

[98] M. D. Stoller and R. S. Ruoff, "Best practice methods for determining an electrode material{'}s performance for ultracapacitors," *Energy Environ. Sci.*, vol. 3, no. 9, pp. 1294–1301, 2010.

[99] S. Shivakumara, B. Kishore, T. R. Penki, and N. Munichandraiah, "Symmetric supercapacitor based on partially exfoliated and reduced graphite oxide in neutral aqueous electrolyte," *Solid State Commun.*, vol. 199, pp. 26–32, Dec. 2014.

[100] F. Béguin and E. Frąckowiak, *Supercapacitors: Materials, Systems and Applications*. John Wiley & Sons, 2013.

[101] J. Zhang, J. P. Cheng, M. Li, L. Liu, F. Liu, and X. B. Zhang, "Flower-like nickel-cobalt binary hydroxides with high specific capacitance: Tuning the composition and asymmetric capacitor application," *J. Electroanal. Chem.*, vol. 743, pp. 38–45, 2015.

[102] T. M. Masikhwa *et al.*, "High performance asymmetric supercapacitor based on CoAl-LDH/GF and activated carbon from expanded graphite," *RSC Adv.*, vol. 6, no. 52, pp. 46723–46732, 2016.

[103] L. Demarconnay, E. Raymundo-Piñero, and F. Béguin, "Adjustment of electrodes potential window in an asymmetric carbon/MnO2 supercapacitor," *J. Power Sources*, vol. 196, no. 1, pp. 580–586, Jan. 2011.

[104] 2013. Electrochemical supercapacitors: scientific fundamentals and technological applications. Springer Science & Business Media Conway, B.E., *Electrochemical*

supercapacitors: scientific fundamentals and technological applications. 2013.

[105] A. Burke, "Ultracapacitors: Why, how, and where is the technology," *J. Power Sources*, vol. 91, no. 1, pp. 37–50, 2000.

[106] W. Zhang *et al.*, "Asymmetric electrochemical capacitors with high energy and power density based on graphene/CoAl-LDH and activated carbon electrodes," *RSC Adv.*, vol. 3, no. 7, p. 2483, Jan. 2013.

[107] W. Yang, Z. Gao, J. Wang, J. Ma, M. Zhang, and L. Liu, "Solvothermal One-Step Synthesis of Ni − Al Layered Double Hydroxide / Carbon Nanotube / Reduced Graphene Oxide Sheet Ternary Nanocomposite with Ultrahigh Capacitance for Supercapacitors," *ACS Appl. Mater. Interfaces*, vol. 5, no. 12, pp. 5443–54, Jun. 2013.

[108] P. L. Taberna, P. Simon, and J. F. Fauvarque, "Electrochemical Characteristics and Impedance Spectroscopy Studies of Carbon-Carbon Supercapacitors," *J. Electrochem. Soc.*, vol. 150, no. 3, p. A292, Mar. 2003.

[109] B. Akinwolemiwa, C. Peng, and G. Z. Chen, "Redox Electrolytes in Supercapacitors," *J. Electrochem. Soc.*, vol. 162, no. 5, pp. A5054–A5059, Jan. 2015.

[110] "Supercapacitors Materials, Systems and Applications - Google Books." .

[111] J. Kowal *et al.*, "Detailed analysis of the self-discharge of supercapacitors," *J. Power Sources*, vol. 196, no. 1, pp. 573–579, Jan. 2011.

[112] F. Barzegar, "Synthesis and characterization of activated carbon materials for supercapacitor applications," Apr. 2016.

[113] A. Laheäär *et al.*, *Appropriate methods for evaluating the efficiency and capacitive behavior of different types of supercapacitors*, vol. 60. Elsevier B.V., 2015, pp. 21–25.

[114] A. Lasia, “Electrochemical Impedance Spectroscopy and its Applications,” in *Modern Aspects of Electrochemistry*, Boston: Kluwer Academic Publishers, 2002, pp. 143–248.

[115] S. Trasatti, “Relative and absolute electrochemical quantities. Components of the potential difference across the electrode/solution interface,” *J. Chem. Soc. Faraday Trans. 1 Phys. Chem. Condens. Phases*, vol. 70, no. 28, p. 1752, Jan. 1974.

[116] D. G. Grahame, “The electrical double layer and the theory of electrocapillarity,” *Chemical Reviews*, vol. 41, no. 3. pp. 441–501, 1947.

[117] W. Sun, R. Zheng, and X. Chen, “Symmetric redox supercapacitor based on micro-fabrication with three-dimensional polypyrrole electrodes,” *J. Power Sources*, vol. 195, no. 20, pp. 7120–7125, Oct. 2010.

[118] L. Cui, J. Li, and X.-G. Zhang, “Preparation and properties of Co3O4 nanorods as supercapacitor material,” *J. Appl. Electrochem.*, vol. 39, no. 10, pp. 1871–1876, Oct. 2009.

[119] W. H. Jr and R. Offeman, “Preparation of graphitic oxide,” *J. Am. Chem. ...*, vol. 80, no. 6, pp. 1339–1339, 1958.

[120] K. Ojha, O. Anjaneyulu, and A. K. Ganguli, “Graphene-based hybrid materials: Synthetic approaches and properties,” *Curr. Sci.*, vol. 107, no. 3, pp. 397–418, 2014.

[121] N. Oger, Y. F. Lin, C. Labrugère, E. Le Grognec, F. Rataboul, and F.-X. Felpin, “Practical and scalable synthesis of sulfonated graphene,” *Carbon N. Y.*, vol. 96, pp. 342–350, Jan. 2016.

[122] *,† Nina I. Kovtyukhova *et al.*, “Layer-by-Layer Assembly of Ultrathin Composite Films from Micron-Sized Graphite Oxide Sheets and Polycations,” 1999.

[123] M. Ciszewski, A. Mianowski, P. Szatkowski, G. Nawrat, and J. Adamek, “Reduced graphene oxide–bismuth oxide composite as electrode material for supercapacitors,” *Ionics (Kiel).*, vol. 21, no. 2, pp. 557–563, Feb. 2015.

[124] H. Z. Kister, *Distillation design*. McGraw-Hill, 1992.

[125] D.-W. Wang *et al.*, “The examination of graphene oxide for rechargeable lithium storage as a novel cathode material,” *J. Mater. Chem. A*, vol. 1, no. 11, p. 3607, 2013.

[126] H. D. Alvarenga, T. Van De Putte, N. Van Steenberge, J. Sietsma, and H. Terryn, “Influence of Carbide Morphology and Microstructure on the Kinetics of Superficial Decarburization of C-Mn Steels,” *Metall. Mater. Trans. A Phys. Metall. Mater. Sci.*, vol. 46, no. 1, pp. 123–133, Jan. 2015.

[127] K. Xiao, H. Wu, H. Lv, X. Wu, and H. Qian, “The study of the effects of cooling conditions on high quality graphene growth by the APCVD method,” *Nanoscale*, vol. 5, no. 12, p. 5524, May 2013.

[128] G. Demazeau and A. Largeteau, “Hydrothermal/solvothermal crystal growth: An old but adaptable process,” *Zeitschrift fur Anorganische und Allgemeine Chemie*, vol. 641, no. 2. WILEY-VCH Verlag, pp. 159–163, 01-Feb-2015.

[129] G. Demazeau, “Solvothermal processes: Definition, key factors governing the involved chemical reactions and new trends,” *Zeitschrift fur Naturforschung - Section B Journal of Chemical Sciences*, vol. 65, no. 8. pp. 999–1006, 2010.

[130] G. Demazeau, “Solvothermal and hydrothermal processes: The main physico-chemical factors involved and new trends,” in *Research on Chemical Intermediates*, 2011, vol. 37, no. 2–5, pp. 107–123.

[131] J. S. Bunch, “Mechanical and Electrical Properties of Graphene Sheets,” *Chem. ...*, no. May, pp. 1–140, 2008.

[132] Somsubhraghosh, V. Sowjanyabomma, P. Laxmiprasanna, Srivani, and Davidbhanji, “NewAnalyticalMethodsinNanotechnology-AReview,” *AsianJ.Res.Pharm.Sci*, vol. 3, pp. 31–41, 2013.

[133] F. G. BELL, “Engineering Geology and Geotechnics,” *Eng. Geol. Geotech.*, pp. 95–144, 1980.

[134] Cullity B.D. ; Stock S.R., *Elements of X-RAY diffraction*, vol. 20, no. 1. Taylor & Francis Group, 2001.

[135] D. L. Dorset, “X-ray Diffraction: A Practical Approach,” *Microsc. Microanal.*, vol. 4, no. 5, pp. 513–515, Oct. 1998.

[136] C. Qiuzi, Y. geoscientist. Xiang, and H. physicist. Li, *Multifunctional two- and three-dimensional polycrystalline X-ray diffractometry*. Bentham Science Publishers, 2011.

[137] Y. C. Tseng *et al.*, “Using Visible Laser-Based Raman Spectroscopy to Identify the Surface Polarity of Silicon Carbide,” *J. Phys. Chem. C*, vol. 120, no. 32, pp. 18228–18234, Aug. 2016.

[138] et al. L.G. Cançado, K. Takai, T. Enoki, M. Endo, Y.A. Kim, H. Mizusaki, “General equation for the determination of the crystallite size L[sub a] of nanographite by Raman spectroscopy,” *Appl. Phys. Lett*, vol. 88, p. 163106, 2006.

[139] R. B. C. A. Jorio, C.A. Achete, E.H.M. Ferreira, L.G. Cançado, *Measuring disorder in graphene with Raman spectroscopy*. INTECH Open Access Publisher, 2011.

[140] M. A. Pimenta, G. Dresselhaus, M. S. Dresselhaus, L. G. Cançado, A. Jorio, and R.

Saito, “Studying disorder in graphite-based systems by Raman spectroscopy,” *Phys. Chem. Chem. Phys.*, vol. 9, no. 11, pp. 1276–1290, 2007.

[141] C. Casiraghi *et al.*, “Raman Spectroscopy of Graphene Edges,” *Nano Lett.*, vol. 9, no. 4, pp. 1433–1441, Apr. 2009.

[142] P. R. Griffiths and J. A. De Haseth, *Fourier transform infrared spectrometry*. Wiley-Interscience, 2007.

[143] S. Brunauer, L. S. Deming, W. E. Deming, and E. Teller, “On a Theory of the van der Waals Adsorption of Gases,” *J. Am. Chem. Soc.*, vol. 62, no. 7, pp. 1723–1732, Jul. 1940.

[144] G. (Gerhard) Ertl and Wiley InterScience (Online service), *Handbook of heterogeneous catalysis*. Wiley-VCH, 2008.

[145] G. Ertl *et al.*, *Handbook of Heterogeneous Catalysis*, vol. 1. Weinheim, Germany: Wiley-VCH Verlag GmbH, 2008.

[146] K. S. W. Sing, “Reporting physisorption data for gas/solid systems with special reference to the determination of surface area and porosity (Recommendations 1984),” *Pure Appl. Chem.*, vol. 57, no. 4, pp. 603–619, Jan. 1985.

[147] X. Liu and W. Yu, “Evaluating the thermal stability of high performance fibers by TGA,” *J. Appl. Polym. Sci.*, vol. 99, no. 3, pp. 937–944, Feb. 2006.

[148] J. A. Reyes-Labarta and A. Marcilla, “Kinetic study of the decompositions involved in the thermal degradation of commercial azodicarbonamide,” *J. Appl. Polym. Sci.*, vol. 107, no. 1, pp. 339–346, Jan. 2008.

[149] S. Hüfner, *Photoelectron Spectroscopy: Principles and Applications*, Third. New York,

2003.

[150] D. J. Kalnicky and R. Singhvi, “Field portable XRF analysis of environmental samples,” *J. Hazard. Mater.*, vol. 83, no. 1–2, pp. 93–122, May 2001.

[151] L. Vincze, “Confocal X-ray Fluorescence Imaging and XRF Tomography for Three-Dimensional Trace Element Microanalysis,” *Microsc. Microanal.*, vol. 11, no. S02, 2005.

[152] C. Jiang *et al.*, “Hydrothermal synthesis of Ni(OH)2 nanoflakes on 3D graphene foam for high-performance supercapacitors,” *Electrochim. Acta*, vol. 173, pp. 399–407, Aug. 2015.

[153] J. Yan, Q. Wang, T. Wei, and Z. Fan, “Recent Advances in Design and Fabrication of Electrochemical Supercapacitors with High Energy Densities,” *Adv. Energy Mater.*, vol. 4, no. 4, p. 1300816, Mar. 2014.

[154] Y. Mao *et al.*, “Cycling stability of ultrafine β-Ni(OH)2 nanosheets for high capacity energy storage device via a multilayer nickel foam electrode,” *Electrochim. Acta*, vol. 211, pp. 44–51, 2016.

[155] Z. S. Wu *et al.*, “Anchoring hydrous RuO2 on graphene sheets for high-performance electrochemical capacitors,” *Adv. Funct. Mater.*, vol. 20, no. 20, pp. 3595–3602, 2010.

[156] W. Wang *et al.*, “Hydrous ruthenium oxide nanoparticles anchored to graphene and carbon nanotube hybrid foam for supercapacitors.,” *Sci. Rep.*, vol. 4, p. 4452, Jan. 2014.

[157] M. Zhou, H. Chai, D. Jia, and W. Zhou, “The glucose-assisted synthesis of a graphene nanosheet–NiO composite for high-performance supercapacitors,” *New J. Chem.*, vol.

38, no. 6, p. 2320, 2014.

[158] D. Han *et al.*, "Trisodium citrate assisted synthesis of hierarchical NiO nanospheres with improved supercapacitor performance," *J. Power Sources*, vol. 235, pp. 45–53, 2013.

[159] K. Wang, X. Zhang, X. Zhang, D. Chen, and Q. Lin, "A novel Ni(OH)2/graphene nanosheets electrode with high capacitance and excellent cycling stability for pseudocapacitors," *J. Power Sources*, vol. 333, pp. 156–163, 2016.

[160] J. Huang *et al.*, "Asymmetric supercapacitors based on β-Ni(OH)2 nanosheets and activated carbon with high energy density," *J. Power Sources*, vol. 246, pp. 371–376, 2014.

[161] T. Meng, Q.-Q. Xu, Y.-T. Li, X.-Y. Xing, C.-S. Li, and T.-Z. Ren, "Graphene Supported Ni-based Nanocomposites as Electrode Materials with High Capacitance," *Electrochim. Acta*, vol. 155, pp. 69–77, 2015.

[162] H. X. Wang *et al.*, "Unifying miscellaneous performance criteria for a prototype supercapacitor via $Co(OH)_2$ active material and current collector interactions," *J. Microsc.*, vol. 267, no. 1, pp. 34–48, 2017.